The impact of protein oxidation on kinase-mediated phosphorylation and cardiac myocyte contractile function

Dissertation

In fulfillment of the requirements for the degree

Doctor of Natural Sciences

Submitted to the Department of Chemistry,

Faculty of Mathematics, Informatics and Natural Sciences

at the

University of Hamburg

by

Simon Diering

from Hamburg

Hamburg 2019

Dissertation approved for publication: 22.03.2019

Reviewer I: Prof. Dr. Friederike Cuello

Reviewer II: Prof. Dr. Christian Betzel

This dissertation was performed at the Institute of Experimental Pharmacology and Toxicology of the University Medical Center Hamburg-Eppendorf between October 2014 and February 2019.

I. List of publications

1. Donzelli S, Goetz M, Schmidt K, Wolters M, Stathopoulou K, **Diering S**, Prysyazhna O, Polat V, Scotcher J, Dees C, Subramanian H, Butt E, Kamynina A, Schobesberger S, King SB, Nikolaev VO, de Wit C, Leichert LI, Feil R, Eaton P, Cuello F (2017) Oxidant sensor in the cGMP-binding pocket of PKGIα regulates nitroxyl-mediated kinase activity. Sci Rep, 7:9938

2. Stathopoulou K, Wittig I, Heidler J, Piasecki A, Richter F, **Diering S**, van der Velden J, Buck F, Donzelli S, Schröder E, Wijnker PJM, Voigt N, Dobrev D, Sadayappan S, Eschenhagen T, Carrier L, Eaton P, Cuello F (2016) S-glutathiolation impairs phosphoregulation and function of cardiac myosin-binding protein C in human heart failure. FASEB J, 30:1849–1864

3. Abstract: ISHR XXII World Congress TU-033 **Diering S**, Goetz M, Schobesberger S, Pasch S, Donzelli S, Stathopoulou K, Piasecki A, King SB, Nikolaev VO, Lutz S, Eaton P, Cuello F (2016) Oxidative activation of cAMP-dependent protein kinase by nitroxyl modulates myofilament protein phosphorylation. J Mol Cell Cardiol

4. Abstract: 15th Dutch-German Joint Meeting of the Molecular Cardiology Groups **Diering S**, Goetz M, Schmidt K, Prysyazhna O, de Wit C, Eaton P, Cuello F (2017) Intradisulfide bond formation in PKGIα by nitroxyl induces vasorelaxation *in vitro* and *in vivo*.

5. Abstract: 34th Meeting of the European Section of the ISHR **Diering S**, Goetz M, Schobesberger S, Stathopoulou K, Piasecki A, Nikolaev VO, Eaton P, Cuello F (2017) Exposure of adult rat ventricular myocytes to nitroxyl induces activation of cAMP-dependent protein kinase through interdisulfide formation and substrate targeting. J Mol Cell Cardiol

II. Table of contents

III. List of figures

IV. List of tables

V. List of abbreviations

Abbreviation	Meaning
(v/v)	Volume per volume
(w/v)	Weight per volume
(w/w)	Weight per weight
$[Ca^{2+}]_i$	Intracellular calcium
µL	Microliter(s)
µm	Micrometer(s)
µmol	Micromole(s)
µU	Microunit(s)
249Asp/250Cys	C1-M-C2 protein with amino acid exchange of cysteine for aspartate at position 249 and serine for cysteine at position 250
3'	3'-End of a single stranded oligonucleotide or DNA strand
4Ala	C1-M-C2 protein with amino acid exchange of serine for alanine at positions 275, 284, 304 and 311
5'	5'-End of a single stranded oligonucleotide or DNA strand
5Ala	C1-M-C2 protein with amino acid exchange of serine for alanine at positions 250, 275, 284, 304 and 311
AC	Adenylate cyclase
ADHF	Acute decompensated heart failure
AI	Autoinhibitory domain
AKAP	A-kinase anchoring protein
AKAR3-NES	FRET-biosensor A-kinase activity reporter 3 coupled to a nuclear export signal
approx.	Approximately
APS	Ammonium persulfate
ARVM	Adult rat ventricular myocyte
AS	Angeli's salt
ATP	Adenosine triphosphate
B56α	A regulatory subunit of protein phosphatase 2A
BDM	2,3-Butanedione monoxime
BirA-cMyBP-C	Fusion protein consisting of cardiac myosin-binding protein C and the myc-tagged biotin protein ligase BirA
BL	Baseline
BL21	Cells from a chemically competent strain of *Escherichia coli*
BSA	Bovine serum albumin
C1-M-C2	Recombinant protein consisting of the N-terminal C1, M and C2 domains of cardiac myosin-binding protein C
Ca_{50}	Concentration of calcium required for 50% maximal activation
CaMKII	Ca^{2+}/calmodulin-dependent protein kinase II
cAMP	3',5'-Cyclic adenosine monophosphate
CFP	Cyan fluorescent protein
cGMP	3',5'-Cyclic guanosine monophosphate
cMyBP-C	Cardiac myosin-binding protein C

cTnC	Cardiac troponin C
cTnI	Cardiac troponin I
cTnT	Cardiac troponin T
CXL	Short for CXL-1020
CXL-1020	Nitroxyl donor compound tested as a treatment for acute decompensated heart failure
CXL-1051	Organic scaffold generated by decomposition of CXL-1020
Cys	Cysteine
Cy^{TM}2	Cyanine^{TM} 2 fluorophore
D/D	Dimerization and docking
DAPI	4′,6-Diamidino-2-phenylindole
DCM	Dilated cardiomyopathy
DH5α^{TM}	*Escherichia coli* bacteria with high transformation efficiency
DIA	Diamide
DiFMUP	6,8-Difluoro-4-methylumbelliferyl phosphate
dL/dt max	Maximal change in (sarcomere) length over time
DMSO	Dimethyl sulfoxide
DNA	Deoxyribonucleic acid
dNTP mix	Mixture of deoxyribonucleotide triphosphates: dATP, dCTP, dGTP and dTTP
DPBS	Dulbecco's phosphate-buffered saline
DTT	Dithiothreitol
E. coli	*Escherichia coli*
EC coupling	Excitation-contraction coupling
ECL^{TM}	Enhanced chemiluminescence^{TM}
EDTA	Ethylenediaminetetraacetic acid
EGTA	Ethylene glycol bis-(β-aminoethyl ether) N,N,N′,N′-tetraacetic acid
EHT	Engineered heart tissue
ELISA	Enzyme-linked immunosorbent assay
ET	Endothelin 1
EZ-Link®	Product line of Thermo-Fisher Scientific
F(ab‘)$_2$	Antigen-binding antibody fragment, generated by pepsin digestion
Fig.	Figure
For	Forward
FOR	Forskolin
FRET	Förster resonance energy transfer
GAPDH	Glyceraldehyde 3-phosphate dehydrogenase
GRK2	G protein-coupled receptor kinase 2
GRK5	G protein-coupled receptor kinase 5
GSH	Reduced form of L-glutathione
GSK3β	Glycogen synthase kinase 3
GSSG	Oxidized form of L-glutathione
h	Hour(s)
H-89	Protein kinase inhibitor with greatest effect on PKA

HBSS	Hanks' Balanced Salt Solution
HEPES	4-(2-Hydroxyethyl)-1-piperazineethanesulfonic acid
hiPSC	Human induced pluripotent stem cell
His	Histidine
HPLC	High-performance liquid chromatography
HRP	Horseradish peroxidase
IB	Western immunoblot
IBMX	3-Isobutyl-1-methylxanthine
ICM	Ischemic cardiomyopathy
IgG	Immunoglobulin G
IPTG	Isopropyl β-D-1-thiogalactopyranoside
IS	Inhibitor sequence
ISHR	International Society for Heart Research
ISO	Isoprenaline
kDa	Kilodalton
KO	knockout
L	Liter(s)
l	(Sarcomere) length
LB	Lysogeny broth
max	maximal
mg	Milligram(s)
min	Minute(s)
mL	Milliliter(s)
MLC2v	Myosin light chain 2v
mmol	Millimole(s)
MOI	Multiplicity of infection
MS	Mass spectrometry
MW	Molecular weight
MyBP-C	Myosin-binding protein C
NC	Nitrocellulose
NCA	1-Nitrosocyclohexyl acetate
NF	Non-failing
NGS	Normal goat serum
Ni-NTA	Nickel-charged affinity resin containing nitrilotriacetic acid
NKA	Na^+, K^+-ATPase
NKY80	Adenylate cyclase inhibitor with selectivity for type V and VI
nmol	Nanomole(s)
NR	Non-reducing
ns	Not significant
OA	Okadaic acid
OD_{492}	Optical density measured at a wavelength of 492 nm
OD_{600}	Optical density measured at a wavelength of 600 nm
ODQ	Inhibitor of soluble guanylate cyclase
PA linker	Proline/alanine-rich linker region
PCR	Polymerase chain reaction
PE	Phenylephrine

PEG	Polyethylene glycol
PFA	Paraformaldehyde
PKA	cAMP-dependent protein kinase A
PKA-C	cAMP-dependent protein kinase A, catalytic subunit
PKA-RI	cAMP-dependent protein kinase A, RI regulatory subunit
PKCμ	Protein kinase C isoform μ, also known as protein kinase D
PKCε	Protein kinase C isoform ε
PKD	Protein kinase D, also known as PKCμ
PKGIα	cGMP-dependent protein kinase isoform Iα
PLA	Proximity ligation assay
PLN	Phospholamban
pmol	Picomole(s)
pp.	pages
PP2A	Phosphoprotein phosphatase 2A
PP2A-C	Phosphoprotein phosphatase 2A, catalytic subunit
pSer	Phosphorylated amino acid serine
PTM	Posttranslational modification
PVDF	Polyvinylidene difluoride
R	Reducing
R^2	Coefficient of determination
Rev	Reverse
R_f	Retardation factor
RFU	Relative fluorescence units
RIPA buffer	Radioimmunoprecipitation assay buffer
RNS	Reactive nitrogen species
ROCK1	Rho-associated protein kinase isoform 1
ROCK2	Rho-associated protein kinase isoform 2
ROS	Reactive oxygen species
RSK2	Ribosomal S6 kinase 2
RT	Room temperature
RyR2	Ryanodine receptor isoform 2
s	Second(s)
S2	Subfragment 2
SDS	Sodium dodecyl sulfate
SDS-PAGE	Sodium dodecyl sulfate-polyacrylamide gel electrophoresis
Ser	Serine
Ser250Ala	C1-M-C2 protein with amino acid exchange of the amino acid serine for alanine at position 250
Ser250Asp	C1-M-C2 protein with amino acid exchange of the amino acid serine for aspartate at position 250
SERCA2a	Sarcoplasmic/endoplasmic reticulum Ca^{2+} ATPase 2a
Sf21	Insect cell line from pupal ovarian tissue of *Spodoptera frugiperda* used for recombinant protein expression
Sf9	Insect cell line from a clone of *Spodoptera frugiperda* Sf21 cells used for recombinant protein expression
sGC	Soluble guanylate cyclase

SOC	Super Optimal broth with catabolite repression
SR	Sarcoplasmic reticulum
SW	Switch helix
$t_{1/2}$	Half-life
Tab.	Table
TBS	Tris-buffered saline
TBST	Tris-buffered saline containing 0.1% Tween® 20
TEMED	N,N,N′,N′-Tetramethylethylenediamine
U	unit
UK	United Kingdom
USA	United States of America
vs.	*Versus*
WT	Wild type
XL10-Gold®	*Escherichia coli* cells with very high transformation efficiency
YFP	Yellow fluorescent protein
β-AR	β-Adrenergic receptor
γ-^{32}P-ATP	Adenosine triphosphate containing radioactive phosphorus-32 on the gamma phosphate group

1 Abstract

Pathologies, such as cancer, inflammatory and cardiac diseases are commonly associated with long-term increased production and release of reactive oxygen species referred to as oxidative stress. Thereby, oxidation of target proteins conferring protein dysfunction contributes to disease progression. Importantly, trials to scavenge oxidants by systemic antioxidant therapy failed. This observation supports the notion that oxidants are indispensable physiological signaling molecules that induce oxidative posttranslational modifications in target proteins. The signaling function of oxidants can even be exploited therapeutically, as it was shown for HNO donors, a class of compounds that act by protein oxidation. HNO donors exert beneficial effects on cardiovascular function and are considered as potential candidates for the clinical treatment of heart failure. Although protein phosphorylation is the main mechanism that governs positive inotropic effects in cardiac myocytes, information is scarce on how acute protein oxidation by HNO leads to the observed enhancement of cardiac myocyte contractile function. To gain understanding of the underlying molecular mechanisms is crucially important as these compounds are tested for their clinical potential to treat patients with acute decompensated heart failure.

This PhD thesis provides a thorough characterization of the molecular mechanisms that are responsible for the positive inotropic effects of experimental (1-nitrosocyclohexyl acetate; NCA) and clinical (CXL-1020) HNO donor compounds. Unexpectedly, experiments performed in adult rat ventricular myocytes revealed that exposure to HNO released by HNO donor compounds enhanced the net phosphorylation state of cardiac myocyte proteins that regulate excitation-contraction coupling. Using Förster resonance energy transfer technology, gel electrophoresis under non-reducing conditions and subcellular protein fractionation, HNO-mediated translocation and activation of the redox-sensitive cAMP-dependent protein kinase (PKA) was found that apparently is responsible for integration of the oxidant stimulus into substrate protein phosphorylation. Furthermore, there is experimental evidence shown that in addition to oxidative activation of PKA, HNO released by CXL-1020 strongly inhibited the oxidant-susceptible protein phosphatase 2A, thus additionally contributing to the observed enhancement in substrate protein phosphorylation. The data obtained during this PhD thesis allow the conclusion that there are significant molecular and functional differences evoked by established HNO donor compounds that strongly recommend characterization of each individual donor before its clinical application. Furthermore, in line with results obtained from human cardiac tissue, the data support the conclusion that phosphorylation remains the main posttranslational modification that reliably triggers enhancement in contractile function by direct modulation of cardiac myocyte proteins. Accordingly, the biological effects of oxidants seem to be substantially determined by their impact on protein phosphorylation.

1.1 Zusammenfassung

Oxidativer Stress bezeichnet die unkontrollierte langandauernde Produktion und Freisetzung von reaktiven Sauerstoff- und Stickstoffspezies. Zudem ist oxidativer Stress an der Entstehung und Progression einer Vielzahl von Erkrankungen, wie beispielsweise Krebs, Entzündung und Herz-Kreislauferkrankungen, maßgeblich beteiligt. Klinische Studien, in denen die systemische Therapie mit Antioxidanzien untersucht wurde, zeigten keinen Behandlungserfolg bei Patienten, sondern verschlechterten im Gegenteil die Symptome. Dieser Befund unterstützt die allgemeine Auffassung, dass endogen produzierte Oxidanzien wichtige Signalmoleküle darstellen, die durch gezielte oxidative posttranslationale Modifikation von Zielproteinen an der zellulären Signaltransduktion beteiligt und damit für die Aufrechterhaltung physiologischer Prozesse unverzichtbar sind. Die Wirkungen von Oxidanzien können sogar therapeutisch genutzt werden. So bewirkt beispielsweise die Behandlung mit der Säure des reduzierten Stickstoffmonoxids, die als Nitroxyl (HNO) bezeichnet wird, eine positiv inotrope und vasorelaxierende Wirkung, die gegenwärtig klinisch in Patienten mit akuter dekompensierter Herzinsuffizienz untersucht wird. Dabei ist jedoch ungeklärt, wie diese pro-oxidativ wirkenden HNO-Donatoren in Kardiomyozyten ihren positiv inotropen Effekt ausüben, der üblicherweise über Änderungen in der Phosphorylierung von Proteinen vermittelt wird, die an der elektromechanischen Kopplung beteiligt sind.

Die Ergebnisse dieser Doktorarbeit liefern eine umfassende Charakterisierung der molekularen Wirkmechanismen, die die positiv inotrope Wirkung experimenteller (1-Nitrosocyclohexylacetat; NCA) und klinischer (CXL-1020) HNO-Donatoren zu erklären versucht. Interessanterweise zeigten Experimente, die in adulten linksventrikulären Ratten-kardiomyozyten durchgeführt wurden, eine vermehrte HNO-vermittelte Phosphorylierung von Proteinen, die an der elektromechanischen Kopplung beteiligt sind. Mittels Förster-Resonanz-Energie-Transfer-Technologie, nicht-reduzierender Gelelektrophorese und subzellulärer Fraktionierung konnte die erhöhte Phosphorylierung auf die oxidative Aktivierung der cAMP-abhängigen Proteinkinase zurückgeführt werden. Zusätzlich konnte gezeigt werden, dass die HNO-Freisetzung durch CXL-1020 zu einer oxidativen Inhibition der Proteinphosphatase 2A führt, was somit einen Beitrag zu der erhöhten Phosphorylierung leisten könnte. Die Ergebnisse dieser Doktorarbeit erlauben die Schlussfolgerung, dass etablierte HNO-Donatoren signifikante Unterschiede in ihren molekularen Wirkmechanismen aufweisen, was eine individuelle Charakterisierung vor der klinischen Applikation dringend erforderlich macht. Im Einklang mit Daten, die in humanem Herzgewebe erhoben wurden, unterstützen diese Resultate die allgemeine Auffassung, dass der Phosphorylierungszustand an der Kontraktion beteiligter Proteine direkt und zuverlässig mit Änderungen in der kontraktilen Antwort korreliert. Die Wirkung von Oxidanzien scheint demnach wesentlich durch die verschiedenartigen Einflüsse auf die Proteinphosphorylierung bestimmt zu sein

2 Introduction

2.1 Cardiac function

The heart muscle supplies the body with nutrients and oxygen, continuously pumping blood through the circulatory system at a rate of 60-100 beats per minute for a lifetime. An approximate sum of 100 000 beats pumping about 7500 L of blood per day highlights the impressive performance of this organ, which only has the size of a closed fist and weighs about 350 or 425 g in female or male adults, respectively (Kumar et al. 2014). The heart is separated into four chambers, two atria and two ventricles. The interatrial and interventricular septa divide the heart into a left and a right compartment. Atrioventricular valves, more specifically named tricuspid (right) and bicuspid or mitral (left) valve, connect the right and left atria to the subjacent right and left ventricles. Blood derived from the anterior and posterior venae cavae enters the right atrium, is pumped into the right ventricle by passing the tricuspid valve and is eventually ejected through the pulmonary valve into the pulmonary artery. In this way, the right half of the heart directs blood that is low in oxygen to the lungs, where it becomes oxygenated. The pulmonary veins supply oxygenated blood to the left atrium, which forwards it to the left ventricle through the bicuspid valve. Contraction of the left ventricle pumps the blood through the aortic valve into the aorta, resulting in the supply of oxygenated blood to the circulation of the body (Katz 2006, pp. 3-4).

2.1.1 The cardiac myocyte

The mammalian heart is composed of various cell types with endothelial cells, fibroblasts and cardiac myocytes being most abundant (Zhou and Pu 2016). The contractile function of the heart muscle, which produces the rhythmic cycle of influx (relaxation) and ejection (contraction) of blood, is accounted to the cardiac myocytes. These cells constitute 18 to 35% of the cardiac cells (Nag 1980; Bergmann et al. 2015; Raulf et al. 2015) and represent approx. 70 to 85% of the heart volume (Mattfeldt et al. 1986; Tang et al. 2009). Cardiac myocytes are cylindrical, elongated cells, which are roughly 20 µm wide and 100 µm long. Adjacent cardiac myocytes are longitudinally connected end to end via intercalated discs. These structures contain desmosomes and adherens junctions to provide mechanical stability of the cell-cell connection, while gap-junctions allow electrical and metabolic coupling of adjacent cells (Vermij et al. 2017). Cardiac myocytes are packed with rod-like contractile bundles, which lengthwise extend through the cells and occupy roughly half of the cell volume (Page 1978). These myofibrils are enveloped by a membranous tubular network, called sarcoplasmic reticulum (SR), which serves as Ca^{2+} storage and plays an essential role for rhythmic contraction. Another network, represented by T-tubules, transverse invaginations of the plasma membrane that also run in the immediate vicinity of the myofibrils, pervades the cardiac myocytes. Providing an interface

to the extracellular space that reaches deep into the cell, T-tubules allow rapid and simultaneous responses to action potentials and extracellular stimuli.
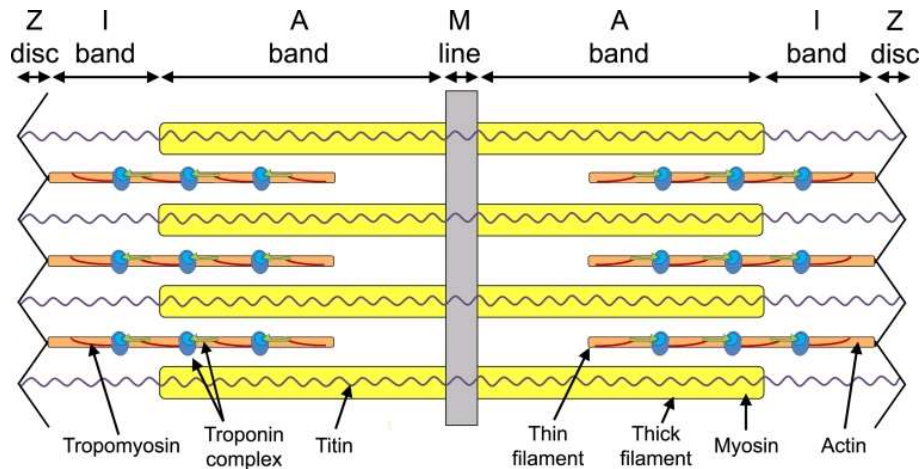
Figure 1: Schematic depiction of striated muscle sarcomere organization The Z-discs (black, vertical) represent the borders of the sarcomere. Thin actin filaments (orange) are anchored to the Z-disc and reach towards the center of the sarcomere. Tropomyosin (red) and the troponin complex (blue and green) are associated with the thin filaments. Thick myosin filaments (yellow) extend over the central M-line (grey) and are aligned by titin filaments (black, horizontal) that reach from Z-disc to M-line. A-band denotes the area of thick filaments with partial overlap of thin filaments. The thick filament-lacking region in proximity to the Z-disc is referred to as I-band. From England and Loughna (2013).

Myofibrils consist of a multitude of basic, aligned units, called sarcomeres, which represent the smallest functional unit of the muscle (Fig. 1; Katz 2006, pp. 18-22). The sarcomeric structure of striated muscle is determined by myosin (thick) filaments, which are surrounded by an array of six actin (thin) filaments each. In the longitudinal direction, the sarcomere is delimited by Z-discs (from German 'Zwischenscheibe' for 'between disc'). These transversal protein structures that in cardiac myocytes have an approx. width of 120 nm are mainly composed of α-actinin (Rowe 1973; Frank and Frey 2011). The length of resulting sarcomeres ranges from approx. 1.8 to 2.2 μm (Rodriguez et al. 1992). While the thin filaments are anchored in the Z-disc, the thick filaments are located in the center of the sarcomere, spreading across the M-line (from German 'Mittelscheibe' for 'middle disc'). Analyzed by polarized light microscopy, this distribution of filaments results in the visibility of a certain substructure, from which the naming of sarcomeric areas is originated: The pale space in proximity to the Z-disc that is not superimposed by thick filaments is referred to as the I-band (from 'isotropic'). The section in which thick filaments are present and partially overlay with thin filaments was named A-band (from 'anisotropic'). The alternation of I- and A-bands accounts for the striated appearance of cardiac and other types of striated muscle when viewed under a microscope. A third type of filaments composed of the giant structural protein titin reaches from Z-disc to M-line and provides sarcomere flexibility, passive tension and alignment of myosin filaments (Maruyama et al. 1985; Fürst et al. 1989; Granzier and Irving 1995). The thin actin filament of the sarcomere is associated with tropomyosin and the troponin complex (Farah and Reinach 1995; Katrukha 2013). Tropomyosin consists of an α-helical double strand and lies within the α-

helical groove of the actin filament. The troponin complex is exclusive to skeletal and cardiac muscle and in the heart consists of cardiac troponin C (cTnC), cardiac troponin I (cTnI) and cardiac troponin T (cTnT). CTnC has the ability to bind Ca^{2+}, while cTnI anchors the protein complex on the actin filament and cTnT interacts with tropomyosin. Tropomyosin and troponin play important roles in the regulation of cardiac contraction. Another essential sarcomeric protein, cardiac myosin-binding protein C (cMyBP-C), is located within the so-called C-zones of the A-band located on both sides of the M-line. Besides structural functions, cMyBP-C is an important regulator of cardiac contractility, which will be described in more detail below (see 2.2).

The sliding filament theory, which explains muscle movement as a sliding motion of sarcomeric muscle proteins past each other, was almost simultaneously introduced by two groups in 1954 (Huxley and Hanson 1954; Huxley and Niedergerke 1954). The observation that the length of the A-band remained unchanged during sarcomere contraction, while the I-band shortened, revealed that the reduction in sarcomere length was entirely attributed to a movement of the Z-discs towards the M-line. In accordance with this model, it is nowadays well established that muscle contraction is based on myosin filaments that move along the surrounding actin filaments towards the Z-discs, resulting in a shortening of the sarcomere (Lin et al. 2017). Cardiac myosin is a hexameric protein that consists of two heavy and four light chains. The two heavy chains form a rod-shaped coiled-coil tail domain, which represents the major part of the myosin filament backbone, while two head-like motor domains extend towards the actin filaments. According to proteolytic fragments obtained from digestion with trypsin and papain, myosin heavy chains can be divided into light meromyosin (tail section), subfragment 1 (motor domain) and subfragment 2 (S2; hinge region). In addition, two light chains (regulatory and essential light chain) are associated with each flexible hinge region that connects the tail and motor domains. During muscle contraction, myosin motor domains bind to actin of adjacent thin filaments. Following hydrolysis of adenosine triphosphate (ATP), the motor domains undergo a conformational change that mediates a movement of the myosin heads along the actin filaments (Cooke 1997; Fitts 2008). Moving the thick filaments towards the Z-discs, this actomyosin interaction, which is also referred to as cross-bridge cycling, results in the shortening of the cardiac sarcomere and, in the bigger scale, cardiac contraction.

2.1.2 Excitation and contraction

Obviously, proper cardiac function demands a tightly synchronized contractile movement of atrial and ventricular cardiac myocytes. Synergistic contraction is achieved through the function of specialized cardiac myocytes of the sinoatrial node, which is located in the upper wall of the right atrium. These non-contractile pacemaker cells have an increased conductance for Na^+ ions, which allows the spontaneous entry of Na^+ into the cells. Due to its unusual nature, this ion current of pacemaker cells is referred to as the 'funny current' (DiFrancesco and Borer

2007; DiFrancesco 2010). The influx of Na^+ results in an increase of the cellular membrane potential and, once it has reached a certain threshold, the opening of voltage-gated Ca^{2+} channels. Positively charged Na^+ and Ca^{2+} ions streaming into the cell cause the plasma membrane to depolarize, generating an action potential, which is transmitted to the cardiac myocytes of the atria, where it induces contraction. The action potential propagates to the atrioventricular node located at the lower section of the interatrial septum between atria and ventricles, where forwarding is slightly slowed down. This delay provides time for atrial contraction and entry of the blood into the ventricles. Via the bundles of His, the action potential is then quickly directed to the apex of both ventricles and further carried to the ventricular walls by Purkinje fibers. This fast conduction of the electrical excitation consequently allows the ventricles to contract in unison (Katz 2006, pp. 413-420 and 427-434).

In ventricular cardiac myocytes, the propagation of an action potential that originates from the sinoatrial node results in a small influx of Na^+ and Ca^{2+} ions through gap junctions. This causes the membrane potential to increase, reaching a threshold that triggers the opening of numerous high conductance voltage-gated Na^+ channels located within the plasma membrane of the cell (phase 0). Consequently, a burst of Na^+ diffuses into the cell and causes both rapid depolarization of the membrane and reclosing of Na^+ channels. Instead, the altered membrane potential induces the opening of transient voltage-gated K^+ channels, leading to an outward K^+ current that results in partial membrane repolarization and is represented by a 'notch' in the action potential (phase 1). Na^+-induced depolarization of the plasma membrane also causes the delayed activation of voltage-gated L-type Ca^{2+} channels, which are located in the T-tubular membrane and mediate an inward current of Ca^{2+}. A simultaneous flow of K^+ and Ca^{2+} in opposite direction accounts for the delay in repolarization, that manifests as the plateau phase in the action potential of ventricular cardiac myocytes (phase 2). Eventual closing of the Ca^{2+} channels with a sustained outward K^+ current causes the plasma membrane to repolarize (phase 3). The resting membrane potential (phase 4) is largely determined by K^+ channels and is near the equilibrium potential of K^+. Ca^{2+} ions that have entered the cell during the action potential are exported by the Na^+/Ca^{2+} exchanger. The Na^+/K^+-ATPase (NKA) transports Na^+ that had streamed in during phase 0 out of the cell (Bers 2008; Santana et al. 2010; Bartos et al. 2015).

The processes that are involved in the translation of an electrical stimulus into a mechanical contraction of the heart are summarized as excitation-contraction coupling (EC coupling). The essential mediator for EC coupling is Ca^{2+}. During the plateau phase (phase 2) of the action potential, Ca^{2+} enters the ventricular cardiac myocytes through L-type Ca^{2+} channels. The binding of Ca^{2+} to type 2 ryanodine receptors (RyR2) positioned in the membrane of the SR triggers a Ca^{2+}-induced Ca^{2+} release of even more Ca^{2+} from the SR. In the sarcomeres, Ca^{2+} binds to cTnC of the troponin complex, which is associated with tropomyosin at the actin

filaments. A conformational change of cTnC results in a movement that shifts tropomyosin along the actin filament, providing accessibility to myosin binding sites on the actin filament that had been buried. Consequently, actomyosin interaction and cross-bridge cycling are enabled and mediate cardiac contraction. The sarcomeres relax when Ca^{2+} is reimported into the SR by the sarcoplasmic/endoplasmic reticulum Ca^{2+} ATPase 2a (SERCA2a). The decrease in Ca^{2+} causes tropomyosin to move back into the α-helical groove of the actin filament, where it obstructs the interaction of actin and myosin until the next action potential occurs (Bers 2002, 2008; Kobayashi and Solaro 2005). Contraction and relaxation phases of the heart muscle are referred to as systole and diastole, respectively.

2.2 Cardiac myosin-binding protein C (cMyBP-C)

A cardiac protein of the contractile apparatus that has been and still is the subject of detailed investigation is cMyBP-C. During the isolation of myosin from skeletal muscle 47 years ago, Starr and Offer (1971) observed contaminations with several myosin-binding proteins. The impurity bands, which they detected in Coomassie-stained gels were labeled alphabetically. Soon after, the contaminant corresponding to band 'C' was characterized and, after initial designation as 'C-protein' (Offer et al. 1973), named myosin-binding protein C (MyBP-C). There are three isoforms of MyBP-C expressed in human muscle. A slow skeletal, a fast skeletal and a cardiac isoform exist, each of them encoded by a separate gene (Weber et al. 1993; Gautel et al. 1995). In cardiac tissue, however, only cMyBP-C is expressed.
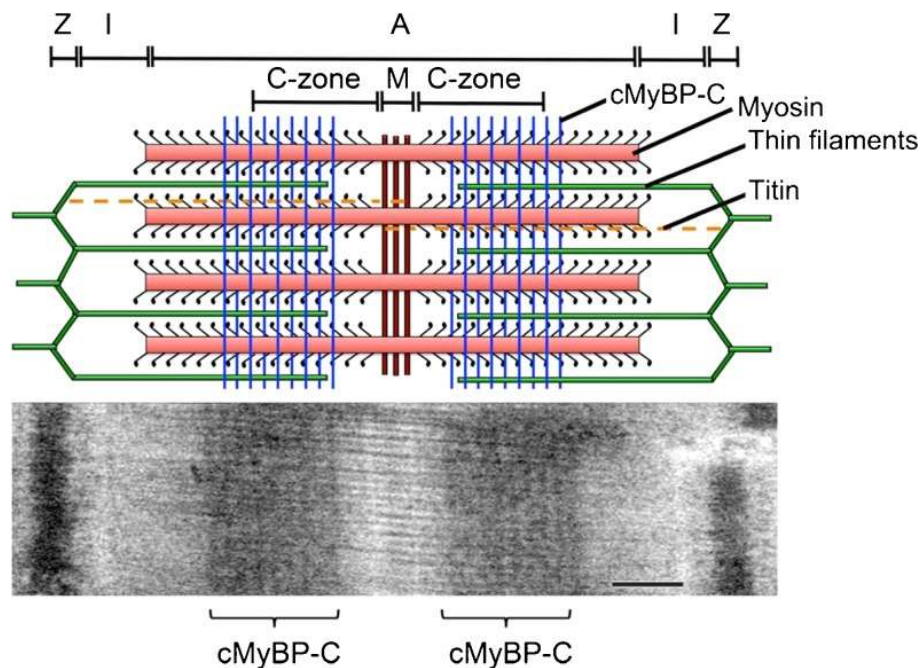
Figure 2: Illustration of the sarcomeric localization of cardiac myosin-binding protein C **Top:** Within the sarcomere of cardiac muscle, cardiac myosin-binding protein C (cMyBP-C) is located at the cross-bridge-bearing C-zones within the A-bands, where it appears as 7-9 transversal stripes that extend over thick myosin and thin actin filaments. **Bottom:** The localization of immunolabeled cMyBP-C of rat cardiac sarcomere is visualized by electron microscopy. Scale bar: 200 nm. From Sadayappan and de Tombe (2012).

MyBP-C is a single polypeptide chain and is located in the C-zone of sarcomeric A-bands, where it forms periodic stripes that transversally cross the actin and myosin filaments (Fig. 2). For cMyBP-C, the presence of 7-9 stripes at 43 nm-intervals was determined in the C-zones of the cross-bridge bearing region on both sides of the M-line (Luther et al. 2008). Notably, this periodicity matches with the pitch of sarcomeric myosin filaments, where three myosin motor domains are distributed in one rotation of 42.9 nm (Huxley and Brown 1967). Initially, a mainly structural function was attributed to cMyBP-C, however, sarcomere stability is maintained upon chemical extraction from the sarcomere (Hofmann et al. 1991). Moreover, mice that lack cMyBP-C still display the typical striated pattern of sarcomeres (Harris et al. 2002). Instead, constitutive cMyBP-C knockout (KO) mice develop cardiac hypertrophy and enhanced sarcomeric sensitivity for Ca^{2+}, which is paralleled by impairment of contraction and relaxation (Harris et al. 2002; Carrier et al. 2004). These findings suggested a regulatory role for cMyBP-C.
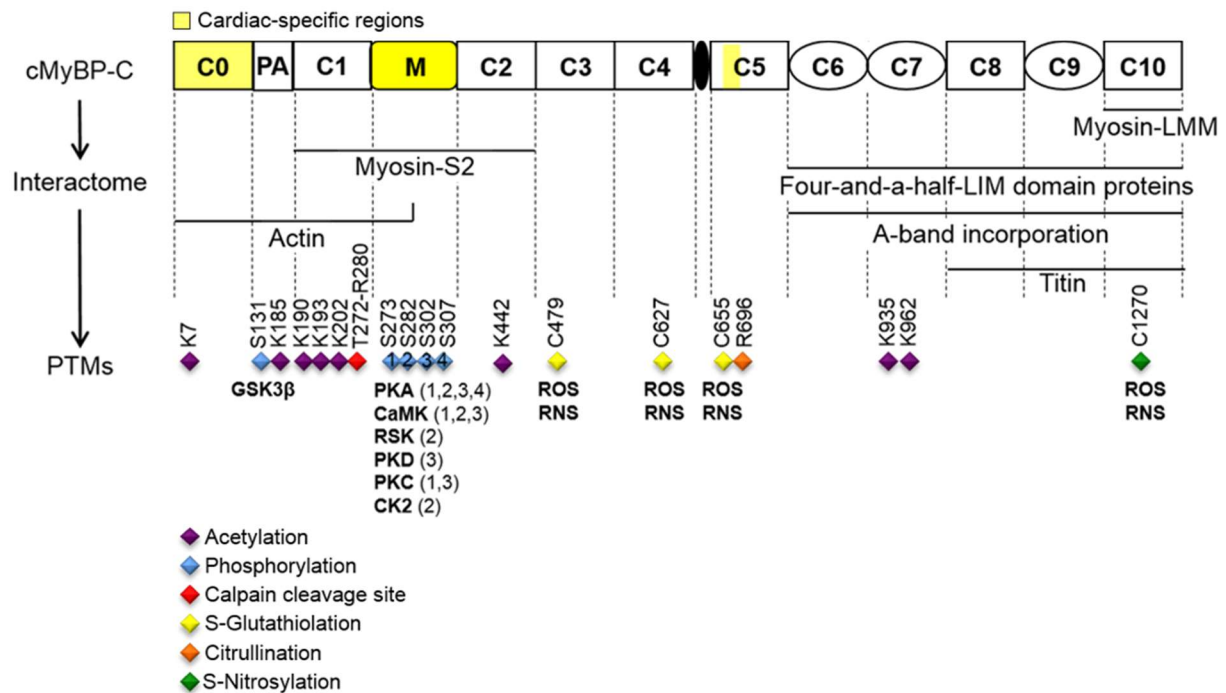
Figure 3: Schematic overview of the cMyBP-C domain structure, interactome and posttranslational modifications The multidomain protein comprises 8 immunoglobulin-like (square) and 3 fibronectin type III-like (circle) domains. Specific to the cardiac isoform are the N-terminal C0 domain, the M-motif located between C1 and C2 and the 28-amino acid sequence within the C5 domain (yellow). PA depicts a proline/alanine-rich linker region. Another linker exists between the domains C4 and C5 (black oval). CMyBP-C contains N-terminal interaction sites for actin and the S2 hinge region of myosin. C-terminal domains mediate thick filament-incorporation and allow interaction with titin and four-and-a-half-LIM domain proteins. Diverse posttranslational modifications (PTMs) of cMyBP-C are indicated below at the reported sites of modification as diamonds (numbering refers to the mouse sequence): Acetylation (purple), phosphorylation (blue), calpain cleavage (red), S-glutathiolation (yellow), citrullination (orange) and S-nitrosylation (green). Protein kinases responsible for phosphorylation at the different phosphorylation sites are indicated below. For M-motif phosphorylation, the phosphorylation sites for each protein kinase are enclosed in brackets. Modified from Carrier et al. (2015).

cMyBP-C has a theoretical mass of 140.8 kDa and consists of 8 immunoglobulin-like and 3 fibronectin type III-like domains (Fig. 3). Additional features specific to the cardiac isoform are the N-terminal C0 domain, an insertion of 28 amino acids within the C5 domain and an N-

terminal motif (M-motif) that contains multiple phosphorylation sites (Kasahara et al. 1994; Gautel et al. 1995; Yasuda et al. 1995). Via its C10 domain, cMyBP-C interacts with light meromyosin (Okagaki et al. 1993; Alyonycheva et al. 1997), which mediates the correct incorporation of its C-terminus into the myosin filaments (Moos et al. 1975). In addition, the N-terminal C1, M and C2 domains of cMyBP-C can bind to the myosin S2 hinge region near the motor domain (Starr and Offer 1978; Gruen and Gautel 1999). While the C-terminus of cMyBP-C also contains binding sites for titin (Fürst et al. 1992), an N-terminal stretch including C0 and the proline/alanine-rich (PA) linker allows interaction with thin actin filaments (Kulikovskaya et al. 2003; Bhuiyan et al. 2012). Although the exact orientation of cMyBP-C in the sarcomere is still not fully understood, different models consensually suggest a C-terminal incorporation into the thick filament (considering binding sites for light meromyosin and titin), with the more flexible N-terminus reaching towards the actin filaments (referring to proposed interaction with myosin S2 and actin; Moolman-Smook et al. 2002; Squire et al. 2003).

2.2.1 Posttranslational modifications regulate cMyBP-C function

A multitude of posttranslational modifications (PTMs) has been reported for cMyBP-C. Acetylation can occur at eight lysine amino acid residues present in the N- and C-termini (Govindan et al. 2012) and citrullination was detected at Arg696 (Fert-Bober and Sokolove 2014). However, the functional impact of these PTMs remains unknown. In contrast, phosphorylation of cMyBP-C has proven to be of major importance for physiological heart function and appears to be the main event through which cMyBP-C exerts its regulatory role. At least three serine residues susceptible to phosphorylation, Ser275, Ser284 and Ser304 (referring to the human sequence; corresponding to Ser273, Ser282 and Ser302 in the mouse sequence), exist within the N-terminal M-motif. Several protein kinases, such as cAMP-dependent protein kinase (PKA), Ca^{2+}/calmodulin-dependent protein kinase II (CaMKII), protein kinase D (PKD) and cGMP-dependent protein kinase G (PKG) have been identified to mediate phosphorylation of at least one of these sites (Jeacocke and England 1980; Schlender and Bean 1991; Bardswell et al. 2010, 2012; Thoonen et al. 2015). Another M-motif phosphorylation site was suggested to involve Ser311 (Jia et al. 2010); for Ser133 of the PA linker region phosphorylation by glycogen synthase kinase 3β (GSK3β) was reported (Kuster et al. 2013). Phosphorylation of the prominent M-motif sites occurs in a hierarchical manner, with Ser284 being the main site, whose modification facilitates phosphorylation of Ser275 and Ser304 (Gautel et al. 1995; Sadayappan et al. 2011).
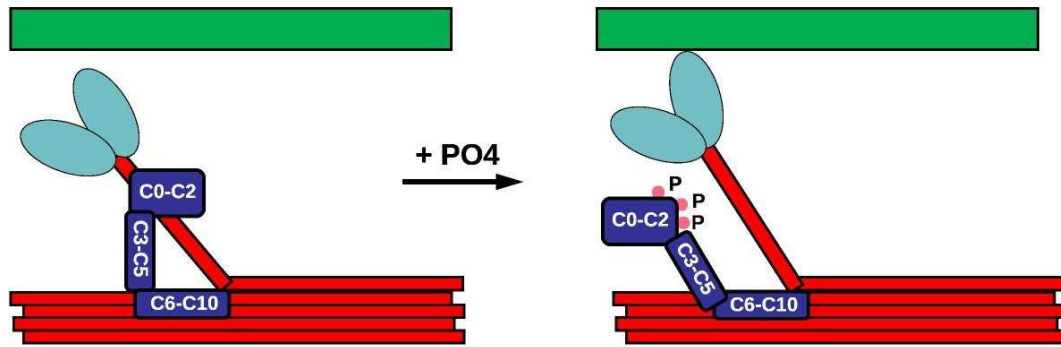
Figure 4: Simplified representation showing the regulation of actomyosin interaction by cMyBP-C phosphorylation In the unphosphorylated state the N-terminal domains of cMyBP-C (blue) bind to the S2 hinge region of thick filament myosin (red) and constrain the interaction between myosin and actin (green). Phosphorylation (+PO$_4$) of the cMyBP-C M-motif present between the C1 and C2 domains abolishes the interaction with myosin S2, resulting in enhanced actomyosin interaction and cross-bridge cycling. Modified from Ababou et al. (2008).

In the unphosphorylated state, an N-terminal stretch of cMyBP-C including the M-motif binds to myosin S2, obstructing the interaction of myosin heads with actin of the thin filaments (Fig. 4). Importantly, this break is released upon phosphorylation of M-motif sites (Gruen et al. 1999; Sadayappan et al. 2006), which results in unrestricted cross-bridge cycling and, consequently, enhanced contraction (positive inotropy; Jeacocke and England 1980; Stelzer et al. 2006). Moreover, M-motif phosphorylation is also required for accelerated cardiac relaxation (positive lusitropy), which involves cMyBP-C-mediated alterations in sarcomere Ca^{2+} sensitivity (Cazorla et al. 2006; Pohlmann et al. 2007). This was demonstrated in mice that express non-phosphorylatable cMyBP-C with functional impairments concerning both contraction and relaxation as a consequence (Sadayappan et al. 2005). The importance of cMyBP-C phosphorylation at the different serine residues of the M-motif was thoroughly investigated by the use of a multitude of phosphodeficient and phosphomimetic recombinant variants of cMyBP-C (Sadayappan et al. 2005, 2006, 2011; Nagayama et al. 2007; Gupta et al. 2013; Gupta and Robbins 2014). These studies confirmed the crucial importance of Ser284, but also showed that overall cMyBP-C phosphorylation was beneficial and indispensable for unperturbed cardiac function. Reduced phosphorylation levels that were detected in failing human hearts further emphasize the crucial role of cMyBP-C phosphorylation for cardiac health (El-Armouche et al. 2007; Copeland et al. 2010; Kooij et al. 2013).

Importantly, cMyBP-C is also subject to irreversible (carbonylation; Stathopoulou et al. 2016) and reversible oxidative modification. S-nitrosylation was detected at one single site at the very C-terminus of cMyBP-C in response to treatment with S-nitrosoglutathione, but no information is available regarding the physiological significance of this modification (Kohr et al. 2011). Oxidative S-glutathiolation was first described for cMyBP-C by Brennan et al. (2006b). Akin to phosphorylation, S-glutathiolation is a reversible modification that has the potential to alter protein function (Humphries et al. 2002; Rao and Clayton 2002). It describes the binding of the tripeptide glutathione (GSH) to the cysteine thiol group of a protein, resulting in the formation

of a mixed disulfide. GSH is a highly abundant low molecular weight antioxidant that prevents damage to cellular components by the reduction and neutralization of reactive oxygen species (ROS; Meister 1988; Forman et al. 2009). Oxidized GSH forms dimers (GSSG), which are retransformed to GSH by the action of cellular glutathione reductase (Couto et al. 2016). However, during conditions of enhanced oxidant load, the ratio between GSH and GSSG shifts towards the more reactive GSSG. As a consequence, disulfide exchange reactions can result in the S-glutathiolation of thiol-containing proteins (Dalle-Donne et al. 2009; Hill and Bhatnagar 2012). In a mouse model of experimentally induced hypertension, diastolic dysfunction was paralleled by enhanced levels of S-glutathiolation of a protein matching the molecular weight of cMyBP-C (Lovelock et al. 2012). Subsequently, S-glutathiolation sites were identified within the N-terminus of cMyBP-C, which were shown to exert a negative crosstalk with phosphorylation of the nearby critical M-motif serine residues. The finding that low levels of phosphorylation coincided with strong S-glutathiolation in human tissue from cardiomyopathy patients was in line with the observed crosstalk and suggests a rather detrimental role of S-glutathiolation in the development of cardiac disease, which demands detailed investigation (Stathopoulou et al. 2016).

2.3 Protein kinase and phosphatase signaling in cardiac myocytes

Protein phosphorylation is one of the most investigated PTMs and represents a major molecular mechanism for the regulation of protein function (Ardito et al. 2017). Protein kinase-mediated phosphorylation is involved in practically every cellular signaling pathway and largely contributes to the translation of extracellular stimuli into a cellular response. A critical characteristic of protein phosphorylation is its reversibility, which is achieved through the orchestrated action of protein kinases and phosphatases that allows regulated and repeated signaling. In cardiac myocytes, the activity of numerous proteins that facilitate contraction and Ca^{2+} cycling is regulated by phosphorylation. As outlined for cMyBP-C above, protein phosphorylation can directly modify cardiac contractility and is the major mechanism for the adaptation of heart function in response to changes in sympathetic tone.

2.3.1 cAMP-dependent protein kinase (PKA)

During exercise or under conditions of excitement, cardiac output is augmented primarily via the release of noradrenaline and adrenaline from nerves of the sympathetic nervous system. In the heart, the catecholamines mainly bind to $G_{S\alpha}$ protein-coupled β_1- and β_2-adrenergic receptors ($\beta_{1/2}$-AR) located at the plasma membrane of cardiac myocytes. Intracellularly, $\beta_{1/2}$-AR activation facilitates the generation of cyclic AMP (cAMP) from ATP by membrane-associated adenylate cyclases 5 and 6 (AC5/6; Defer et al. 2000). The second messenger cAMP subsequently leads to the activation of PKA, which elicits positive cardiac inotropy and lusitropy (Posner et al. 1965; Walsh et al. 1968). PKA was first described by Walsh et al.

(1968), who purified the cAMP-dependent enzyme from rabbit skeletal muscle. The crystal structure of the PKA catalytic subunit (PKA-C), which was solved in 1991, was the first structure of a protein kinase to be established (Knighton et al. 1991). To date, PKA is the best-characterized member of the kinome. Within the group of AGC protein kinases, PKA represents one of the 14 kinase subtypes. The inactive PKA holoenzyme is composed of two catalytic subunits, which are inhibited by a dimer of regulatory subunits (PKA-R). Binding of two molecules of cAMP to each of the regulatory subunits induces the release of the catalytic subunits, which represents the active form of the kinase that consequently catalyzes the transfer of a phosphate group from ATP to a substrate protein.

In human tissue, three isoforms of PKA-C are expressed, Cα, Cβ and Cγ. Cα is found ubiquitously, while Cβ is mainly restricted to the nervous system and expression of Cγ seems to be exclusive to testis (Beebe et al. 1990; Fagerberg et al. 2014). Two types of regulatory subunits, RI (PKA-RI) and RII, exist for PKA and association with either of the two renders the holoenzyme as PKA type I or type II. The expression of the two types of regulatory subunits differs strongly between tissues. In the heart, PKA-RI activity was found to prevail (Corbin et al. 1975). PKA-R subunits can be further divided into RIα, RIβ, RIIα and RIIβ. In general, the α-isoforms are expressed ubiquitously, while β subunits display higher tissue specificity. Transcripts for PKA-RIβ were detected in brain and testis but not in the heart (Clegg et al. 1988; Cadd and McKnight 1989), where the α-isoform appears to dominate (Krall et al. 1999; Fagerberg et al. 2014). The catalytic subunit of PKA contains the catalytic core and sites for substrate docking and ATP binding. The different isoforms of the regulatory subunit share the same basic architecture (Fig. 5). At the N-terminus a dimerization and docking (D/D) domain exists, which mediates RI dimerization. It is followed by a substrate-like inhibitor sequence that reaches into the active site cleft of PKA-C in the cAMP-unbound state (Kim et al. 2005). Approx. two thirds of the protein consist of the two cAMP-binding domains, which extend to the C-terminus of the subunit (Taylor et al. 2008).
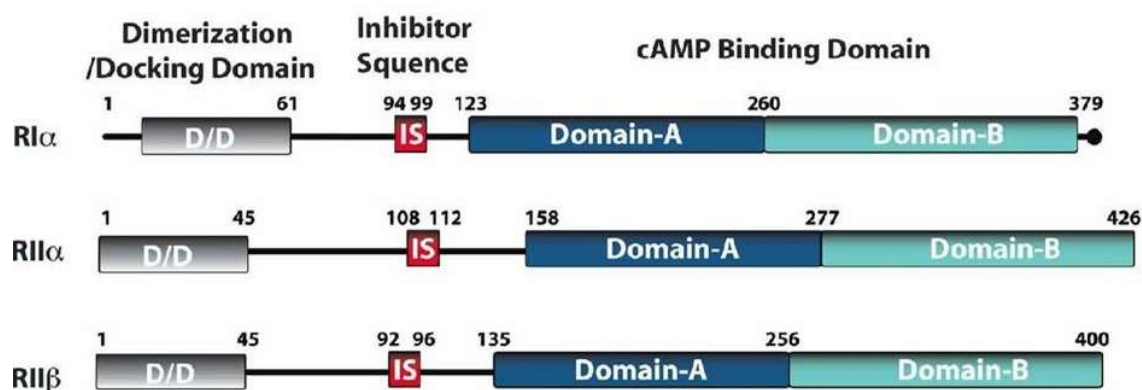
Figure 5: Domain structure of PKA regulatory subunits Consistently, the isoforms of PKA regulatory subunits possess an N-terminal dimerization and docking domain (D/D), which is followed by an inhibitor sequence (IS) that inhibits PKA-C activity in the absence of cAMP. The largest part of the proteins consists of two cAMP-binding domains (domain-A/B), which extend to the C-terminus. Modified from Taylor et al. (2008).

The main targets of PKA in the heart are proteins involved in EC coupling. PKA-mediated phosphorylation of the α_{1C} (Ser1928) and the β_2 subunits (Ser479/479) of plasma membrane-associated L-type Ca^{2+} channels leads to enhanced Ca^{2+} import and thus promotes the inotropic response (Gao et al. 1997; Bünemann et al. 1999). In the SR membrane, phospholamban (PLN) and RyR2 are susceptible to phosphorylation by PKA. PLN is associated with SERCA2a at the SR and inhibits SERCA2a-mediated import of Ca^{2+}. This effect is abolished upon phosphorylation of PLN at Ser16, resulting in an accelerated Ca^{2+} import into the SR, which contributes to the lusitropic effects observed in response to PKA activation, and consequently allows a profound Ca^{2+} release via the RyR2 during systole (Tada and Kirchberger 1976; Wegener et al. 1989; Kim et al. 1990). RyR2 function is also amplified upon PKA-mediated phosphorylation, leading to accelerated Ca^{2+} release and contraction (Marx et al. 2000). In the sarcomere, PKA phosphorylates cMyBP-C and cTnI. CMyBP-C phosphorylation at all three sites of the M-motif releases its brake function on myosin S2 and thereby allows accelerated cross-bridge cycling, resulting in enhanced contraction (Gautel et al. 1995; Sadayappan and de Tombe 2012). Moreover, cMyBP-C phosphorylation has been associated with improved sarcomere relaxation by reducing Ca^{2+} sensitivity (Sadayappan et al. 2005; Cazorla et al. 2006; Pohlmann et al. 2007). PKA-mediated phosphorylation of cTnI of the troponin complex at Ser23/24 (Perry and Cole 1974; Mittmann et al. 1990) reduces the Ca^{2+} affinity of the cTnC subunit, thereby further contributing to decreased Ca^{2+} sensitivity of the sarcomere and acceleration of cardiac relaxation during diastole (Robertson et al. 1982; Garvey et al. 1988; Kentish et al. 2001). Taken together, activation of PKA results in elevated cardiac performance with positive inotropic, lusitropic and chronotropic (increase in heart rate) effects (Sequeira et al. 2014).

While type I PKA is mainly present in the cytosol (Brennan et al. 2004, 2006a), a large proportion of PKA type II is associated with the cell membrane or other subcellular structures (Corbin et al. 1977). This association was shown to be mediated by the interaction of RII subunits with scaffold proteins named A-kinase anchoring proteins (AKAPs). AKAPs are crucial mediators of intracellular signaling, which localize PKA to subcellular compartments, thereby allowing fine-tuned spatiotemporal regulation of PKA activity. Some of these scaffolding proteins possess additional binding sites for other enzymes, such as cAMP-degrading phosphodiesterases, protein phosphatases or other protein kinases, supporting their function as intracellular signaling hubs (Klauck et al. 1996; Carlisle Michel et al. 2004). All AKAPs share an amphipathic helix, which mediates the interaction with a hydrophobic groove on the surface of the N-terminal D/D domain of PKA regulatory subunits (Scott et al. 1990; Carr et al. 1991). Notably, despite differences within the D/D domain-containing N-terminus of PKA type I, dual-specific AKAPs have been identified that are capable to scaffold both type I and II PKA enzymes (Huang et al. 1997; Banky et al. 1998). To date, several AKAPs that

localize PKA to different sites within cardiac myocytes, such as the plasma membrane, the myofilaments, the nuclear envelope or the SR have been identified and play important roles for physiological PKA signaling (Lygren et al. 2007; Sumandea et al. 2011; Diviani et al. 2011). PKA activity can be further modified by oxidative PTM of regulatory and catalytic subunits. The two cysteine residues of PKA-C, Cys199 and Cys343 are susceptible to oxidation (First and Taylor 1989). Cys199 is located within the activation loop and is modified by intradisulfide formation and S-glutathiolation. Both oxidation events have been described to inhibit the catalytic activity of the kinase (Humphries et al. 2002).
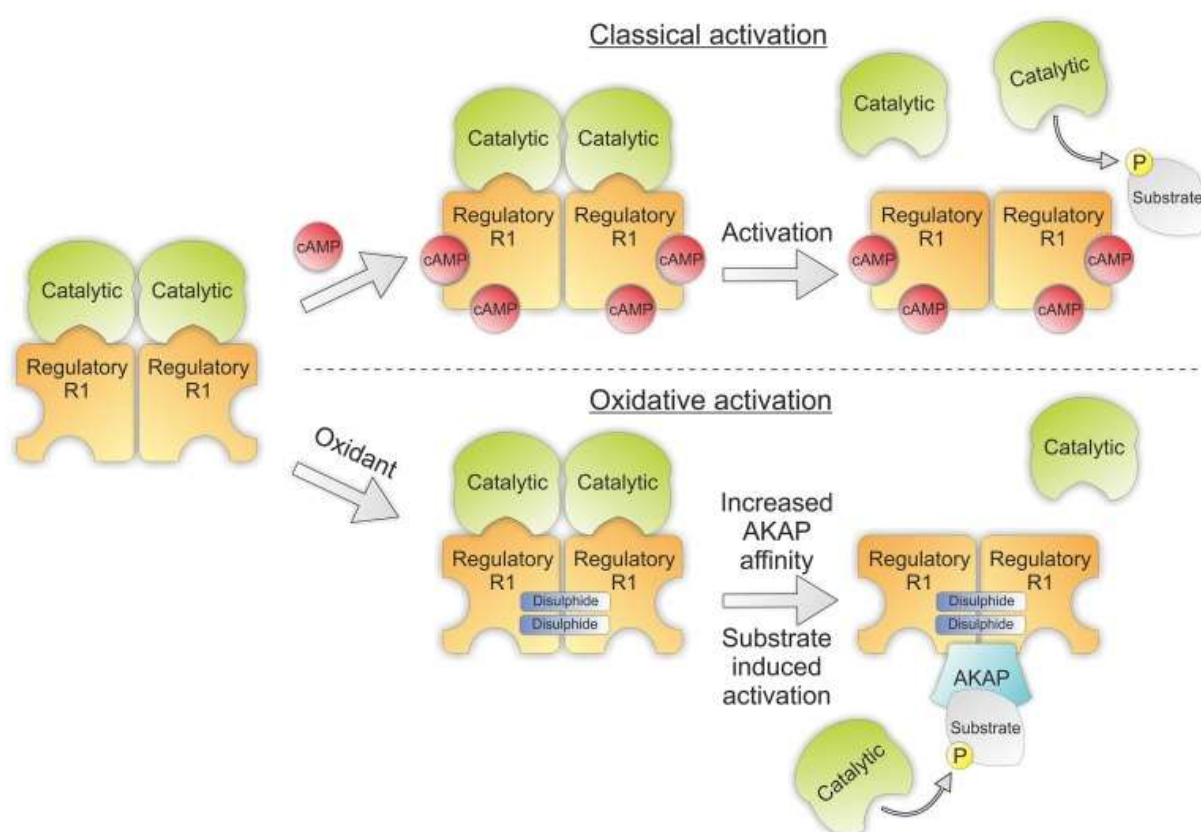
Figure 6: Classical and oxidant-mediated activation of PKA type I PKA is classically activated by two molecules of cAMP that bind to each PKA regulatory subunit, thus triggering the release of the active catalytic subunits. Alternatively, activation of PKA type I can occur in a cAMP-independent fashion. The oxidation of RI regulatory subunits results in the formation of two antiparallel interdisulfide bonds, which are suggested to increase the affinity for certain A-kinase anchoring proteins (AKAPs). Following a translocation process into the vicinity of a substrate protein, substrate-induced activation initiates the release of catalytic subunits. From Johnston et al. (2015).

Akin to the catalytic subunit, PKA-RI regulatory subunits also contain two N-terminal redox-sensitive cysteine residues at position 17 and 38 (in human, rat and mouse), which are absent in RII. Upon exposure to oxidants, these cysteines form antiparallel interdisulfide bonds between two RI subunits, which were initially assumed to exist constitutively (Potter and Taylor 1980; Banky et al. 1998). However, this was refuted by Brennan et al. (2004, 2006a), who showed that dimerization of PKA-RI subunits could be triggered by oxidant treatment in rat ventricular cardiac myocytes. Moreover, the H_2O_2-mediated formation of oxidative PKA-RI dimers was reported to result in the activation of the protein kinase, describing a novel, cAMP-

independent mechanism for the activation of PKA (Fig. 6; Brennan et al. 2006a). Subcellular translocation of dimerized RI subunits gave rise to the hypothesis of disulfide-mediated alterations in the affinity to certain AKAPs and subsequent substrate-induced release of the catalytic subunit.

2.3.2 cGMP-dependent protein kinase (PKG)

Another member of the AGC family of protein kinases that participates in the regulation of cardiac contractility is the cGMP-dependent protein kinase I (PKGI). According to its name, PKGI is activated by the second messenger cyclic GMP (cGMP), which is either generated by membrane-bound particulate guanylate cyclase upon extracellular binding of natriuretic peptides (Potter et al. 2006) or by cytosolic NO-activated soluble guanylate cyclase (sGC; Pyriochou and Papapetropoulos 2005). In contrast to PKA, PKGI exists as a parallel homodimer of polypeptide chains that each contain both regulatory and catalytic elements. The dimeric structure of PKGI is maintained by the interaction between leucine zipper regions within a D/D domain present at the N-terminus of the polypeptide chain. The N-terminal portion of the protein further harbors an autoinhibitory region, which is followed by a high and a low affinity cGMP binding site. A switch helix separates the regulatory part of the protein from the C-terminal catalytic domains. These include an ATP binding site and the catalytic core that interacts with the substrate protein. In the absence of cGMP, the pseudo-substrate sequence of the flexible autoinhibitory segment interferes with the catalytic center of the kinase. Binding of cGMP to the N-terminal binding sites results in a conformational change that activates the kinase while maintaining its dimeric architecture (Francis and Corbin 1994; Osborne et al. 2011).

PKGI and PKA share several substrates within the cardiac myocyte. Like PKA, PKGI phosphorylates the sarcomeric proteins cTnI (Blumenthal et al. 1978) and cMyBP-C (Thoonen et al. 2015) as well as SERCA2a-associated PLN in the membrane of the SR (Sabine et al. 1995). In contrast and different from PKA-mediated effects, activation of PKGI is commonly associated with a reduced inotropic response and positive lusitropy (Wegener et al. 2002; Layland et al. 2002). This apparent difference is most likely explained by the fact that PKGI does not induce the enhancement of cytosolic Ca^{2+} by phosphorylation-mediated activation of the L-type Ca^{2+} channel and RyR2 during systole. Phosphorylation of these two proteins largely contributes to the enhancement of contraction that is induced by the activation of PKA. Instead, PKGIα phosphorylates the $\beta_{2\alpha}$ subunit of the L-type Ca^{2+} channel at Ser496, which inhibits channel activity (Yang et al. 2007). In addition, the phosphorylation of cTnI, cMyBP-C and PLN by PKGI leads to reduced Ca^{2+} sensitivity of the sarcomere and promotes the import of Ca^{2+} into the SR during diastole. In this way, PKGI mediates accelerated cardiac myocyte relaxation without promoting contractile force.
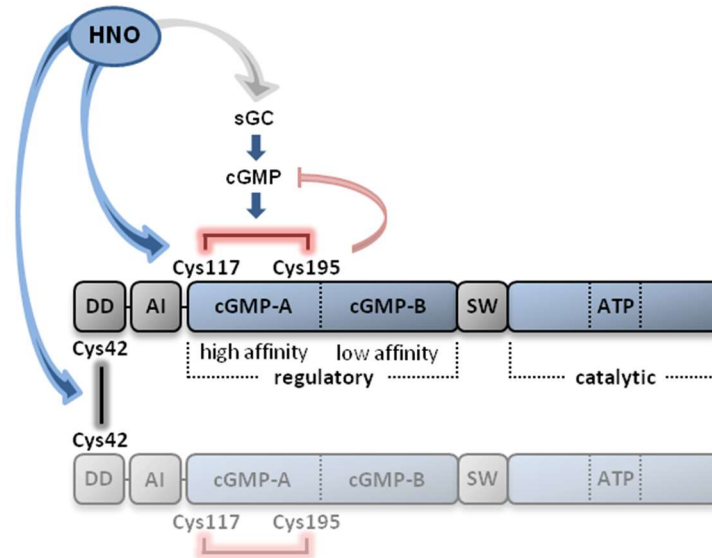
Figure 7: Oxidant-mediated activation of PKGIα HNO-mediated oxidation of PKGIα results in cGMP-independent activation of the protein kinase. An interdisulfide bond can form between Cys42 residues within the N-terminal dimerization and docking (DD) domains of two PKGIα monomers. In addition, an intradisulfide that links Cys117 and Cys195 located within the high affinity cGMP binding site mimics and competes with cGMP binding. Both disulfide bonds are associated with increased PKGIα activity. AI: autoinhibitory domain, SW: switch helix, sGC: soluble guanylate cyclase. From Donzelli et al. (2017).

The PKGI splice variant α is the predominant isoform in the heart but is also expressed in smooth muscle cells of the vasculature, where it plays an important role in the maintenance of vascular tone and blood pressure (Geiselhöringer et al. 2004). In this context, it was found that PKGIα, as observed for PKA, can be activated by oxidation and thus independently from its second messenger. A redox sensor cysteine residue at position 42 located in the D/D domain was found to form an interdisulfide bond between PKGIα monomers that tethers the kinase in substrate vicinity, resulting in PKGIα-mediated vasorelaxation (Fig. 7; Burgoyne et al. 2007). Moreover, a pair of reactive cysteines, Cys117 and Cys195, was identified within the high affinity cGMP binding site of PKGIα. Oxidant-induced formation of an intradisulfide bond between these cysteines altered kinase activity, potentially by mimicking cGMP binding (Donzelli et al. 2017).

2.3.3   Protein phosphatase 2A (PP2A)

The human kinome contains 518 genes that putatively encode for protein kinases, while only 189 genes were identified to encode for protein phosphatases (Manning et al. 2002; Chen et al. 2017). While serine/threonine kinases represent the biggest group, the majority of identified phosphatases is specific for tyrosine, leaving only a small group of serine/threonine phosphatases to counteract the action of the corresponding kinases (Alonso et al. 2004). Protein phosphatases being outnumbered is counterbalanced by the combination of conserved catalytic subunits with a variety of regulatory subunits. One of the most abundant and important serine/threonine protein phosphatases, protein phosphatase 2A (PP2A), is composed of a scaffold and a catalytic subunit (PP2A-C), which together form the core enzyme. The

combination with one out of at least 18 regulatory subunits constitutes the active holoenzyme. The regulatory subunits, which display a surprisingly low similarity in sequence, are assumed to mediate substrate specificity and subcellular localization of the holoenzyme (Janssens and Goris 2001; Shi 2009; Lubbers and Mohler 2016). The regulatory subunit B56α, for example, was shown to be present in the myofilament fraction of cardiac myocyte preparations, suggesting an involvement in PP2A translocation to its sarcomeric substrates (Yin et al. 2010). In cardiac myocytes, PP2A facilitates the dephosphorylation of many PKA substrate proteins, such as cMyBP-C (Schlender et al. 1987), cTnI (Jideama et al. 2006) and to a lesser extent PLN (MacDougall et al. 1991).

Like PKA and PKGIα, PP2A-C was determined to be susceptible to oxidative modification when exposed to various oxidizing agents, which was associated with a reduced activity of the enzyme (Rao and Clayton 2002; Foley and Kintner 2005). Several studies investigating the molecular mechanisms of PP2A inhibitors consistently identified Cys269 in PP2A-C as the binding site of the inhibitory drugs (Teruya et al. 2005; Takeuchi et al. 2009; Ikehara et al. 2009). In line with these observations, an inhibitory intradisulfide bond was suggested to form between Cys266 and Cys269 and the involved cysteine residues proposed to act as regulatory redox switches (Foley et al. 2007).

2.4 Nitroxyl (HNO) as a treatment for heart failure

Cardiovascular diseases represent the most significant cause of death worldwide with 17.9 million fatalities in 2016 (World Health Organization 2017). Commonly, cardiovascular events are associated with an injury of the heart muscle, which can subsequently lead to heart failure, a clinical syndrome in which the contractile function of the heart is no longer able to satisfy the needs of the body. In the failing heart, adequate blood supply is sustained via the release of the catecholamines noradrenaline and adrenaline from the sympathetic nervous system, which enhances cardiac contractility. The catecholamines stimulate β-ARs and induce the acceleration of contraction and strengthening of contractile force, which is acutely beneficial. However, in a chronic state, continuous release of noradrenaline and adrenaline induces cardiac remodeling, which is accompanied by numerous deteriorating side effects, such as cardiac myocyte hypertrophy, fibrosis and cell death, which further compromise cardiac function (Fig. 8; El-Armouche and Eschenhagen 2009).
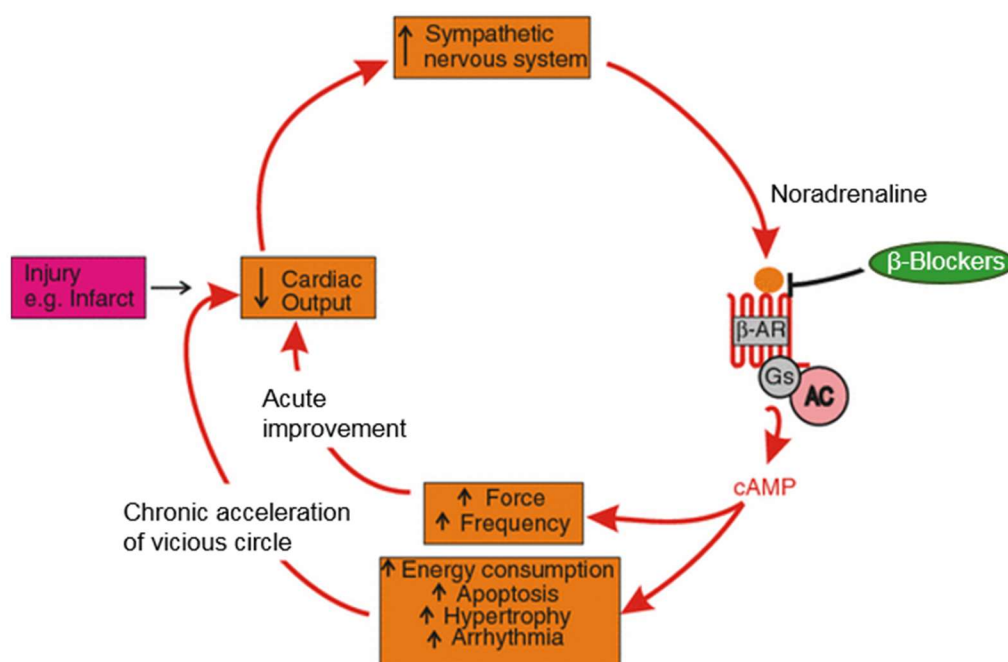
Figure 8: The vicious circle in heart failure Following cardiac injury, noradrenaline is released by the sympathetic nervous system, binds to β-adrenergic receptors (β-AR) of cardiac myocytes and induces the cAMP-mediated activation of PKA. As a result, inotropy (force) and chronotropy (frequency) of contraction by the remaining intact tissue are increased, securing adequate supply of the body. In the chronic state sympathetic activation turns harmful and promotes arrhythmias. Moreover, it is associated with cardiac myocyte hypertrophy, increased energy consumption and apoptosis. Altogether the continuous release of noradrenaline contributes to a deterioration of cardiac function and propels a vicious circle. In the treatment of heart failure, β-AR antagonists (β-blockers) are applied to limit myocardial toxicity caused by ongoing β-AR stimulation. Modified from El-Armouche and Eschenhagen (2009). Gs: Stimulatory G protein, AC: adenylate cyclase

Ongoing sympathetic stimulation is also associated with β-AR desensitization, a mechanism that protects the heart by limiting harmful β-AR-mediated side effects (Bristow et al. 1982; Lohse et al. 2003). In accordance, β-AR antagonists (β-blockers) have emerged as the standard treatment for heart failure (CIBIS II Investigators and Committees 1999; Eschenhagen 2008). β-Blockers compete with catecholamines for β-AR binding and restrict the activation of downstream signaling pathways. In this way, side effects are reduced and a partial β-AR 'resensitization' is enabled. Drugs like dopamine or milrinone stimulate cardiac contractility by elevating intracellular cAMP levels, which is mediated via the activation of β-ARs or the prevention of cAMP degradation, respectively. However, chronic administration of such so-called inotropes has been associated with increased long-term mortality and is highly controversial (Packer et al. 1991; Packer 1993; Belletti et al. 2015). Another constraint of positive inotropic β-AR agonists is the attenuation of effect due to the reduced number of responsive β-AR present in the plasma membrane under failing conditions. To date, inotropes are mainly administered for short-term treatment of acute heart failure (Petersen and Felker 2008; Bistola and Chioncel 2017). Acute decompensated heart failure (ADHF) denotes a sudden exacerbation of symptoms from mostly preexisting heart failure. ADHF is mostly treated with loop diuretics that reduce pulmonary congestion and vasodilators that decrease ventricular afterload (Felker et al. 2009). These treatments frequently prove insufficient and

require additional strengthening of contractile function, which is achieved with inotropes (Petersen and Felker 2008; Bistola and Chioncel 2017). However, there is still a lack of inotropic therapies that uncouple the beneficial cardiac effects from undesired myocardial toxicity.

2.4.1 The regulatory role of oxidants

A critical characteristic of heart failure is oxidative stress (Belch et al. 1991; Tsutsui et al. 2011). Reactive oxygen and nitrogen species (ROS/RNS), which serve as signaling molecules under physiological conditions, become harmful when the production exceeds the cellular antioxidant capacity, a situation that is termed oxidative stress. In heart failure, this imbalance arises from increased ROS/RNS generation by mitochondria (Ide et al. 1999), NADPH oxidases (Satoh et al. 2006) and other ROS-generating enzymes and is associated with cardiac remodeling, contractile dysfunction, cell damage and disease progression (Takimoto and Kass 2007). Interestingly, the attempt to scavenge excess oxidants with systemic antioxidant therapies failed (Miller et al. 2005; Bjelakovic et al. 2014). Instead of preventing cardiovascular and other chronic diseases, the supplementation with high doses of organic molecules that possess antioxidant potential, such as vitamin A, vitamin E or β-carotene, turned out to lack beneficial effects. On the contrary, in many cases antioxidant supplementation was associated with increased risk of cancer development and increased all-cause mortality. Nowadays, oxidants are recognized as important molecules for inter- and intracellular signaling, and it is not surprising that a broad disruption of oxidant signaling events might be just as detrimental as oxidative stress. Precisely targeted antioxidant delivery, however, holds the potential to counteract pathological ROS production in a cellular organelle or another microenvironment, thus preventing oxidative damage. One example is MitoC, a mitochondrial-targeted variant of ascorbate (Finichiu et al. 2015). MitoC is effectively taken up by mitochondria, which is achieved by linking the antioxidant ascorbate to a lipophilic triphenylphosphonium cation that renders MitoC membrane-permeable. The mitochondrial membrane potential causes ascorbate to accumulate within the mitochondria, where it scavenges free radicals to form an ascorbyl radical and subsequently dehydroascorbate. The latter either hydrolyzes spontaneously or is converted back to ascorbate through the reduction by GSH. In this way, the application of MitoC prevents oxidative mitochondrial damage and the resulting threat of apoptosis in a situation of oxidative stress. A related antioxidant compound named MitoQ allows triphenylphosphonium-mediated delivery of a ubiquinone derivative to mitochondria (Kelso et al. 2001). The fact that MitoQ was used in humans during two clinical studies emphasizes the great potential of these targeted antioxidant molecules (Gane et al. 2010; Snow et al. 2010). One major limitation that triphenylphosphonium-based antioxidants have in common is the putative association of triphenylphosphonium with cytotoxic effects (Guzman-Villanueva et al. 2015; Trnka et al. 2015).

Redox signaling involves a multitude of mostly reversible but also irreversible PTMs that predominantly occur at protein cysteine residues. Protein oxidation is a well-regulated process and depends on the microenvironment of the respective cysteine residue, its accessibility and the local presence of cellular antioxidant molecules, mainly thioredoxin and GSH. Additionally, the type of oxidative modification or, more precisely, the generation and stability of the corresponding oxidant at the microdomain of modification is a key factor that determines the susceptibility of a protein to a certain mechanism of redox regulation. Cysteines of redox-sensitive proteins usually possess a low pK_a value, which is stabilized by proximal basic amino acids and causes the thiol group to be present in the deprotonated, more reactive thiolate state (RS^-; Rudyk and Eaton 2014). Commonly, so-called redox switches involve the formation of a reversible disulfide bond that can form in response to different oxidizing agents, such as H_2O_2. But also S-nitrosylation, S-glutathiolation and other modifications can occur at these reactive sites to influence enzyme activity, protein-protein interaction and intracellular localization of redox-sensitive proteins (Klomsiri et al. 2011; Burgoyne et al. 2012; Santos et al. 2016). In cardiac myocytes, numerous proteins that were identified to be susceptible to redox regulation are expressed. Besides PKA type I and PKGIα (Burgoyne and Eaton 2010) also proteins involved in EC coupling display redox sensitivity (Lancel et al. 2009; Zima and Mazurek 2016; Cuello et al. 2018). An example of a protein whose reversible oxidation regulates protein phosphorylation is cMyBP-C. H_2O_2-mediated S-glutathiolation at the main acceptor site at Cys249 was shown to negatively affect cMyBP-C phosphorylation within its M-domain, a modification which in turn constitutes a regulatory mechanism for myofilament actomyosin interaction (Stathopoulou et al. 2016).

2.4.2   Nitroxyl (HNO) and donor compounds

Considering the harmful effects of increased oxidant concentrations in the heart, it appears controversial that a class of compounds that primarily act via protein oxidation has drawn attention as novel promising candidates for the treatment of heart failure and ADHF. In the early 2000s, Paolocci et al. for the first time reported positive inotropic and lusitropic effects for the small electrophilic molecule nitroxyl (HNO) (Paolocci et al. 2001, 2003). Importantly, the effects exerted by HNO were maintained in a dog heart failure model, demonstrating the independence from β-AR signaling. A vasorelaxing property of HNO had been described previously (Fukuto et al. 1992) and was also confirmed in this study. Together, these findings evoked substantial interest in HNO, which appeared to combine multiple beneficial features for a promising clinical use in heart failure therapy.
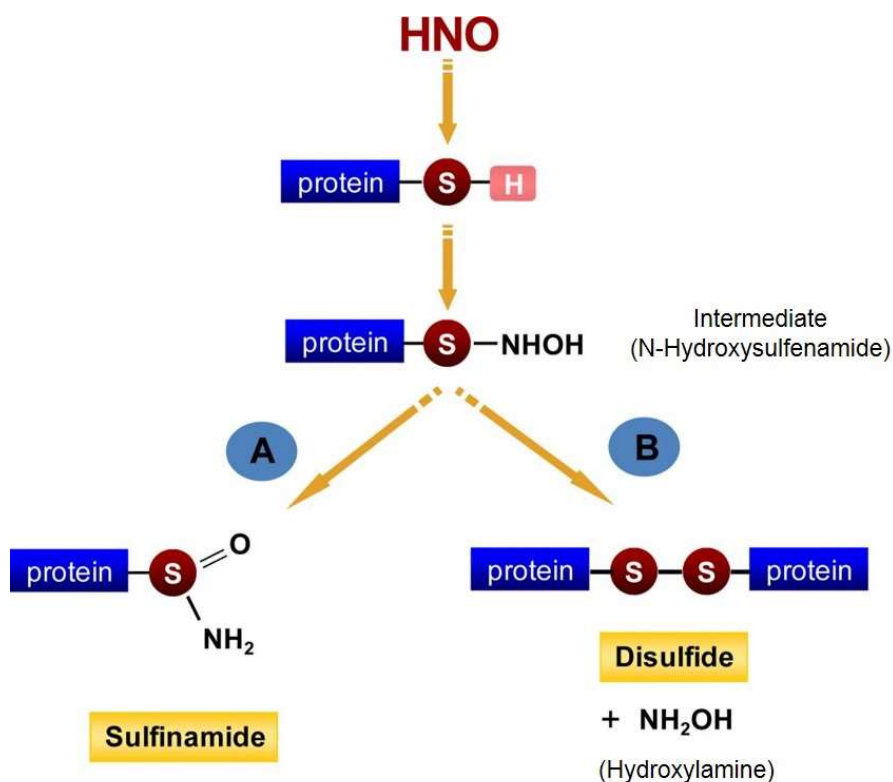
Figure 9: Schematic illustration of the reaction of HNO with a protein thiol The reaction of HNO with a thiol group of a protein cysteine residue generates the N-hydroxysulfenamide intermediate. The rearrangement of the intermediate gives rise to an irreversible sulfinamide (A). Alternatively, the reaction with another proximate thiol group results in the formation of a protein disulfide and hydroxylamine (B). Modified from Gao et al. (2012).

HNO is the one electron-reduced, protonated sibling of nitric oxide (NO) and displays distinct biological properties and unique effects on the cardiovascular system (Wink et al. 2003). Although HNO was shown to activate the metalloprotein sGC (Fukuto et al. 1992; Lin et al. 2012), the vast majority of HNO-mediated effects is attributed to protein oxidation and the generation of thiol disulfides (Froehlich et al. 2008; Fukuto and Carrington 2011; Gao et al. 2012; Donzelli et al. 2017). The reaction of HNO with a protein thiol generates an N-hydroxysulfenamide intermediate, which in the presence of another thiol group further reacts to form a thiol disulfide and hydroxylamine (Fig. 9; Doyle et al. 1988; Paolocci et al. 2007). Alternatively, N-hydroxysulfenamide can undergo spontaneous rearrangement to produce a sulfinamide (Wong et al. 1998). Endogenous generation of HNO is considered likely but is still a matter of debate. Although several pathways have been suggested to potentially involve the formation of HNO, *in vivo* generation of HNO remains unconfirmed, probably in part due to difficulties in its detection (Tocchetti et al. 2011). In aqueous solution, HNO quickly dimerizes to form hyponitrous acid ($H_2N_2O_2$), which further dehydrates to generate nitrous oxide (N_2O) and water (H_2O; $k = 8 \times 10^6$ M^{-1} s^{-1}; Shafirovich and Lymar 2002). Consequently, HNO donor compounds are required that allow the directed release of bioactive HNO *in situ*. Different HNO donors have been applied for the examination of HNO-mediated effects (Sha et al. 2006; Tocchetti et al. 2007; Sabbah et al. 2013). Since these compounds share most of the cellular responses they induce, findings that were accounted to HNO were commonly assumed to

equally apply for the other donor compounds. Consequently, results gathered for one donor were scarcely confirmed by the use of another compound or examined in a comparative manner. Small but potentially meaningful differences between effects exerted by the different HNO donor compounds might be attributed to different release kinetics and the generation of by-products, but they also encourage caution when data obtained from one compound are directly translated to another. The three HNO donor compounds used in this study and the main findings obtained for each of them are outlined below.

Angeli's salt (AS)
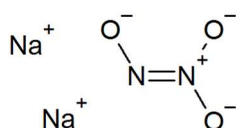
Figure 10: Structural formula of Angeli's salt (AS)

Angeli's salt (AS; $Na_2N_2O_3$) was first described in 1896 by the chemist Angelo Angeli (Angeli 1896). It is the most frequently used HNO donor compound in studies aiming to investigate the biological role of HNO and was applied when the first discoveries of beneficial cardiovascular effects of HNO were reported (Fukuto et al. 1992; Paolocci et al. 2001, 2003). At 37 °C and neutral pH, AS has a half-life ($t_{1/2}$) of 2.3 min (Maragos et al. 1991). Under physiological conditions, protonation of the basic $N_2O_3^{2-}$ anion generates $HN_2O_3^-$. $HN_2O_3^-$ subsequently decomposes to the final products nitrous oxide (N_2O) and nitrite (NO_2^-), whereas the formation of N_2O indicates the dimerization and dehydration of initially released HNO (Bonner and Ravid 1975). Notably, the by-product nitrite also has biological functions and is considered to serve as a storage of NO, which in turn represents a gaseous signaling molecule that can affect cellular processes (Dejam et al. 2004; Gladwin et al. 2005). Furthermore, the direct generation of NO was detected during AS decomposition, supposedly arising from the oxidation of $N_2O_3^{2-}$ (Amatore et al. 2007). In the circulation of dogs, AS was reported to induce β-AR-independent positive inotropic and lusitropic effects, which are preserved under heart failure conditions (Paolocci et al. 2001, 2003). In isolated murine ventricular cardiac myocytes, AS-mediated HNO-release was shown to enhance contractility and the intracellular Ca^{2+} ($[Ca^{2+}]_i$) transient amplitude independently from the formation of cAMP and cGMP or the activity of the corresponding protein kinases PKA and PKG (Tocchetti et al. 2007; Kohr et al. 2010; Sivakumaran et al. 2013). Additionally, SR Ca^{2+} uptake was accelerated in response to AS-exposure. Experiments performed in rat ventricular trabeculae further demonstrated that the application of AS leads to increased maximal force but does not alter myofilament Ca^{2+} sensitivity (Ca_{50}; Dai et al. 2007). The effects of AS on cardiac function are attributed to oxidative modification of Ca^{2+} cycling and myofilament proteins at redox-sensitive cysteine residues. At the SR, the HNO donor increases the open probability of RyR2, promoting the

systolic release of Ca^{2+} (Cheong et al. 2005; Tocchetti et al. 2007). SR Ca^{2+} uptake is accelerated through direct HNO-mediated S-glutathiolation of SERCA at Cys674 and the formation of disulfide-based PLN oligomers that are no longer available for SERCA-inhibition (Lancel et al. 2009; Sivakumaran et al. 2013). This enhancement of SR Ca^{2+} currents is supported by disulfide bonds that were suggested to form between myosin heavy chain and myosin light chain 1 or two monomers of myosin light chain 1 of the contractile machinery and which might contribute to the observed increase in maximal force (Gao et al. 2012). AS was also used in studies investigating the impact of HNO donors on the vasorelaxation of mouse, rat and human vessels (Fukuto et al. 1992; Andrews et al. 2009, 2015). Although AS-induced disulfide bond formation in PKGIα suggested a contribution of this modification to the observed vasorelaxation (Donzelli et al. 2017), this effect was largely mediated by a direct activation of sGC, as it could be almost completely inhibited by pretreatment with the sGC inhibitor ODQ (Irvine et al. 2007; Andrews et al. 2009).

1-Nitrosocyclohexyl acetate (NCA)
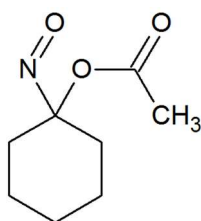
Figure 11: Structural formula of 1-Nitrosocyclohexyl acetate (NCA)

1-Nitrosocyclohexyl acetate (NCA) is a bright blue liquid and was introduced in 2006 by Sha and colleagues (Sha et al. 2006). NCA belongs to the group of acyloxy nitroso compounds, which compared to AS provides improved possibilities for chemical alteration of organic groups to modulate the rate of HNO-release. Through hydrolysis, NCA decomposes to HNO, acetic acid and cyclohexanone at a $t_{1/2}$ of 800-890 min and generates only small amounts of NO and NO_2^- (Sha et al. 2006; Shoman et al. 2011). Like AS, NCA exerts positive effects on cardiac myocyte contraction, which are maintained in a situation of β-AR desensitization, as measured in single isolated murine ventricular cardiac myocytes (El-Armouche et al. 2010). A positive lusitropic effect of NCA was not reported. While Gao et al. (2012) did not detect any differences in $[Ca^{2+}]_i$ transient, an increased $[Ca^{2+}]_i$ peak amplitude was reported by El-Armouche et al. (2010) following NCA-treatment. However, the alteration in $[Ca^{2+}]_i$ transient was insufficient to explain the increase in force, indicating a combined effect on SR Ca^{2+} cycling and myofilament Ca^{2+} sensitivity. The oxidation-mediated influence on SR Ca^{2+} channels was described for AS and might occur similarly for NCA, providing an explanation for enhanced systolic $[Ca^{2+}]_i$. But while NCA was found to enhance maximal force in isolated rat cardiac muscle like AS, it indeed also increased sarcomere Ca^{2+} sensitivity (Ca_{50}; Gao et al. 2012). Elevated Ca^{2+}

responsiveness is conserved upon muscle skinning, demonstrating that a modification of the contractile machinery is the underlying mechanism. This alteration in Ca^{2+} sensitivity was suggested to rely on a disulfide bond that might form between sarcomeric tropomyosin and actin, since a pair of potentially redox-sensitive cysteine residues was detected following treatment with NCA but not with AS. The formation of interdisulfide-linked actin-tropomyosin heterodimers could result in a slight relocation of tropomyosin on the thin actin filaments, consequently facilitating the Ca^{2+}-mediated permission of actomyosin interaction. In comparison to AS, vasorelaxation in response to NCA was only partially inhibited by pretreatment with the sGC inhibitor ODQ (Donzelli et al. 2013), suggesting the modification of other proteins to contribute to the vasorelaxing effects. The observation of PKGIα disulfide bonds that formed in response to NCA treatment (Donzelli et al. 2017) suggested that besides the activation of sGC, the oxidation of PKGIα plays a role in NCA-mediated vasorelaxation.

CXL-1020
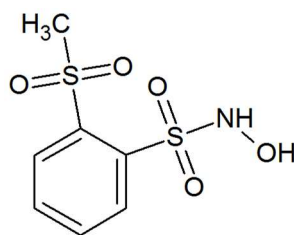
Figure 12: Structural formula of CXL-1020

With the novel HNO donor CXL-1020, the development of a compound that exclusively decomposes into HNO and a biologically inactive organic scaffold (CXL-1051) was reported (Sabbah et al. 2013). Lacking bioactive by-products, CXL-1020 is better suited for the investigation of biological HNO effects, but also represents a marked improvement in the effort to generate a compound that allows the therapeutic use of HNO. In phosphate-buffered saline, CXL-1020 has a $t_{1/2}$ of 1.9 min. In accordance with the positive inotropic and lusitropic effects reported for HNO, treatment of murine ventricular cardiac myocytes with CXL-1020 was shown to induce increased sarcomere shortening and accelerated cardiac myocyte relaxation. These effects were paralleled by a minor enhancement of $[Ca^{2+}]_i$ transient amplitude and accelerated $[Ca^{2+}]_i$ transient decay, potentially relying on thiol modification of RyR2, PLN and SERCA as described for AS. In ventricular cardiac myocytes isolated from mice with induced heart failure, sarcomere shortening and relaxation were reduced upon exposure with the β-AR agonist isoprenaline (ISO) but preserved with CXL-1020, indicating that functions exerted by CXL-1020 are β-AR-independent and maintained in a situation of β-AR desensitization. Similarly, blunted ISO-mediated effects in failing cardiac myocytes were reported for $[Ca^{2+}]_i$ transient and its decay, which remained more pronounced upon exposure to CXL-1020 (Sabbah et al. 2013).

Comparable results were obtained from a rat heart failure model, where single ventricular cardiac myocytes from failing and control hearts equally displayed a CXL-1020-induced enhancement in sarcomere shortening and $[Ca^{2+}]_i$ transient amplitude as well as accelerated relaxation and SR Ca^{2+} uptake (Roof et al. 2017). Interestingly, this study also demonstrated that the effects of CXL-1020 on ventricular relaxation in failing rat hearts and shortening of single failing cardiac myocytes are more pronounced than in response to the inotrope milrinone. In line with independence from β-AR signaling, incubation with CXL-1020 did not affect cAMP and cGMP levels of murine ventricular myocardium (Zhu et al. 2015). CXL-1020 was further tested in two canine models of ischemic cardiomyopathy (ICM) and heart failure. Under both disease conditions, improved cardiac function and beneficial effects on parameters that affect cardiac afterload were obtained for the compound. Consequently, CXL-1020 was the first HNO donor to be tested in patients suffering from ADHF. The clinical study revealed that CXL-1020 induced an increase in cardiac and stroke volume indices, reflecting improved contractile function. Simultaneously, systemic vascular resistance and mean arterial pressure declined, indicating vasorelaxation and reduced cardiac afterload. CXL-1020-mediated vasorelaxation, but not its inotropic property, was shown to depend on sGC and, unlike AS and NCA, does not seem to involve direct oxidation and activation of PKGIα (Zhu et al. 2015). While vasorelaxation was blunted in mice that lacked the β subunit of sGC, it remained unchanged in mice which expressed a PKGIα mutant that was unable to dimerize. At present, the development of CXL-1020-successor compounds with improved suitability for therapeutic application, e.g. reduced injection site-inflammation, are being developed by Cardioxyl Pharmaceuticals in order to soon allow patients to benefit from the positive inotropic, lusitropic and vasorelaxing properties of HNO donor compounds (Hartman et al. 2018).

2.5 Aim of the study

The overarching aim of this doctoral thesis was to investigate the effect of oxidation on the prototypical phosphorylation-regulated contractile function of cardiac myocytes. Different oxidizing agents that either mimic cellular oxidative stress or release the therapeutically promising molecule HNO were applied to address the following main questions: (i) How does oxidation by chemically distinct oxidizing agents affect the PTM spectrum of myofilament proteins and how does this translate into changes in contractile function? (ii) Which molecular mechanisms underly oxidation-induced PTM and how can beneficial effects of therapeutically applied oxidants be rationalized? (iii) In which way do oxidative and non-oxidative PTMs of myofilament proteins interfere with each other and how does this crosstalk contribute to cardiac myocyte contractile function?

An attempt to answer these questions should broaden the understanding of myocardial redox regulation and provide a prerequisite for subsequent successful clinical use of HNO donor compounds for the treatment of heart failure.

3 Results

The data presented in this doctoral thesis were divided into two parts. In the first section, the modulation of cardiac myocyte protein kinase and phosphatase signaling was investigated as a potential contributor to oxidant-mediated changes in myofilament protein PTMs and resulting changes in contractility. In the second section, direct oxidative modification of a prototypical myofilament protein and its crosstalk with regulatory non-oxidative PTM was examined.

3.1 HNO donor compounds regulate contractile function by impacting on PKA and PP2A signaling

Initial experiments performed in adult rat ventricular myocytes (ARVMs) showed that phosphorylation of the sarcomeric protein cMyBP-C, which is critical for unrestricted cardiac function, was reduced after preceding protein oxidation by H_2O_2 (Stathopoulou et al. 2016). In contrast to this finding, several studies by other groups had reported elevated cMyBP-C phosphorylation and beneficial effects on cardiac myocyte function as a consequence of oxidant-treatment (Paolocci et al. 2001; Brennan et al. 2006a; Sabbah et al. 2013). To investigate how oxidation can modulate phosphorylation-regulated cardiac myocyte function, the status of protein phosphorylation elicited by various oxidizing compounds was analyzed.

3.1.1 The effect of oxidants on cardiac myocyte protein phosphorylation

The ability of various oxidizing agents to modulate cardiac myocyte protein phosphorylation was investigated by fluorescence-labeling of phosphorylated proteins from ARVMs following oxidant-treatment. ARVMs were exposed to the HNO donor compounds NCA, AS and CXL-1020 as well as H_2O_2, the disulfide inducing agent diamide (DIA) or the β-AR agonist ISO, which induces protein phosphorylation by receptor-mediated activation of PKA and served in experiments as a positive control. Alterations in the abundance of protein phosphorylation were assessed by sodium dodecyl sulfate-polyacrylamide gel electrophoresis (SDS-PAGE) with subsequent staining for phosphorylated proteins using Pro-Q Diamond.
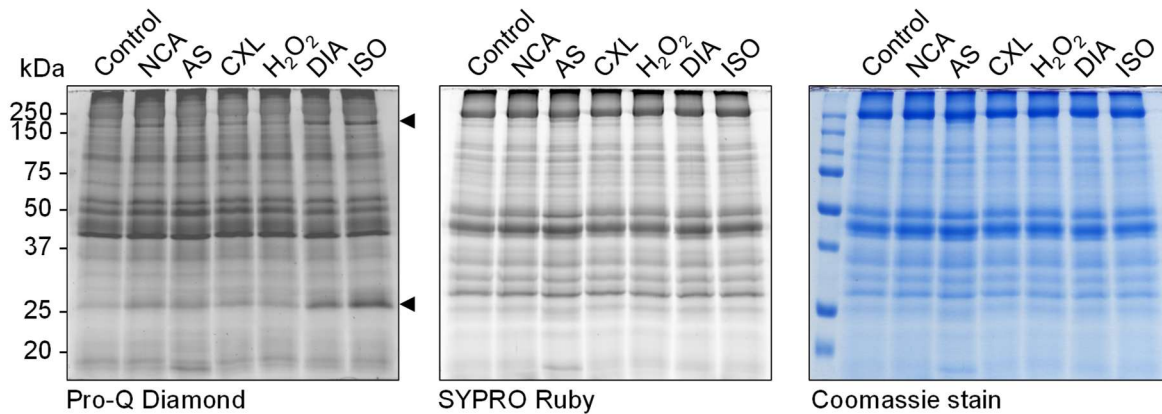
Figure 13: Detection of cardiac myocyte protein phosphorylation in response to oxidant-exposure ARVMs were incubated with vehicle (control), NCA (100 µmol/L, 30 min), AS (500 µmol/L, 15 min), CXL-1020 (300 µmol/L, 15 min), H_2O_2 (100 µmol/L, 10 min), DIA (500 µmol/L, 10 min) or ISO (10 nmol/L, 10 min) and lysate proteins resolved by SDS-PAGE. Phosphoproteins were visualized using Pro-Q Diamond gel stain. Total protein content was determined by post-staining with SYPRO Ruby and colloidal Coomassie.

Enhanced phosphorylation of cardiac proteins migrating at molecular weights of approx. 25 and 150 kDa following incubation with ISO compared to the control sample demonstrated the suitability of this method (Fig. 13, left panel, arrowheads). Whilst treatment with CXL-1020 and H_2O_2 did not allow the detection of increased signal intensities, exposure to NCA and DIA resulted in intensified bands migrating at 25 and 150 kDa. These signals were likely to correspond to the same phosphoproteins that were detected after treatment with ISO, indicating NCA- and DIA-mediated phosphorylation of prototypical PKA substrate proteins. In samples that were exposed to AS only, enhancement of a band migrating slightly below 20 kDa was observed. However, this signal did not represent enhanced protein phosphorylation as it was also pronounced after total protein staining of the same gels by SYPRO Ruby and Coomassie, respectively (Fig. 13, middle and right panel).

Pursuing the finding of oxidant-mediated cardiac myocyte protein phosphorylation and judging from the apparent molecular weight of the phosphoproteins on the Pro-Q Diamond gels, the phosphorylation status of PKA substrate proteins was analyzed after exposure of ARVMs to NCA, AS, CXL-1020, H_2O_2, DIA or ISO. Phosphorylation of the PKA substrate proteins cMyBP-C and PLN was assessed by Western immunoblotting with the use of antibodies with specificity for the respective PKA consensus phosphorylation sites.
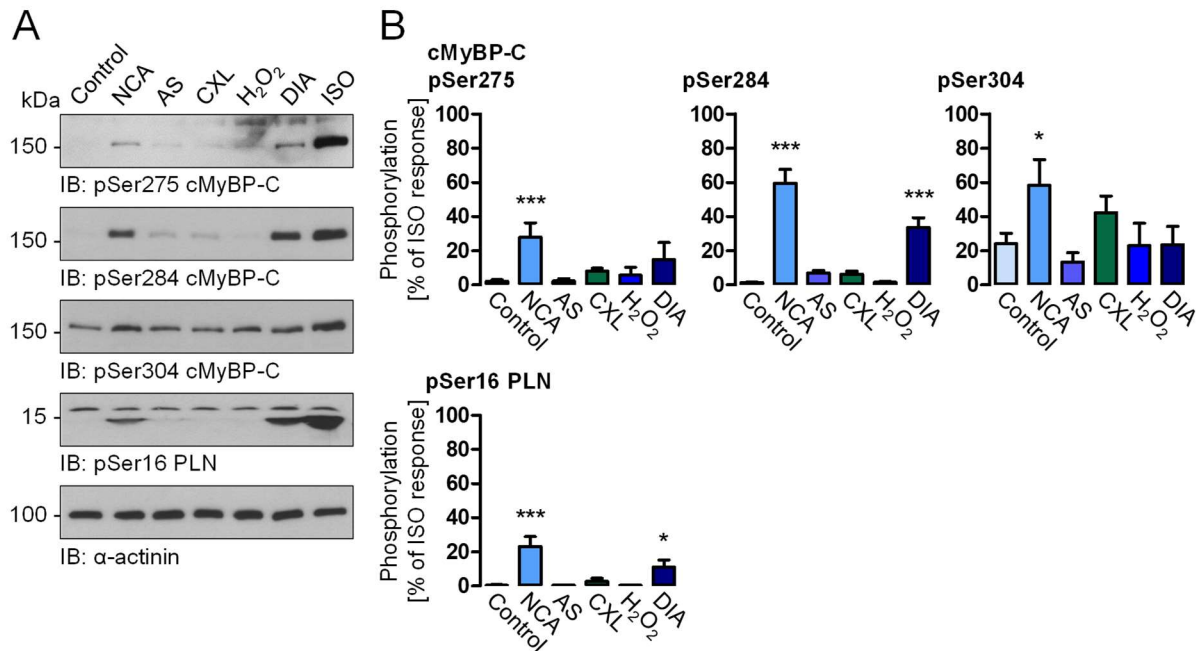
Figure 14: Effect of oxidant-treatment on PKA substrate protein phosphorylation in ARVMs ARVMs were exposed to vehicle (control), NCA (100 µmol/L, 30 min), AS (500 µmol/L, 15 min), CXL-1020 (300 µmol/L, 15 min), H_2O_2 (100 µmol/L, 10 min), DIA (500 µmol/L, 10 min) or ISO (10 nmol/L, 10 min). **A** Cell lysates were subjected to Western immunoblotting to assess the phosphorylation levels of cMyBP-C at Ser275, Ser284 and Ser304 and PLN at Ser16 using phospho-specific antibodies. α-Actinin served as loading reference. **B** Bar charts show the quantification of Western immunoblots for the phosphorylation of cMyBP-C (n=7-15) and PLN (n=4-10) normalized to α-actinin. Data are expressed as % of the signal induced by ISO. * P<0.05, *** P<0.001 for comparison with vehicle control by one-way ANOVA with Dunnett's Multiple Comparison post-test.

Treatment of ARVMs with ISO induced distinct phosphorylation of cMyBP-C at three phosphorylation sites (Ser275, Ser284 and Ser304) and PLN at Ser16, as expected. The HNO donors AS and CXL-1020 at the concentrations used here as well as H_2O_2 did not induce apparent phosphorylation of cMyBP-C or PLN. Exposure to the HNO donor compound NCA, however, resulted in increased phosphorylation of cMyBP-C at all the three major sites and of PLN at Ser16 (Fig. 14). Phosphorylation levels of cMyBP-C in response to NCA-treatment accounted for 28.1 ± 8.4% (Ser275), 59.5 ± 8.0% (Ser284) and 58.2 ± 15.1% (Ser304) of the corresponding signal that was induced by ISO and considered here as the maximum; signal intensity reached 23.3 ± 5.6% for PLN (Ser16). The intensity of the phosphorylation most likely will translate into a functional response. NCA-mediated phosphorylation of the two PKA substrate proteins gave rise to the hypothesis of NCA acting via modulation of PKA activity. Incubation with DIA resulted in enhanced phosphorylation of cMyBP-C at Ser284 (33.6 ± 5.7% of ISO response) and PLN (11.0 ± 4.3% of ISO response), whilst phosphorylation levels at Ser275 and Ser304 of cMyBP-C remained unchanged.

To substantiate the hypothesis that the phosphorylation of PKA substrate proteins in response to NCA is mediated by PKA, Förster resonance energy transfer (FRET) was applied as an alternative methodology in intact cells to investigate PKA activation in ARVMs that express a cytosolic A-kinase-activity-reporter (AKAR3-NES; Fig. 15, B).
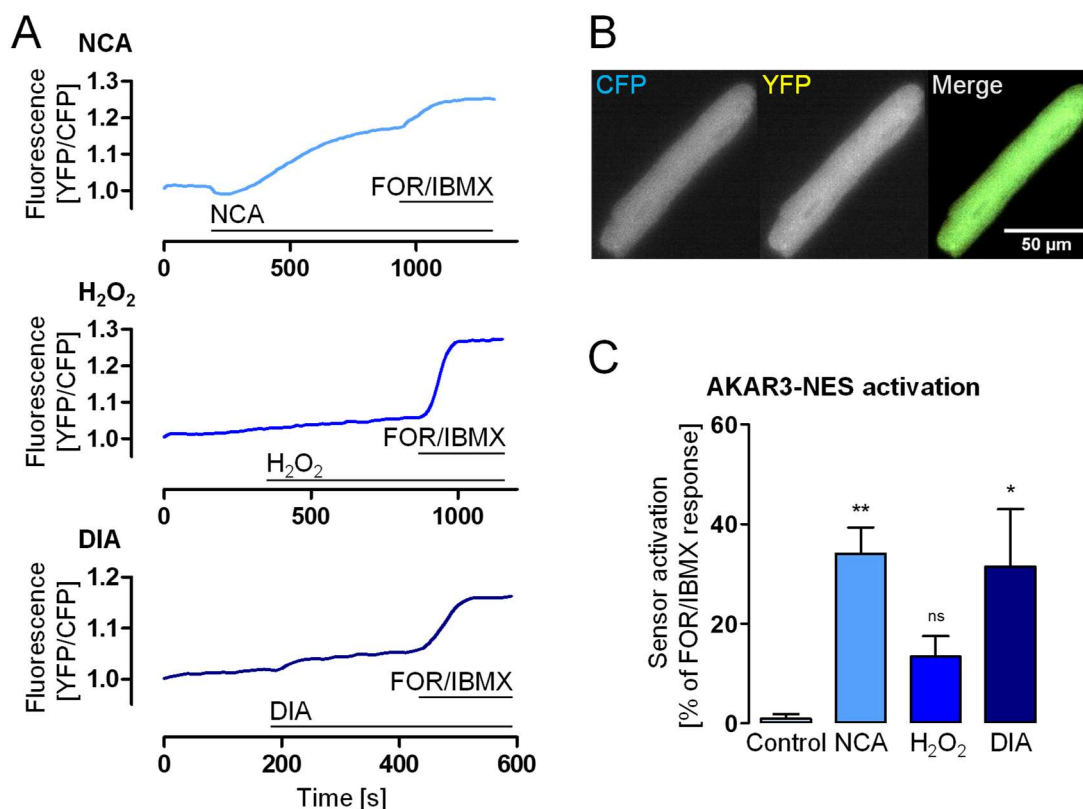
Figure 15: Measurement of PKA activity by Förster resonance energy transfer Adenovirally transduced ARVMs expressing the biosensor AKAR3-NES were used to measure Förster resonance energy transfer (FRET) signals under baseline conditions followed by recordings of FRET changes in response to NCA (100 µmol/L), H_2O_2 (100 µmol/L) or DIA (500 µmol/L). Maximal sensor activation was achieved by subsequent addition of forskolin (FOR) and 3-isobutyl-1-methylxanthine (IBMX). **A** Exemplary FRET traces showing the ratio of AKAR3-NES yellow fluorescent protein (YFP) to cyan fluorescent protein (CFP) fluorescence during baseline recording, upon exposure to NCA, H_2O_2 or DIA and at maximal sensor activation by FOR/IBMX. **B** Representative images show CFP and YFP fluorescence and an overlay image from an ARVM expressing the AKAR3-NES biosensor. **C** The bar chart summarizes AKAR3-NES activation by vehicle (control, n=10), NCA (n=32), H_2O_2 (n=21) or DIA (n=7). Data are expressed as % of maximal sensor activation by FOR/IBMX; * $P<0.05$, ** $P<0.01$ for comparison with vehicle control by one-way ANOVA with Dunnett's Multiple Comparison post-test. ns: not significant

Whilst the exposure to H_2O_2 did not result in significant activation of the biosensor, treatment with NCA or DIA induced significant FRET responses, suggesting a phosphorylation-mediated conformational change of the AKAR3-NES sensor (Fig. 15, A). The change in FRET ratio accounted for $34.1 \pm 5.2\%$ (NCA) and $31.5 \pm 11.5\%$ (DIA) of maximal sensor activation achieved by subsequent application of forskolin (FOR) and 3-isobutyl-1-methylxanthine (IBMX; Fig. 15, C). These findings were in line with the data observed by Western immunoblot analysis and confirmed again the activation of PKA by NCA.

To investigate if NCA-mediated activation of PKA was a direct effect or whether it was due to oxidation of upstream components of the β-AR signaling pathway that lead to the activation of the kinase, the effect of inhibition of β-AR or AC on the response to NCA was analyzed by Western immunoblot analysis. To inhibit β-AR signaling, ARVMs were exposed to the β1-AR antagonist atenolol before exposure to NCA or ISO. As expected, exposure to ISO induced phosphorylation of cMyBP-C at Ser275, Ser284 and Ser304, which was used as an established readout for PKA activation. In line with ISO acting via β1-AR activation, atenolol-

pretreatment blocked ISO-mediated phosphorylation of cMyBP-C at all the three analyzed sites (Fig. 16). Incubation with NCA resulted in enhanced phosphorylation levels of cMyBP-C, which were unaffected by atenolol-pretreatment, suggesting a β_1-AR-independent mechanism of PKA activation by NCA.
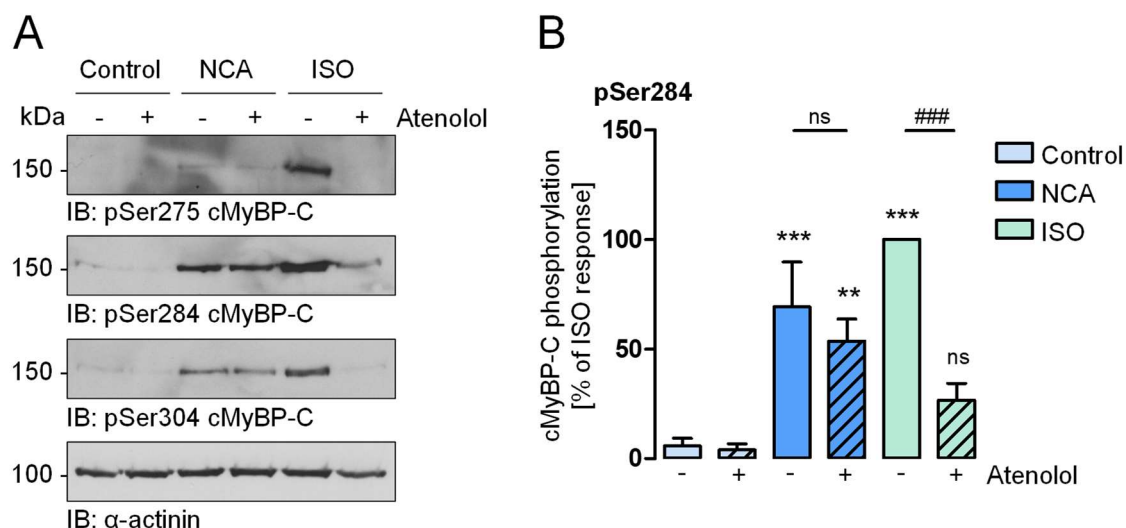
Figure 16: Influence of β_1-adrenergic receptor inhibition on NCA-mediated cMyBP-C phosphorylation ARVMs were incubated with vehicle (control), NCA (100 µmol/L, 30 min) or ISO (10 nmol/L, 10 min) following pretreatment with the β_1-adrenergic receptor (β_1-AR) antagonist atenolol (1 µmol/L, 5 min). **A** In a Western immunoblot, phospho-specific antibodies for pSer275, pSer284 and pSer304 of cMyBP-C were used to analyze protein phosphorylation at the respective sites. Detected α-actinin signals served as loading control. **B** The bar chart summarizes the phosphorylation of cMyBP-C at Ser284 of 4 independent experiments. Data are normalized to α-actinin and expressed as % of the ISO signal without atenolol-pretreatment (ISO -). ** $P<0.01$, *** $P<0.001$ for comparison with the corresponding vehicle control, ### $P<0.001$ for comparison of the corresponding samples with and without atenolol-pretreatment by two-way ANOVA with Bonferroni post-test. ns: not significant

For the inhibition of AC-mediated cAMP production, ARVMs were treated with the AC type V/VI inhibitor NKY80 prior to incubation with NCA or ISO. NKY80-pretreatment resulted in a potentiation of cMyBP-C phosphorylation at Ser284 in control samples and following NCA exposure (Fig. 17). Inconsistent with the expected effects of AC inhibition, NKY80 did not reduce cMyBP-C phosphorylation in response to ISO. Altogether these results indicated that NKY80 did not successfully block AC type V/VI activity as anticipated and, therefore, did not allow any conclusions concerning AC involvement in NCA-mediated phosphorylation events.

A

B
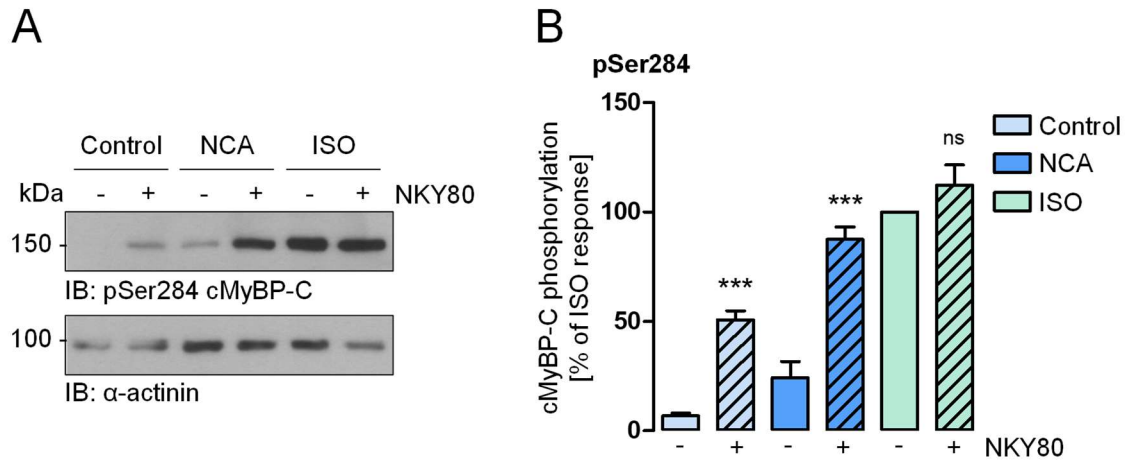
Figure 17: Treatment of ARVMs with the adenylate cyclase inhibitor NKY80 After pretreatment with the adenylate cyclase (AC) type V/VI inhibitor NKY80 (100 µmol/L, 10 min), ARVMs were incubated with vehicle (control), NCA (100 µmol/L, 30 min) or ISO (10 nmol/L, 10 min). **A** A phospho-specific antibody for pSer284 of cMyBP-C was used to analyze protein phosphorylation by Western immunoblot analysis. α-Actinin signals were used as loading control. **B** The bar chart summarizes the phosphorylation of cMyBP-C at Ser284 of 3 independent experiments. Data are normalized to α-actinin and expressed as % of the ISO signal without NKY80-pretreatment (ISO -). *** $P<0.001$ for comparison with the corresponding sample without NKY80-pretreatment by two-way ANOVA with Bonferroni post-test. ns: not significant

Potential interference of NCA with classical cAMP-dependent PKA signaling was examined by exposure of ARVMs to NCA or CXL-1020 followed by treatment with ISO. Western immunoblot analysis of cell lysates showed that neither pretreatment with NCA nor with CXL-1020 altered Ser284 phosphorylation of cMyBP-C in response to subsequent incubation with ISO (Fig. 18). This result indicated that NCA and CXL-1020 did not interfere with cAMP-mediated activation of PKA.

A

B
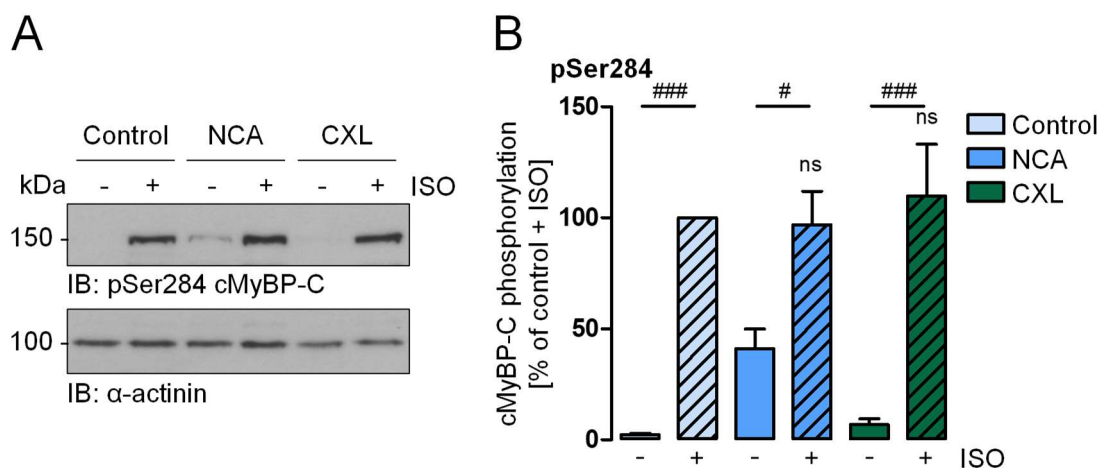
Figure 18: Impact of NCA and CXL-1020 on ISO-mediated activation of PKA Following exposure to vehicle (control), NCA (100 µmol/L, 30 min) or CXL-1020 (300 µmol/L, 15 min), ARVMs were incubated with ISO (10 nmol/L) for 10 min. Resulting protein phosphorylation of cMyBP-C at Ser284 was assessed by Western immunoblotting. α-Actinin served as loading reference. Results of 4 independent experiments are summarized in the bar chart. Bands arising from Ser284 phosphorylation were normalized to α-actinin and expressed as % of the signals detected in control samples with ISO-treatment (control +). * $P<0.05$ for comparison with the corresponding vehicle control, # $P<0.05$, ### $P<0.001$ for comparison of the corresponding samples with and without subsequent ISO-treatment by two-way ANOVA with Bonferroni post-test. ns: not significant

3.1.2 Oxidant-induced dimerization of PKA-RI

For PKA type I, a cAMP-independent activation mechanism involving the formation of inducible interdisulfide bonds between RI regulatory subunits was reported by Brennan et al. (2006a). To investigate whether PKA activation by NCA occurred through this mechanism, ARVMs were exposed to oxidants and cell lysates analyzed by Western immunoblot analysis under non-reducing conditions.
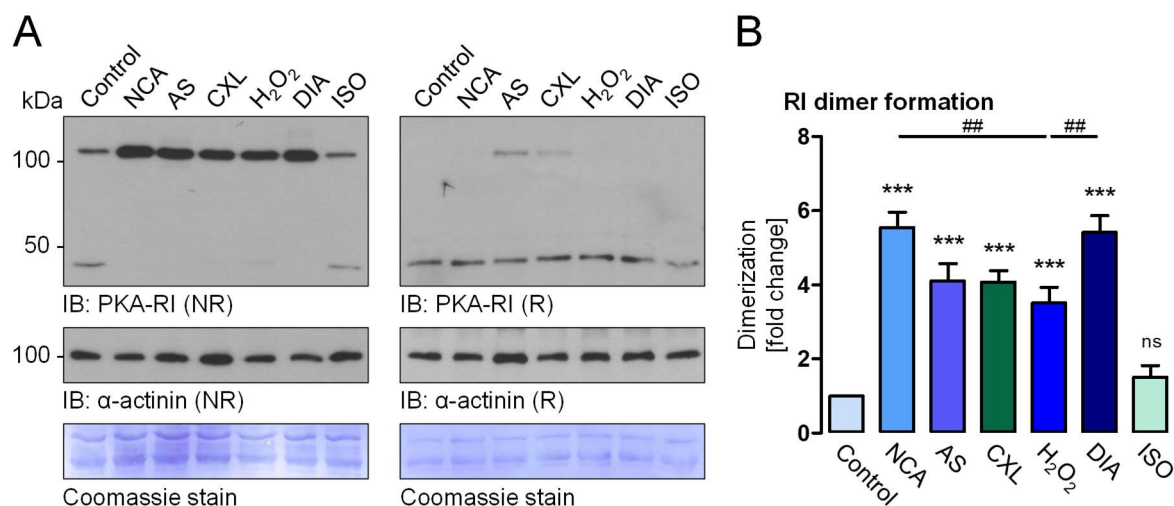
Figure 19: Dimerization of PKA-RI in response to oxidant-treatment After exposure to vehicle (control), NCA (100 µmol/L, 30 min), AS (500 µmol/L, 15 min), CXL-1020 (300 µmol/L, 15 min), H_2O_2 (100 µmol/L, 10 min), DIA (500 µmol/L, 10 min) or ISO (10 nmol/L, 10 min), ARVMs were harvested under non-reducing (NR) conditions and subjected to Western immunoblot analysis. **A** The oxidation state of PKA-RI was detected with the corresponding antibody. The α-actinin content was used as loading reference. Samples were supplemented with 10% (v/v) β-mercaptoethanol for Western immunoblot detection of PKA-RI and α-actinin under reducing (R) conditions (right panel). **B** Treatment-induced formation of dimerized PKA-RI from 10 independent experiments is represented in the bar chart. Values were normalized to α-actinin (R) and expressed as fold change of the vehicle control. *** $P<0.001$ for comparison with vehicle control and ## $P<0.01$ for comparison between treatments by one-way ANOVA with Bonferroni's Multiple Comparison post-test. ns: not significant

In control samples and after treatment with ISO, monomeric PKA-RI was detected at a molecular weight of approx. 47 kDa (Fig. 19, A, left panel). Another signal was present migrating slightly above the 100 kDa marker band, most likely representing dimerized PKA-RI due to high susceptibility to oxidation at basal conditions. Treatment with AS, CXL-1020 and H_2O_2 also resulted in a distinct increase in RI dimer formation, with only faint signals detectable for the RI monomer (Fig. 19, A, left panel and B). PKA-RI dimerization was even more pronounced after exposure to NCA and DIA, where complete conversion of RI subunits into the interdisulfide dimer state allowed no further detection of the monomeric subunit. PKA-RI dimer formation was reversible by addition of the reducing agent β-mercaptoethanol, confirming that RI dimers were based on the formation of oxidative interdisulfide bonds (Fig. 19, A, right panel). However, RI dimerization did not directly correlate with the activation of PKA, showing that RI oxidation alone was not sufficient to induce the phosphorylation of PKA substrates.

A potential coherence of NCA-mediated PKA-RI dimerization and PKA substrate protein phosphorylation was investigated by monitoring the temporal order of the two events by Western immunoblot analysis in time course experiments.
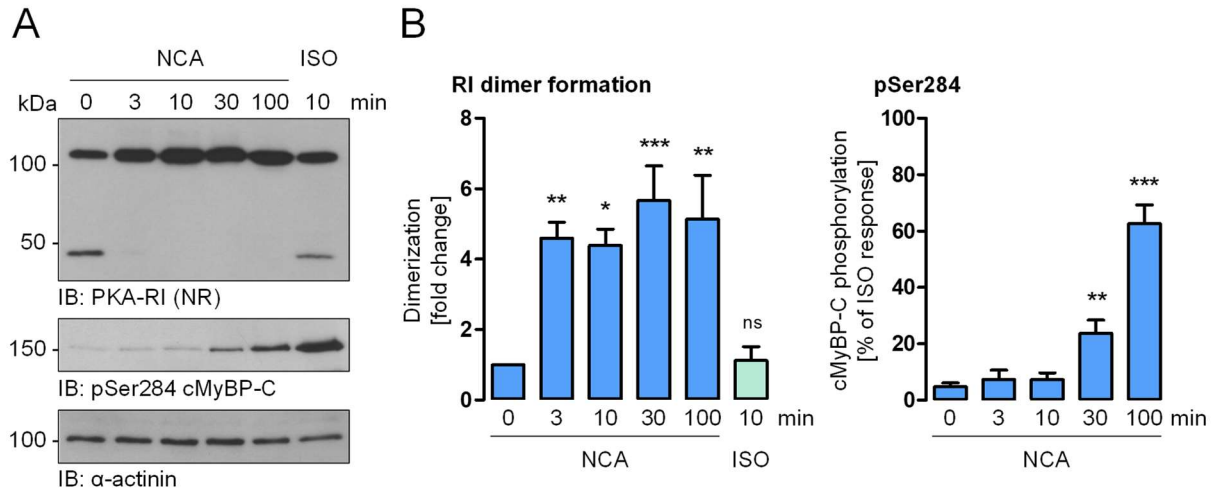
Figure 20: NCA-induced PKA-RI dimerization and cMyBP-C phosphorylation over time ARVMs were exposed to vehicle for 100 min (sample 0 min), NCA (100 µmol/L) for 3, 10, 30 or 100 min or ISO (10 nmol/L) for 10 min. **A** PKA-RI dimer formation was analyzed in cell lysates by Western immunoblot analysis performed under non-reducing conditions (NR). For the visualization of cMyBP-C phosphorylation at Ser284, lysate samples were reduced by adding 10% (v/v) β-mercaptoethanol before Western immunoblotting with the corresponding phospho-specific antibody was performed. As loading reference α-actinin was detected. **B** Bar charts showing PKA-RI dimer formation expressed as fold change of the corresponding vehicle control and cMyBP-C phosphorylation at Ser284 as % of the effect induced by ISO are representative for 4 independent experiments. Signals were normalized to α-actinin. * $P<0.05$, ** $P<0.01$, *** $P<0.001$ for comparison with vehicle control (sample 0 min) by one-way ANOVA with Dunnett's Multiple Comparison post-test. ns: not significant

Under control conditions and after exposure to ISO, both the monomeric and dimerized state of PKA-RI were present as observed previously (Fig. 20, A). NCA-treatment for 3 min was sufficient to induce RI subunit dimerization to a significant degree and dimer levels remained constant over the entire duration of the experiment (Fig. 20, A and B). Phosphorylation of cMyBP-C at Ser284, in contrast, was first detectable after 30 min of NCA-treatment and was further increased after exposure to NCA for 100 min. These results demonstrated that PKA substrate phosphorylation does not directly coincide with oxidation of RI subunits, but occurs with a time delay.

Considering the molecular weight of approx. 47 kDa for monomeric PKA-RI, the expected molecular weight of the dimerized form was approx. 100 kDa, however, RI dimers were found to migrate slower than the 100 kDa marker band in Western immunoblots and thus appeared at a higher molecular weight of approx.110 kDa. To allow a better estimation of the molecular weight of PKA-RI dimers, ARVMs were exposed to oxidants as before, and lysates subjected to Western immunoblot analysis under non-reducing conditions to detect dimerized PKA-RI (Fig. 21, A).
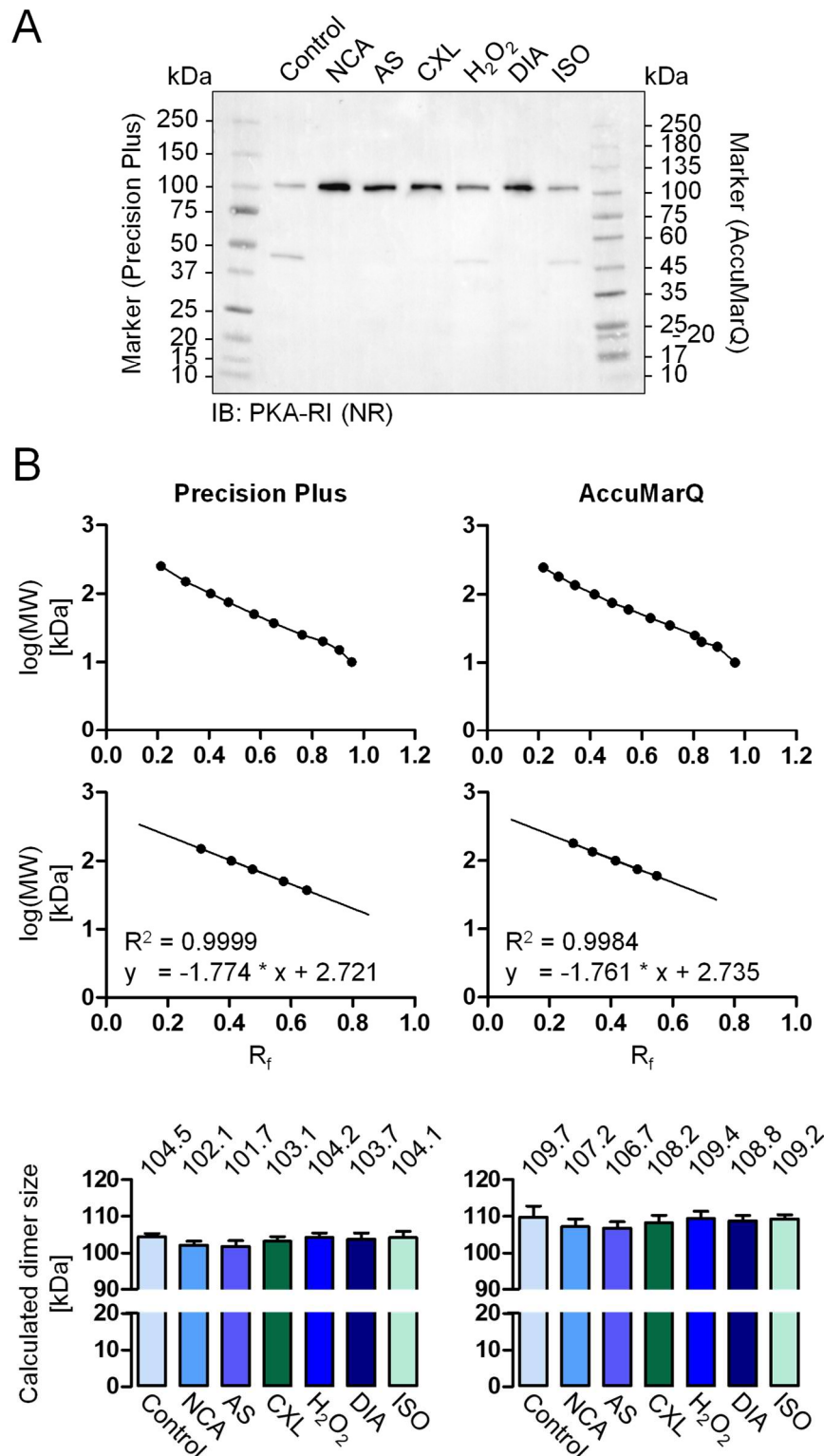
Figure 21: Molecular weight estimation of dimerized PKA-RI ARVMs were incubated with vehicle (control), NCA (100 µmol/L, 30 min), AS (500 µmol/L, 15 min), CXL-1020 (300 µmol/L, 15 min), H_2O_2 (100 µmol/L, 10 min), DIA (500 µmol/L, 10 min) or ISO (10 nmol/L, 10 min) and harvested under non-reducing conditions (NR). **A** Lysates were resolved by SDS-PAGE flanked by two molecular weight markers and subjected to Western immunoblot analysis for the detection of PKA-RI. **B** Marker bands were used to calculate R_f values from the respective migration distance. Standard curves were established by plotting the logarithm of marker band molecular weight log(MW) against R_f (top graphs). A fit with linear regression ($R^2 > 0.998$) was applied to generate the corresponding functional equation (bottom graphs). R_f values calculated from Western immunoblot signals representing dimerized PKA-RI from 4 individual experiments were inserted into the equations obtained from standard curves to yield molecular weight estimations of these bands (bar charts). With * $P<0.05$ for comparison between treatments by one-way ANOVA with Bonferroni's Multiple Comparison post-test, differences were not significant. Mean values are indicated above the corresponding bars. R_f: retardation factor

Two molecular weight markers were used to establish standard curves from marker band retardation factors (R_f; Fig. 21, B). From these curves, linear functional equations were generated and applied to calculate the molecular weight of PKA-RI dimer signals from their corresponding R_f values. Averaged calculated molecular weight ranged from 101.7 ± 1.6 to 104.5 ± 0.8 kDa (Precision Plus) and 106.7 ± 1.7 to 109.7 ± 3.0 kDa (AccuMarQ), respectively, with the AccuMarQ standard curve yielding values approx. 5 kDa higher than those calculated from the Precision Plus marker (Fig. 21, C). With both standard curves, RI dimer molecular weight displayed no significant difference between the preceding treatments. These results suggested a structural similarity between RI dimers induced by the different compounds that lead to equally decelerated migration during electrophoresis.

3.1.3 NCA-mediated myofilament translocation of PKA and PP2A subunits

A process that might explain the time lag that was observed between NCA-induced PKA-RI oxidation and the phosphorylation of cMyBP-C is a potential translocation process of cytosolic PKA to the myofilaments, where cMyBP-C is located. Therefore, the intracellular localization of type I PKA following exposure to NCA was investigated by subcellular fractionation of ARVMs into a soluble fraction (containing cytosolic proteins), a Triton-soluble fraction (comprising all membrane-bound proteins) and a myofilament-containing Triton-insoluble fraction. Successful fractionation of the cardiac myocyte homogenates was confirmed by Western immunoblot detection of the cytosolic enzyme glyceraldehyde 3-phosphate dehydrogenase (GAPDH), the membrane-bound enzyme NKA and the myofilament protein cTnI, which served as established fraction markers (Fig. 22). Irrespective of the treatment applied, both, the RI regulatory and the catalytic subunit of PKA were mainly detectable in the soluble fraction. Presence of PKA-C was to a small extent also found in the membrane fraction. After NCA exposure, an enrichment of PKA-RI was found in the Triton-insoluble fraction, which was paralleled by a pronounced signal for PKA-C in comparison to vehicle- and ISO-treated cardiac myocytes. Consistent with previous results, this suggests an NCA-induced translocation of PKA to the myofilament compartment in ARVMs.
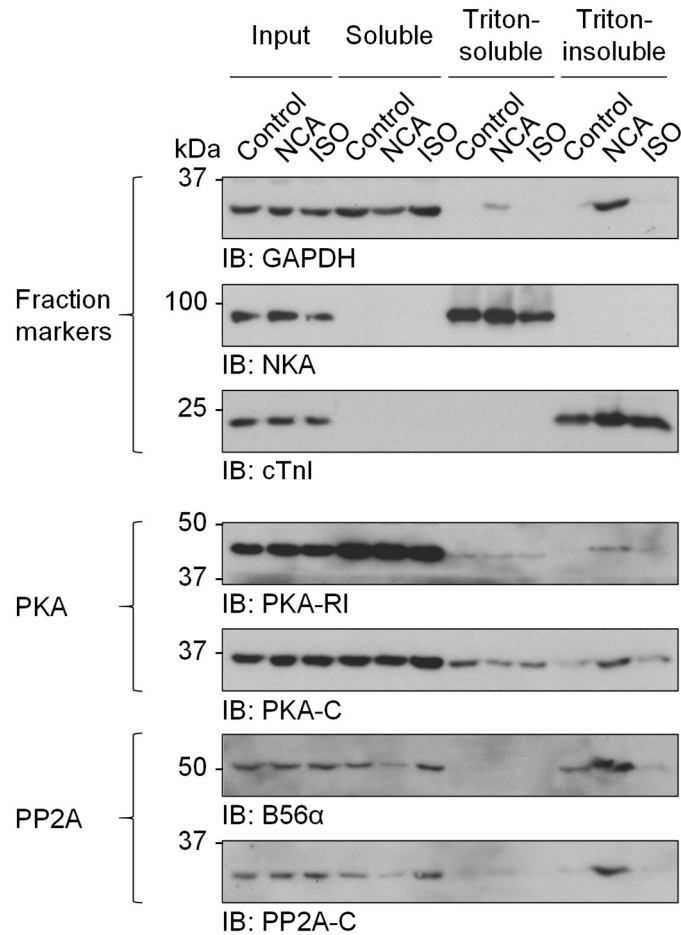
Figure 22: NCA-mediated subcellular localization of PKA and PP2A subunits Following exposure to vehicle (control), NCA (100 µmol/L, 30 min) or ISO (10 nmol/L, 10 min), ARVMs were subjected to subcellular fractionation. Western immunoblot analysis of the selected marker proteins for the cytosolic soluble (glyceraldehyde 3-phosphate dehydrogenase, GAPDH), Triton-soluble (NKA) and myofilament-containing Triton-insoluble (cTnI) fractions confirmed their successful separation. The subcellular localization of PKA (PKA-RI, PKA-C) and PP2A subunits (B56α, PP2A-C) was determined in crude lysate (input) and cardiac myocyte fractions. Immunoblots are representative for 5 individual experiments.

As a major cardiac myocyte protein phosphatase, which has been described to counteract the phosphorylation of cMyBP-C, the content of PP2A was as well evaluated in the different cardiac myocyte fractions. Interestingly, incubation with NCA resulted in diminished protein levels of PP2A-C and the B56α regulatory subunit in the soluble fraction (Fig. 22). This decrease was accompanied by protein accumulation in the myofilament-containing fraction (Triton-insoluble), suggesting a translocation of PP2A subunits from the cytosol to the myofilaments alongside with PKA.
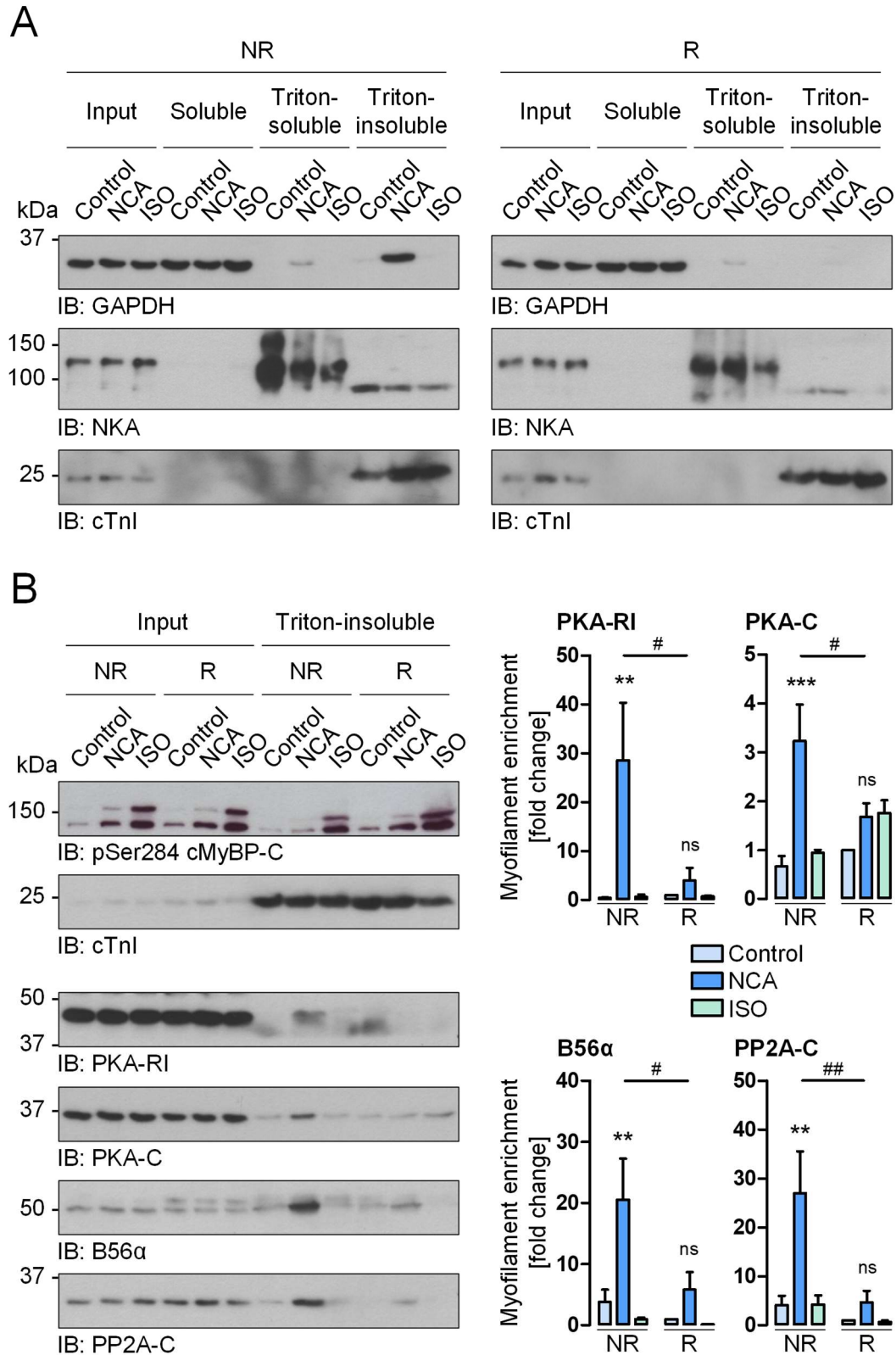
Figure 23: Effect of reducing conditions on PKA and PP2A translocation ARVMs were treated with vehicle (control), NCA (100 µmol/L, 30 min) or ISO (10 nmol/L, 10 min) and harvested under non-reducing (NR) or reducing (R) conditions. Subcellular fractionation was performed to separate cardiac myocyte proteins into soluble, Triton-soluble and myofilament-containing Triton-insoluble fractions and samples were analyzed by Western immunoblotting. **A** The presence of fraction marker proteins GAPDH, NKA and cTnI in crude lysates (input) and cardiac myocyte fraction samples was visualized. **B** Crude lysates (input) and Triton-insoluble fractions of samples harvested under non-reducing (NR) or reducing (R) conditions were examined concerning the phosphorylation of cMyBP-C at Ser284, the content of cTnI as well as detectability of PKA-RI, PKA-C, B56α and PP2A-C. The results of 3 experiments are summarized in each bar chart, representing the content of PKA-RI, PKA-C, B56α and PP2A-

C in Triton-insoluble fractions from both harvesting conditions normalized to the corresponding input signals and expressed as fold change of signal from vehicle control (R). ** P<0.01, *** P<0.001 for comparison with the corresponding vehicle control, # P<0.05, ## P<0.01 for comparison between similar treatments from different harvesting conditions by two-way ANOVA with Bonferroni post-test. ns: not significant

To investigate whether NCA-induced translocation events were based on oxidation, ARVMs were exposed to NCA or ISO and subcellular fractionation performed after harvesting in non-reducing (NR) or dithiothreitol (DTT)-containing reducing (R) buffer. In Western immunoblots, the fraction marker proteins GAPDH, NKA and cTnI exhibited the expected localizations under both harvesting conditions, confirming that separation of lysates into soluble, Triton-soluble and Triton-insoluble fraction had been achieved irrespective of buffer composition (Fig. 23, A). Robust phosphorylation of cMyBP-C at Ser284 in response to ISO-treatment was detected in whole lysates (input) and Triton-insoluble fractions of samples harvested under non-reducing and reducing conditions, as expected (Fig. 23, B). Comparable protein content in the Triton-insoluble fractions was demonstrated by the detection of similar signal intensities for cTnI. As observed previously, in cardiac myocytes harvested under non-reducing conditions, exposure to NCA resulted in a significant translocation of PKA-RI and PKA-C compared to cells treated with vehicle or ISO. Comparable protein enrichment in the Triton-insoluble fraction was found for the catalytic and the B56α regulatory subunit of PP2A. Interestingly, protein accumulation of PKA and PP2A subunits was considerably diminished when cardiac myocytes were harvested in the presence of a reducing agent, highlighting the oxidative nature of NCA-induced translocation and its reversibility by DTT-reduction.

The chronology of the translocation process that was induced by NCA was analyzed by the determination of PKA and PP2A presence in ARVM myofilament fractions following exposure to NCA for an increasing duration. Western immunoblot analysis showed that NCA-mediated phosphorylation of cMyBP-C at Ser284 in input lysates and Triton-insoluble myofilament fractions was enhanced between 10 and 30 min of treatment as observed previously (Fig. 24). Visualization of cTnI assured similar protein content in Triton-insoluble fraction samples at the different time points.
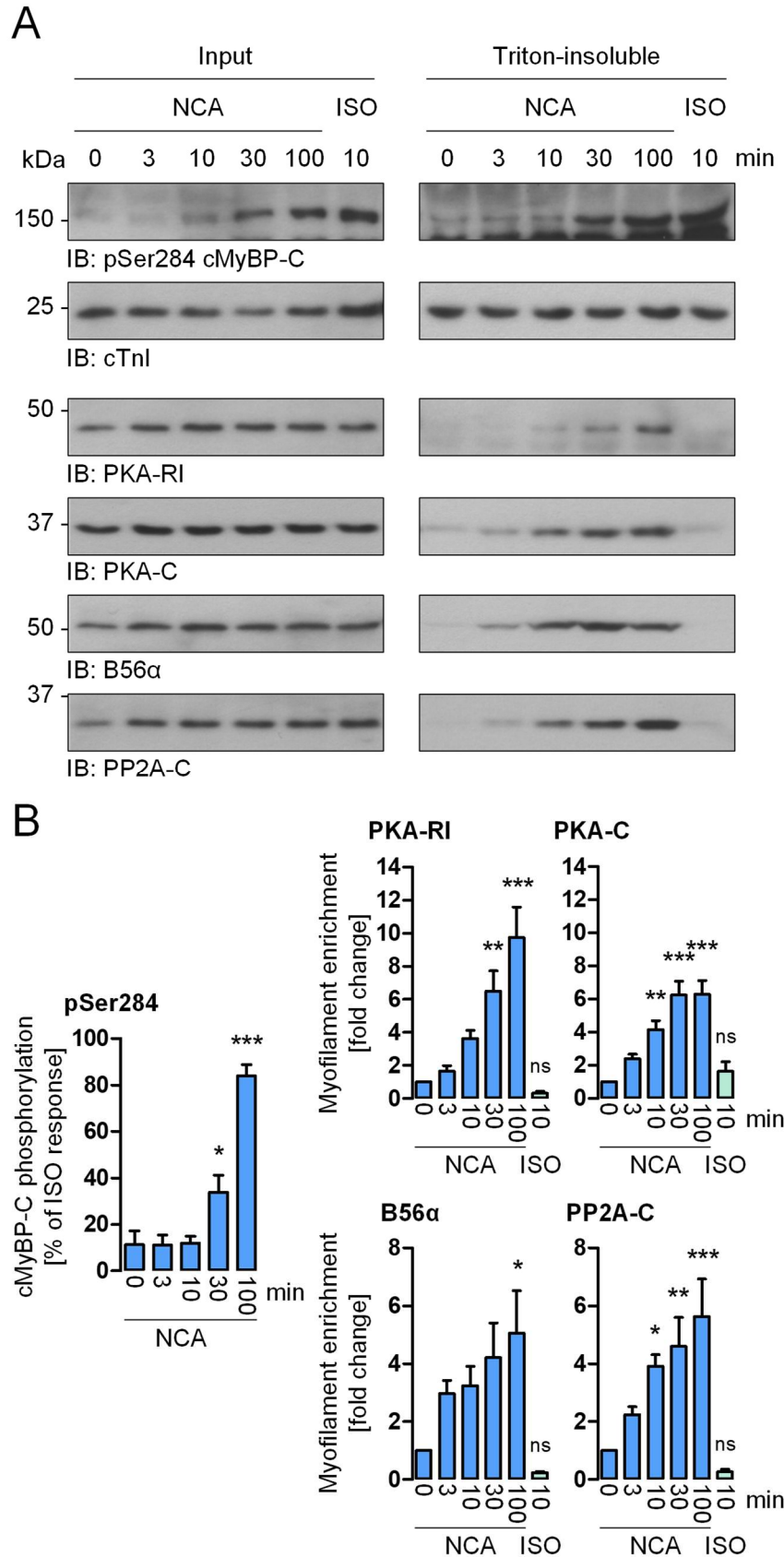
Figure 24: Time course of NCA-mediated translocation of PKA and PP2A subunits Following treatment with vehicle (control) for 100 min (sample 0 min), NCA (100 µmol/L) for 3, 10, 30 or 100 min or ISO (10 nmol/L) for 10 min the myofilament-containing Triton-insoluble fractions of ARVM lysates were collected by one-step fractionation. **A** Full lysates (input) and Triton-insoluble fractions were examined in Western immunoblot experiments, probing for cMyBP-C phosphorylation at Ser284 and the content of cTnI, PKA-RI, PKA-C, B56α and PP2A-C. **B** Bar charts summarize Ser284 phosphorylation of cMyBP-C from input samples normalized to

corresponding Coomassie stain signals (not shown) expressed as % of the ISO-response (n=6) and the signals of PKA-RI (n=4), PKA-C (n=6), B56α (n=5) and PP2A-C (n=6) detected in Triton-insoluble fractions normalized to the corresponding inputs and expressed as fold change of the control signal (sample 0 min). * $P<0.05$, ** $P<0.01$, *** $P<0.001$ for comparison with the corresponding vehicle control (sample 0 min) by one-way ANOVA with Dunnett's Multiple Comparison post-test. ns: not significant

Within the first 3 min of exposure to NCA, the presence of both PKA-RI and PKA-C as well as PP2A subunits B56α and PP2A-C in the Triton-insoluble fractions started to increase. For PKA-RI a significant accumulation was apparent after 30 min of treatment, whilst signal intensities representing PKA-C were already significantly enhanced after 10 min of NCA-exposure (Fig. 24, B). This temporal sequence was in line with the hypothesis of NCA-mediated PKA-RI dimerization being the trigger for PKA translocation to the myofilaments and consequently culminating in myofilament protein phosphorylation. The PP2A subunits B56α and PP2A-C displayed comparable accumulation behaviors with protein levels starting to rise in the respective fraction within the first 3 min of treatment, reaching significance after 10 (PP2A-C) and 100 min (B56α), respectively.

To support the finding of NCA-induced myofilament translocation, the localization of PKA-RI and B56α was analyzed by immunofluorescence staining of 'skinned' ARVMs whose plasma membrane had been removed by detergent-treatment. In each sample probed for PKA-RI, coimmunostaining for cMyBP-C displayed the expected striated doublet pattern (Fig. 25). After exposure to vehicle, AS, CXL-1020, H_2O_2 and ISO, PKA-RI displayed an equal distribution of a faint signal without detectable accumulation within the myofilament lattice. Incubation with NCA and DIA resulted in enhanced overall immunofluorescence for PKA-RI and pronounced signals that appeared as clear striations located between the cMyBP-C doublet signals. With cMyBP-C being located on both sides of the sarcomeric M-line within the C-zone of A-bands, this suggests NCA and DIA-mediated accumulation of PKA-RI at myofilament Z-discs. The signal intensity distribution reports revealed enhanced intensities for PKA-RI on both sides of cMyBP-C double peaks following incubation with NCA and DIA, but not under unstimulated control conditions, supporting indeed a Z-disc translocation of PKA-RI in response to NCA- and DIA-treatment as visually suspected before (Fig. 25, B).
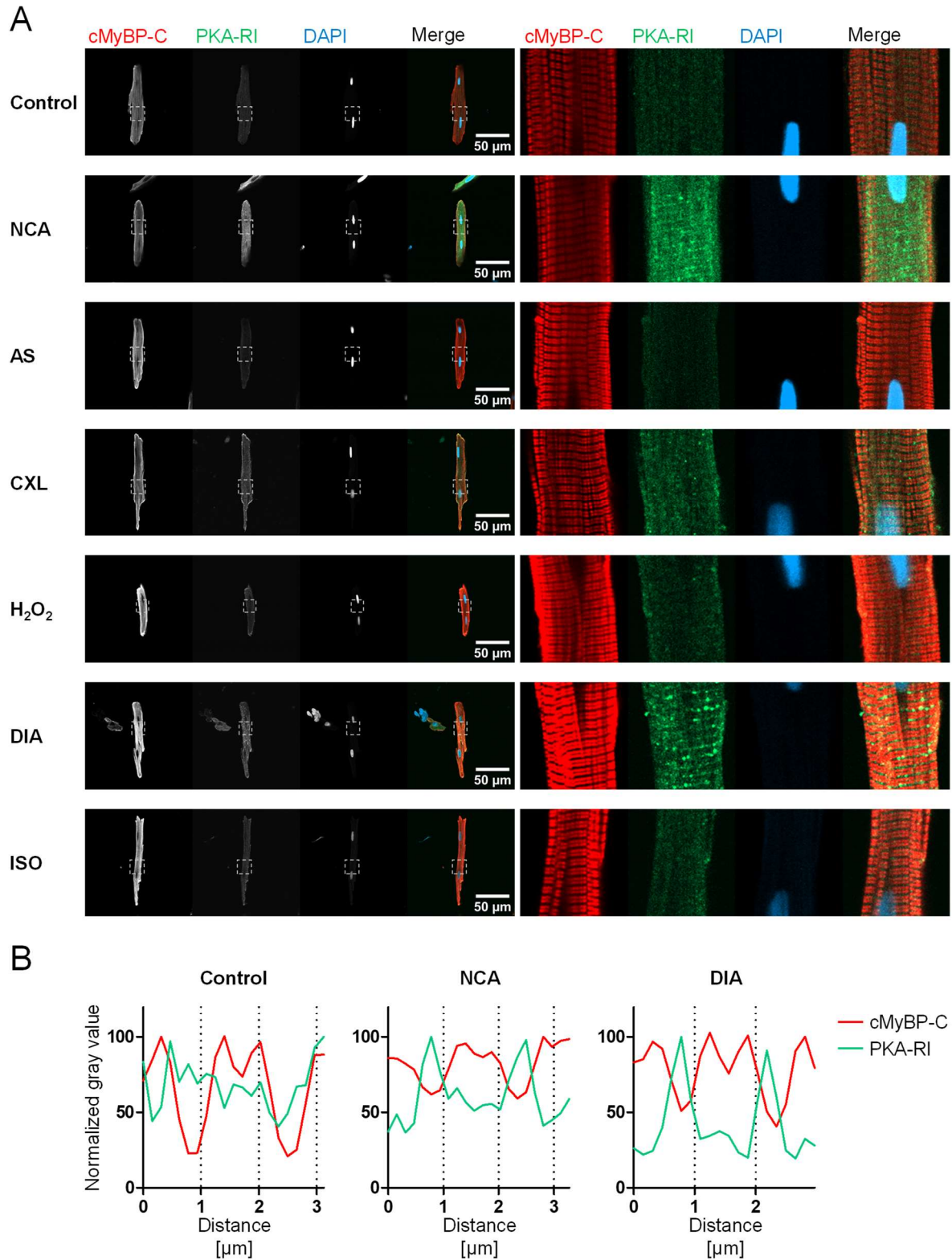
Figure 25: Investigation of NCA-mediated PKA-RI translocation by immunofluorescence imaging Following exposure to vehicle (control), NCA (100 µmol/L, 30 min), AS (500 µmol/L, 15 min), CXL-1020 (300 µmol/L, 15 min), H_2O_2 (100 µmol/L, 10 min), DIA (500 µmol/L, 10 min) or ISO (10 nmol/L, 10 min), ARVMs were skinned and fixed. PKA-RI was detected using a combination of the specific primary antibody, a biotinylated secondary antibody and Cy2-labeled streptavidin. Costaining of cMyBP-C was achieved by incubation with the specific primary antibody and a secondary antibody linked to DyLight 549. DNA was visualized by 4′,6-diamidino-2-phenylindole (DAPI). All samples were analyzed at the same settings. **A** Representative images from confocal microscopy following either treatment were selected from at least 12 images taken from at least 2 individual sample preparations. Dashed boxes indicate the area magnified in the images on the right. **B** Signal intensities for cMyBP-C and PKA-RI were measured

along a myofilament in a line report. Values are presented as % of the highest signal intensity measured for each protein.

Skinned ARVMs that were stained for B56α again exhibited a clear doublet pattern with coimmunolabeled cMyBP-C (Fig. 26). Under control conditions and following exposure to ISO, signals captured for B56α showed no distinct localization but an even background fluorescence (Fig. 26, A). In contrast, specimen that had been previously incubated with NCA revealed considerably increased signal intensities for B56α, describing a pattern of equidistant striations. The overlay with signals detected for cMyBP-C demonstrated a sharp M-line localization of B56α in these cells.
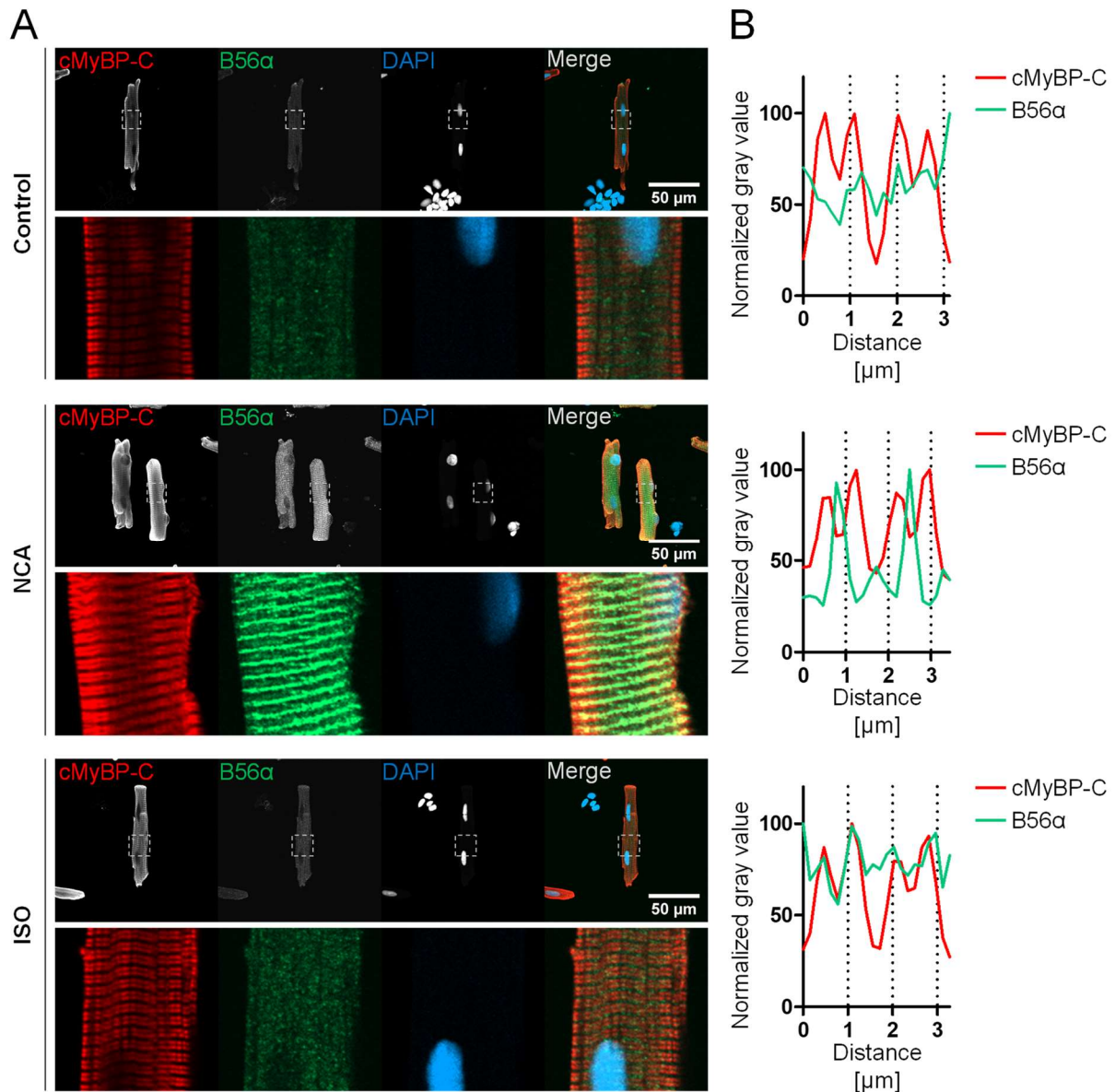
Figure 26: Evaluation of NCA-mediated translocation of B56α by immunofluorescence imaging ARVMs were treated with vehicle (control), NCA (100 µmol/L, 30 min) or ISO (10 nmol/L, 10 min) prior to skinning and fixing. B56α was detected via a combination of the specific primary antibody, a biotinylated secondary antibody and Cy2-labeled streptavidin. Costaining of cMyBP-C was achieved by incubation with the specific primary antibody and a secondary antibody linked to DyLight 549. DNA was visualized by 4′,6-diamidino-2-phenylindole (DAPI). All samples were analyzed at the same settings. **A** Exemplary images from confocal microscopy following either treatment were selected from at least 21 images taken from 3 individual sample preparations. Dashed boxes indicate the area

magnified in the images below. **B** Signal intensities of cMyBP-C and B56α along a myofilament were measured in a line report. Values are presented as % of the highest signal intensity measured for each protein.

This NCA-mediated accumulation of B56α was also supported by the signal intensity distribution reports for cMyBP-C and B56α within the myofilament lattice (Fig. 26, B). Whilst no salient intensity was present for B56α in control and ISO samples, signals peaked in-between the cMyBP-C doublets in NCA-treated cells, highlighting an NCA-induced accumulation of B56α at the M-line of the sarcomere.

To examine whether the NCA-mediated translocation of PKA and the phosphorylation of cMyBP-C were paralleled by a spatial rapprochement, the proximity of PKA-RI to cMyBP-C, myosin light chain 2v (MLC2v) and α-actinin was investigated by proximity ligation assay (PLA) in skinned ARVMs. An increased number of fluorescence signals, indicating enhanced protein colocalization, was detected when the proximity between PKA-RI and cMyBP-C was assessed following exposure to NCA (Fig. 27). A similar increase of PLA counts in response to incubation with NCA was observed for PKA-RI and MLC2v. Since cMyBP-C and MLC2v are both associated with the thick myosin filaments, this result was supportive of enhanced PKA levels to exist in the vicinity of cMyBP-C after incubation with NCA. Unexpectedly, exposure to ISO induced similar or even further enhanced PLA signals for PKA-RI with cMyBP-C or MLC2v, respectively. In contradiction with the previous immunofluorescence detection of PKA-RI at the sarcomeric Z-disc, an NCA-induced decrease in PLA counts obtained from PKA-RI and the Z-disc protein α-actinin suggested a reduced colocalization of the two proteins. The proximity between PKA-RI and α-actinin was not determined following exposure to ISO.
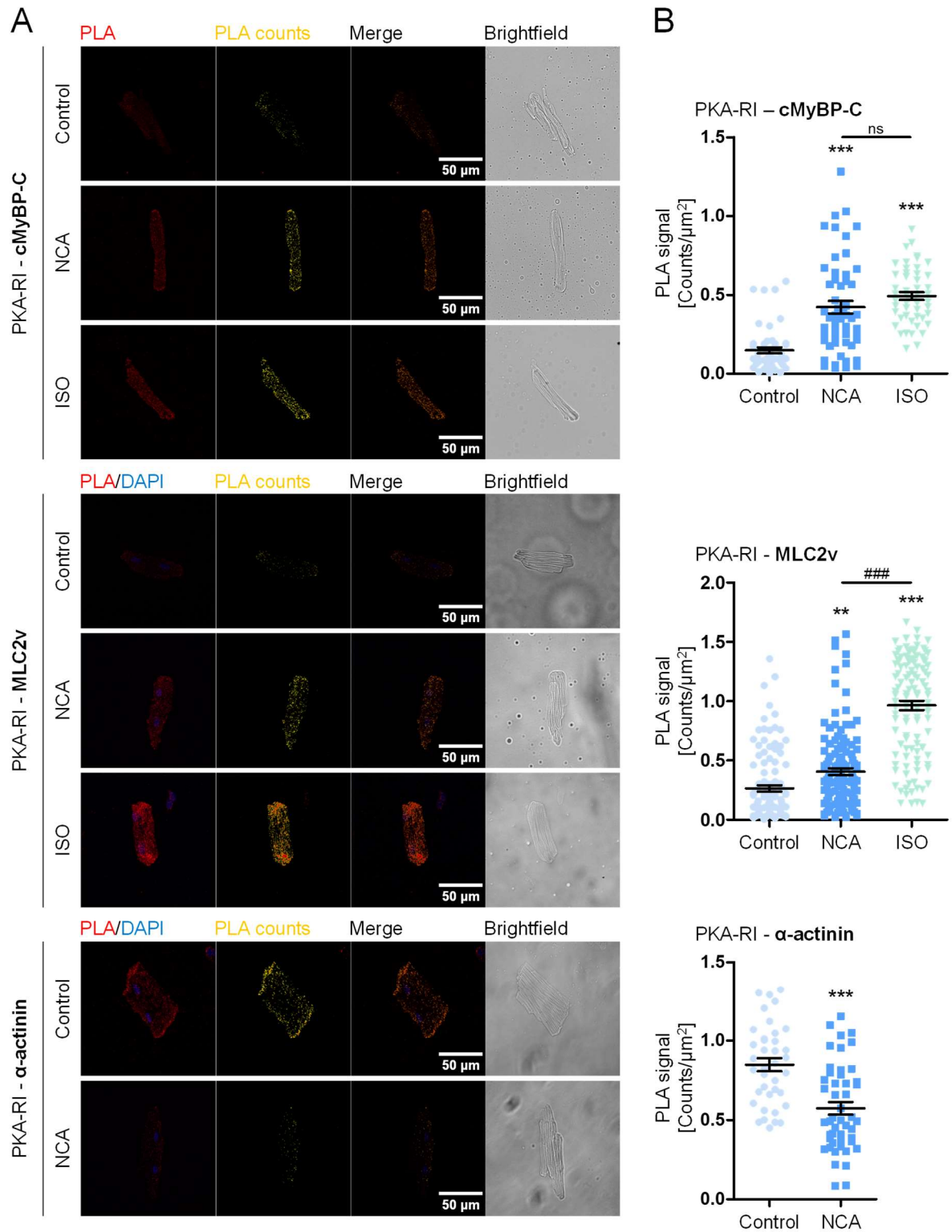
Figure 27: Visualization of PKA-RI colocalization with cMyBP-C, MLC2v and α-actinin by proximity ligation assay Following treatment with vehicle (control), NCA (100 µmol/L, 30 min) or ISO (10 nmol/L, 10 min), ARVMs were skinned, fixed and subjected to labeling for proximity ligation assay (PLA). The colocalization of PKA-RI with cMyBP-C, MLC2v or α-actinin was assessed from PLA signal counts obtained after digital analysis of confocal microscopy z-stack images. PLA counts for PKA-RI and α-actinin have not been measured after treatment with ISO. A Representative confocal images show unprocessed PLA immunofluorescence signals with DNA-costaining by DAPI, processed PLA signals used to determine PLA counts, a merged image of both and a brightfield image of the analyzed cell. DAPI-staining was not included in PLA experiments examining the colocalization between PKA-RI and cMyBP-C. B Scatter plots summarize PLA counts/µm², indicating the proximity between PKA-RI and cMyBP-C (control: n=53, NCA: n=54, ISO: n=50), MLC2v (control: n=117, NCA: n=130, ISO: n=114) or α-actinin (control: n=38, NCA: n=48). PKA-RI – cMyBP-C and PKA-RI – MLC2V: ** P<0.01, *** P<0.001 for comparison with the corresponding vehicle control and ### P<0.001 for comparison between NCA- and ISO-treated samples by one-way

ANOVA with Bonferroni's Multiple Comparison post-test. PKA-RI - α-actinin: *** P<0.001 for comparison with vehicle control by unpaired, two-tailed t-test. ns: not significant, DAPI: 4′,6-Diamidino-2-phenylindole

A potential NCA-mediated colocalization of cMyBP-C with PKA or PP2A subunits was further investigated in neonatal ventricular cardiac myocytes isolated from *Mybpc3*-targeted KO mice that heterologously express a biotin ligase (BirA)-fused version of cMyBP-C. In response to NCA-treatment, biotinylated proteins were precipitated and analyzed by Western immunoblotting.
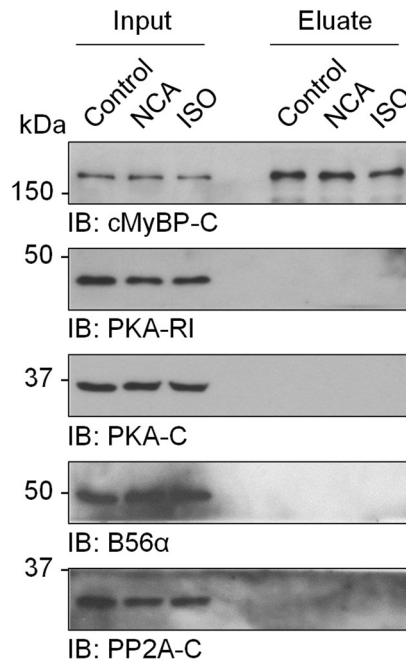
Figure 28: Assessment of NCA-mediated translocation of PKA and PP2A subunits to the vicinity of cMyBP-C Neonatal cMyBP-C KO mouse ventricular cardiac myocytes were transduced for the expression of biotin ligase BirA-linked cMyBP-C. After incubation with vehicle (control), NCA (100 µmol/L, 30 min) or ISO (10 nmol/L, 10 min), the presence of PKA (PKA-RI and PKA-C) and PP2A (B56α and PP2A-C) subunits in input lysates and eluates obtained from streptavidin-agarose-precipitation of biotinylated proteins was investigated by Western immunoblot analysis. Detection of cMyBP-C was performed to assure expression of the BirA-cMyBP-C fusion protein.

Successful viral transduction of cardiac myocytes was confirmed by the detection of cMyBP-C migrating at a molecular weight consistent with the 150 kDa protein fused to 37 kDa BirA in input lysates (Fig. 28). Anticipated auto-biotinylation of the fusion protein was demonstrated by the visualization of corresponding bands in eluate samples of precipitated modified proteins from either treatment condition. The regulatory and catalytic subunits of PKA and PP2A (PKA-RI/PKA-C and B56α/PP2A-C, respectively) were present in input lysates at comparable amounts. However, enhancement of biotin labeling of PKA and PP2A subunits in response to NCA-exposure that would indicate the translocation to the immediate vicinity of cMyBP-C could not be detected, as no signals were visible in eluate samples.

3.1.4 Oxidation of PKA and PP2A subunits by NCA

Since fractionation experiments revealed PKA and PP2A subunit translocation upon oxidation, direct oxidative modification of PKA and PP2A subunits was determined using the polyethylene

glycol (PEG)-switch method. After oxidant-treatment of ARVMs, oxidized cysteine amino acid residues were labeled with 5 kDa PEG-maleimide and the mass increment of PEGylated proteins visualized by Western immunoblot analysis.
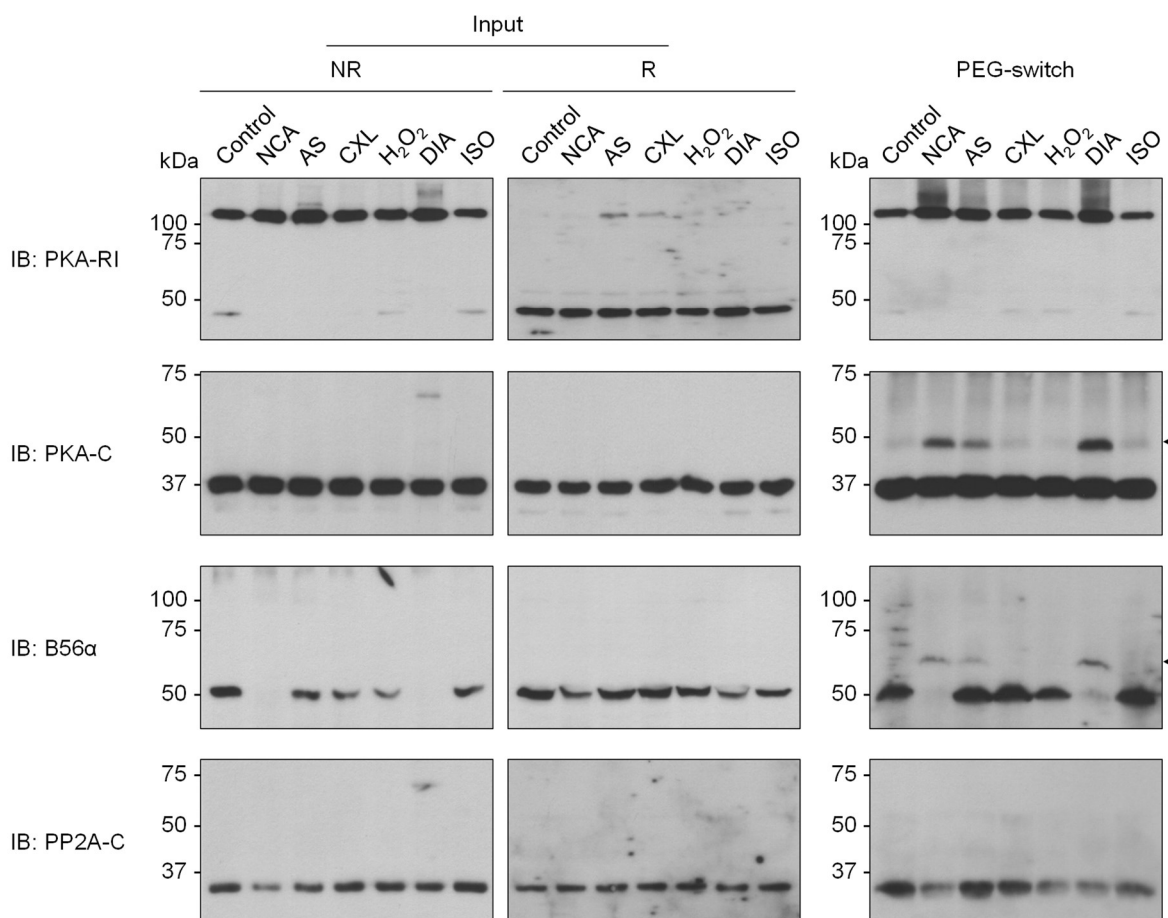
Figure 29: PEG-switch-labeling of oxidized PKA and PP2A subunits following treatment with oxidizing agents ARVMs were exposed to vehicle (control), NCA (100 µmol/L, 30 min), AS (500 µmol/L, 15 min), CXL-1020 (300 µmol/L, 15 min), H_2O_2 (100 µmol/L, 10 min), DIA (500 µmol/L, 10 min) or ISO (10 nmol/L, 10 min) and lysates subjected to PEG-switch-labeling of oxidized cysteine residues with 5 kDa PEG-maleimide. Inputs under both non-reducing (NR) and reducing (R) conditions as well as PEG-labeled samples were analyzed by Western immunoblot analysis. Protein oxidation and subsequent PEG-labeling was investigated by the detection of PKA-RI, PKA-C, B56α and PP2A-C. Arrowheads indicate PEG-induced shifts in molecular weight.

In input samples harvested under non-reducing conditions (NR), the oxidized form of PKA-RI was predominantly detectable, whilst supplementation with a reducing agent resulted in a shift to the monomeric state (Fig. 29, left and middle panel). For B56α, no signals were detectable in cardiac myocyte input samples, which had been exposed to NCA or DIA under non-reducing conditions. Interestingly, detectability of B56α was restored upon reduction of the samples, pointing towards an oxidative modification interfering with antibody binding. PKA-C and PP2A-C did not show any additional bands under non-reducing conditions apart from those migrating at the expected molecular weights, which were also detectable under reducing conditions. Analysis of the PEG-labeled samples revealed that the dissociation of PKA-RI dimers had not been achieved successfully during sample processing (Fig. 29, right panel, arrowheads). The pattern of signals was as observed in non-reducing crude lysates, illustrating that slower migrating bands occurred due to persistent oxidation by molecular air, but were not a result of

PEG attachment. In Western immunoblots probed for PKA-C, a distinct additional band was detectable in cardiac myocyte lysates following incubation with NCA and DIA and, to a lesser extent, also after treatment with AS. This higher molecular weight band depicted an increase in size of approx. 10 kDa, suggesting the presence of two PEG-labeled cysteine residues that were previously oxidatively modified during exposure to NCA, DIA and AS. A comparable pattern was observed for B56α, where treatment with NCA, DIA but also AS again resulted in the appearance of a band of increased molecular weight. Notably, upon exposure to NCA and DIA, the shift of the signal was accompanied by a lack of detectable unmodified protein. As also shown in non-reducing crude lysates, this implied an almost entire oxidation of B56α in response to treatment with NCA or DIA. No PEG-induced shift in molecular weight was observed for PP2A-C.

To avoid potential interference of PEG-labeling with antibody binding and thus protein detection, examination of PKA and PP2A subunit oxidation was pursued additionally by biotin-switch experiments. After treatment of ARVMs with NCA, CXL-1020 or ISO, oxidized cysteine thiol groups were labeled with biotin-maleimide and biotin-bound proteins collected by streptavidin-mediated precipitation (Fig. 30, B). Variations in overall protein biotinylation between treatments suggested different degrees of protein oxidation that was mediated by the applied oxidizing agents (Fig. 30, C). The loss of labeled proteins during precipitation appeared to be comparable between samples. By Western immunoblot analyses, a prominent signal for both precipitated PKA-RI and PKA-C could be detected in all three replicates of the experiment after exposure to NCA (Fig. 30, A). Notably, the signal intensities observed in samples from CXL-1020- and ISO-treated cells varied considerably, resulting in a significantly increased presence of PKA-C, but not PKA-RI following NCA-treatment. Whilst for PKA-C this result was in line with data obtained from previous PEG-switch experiments, concerning the oxidation of PKA-RI it showed a trend, which matched with the strong RI dimer formation in response to NCA that had been determined in previous experiments (see Figs. 19-21). Biotinylated PP2A-C and B56α regulatory subunit could only be visualized in one experiment. Both subunits showed a similar pattern with enhanced signals in NCA treated samples, but also after exposure to ISO.
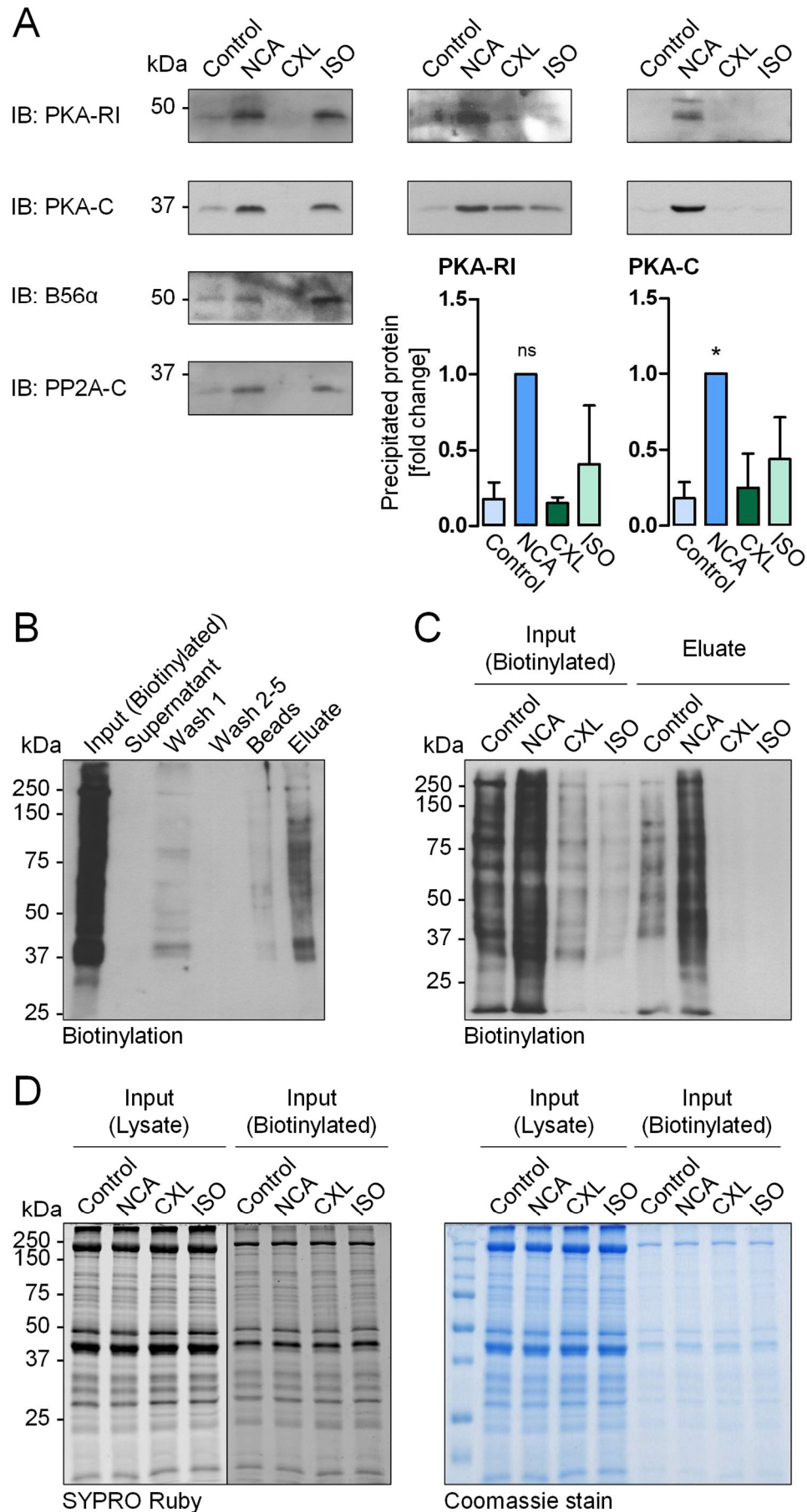
Figure 30: Investigation of NCA- and CXL-1020-mediated oxidation of PKA and PP2A subunits by biotin-switch After incubation with vehicle (control), NCA (100 µmol/L, 30 min), CXL-1020 (300 µmol/L, 15 min) or ISO

(10 nmol/L, 10 min) ARVM lysates were processed by biotin-labeling of oxidized thiol groups and subsequent precipitation of labeled proteins. **A** PKA-RI, PKA-C, B56α and PP2A-C were detected in precipitated samples by Western immunoblot analysis. Results for PKA-RI and PKA-C are summarized in bar charts (n=3). Western immunoblot signals were normalized to SYPRO Ruby total protein stain (biotinylated input) and expressed as fold change of the corresponding NCA signal. * P<0.05 for comparison with the corresponding vehicle control by one-way ANOVA with Dunnett's Multiple Comparison post-test. **B** Exemplary image displaying the purification of biotinylated proteins from a control sample by precipitation with streptavidin-agarose beads. The solution with biotinylated proteins (input), the supernatant after incubation with beads, solutions obtained from washing steps as well as beads after elution and the eluted biotin-switch sample were analyzed for biotinylated proteins by chemiluminescent detection using streptavidin-HRP. **C** Exemplary image showing biotinylated protein samples before (input) and after streptavidin-agarose precipitation (eluate). Biotinylation was visualized by chemiluminescent detection with streptavidin-HRP. **D** Total protein content from inputs taken before biotin labeling (lysate) or immediately before streptavidin-agarose precipitation (biotinylated) was examined using SYPRO Ruby and Coomassie stain as loading reference. ns: not significant

3.1.5 Effect of HNO donor compounds on PP2A and PKA catalytic activity

Oxidation of PKA-C by NCA in PEG- and biotin-switch experiments was in line with reports of the catalytic subunit containing redox sensor cysteine residues, whose oxidation affects kinase function (Humphries et al. 2002). To investigate the effect of NCA on PKA catalytic activity, the phosphorylation of a recombinantly expressed His-tagged N-terminal C1-M-C2 fragment of human cMyBP-C by active PKA-C was assessed in *in vitro* kinase assays.
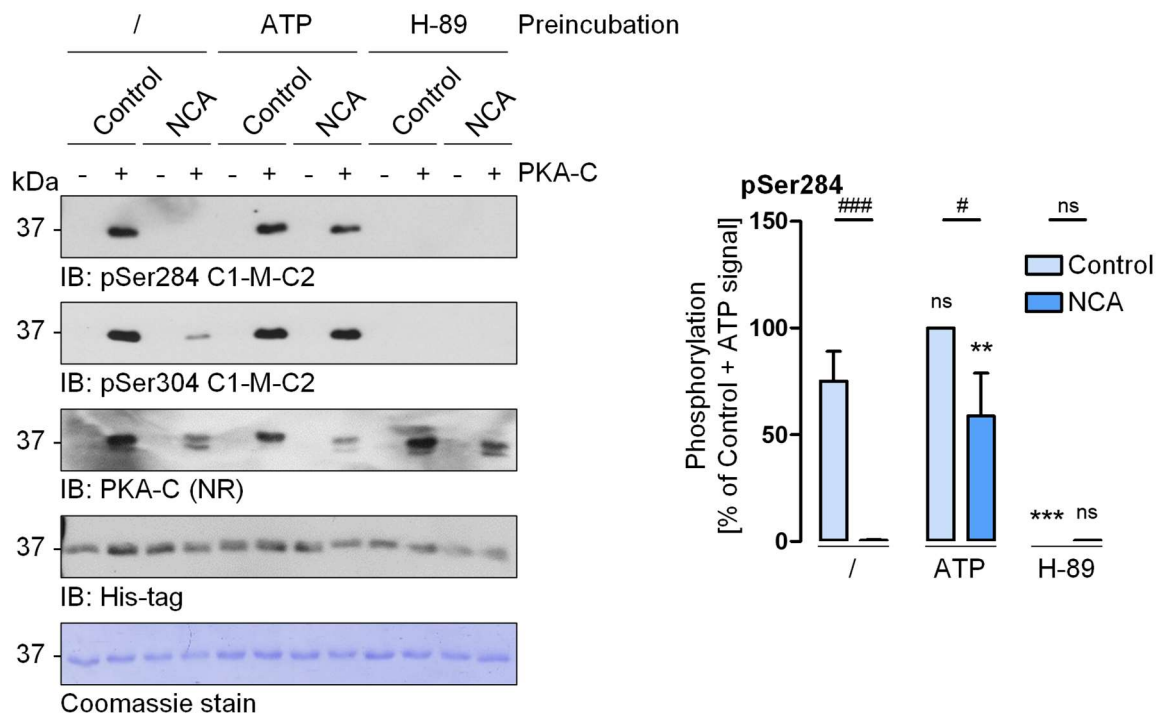
Figure 31: Modulation of PKA-C catalytic activity by NCA in an in vitro kinase assay Active recombinant PKA-C was preincubated with ATP (100 µmol/L), the PKA inhibitor H-89 (25 µmol/L) or without supplementation (/) for 10 min before treatment with vehicle (control) or NCA (100 µmol/L) for 30 min. ATP (100 µmol/L) was added to H-89 and unpretreated samples and the reaction initiated by addition of 100 pmol of the cMyBP-C fragment C1-M-C2 as substrate. The reaction was stopped by the addition of 3x non-reducing Laemmli sample buffer after 30 min of incubation. For every sample, a duplicate lacking PKA-C (-) was generated. By Western immunoblot analysis, PKA-C was visualized under non-reducing conditions (NR). Immunoblot detection of C1-M-C2 phosphorylation at Ser284 and Ser304 (referring to the entire protein) and total C1-M-C2 (His-tag) was performed after sample reduction with 10% (v/v) β-mercaptoethanol. Coomassie stain is shown as additional loading reference. The bar chart shows C1-M-C2 phosphorylation at Ser284 obtained from 4 independent experiments. Data are expressed as fold change of the vehicle control after ATP-preincubation. ** P<0.01, *** P<0.001 for comparison with the corresponding sample without pretreatment, # P<0.05, ### P<0.001 for comparison between corresponding samples with and without NCA-treatment by two-way ANOVA with Bonferroni post-test. ns: not significant

Under control conditions, incubation with PKA-C led to considerable phosphorylation of C1-M-C2 at Ser284 and Ser304 (referring to the entire protein) as detected by Western immunoblot analysis, as expected (Fig. 31). Notably, treatment of the kinase with NCA resulted in the attenuation of C1-M-C2 phosphorylation ($0.6 \pm 0.4\%$ of control pSer284 signal). Interestingly, pretreatment with ATP prior to NCA exposure protected and partially maintained the ability of PKA-C to phosphorylate its substrate ($58.7 \pm 20.0\%$ of control pSer284 signal). The PKA inhibitor H-89, in contrast, abolished detectable C1-M-C2 phosphorylation completely. Under non-reducing conditions, PKA-C was detectable as a double band by western immunoblot analysis. Whilst in control samples the upper band was more pronounced, both signals were of similar intensity after exposure to NCA. Following ATP-pretreatment and NCA incubation, however, the bottom band appeared weaker, giving rise to the hypothesis that ATP binding to the kinase might protect PKA-C from the formation of an NCA-mediated inhibitory intradisulfide bond in the ATP binding site of the kinase.

Because PP2A subunits were found enriched in Triton-insoluble fractions of NCA-treated ARVMs alongside with PKA, the influence of HNO donor compounds on PP2A enzymatic activity was assessed. Active recombinant PP2A-C was incubated with NCA, CXL-1020 or the potent protein phosphatase inhibitor okadaic acid (OA) and dephosphorylation of the fluorogenic substrate 6,8-difluoro-4-methylumbelliferyl phosphate (DiFMUP) recorded in a fluorescence assay.
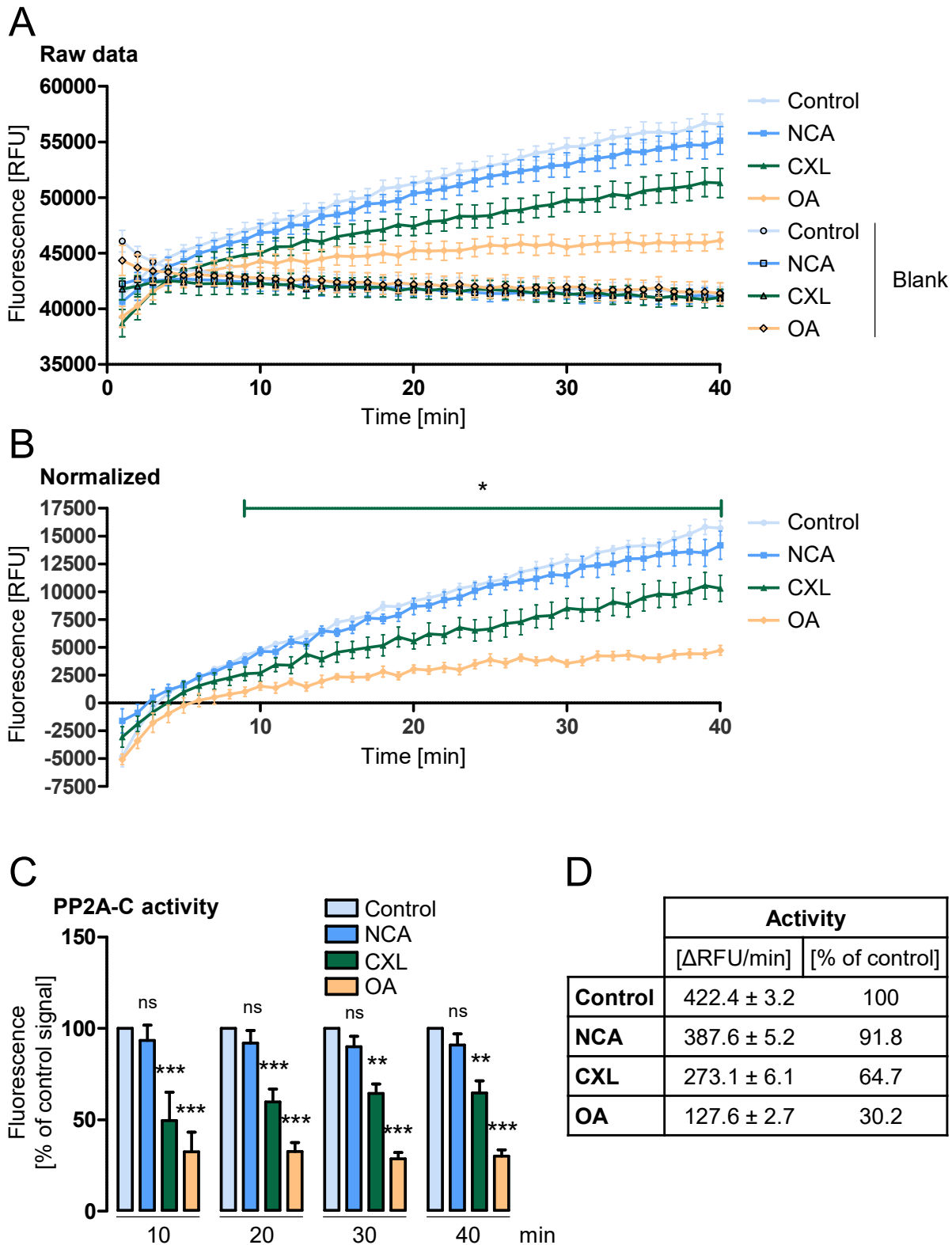
Figure 32: Effect of NCA and CXL-1020 on PP2A-C activity Active recombinant human PP2A catalytic subunit was supplemented with vehicle (control), NCA (100 µmol/L), CXL-1020 (300 µmol/L) or OA (10 nmol/L) and the substrate DiFMUP. Fluorescence reflecting substrate turnover was monitored over a period of 40 min. For each treatment condition, a blank sample lacking the protein phosphatase was included in the measurement. **A** The results of 5-6 independent experiments are displayed in the diagram as relative fluorescence units (RFU) over time. **B** Values from A are presented after normalization to the corresponding blank samples. CXL-1020 exerted a significant reduction of RFU up from 9 min after initiation of the reaction when compared to control and expressed as % of corresponding control values. * $P < 0.05$ by one-way ANOVA with Bonferroni's Multiple Comparison post-test. **C** The bar charts show RFU values of 5-6 experiments after 10, 20, 30 and 40 min of reaction duration. Measured fluorescence was normalized to blank values and expressed as % of the control signal. ** $P < 0.01$,

Blank samples from either treatment without protein phosphatase displayed similar fluorescence emissions, indicating that neither of the compounds had a direct impact on detectable fluorescence signals or DiFMUP turnover (Fig. 32, A). After normalization to blank values, control reactions displayed an average increase in fluorescence over time by 422.4 ± 3.2 relative fluorescence units (RFU)/min, reflecting the successful dephosphorylation of DiFMUP by active phosphatase. Emission of fluorescence was significantly decreased in samples containing OA, with an average PP2A activity amounting to 30.2% of the control value, as expected. Whilst NCA had no significant effect on DiFMUP-dephosphorylation (91.8% of control), CXL-1020 reduced the measured fluorescence by an average of 35.3% and reached significance 9 min after the reaction was started. These data illustrate that NCA did not interfere with PP2A catalytic activity, whilst CXL-1020 exerted a significant inhibitory effect on the protein phosphatase *in vitro*.

3.1.6 NCA and CXL-1020 alter cardiac myocyte contractility

The impact of NCA and CXL-1020 on cardiac myocyte function was determined by single cell contractility measurements in ARVMs. Under vehicle conditions (control), cardiac myocytes displayed no alterations of the observed contractile parameters, whilst β-AR stimulation with ISO resulted in the expected enhancement of contractility (+8.5 ± 0.6% sarcomere shortening *vs.* baseline) with increased maximal contraction and relaxation velocities (Fig. 33 and Fig. 34, left column). Exposure to NCA induced significantly increased sarcomere shortening (+4.8 ± 0.7% *vs.* baseline) as well as maximal contraction and relaxation velocities of cardiac myocytes within 1 min after compound application (Fig. 34, middle column). However, this response was only transient and was reversed when measurement parameters reached a plateau state after 4.5 min on average. Notably, diastolic sarcomere length considerably decreased during the exposure to NCA from 1.72 ± 0.03 µm (baseline) to 1.61 ± 0.02 µm (-6.3 ± 0.9%). Alongside with the observation of an absent response to subsequent application of ISO, this finding suggests perturbed cardiac myocyte relaxation and impaired β-AR signaling.
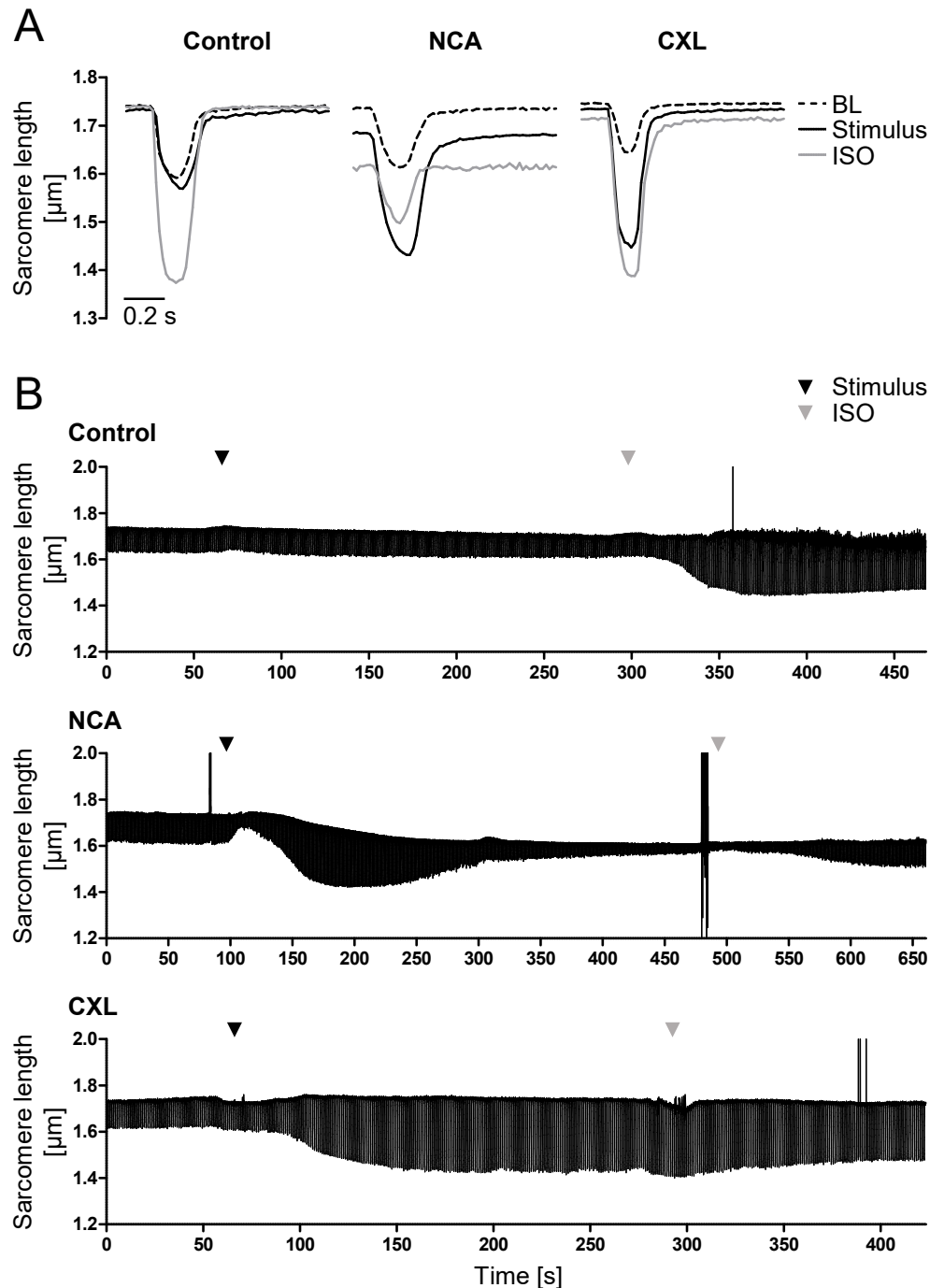
Figure 33: NCA- and CXL-1020-mediated changes in ARVM contractility Sarcomere length of single ARVMs paced at 1 Hz was recorded under basal conditions (baseline, BL) and upon exposure to vehicle (control), NCA (100 µmol/L) or CXL-1020 (300 µmol/L) until a plateau phase was reached. Subsequently, ISO (10 nmol/L) was added. **A** Representative single contraction peaks from ARVM measurements with vehicle (control), NCA or CXL-1020 are shown at baseline (BL, dashed graph), upon stimulation (continuous black graph) and after application of ISO (continuous grey graph). Except for NCA (displayed graph shows the response after 1 min of NCA-exposure), stimulus peaks were derived from plateaued responses. **B** Exemplary records of ARVM measurements present sarcomere shortening at baseline, upon stimulation with vehicle (control), NCA or CXL-1020 (black arrowhead) and after application of ISO (grey arrowhead). Outliers visible as vertical lines are caused by disturbances during the measurements.

In contrast to NCA, CXL-1020 induced significantly enhanced sarcomere shortening, which was persistent when a plateau phase was reached (+4.1 ± 0.7% *vs.* baseline; Fig. 34, right column). The CXL-1020-mediated increase in contractility was again paralleled by enhanced maximal contraction and relaxation velocities.
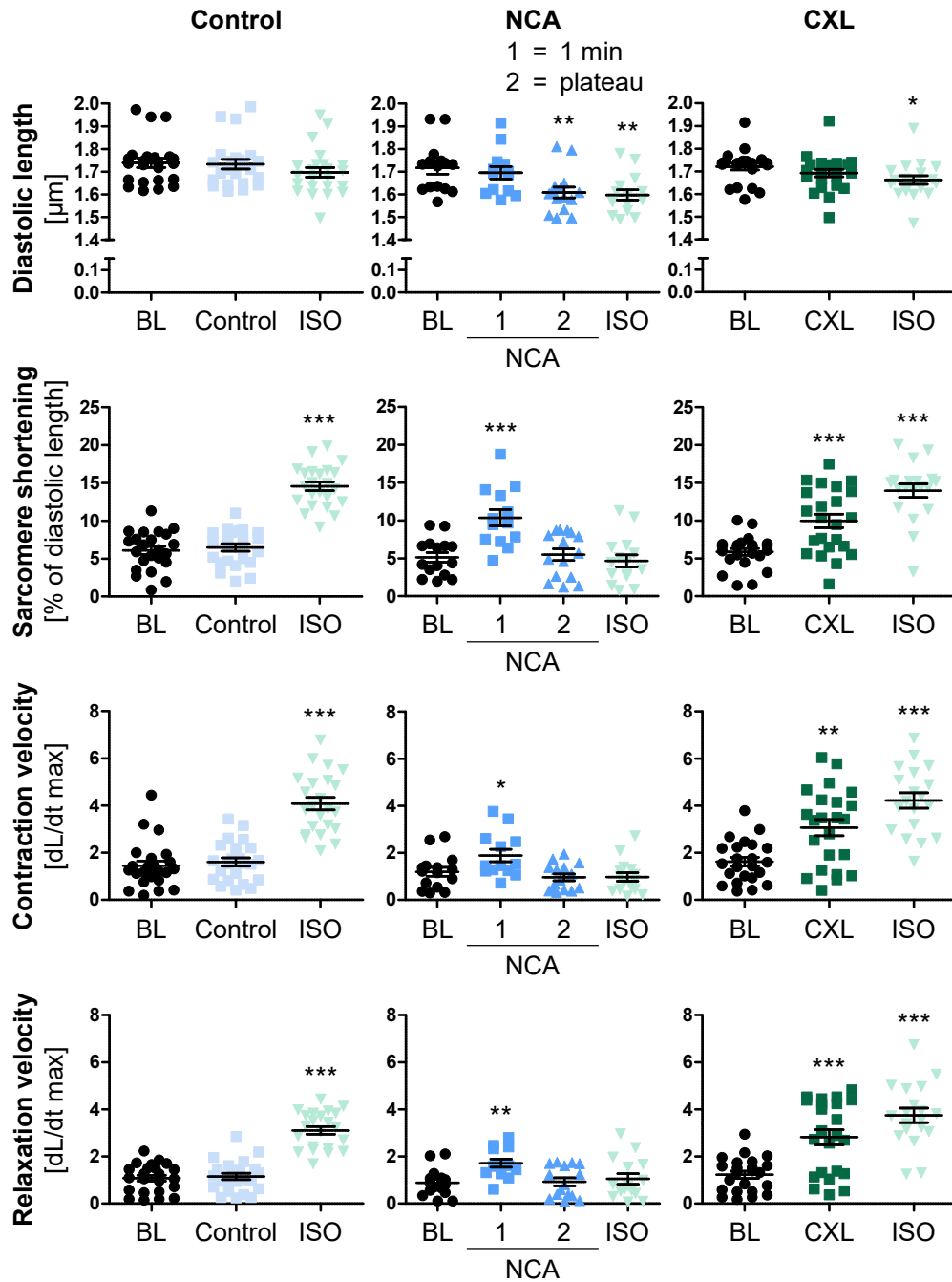
Figure 34: Alteration of ARVM contractility parameters in response to NCA and CXL-1020 Contractility parameters of single ARVMs paced at 1 Hz were determined under basal conditions (baseline, BL) and upon exposure to vehicle (control), NCA (100 µmol/L) or CXL-1020 (300 µmol/L). Subsequently, cells were stimulated with ISO (10 nmol/L). Diastolic sarcomere length, sarcomere shortening and maximal contraction and relaxation velocities of ARVMs are shown under baseline conditions, during exposure to vehicle (control; n=23), NCA (n=13-15) or CXL-1020 (n=19-23) and following supplementation with ISO. The response to NCA was evaluated both after 1 min and when a plateau was reached (average 4.5 min). * P<0.05, ** P<0.01, *** P<0.001 for comparison with corresponding baseline values by one-way ANOVA with Dunnett's Multiple Comparison post-test.

For direct comparison of data that were obtained from control measurements and upon exposure to NCA and CXL-1020, results from contractility measurements were expressed as fold change of their respective baseline values. The decrease of diastolic length during NCA exposure as well as enhanced sarcomere shortening and increased maximal relaxation velocity after 1 min remained significantly altered when compared to control measurement

parameters (Fig. 35). Moreover, contraction time (time to peak) was significantly higher than under control conditions, both after 1 min and during the plateau phase.
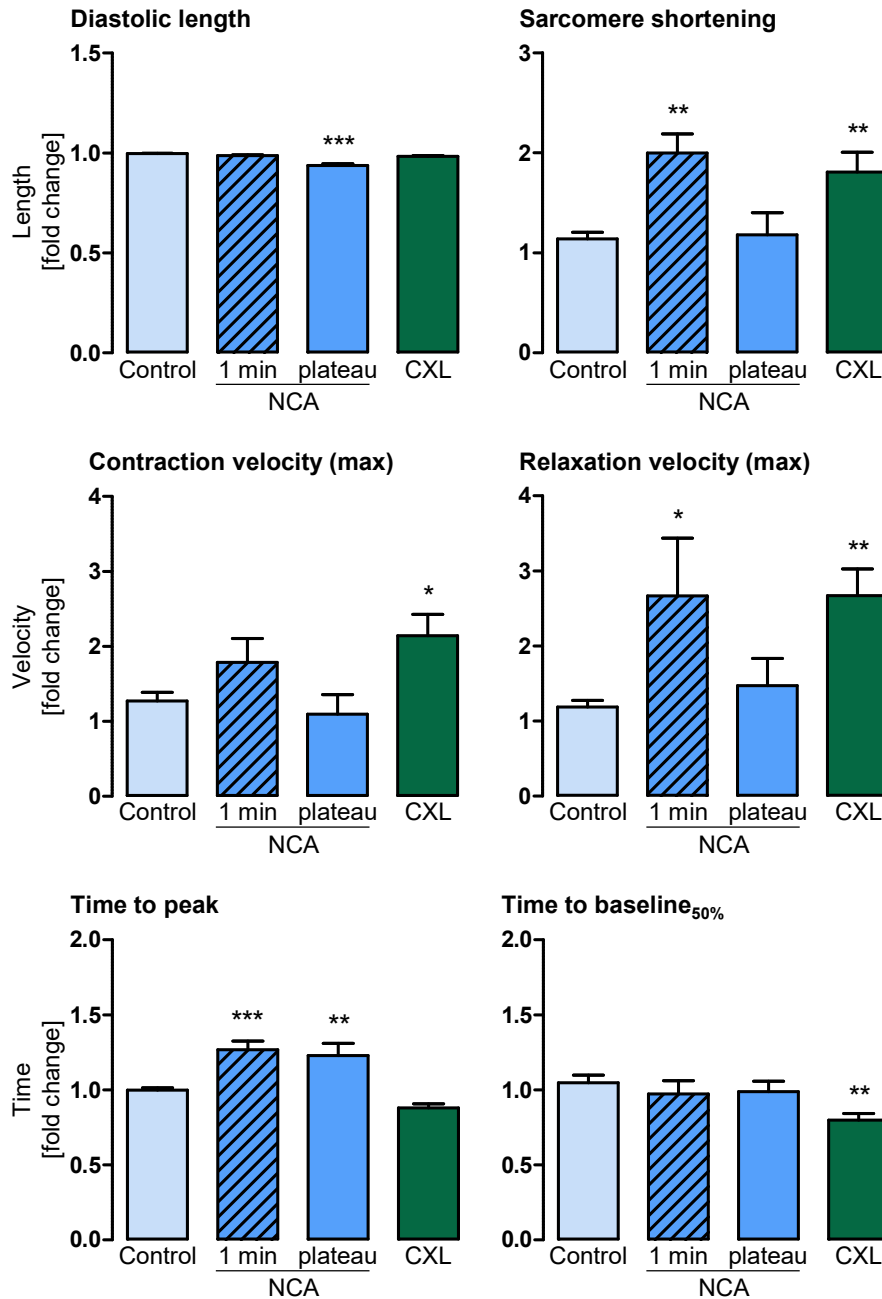
Figure 35: Comparison of ARVM contractility parameters mediated by NCA and CXL-1020 Contractility parameters of single ARVMs paced at 1 Hz were determined under basal conditions and upon exposure to vehicle (control), NCA (100 µmol/L) or CXL-1020 (300 µmol/L). Diastolic sarcomere length, sarcomere shortening, maximal contraction and relaxation velocities, as well as time to peak and time to baseline$_{50\%}$ of ARVMs are shown in response to vehicle (control; n=23), NCA (1 min: n=13; plateau: n=15) and CXL-1020 (n=23) as fold change of their respective baseline values. The response to NCA was evaluated both after 1 min and at a plateau phase (average 4.5 min). * $P<0.05$, ** $P<0.01$, *** $P<0.001$ for comparison with vehicle control by one-way ANOVA with Dunnett's Multiple Comparison post-test.

In response to CXL-1020, sarcomere shortening, as well as maximal contraction and relaxation velocities were increased when compared to control values (Fig. 35). In line with the enhanced maximal relaxation velocity, time to baseline$_{50\%}$ was significantly reduced. Taken together, contractility data revealed an NCA-induced transient increase in contractility, which was quickly

replaced by effects that suggest damages to the contractile machinery, such as impaired relaxation and a blunted response to β-AR stimulation. Exposure to CXL-1020 led to enhanced contractile function and positive lusitropy, without any detectable adverse side effects.
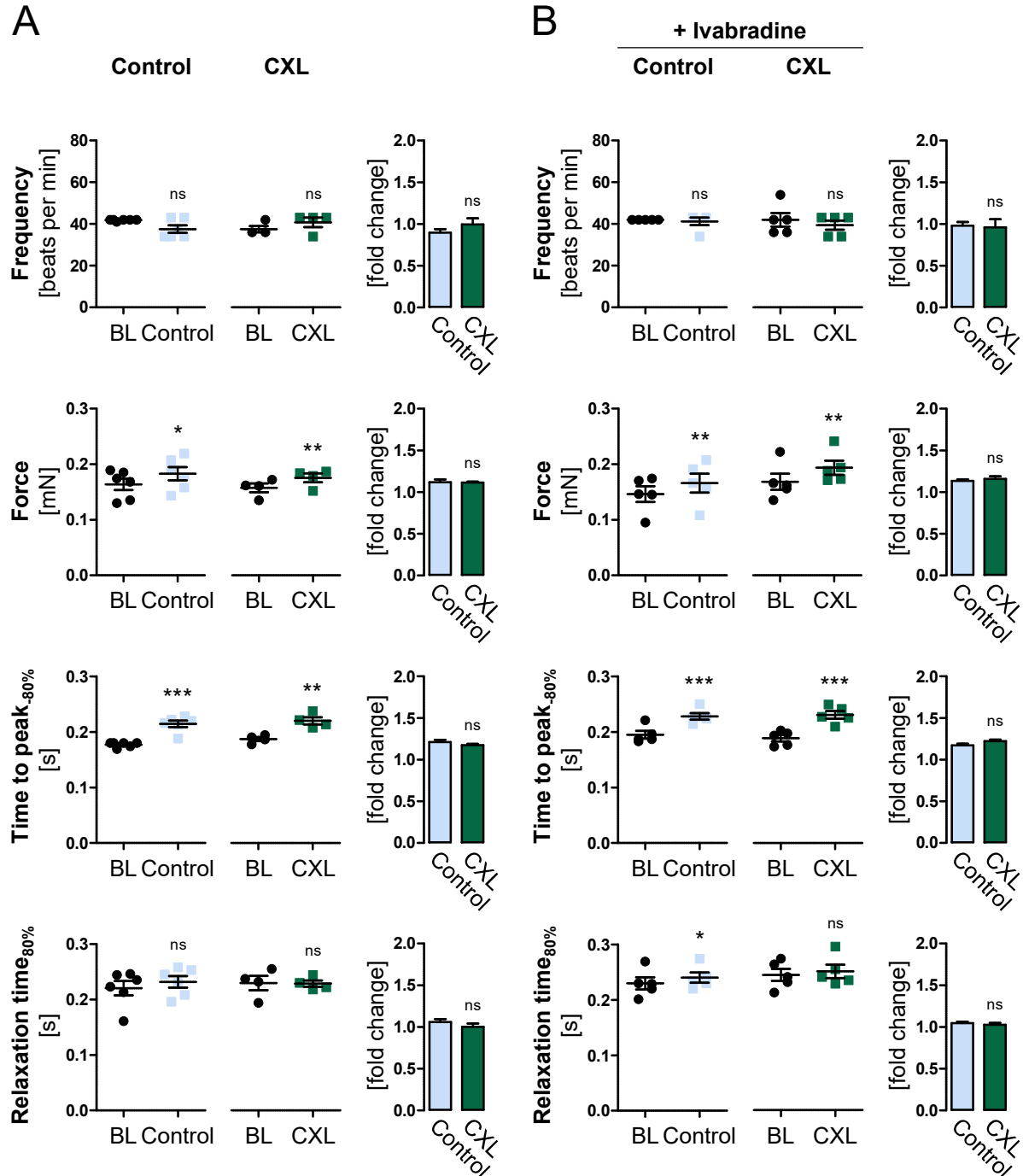
Figure 36: Contractility of engineered heart tissues in response to CXL-1020 Contraction frequency, force of contraction, time to peak$_{-80\%}$ and relaxation time$_{80\%}$ of engineered heart tissues (EHTs) generated from human induced pluripotent stem cell (hiPSC)-derived cardiac myocytes were measured during pacing at 0.7 Hz at baseline (BL) and in response to vehicle (control; n=6) or 300 µmol/L CXL-1020 (n=4; **A**). EHT contractility was additionally examined following pretreatment with 300 nmol/L of ivabradine to reduce the frequency of spontaneous beating (**B**). These measurements (n=5 for control and CXL-1020) were performed in the presence of ivabradine. Similar results were obtained in another independently performed experiment (data not shown).

The effect of CXL-1020 on cardiac myocyte contractility was further investigated in a model of contractile engineered heart tissues (EHTs) composed of human induced pluripotent stem cell (hiPSC)-derived cardiac myocytes. EHTs were paced to contract with a frequency of 0.7 Hz. After the establishment of a stable baseline, EHTs were allocated into a control and an intervention group (Fig. 36, A). CXL-1020, but also the vehicle (control) significantly increased force of contraction and time to peak$_{-80\%}$ when compared to baseline, whilst relaxation time$_{80\%}$ remained unchanged. Comparison of the relative change of contraction parameters from baseline values revealed no difference between control and CXL-1020-treated tissues. Pretreatment of EHTs with ivabradine to reduce spontaneous beating frequencies led to similar results without detectable differences between effects exerted by vehicle (control) and CXL-1020 (Fig. 36, B).

3.1.7 The role of sGC, PKG and ROCK in CXL-1020-mediated contractility

The activation of PKG is associated with cellular events that contribute to accelerated cardiac myocyte relaxation (Blumenthal et al. 1978; Sabine et al. 1995). Hence, sGC-mediated activation of PKG was investigated as a potential mechanism that might be involved in the positive lusitropic effect observed for CXL-1020 in single ARVMs. As determined in previous contractility measurements, CXL-1020 led to enhanced sarcomere shortening and maximal contraction and relaxation velocities of ARVMs, which was paralleled by reduced time to baseline$_{50\%}$ (Fig. 37, left panel). After pretreatment with the sGC inhibitor ODQ, sarcomere shortening and maximal contraction velocity in response to CXL-1020 were comparable to values obtained from control measurements (Fig. 37, right panel). Notably, maximal relaxation velocity also remained increased after ODQ-pretreatment, suggesting that CXL-1020-mediated effects observed in isolated ARVMs were not mediated by sGC activation. Although time to baseline$_{50\%}$ was significantly reduced in control experiments only, the direct comparison between control and ODQ-treated cells emphasized the assumption of an sGC-independent mechanism for CXL-1020 in cardiac myocytes (Fig. 37, bar charts).
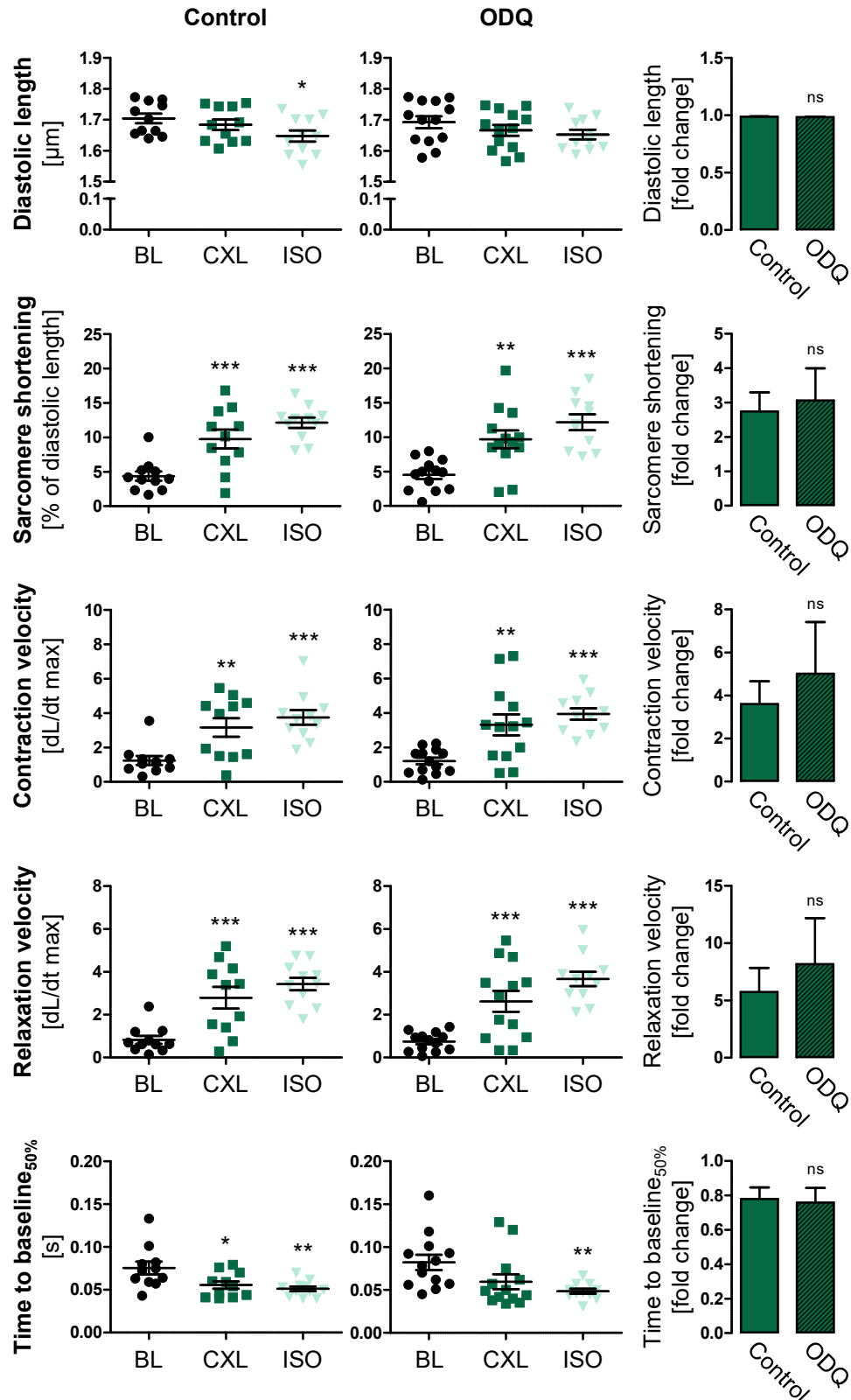
Figure 37: Impact of sGC-inhibition on CXL-1020-mediated lusitropy ARVMs were preincubated with vehicle (control; n=11) or the sGC inhibitor ODQ (20 µmol/L; n=11-13) for 10 min prior to assessment of contractility parameters from single ARVMs paced at 1 Hz under basal conditions (baseline, BL), upon exposure to CXL-1020 (300 µmol/L) and after supplementation with ISO (10 nmol/L). Diastolic sarcomere length, sarcomere shortening, maximal contraction and relaxation velocities, as well as time to baseline$_{50\%}$ are shown as raw data (scatter plots) and the CXL-1020 response as fold change of their respective baseline values (bar charts). Scatter plots: * P<0.05, ** P<0.01, *** P<0.001 for comparison with corresponding baseline values by one-way ANOVA with Dunnett's Multiple Comparison post-test. Bar charts: * P<0.05 for comparison with the corresponding vehicle control by unpaired, two-tailed t-test. ns: not significant

Like PKA type I, PKGIα can be activated in a cyclic nucleotide-independent manner via oxidation of redox sensor cysteine residues (Burgoyne et al. 2007). Therefore, the oxidation status of PKGIα and the contribution of sGC in the cellular response to CXL-1020 were investigated by Western immunoblot analysis of ARVM lysates.
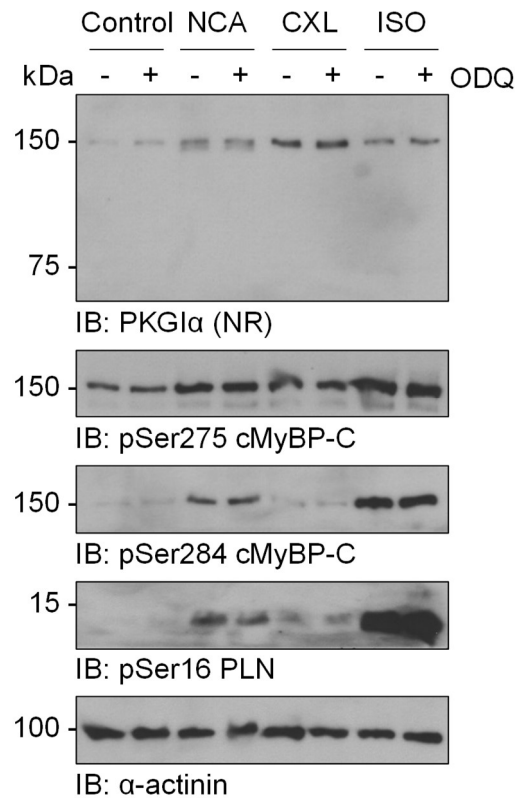
Figure 38: The role of sGC in cMyBP-C and PLN phosphorylation in ARVMs After pretreatment with ODQ (20 µmol/L) for 10 min, ARVMs were exposed to vehicle (control, 30 min), NCA (100 µmol/L, 30 min), CXL-1020 (300 µmol/L, 15 min) or ISO (10 nmol/L, 10 min) and cardiac myocyte lysates examined by Western immunoblot analysis. For detection of PKGIα samples were processed under non-reducing conditions (NR). For analysis of phosphorylation of cMyBP-C at Ser275 and Ser284 as well as PLN at Ser16 reducing conditions were applied. α-Actinin is shown as loading reference.

Under non-reducing conditions, PKGIα was observed at a molecular weight of 150 kDa in control samples, likely corresponding to the interdisulfide containing protein kinase due to basal oxidation (Fig. 38). Monomeric PKGIα, expected to migrate at 75 kDa, could not be detected. Incubation with NCA led to a small enhancement of PKGIα dimer signal intensity with an additional faint band migrating immediately below the dimer, reflecting NCA-mediated formation of a previously reported oxidative intradisulfide bond (Donzelli et al. 2017). In response to CXL-1020, enhanced dimer formation was found without appearance of the extra band, potentially pointing towards oxidative activation of PKGIα. Western immunoblot signals detected for the protein kinase were unaffected by the ODQ-mediated inhibition of sGC prior to the respective treatment. As observed in earlier experiments, cMyBP-C phosphorylation at Ser275 and Ser284 was enhanced after treatment with NCA and ISO but remained unaffected by CXL-1020 when compared to control samples. This was paralleled by clear NCA- and ISO-induced phosphorylation of PLN, whilst only a minor signal was observed following exposure

to CXL-1020. Pretreatment with ODQ did not result in any observed alterations of CXL-1020-induced phosphorylation of cMyBP-C or PLN, suggesting that modulation of sGC activity and cGMP-mediated activation of PKGIα in cardiac myocytes by CXL-1020 is not the paramount mechanism of compound action. However, the increase in activatory PKGIα dimer formation, which was accompanied by a small increase in PLN phosphorylation requested further investigation of a potential direct activation of the kinase by CXL-1020.

To determine if lusitropic effects of CXL-1020 were based on the formation of interdisulfide bonds between PKGIα monomers and the resulting activation of the kinase, CXL-1020 was compared to the drug G1, a molecule that was recently reported to act through interdisulfide formation in PKGIα as the underlying molecular mechanism of action (Burgoyne et al. 2017). As shown before, sarcomere shortening and maximal contraction and relaxation velocities of single ARVMs increased with CXL-1020 (Fig. 39 and Fig. 40, right panel). In line with the activation of PKGIα, exposure to G1 enhanced maximal relaxation velocity (Fig. 40, middle panel). However, this response was accompanied by increased sarcomere shortening and maximal contraction velocity. In addition, diastolic sarcomere length was significantly reduced upon treatment with G1 and the effect of subsequently applied ISO was blunted. When compared to control measurements, the G1-mediated increase in relaxation velocity was non-significant, whilst time to baseline$_{50\%}$ and time to peak increased (Fig. 39, B). Taken together, G1 mainly enhanced ARVM contractility without apparent effects on relaxation and appeared to obstruct β-AR signaling similar as observed for NCA. These effects were incompatible with the assumption of G1 acting exclusively via PKGIα.
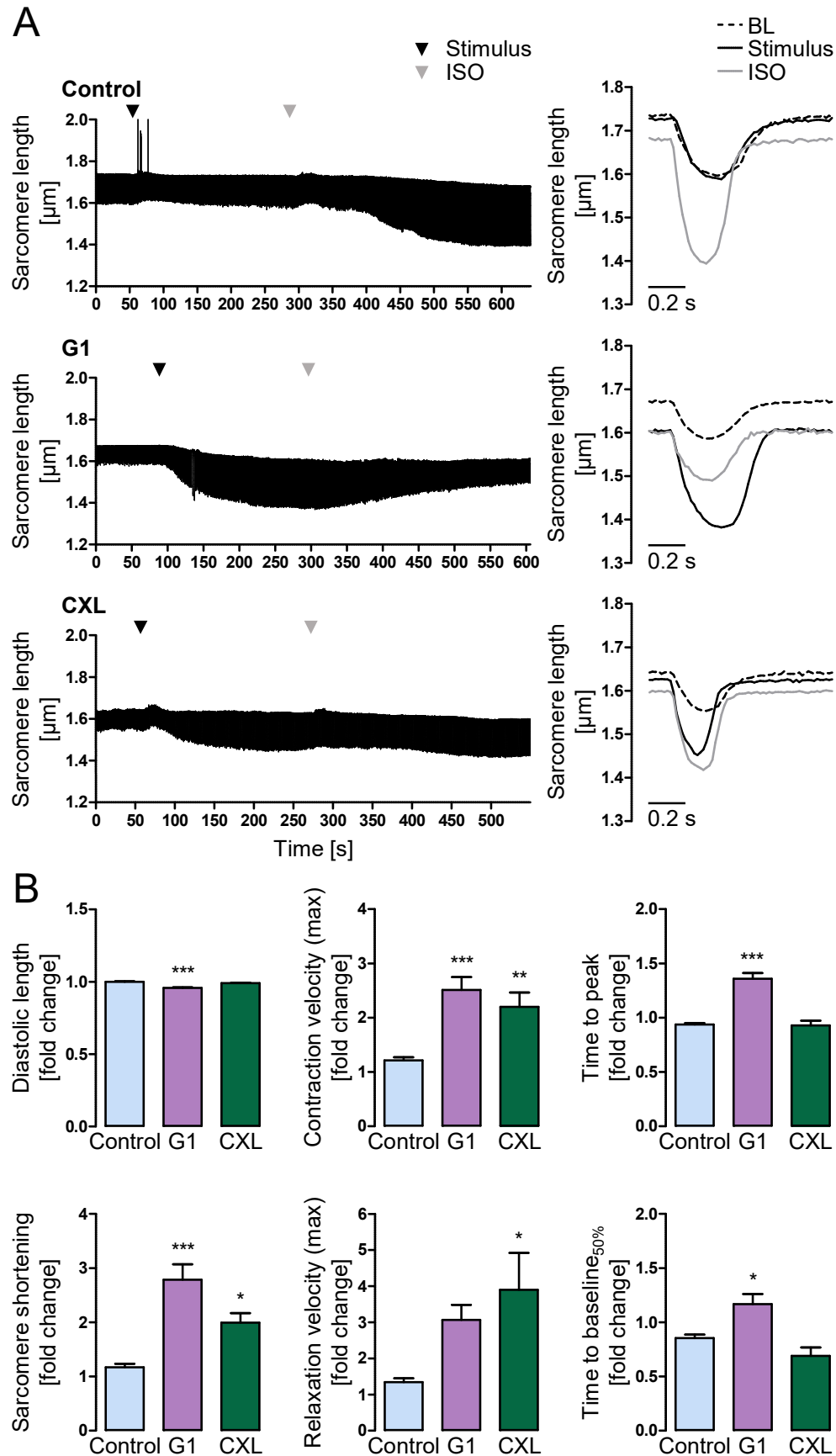
Figure 39: Comparison of single ARVM contractility in response to drug G1 and CXL-1020 Sarcomere length of single ARVMs paced at 1 Hz was recorded under basal conditions (baseline, BL) and upon exposure to vehicle (control), G1 (2 µmol/L) or CXL-1020 (1 mmol/L) until a plateau phase was reached. Subsequently, ISO (10 nmol/L) was added. **A** Exemplary records of ARVM measurements and corresponding representative single contraction peaks are shown at baseline (BL, dashed graph), upon stimulation (black arrowhead and continuous black graph)

and after supplementation with ISO (grey arrowhead and continuous grey graph). **B** Diastolic sarcomere length, sarcomere shortening, maximal contraction and relaxation velocities, as well as time to peak and time to baseline$_{50\%}$ of ARVMs are shown in response to vehicle (control; n=9), G1 (n=12) and CXL-1020 (n=9) as fold change of their respective baseline values. * P<0.05, ** P<0.01, *** P<0.001 for comparison with vehicle control by one-way ANOVA with Dunnett's Multiple Comparison post-test.
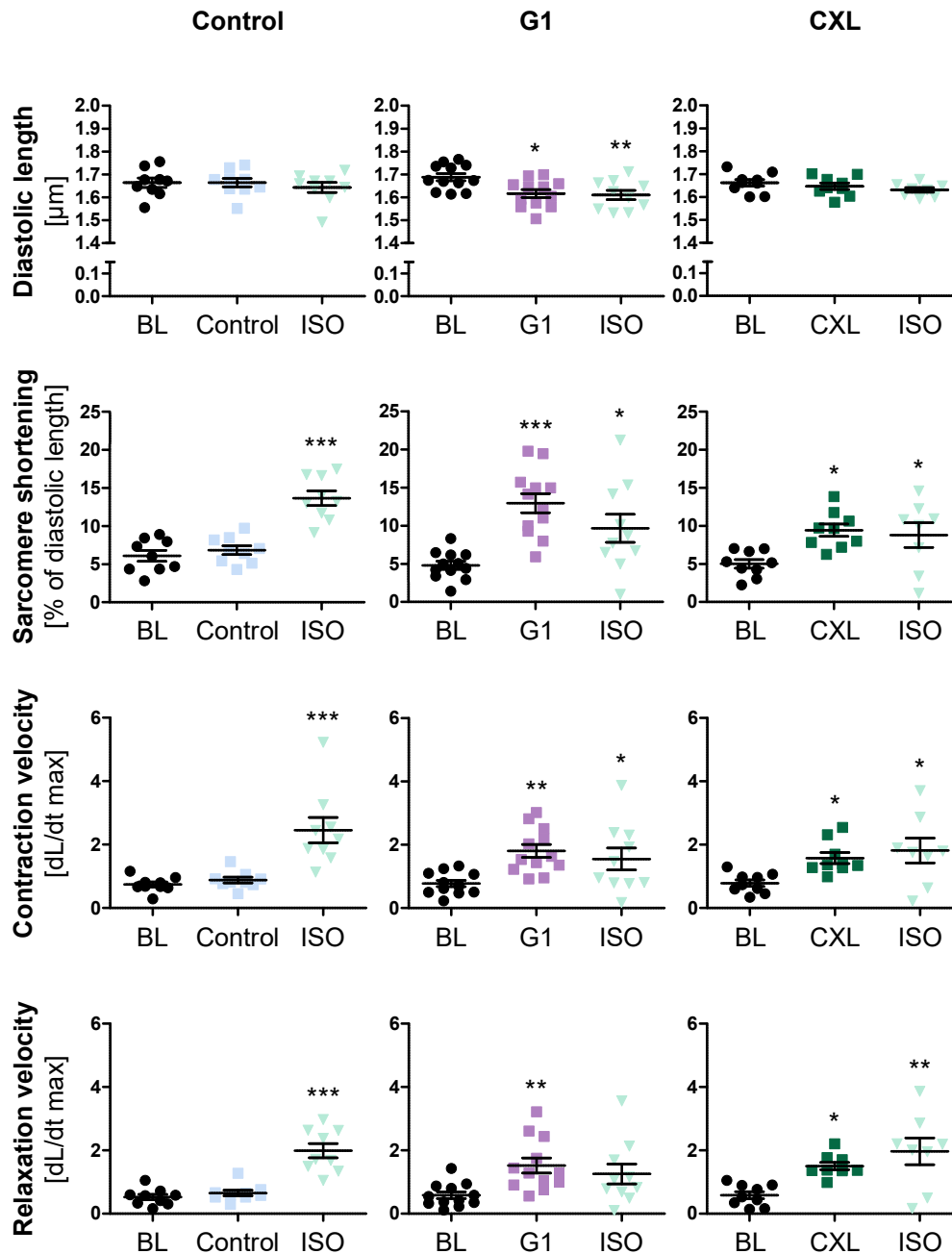
Figure 40: The effect of drug G1 and CXL-1020 on single ARVM contractility Contractility parameters of single ARVMs paced at 1 Hz were determined under basal conditions (baseline, BL) and upon exposure to vehicle (control), G1 (2 µmol/L) or CXL-1020 (1 mmol/L). Finally, ARVMs were stimulated by the application of ISO (10 nmol/L). Diastolic sarcomere length, sarcomere shortening and maximal contraction and relaxation velocities of ARVMs are shown under baseline conditions, during exposure to vehicle (control; n=9), G1 (n=10-12) or CXL-1020 (n=8-9) and final supplementation with ISO. * P<0.05, ** P<0.01, *** P<0.001 for comparison with corresponding baseline values by one-way ANOVA with Dunnett's Multiple Comparison post-test.

The effects exerted by G1 in ARVMs were further characterized by Western immunoblotting. While the dimerization of PKGIα increased in response to CXL-1020, exposure to G1 at increasing concentrations of 0.2, 2 and 20 µmol/L did not impact on PKGIα interdisulfide bond

formation (Fig. 41, A). G1 also did not lead to the formation of PKA-RI dimers or the phosphorylation of cMyBP-C, which were clearly induced by CXL-1020 or ISO, respectively.
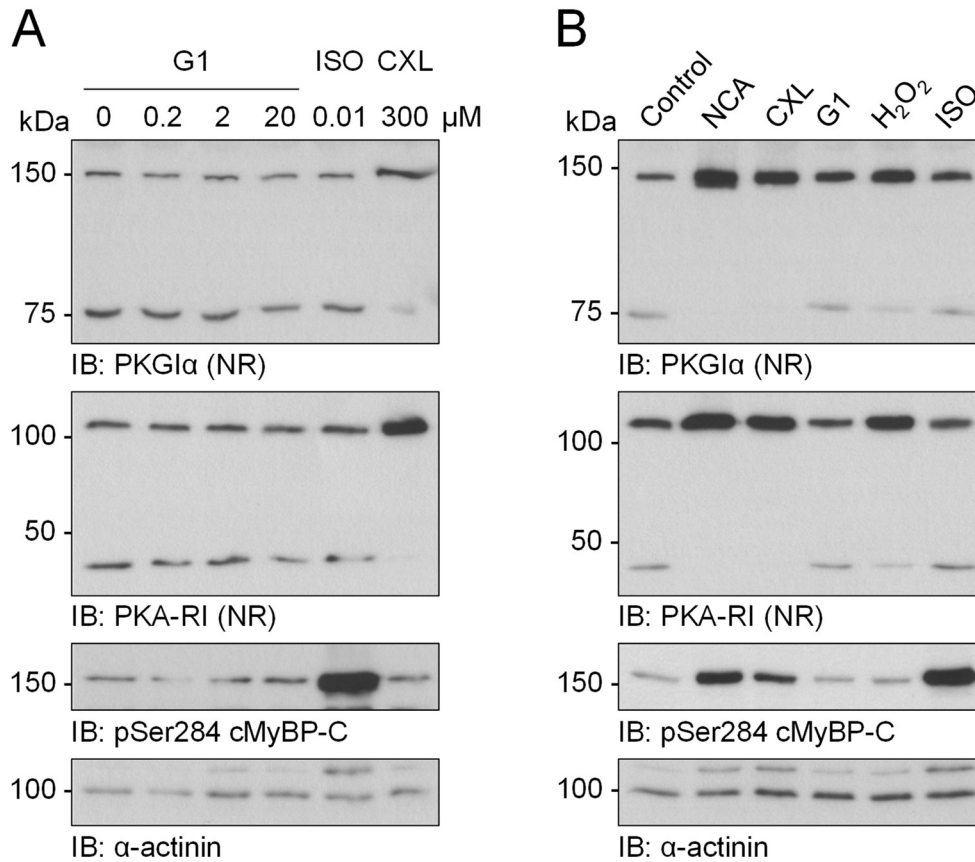
Figure 41: The effect of drug G1 on PKGIα and PKA-RI dimerization and cMyBP-C phosphorylation ARVMs were exposed to vehicle (control), G1, CXL-1020, NCA, H_2O_2 or ISO and harvested in non-reducing (NR) sample buffer. Lysates were examined by Western immunoblot analysis detecting PKGIα or PKA-RI. Prior to the evaluation of cMyBP-C phosphorylation at Ser284 samples were reduced by the addition of 10% (v/v) β-mercaptoethanol. As a loading reference, α-actinin levels were detected. **A** Treatment of ARVMs was performed with vehicle (control, 15 min), 0.2, 2, or 20 µmol/L G1 (15 min), 10 nmol/L ISO (10 min) or 300 µmol/L CXL-1020 (15 min). **B** ARVMs were incubated with vehicle (control, 30 min), 100 µmol/L NCA (30 min), 1 mmol/L CXL-1020 (15 min), 2 µmol/L G1 (15 min), 100 µmol/L H_2O_2 (10 min) or 10 nmol/L ISO (10 min).

This lack of effect was apparent by comparing 2 µmol/L of G1 with NCA, CXL-1020, H_2O_2 and ISO (Fig. 41, B). Whilst NCA and CXL-1020 induced a strong increase in dimerized PKGIα and PKA-RI, the effect of H_2O_2 was less strong, as determined by the residual presence of monomeric protein. Bands of PKGIα and PKA-RI detected for G1, however, displayed a pattern that was similar to that in controls and after ISO-treatment. These findings do not support the effect of G1 to exert its dimerizing effect on PKGIα in ARVMs. Also, again no phosphorylation of cMyBP-C was detectable following incubation with G1. Notably, in these experiments, CXL-1020 reproducibly induced a considerable degree of cMyBP-C phosphorylation.

As another protein kinase potentially involved in CXL-1020-mediated effects besides PKA and PKG, the role of Rho-associated protein kinase (ROCK) was analyzed in contractility measurements. Under both control conditions and following pretreatment with the ROCK inhibitor H1152, ARVMs displayed significantly enhanced sarcomere shortening and maximal

contraction and relaxation velocities, when exposed to CXL-1020 (Fig. 42). None of the determined parameters displayed significant changes after H1152-preincubation when normalized data were compared to control measurements, suggesting that the activation of ROCK is not responsible for CXL-1020-induced enhancement of contractility.
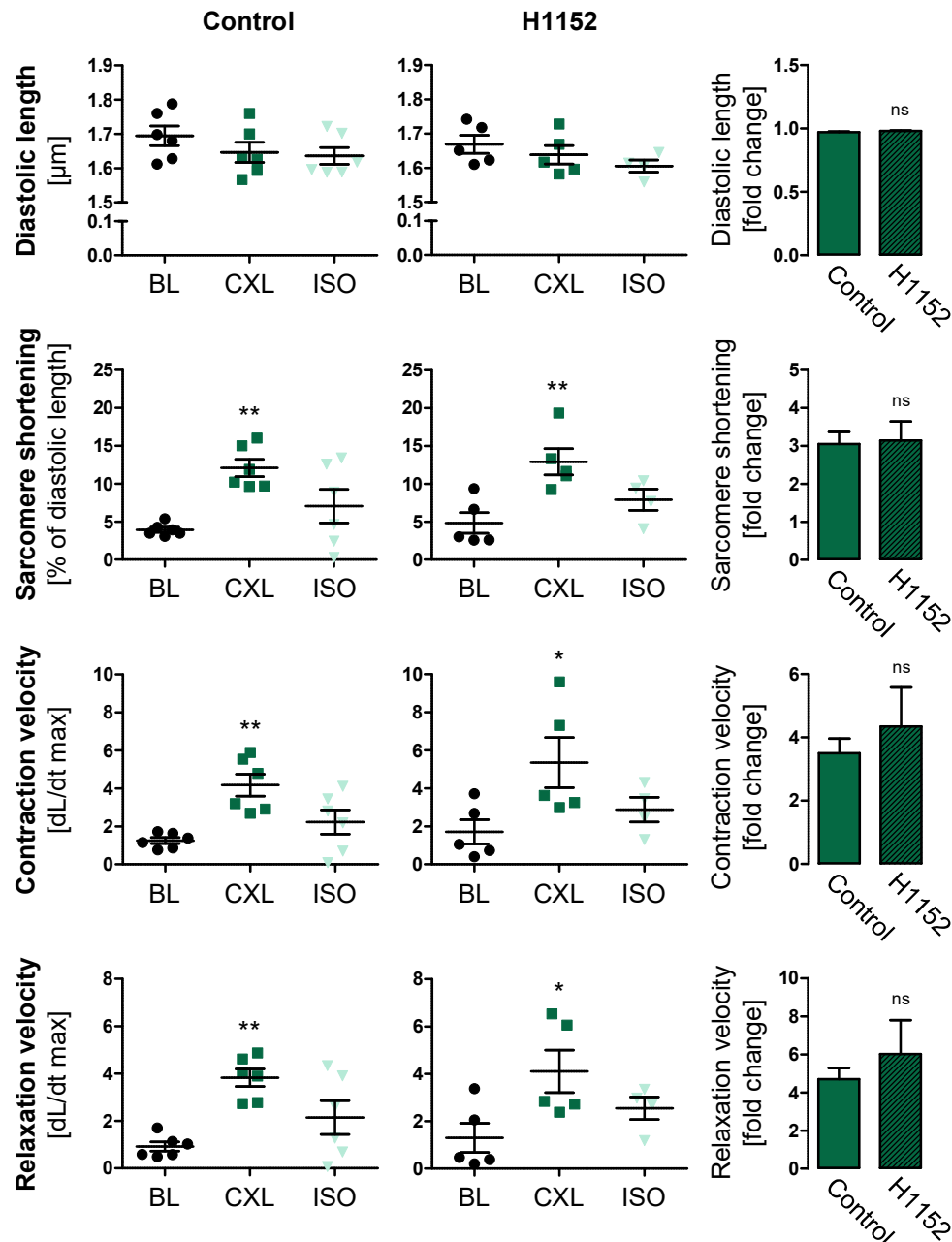
Figure 42: Effect of ROCK-inhibition for CXL-1020-mediated contractility Following pretreatment of ARVMs with vehicle (control; n=6) or the ROCK inhibitor H1152 (1 µmol/L; n=4-5) for 30 min, contractility parameters of single ARVMs paced at 1 Hz were measured under basal conditions (baseline, BL), upon exposure to CXL-1020 (300 µmol/L) and after supplementation with ISO (10 nmol/L). Diastolic sarcomere length, sarcomere shortening and maximal contraction and relaxation velocities are shown as raw data (scatter plots) and the CXL-1020 response as fold change of their respective baseline values (bar charts). Scatter plots: * P<0.05, ** P<0.01 for comparison with corresponding baseline values by one-way ANOVA with Dunnett's Multiple Comparison post-test. Bar charts: * P<0.05 for comparison with the corresponding vehicle control by unpaired, two-tailed t-test. ns: not significant

3.1.8 Time- and concentration-dependent effects of CXL-1020 in ARVMs

Contractility measurements performed in single ARVMs demonstrated that the response to CXL-1020 became apparent shortly after addition of the compound. To confirm that the requirements for Western immunoblot detection of CXL-1020-induced effects had been met at the incubation conditions used in previous experiments (300 µmol/L, 15 min), the treatment was tested with different incubation times and varying compound concentrations.
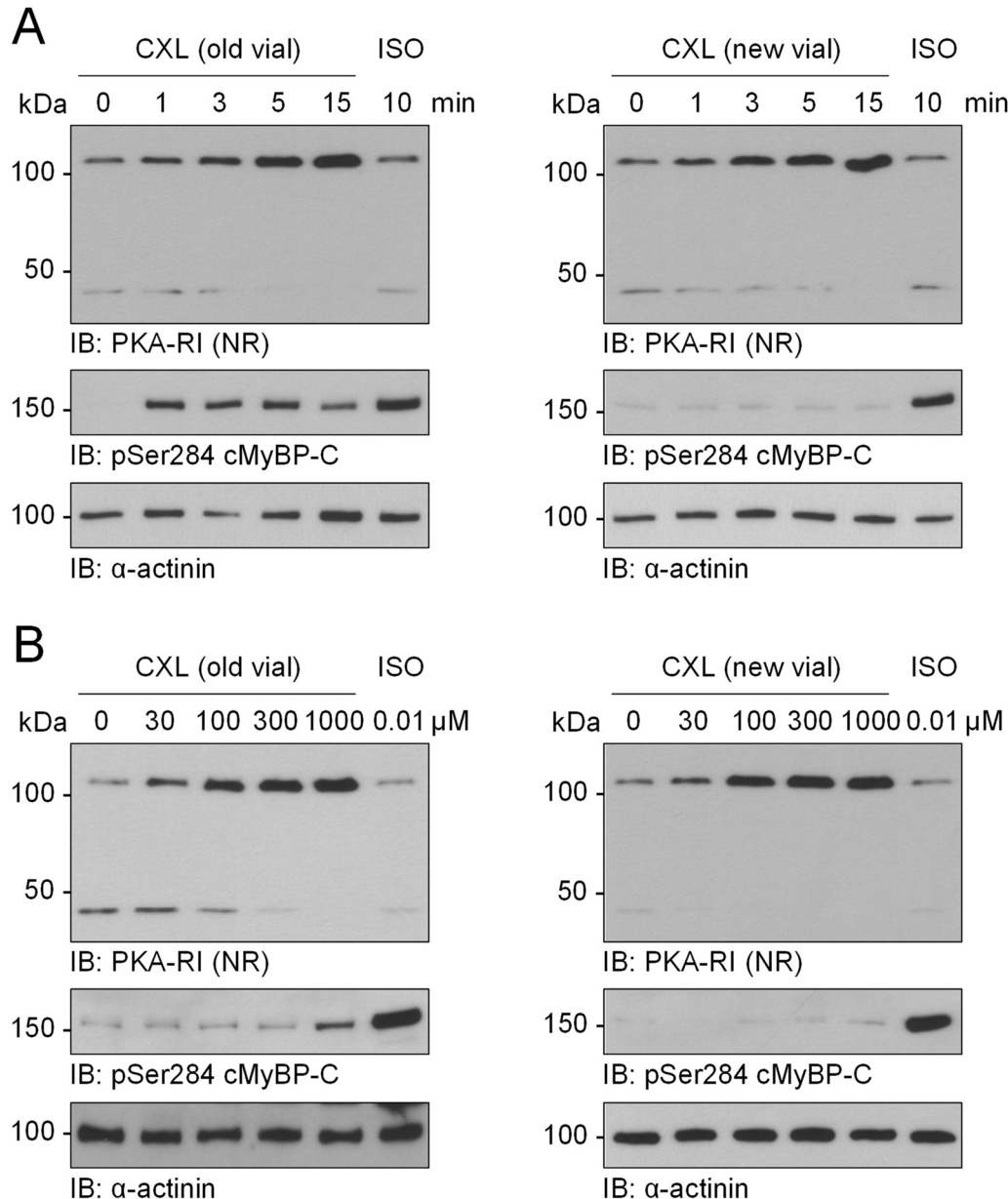
Figure 43: Comparison of old and new CXL-1020 in time course treatment and concentration curve ARVMs were exposed to CXL-1020 from the standard stock (old vial) or a new vial for an increasing duration (**A**) or with increasing compound concentration (**B**). PKA-RI dimer formation and cMyBP-C phosphorylation at Ser284 were detected in cell lysates by Western immunoblot analysis performed under non-reducing (NR) or reducing conditions, respectively. α-Actinin is shown as loading reference. **A** Time course treatment: ARVMs were exposed to vehicle for 15 min (sample 0), CXL-1020 (300 µmol/L) from either vial for 1, 3, 5 or 15 min or ISO (10 nmol/L) for 10 min. **B** Concentration curve treatment: ARVMs were exposed to vehicle for 15 min (sample 0), 30, 100, 300 or 1 mmol/L (1000 µM) of CXL-1020 from either vial for 15 min or ISO (10 nmol/L) for 10 min.

In time-course experiments, ARVMs were incubated with 300 µmol/L of CXL-1020 for 1 to 15 min with compound either derived from the standard stock (old vial) or from a new vial in

parallel and lysates examined by Western immunoblot analysis. In control and ISO-treated samples analyzed under non-reducing conditions, both monomeric and dimeric PKA-RI were visualized, migrating at a molecular weight of approx. 48 or 100 kDa, respectively (Fig. 43, A). Upon exposure to CXL-1020 derived from either vial, PKA-RI dimer formation increased steadily with prolonged incubation time, beginning within the first 3 min of treatment. In parallel, the intensity of signal representing monomeric protein decreased continuously. A similar course of PKA-RI dimerization was shown in response to NCA previously (see Fig. 20). With CXL-1020 from either vial, phosphorylation levels of cMyBP-C at Ser284 were negligible under control conditions, but were enhanced following exposure to ISO, as expected. Notably, compound derived from the standard stock (old vial) induced a clear increase in phosphorylation, which was already apparent after 1 min of treatment and persisted for 15 min. Compound from the new vial, however, did not induce cMyBP-C phosphorylation of similar magnitude, highlighting a potential difference in potency between the vials. Moreover, with CXL-1020 from either vial, PKA-RI dimer formation and phosphorylation of cMyBP-C over time did not correlate. As this had already been shown for NCA, it supported the hypothesis that PKA-RI dimerization and activation of the kinase were not directly linked. To establish a concentration-response curve, ARVMs were exposed to concentrations of 30 to 1000 µmol/L of CXL-1020, which was either derived from the standard stock (old vial) or from a new vial for 15 min. By Western immunoblot analysis performed under non-reducing conditions, again both basally oxidized and monomeric PKA-RI moieties were detected in control samples and following exposure to ISO (Fig. 43, B). Treatment with increasing concentrations of CXL-1020 from old and new vial led to an accumulation of dimerized PKA-RI and a correlative reduction of the monomeric form. Phosphorylation of cMyBP-C at Ser284, which could be generated by ISO-treatment, was also induced by 1 mmol/L of CXL-1020 from the old vial. Once again pointing towards differences in compound potency between the vials, exposure to the same concentration of CXL-1020 derived from the new vial did not lead to a robust degree of phosphorylation. The data obtained from these experiments showed that an incubation time of 15 min was suitable for the detection of CXL-1020 effects on PKA-RI dimer formation and phosphorylation of cMyBP-C. Although phosphorylation levels were enhanced after exposure to the highest concentration (1000 µmol/L) of old vial CXL-1020, 300 µmol/L from the same vial seemed eligible, as this concentration had been sufficient to induce considerable phosphorylation during time course treatment. Taken together, treatment parameters used in previous experiments (300 µmol/L, 15 min) had been appropriate for the investigation of CXL-1020-mediated effects on PKA-R oxidation and cMyBP-C phosphorylation.

3.1.9   NCA-mediated oxidation of GAPDH

In subcellular fractionation experiments, the cytosolic enzyme GAPDH, which had been selected as a marker protein of the soluble fraction, showed enhanced translocation to the

Triton-insoluble fraction in NCA-treated ARVMs (see Fig. 22). The influence of NCA on GAPDH subcellular localization was further examined by the detection of GAPDH in samples of subcellular fractionation experiments that involved non-reducing and reducing harvesting conditions (see Fig. 23) or a time course incubation with NCA (see Fig. 24).
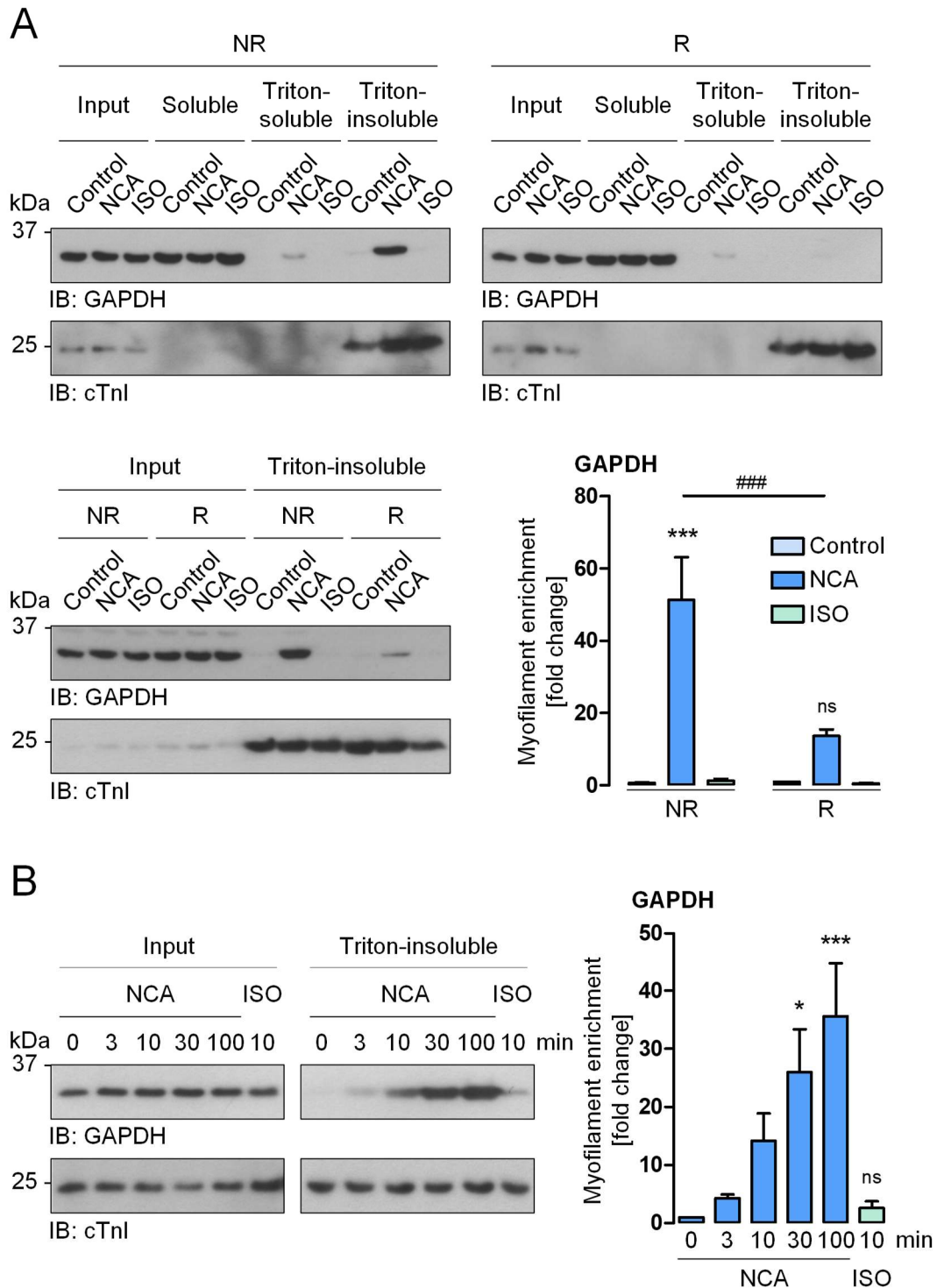
Figure 44: Translocation of GAPDH in fractionation experiments Translocation of GAPDH in ARVMs was investigated in fractionation experiments comparing non-reducing and reducing conditions or the effect of NCA over time, respectively, by Western immunoblot analysis. **A** ARVMs were treated with vehicle (control), NCA (100 µmol/L, 30 min) or ISO (10 nmol/L, 10 min), harvested under non-reducing (NR) or reducing (R) conditions and lysates used for subcellular fractionation into soluble, Triton-soluble and Triton-insoluble fractions. For both harvesting conditions, the presence of GAPDH and cTnI in cardiac myocyte fraction samples was determined (top). The

content of GAPDH and cTnI in crude lysates (input) and Triton-insoluble fractions from both harvesting conditions was compared (bottom). The bar chart represents the results of 3 independent experiments and shows GAPDH content in Triton-insoluble fractions from both harvesting conditions normalized to GAPDH input signals and expressed as fold change of vehicle control (R). *** $P<0.001$ for comparison with the corresponding vehicle control, ### $P<0.001$ for comparison between different harvesting conditions by two-way ANOVA with Bonferroni post-test. Data from this experiment was also shown in Fig 23. **B** Following treatment with vehicle (control) for 100 min (sample 0 min), NCA (100 µmol/L) for 3, 10, 30 or 100 min or ISO (10 nmol/L) for 10 min, ARVMs were separated into Triton-soluble and Triton-insoluble fractions. Full lysates (input) and Triton-insoluble fractions were examined by detection of GAPDH and cTnI. Data from 5 independent experiments were summarized in the bar chart, which presents the signals of GAPDH obtained from Triton-insoluble fractions normalized to the GAPDH input signals and expressed as fold change of control (sample 0 min). * $P<0.05$, *** $P<0.001$ for comparison with the corresponding vehicle control (sample 0 min) by one-way ANOVA with Dunnett's Multiple Comparison post-test. Data from this experiment was also shown in Fig 24. ns: not significant

In cardiac myocyte fractions obtained from ARVMs either harvested under non-reducing (NR) or reducing (R) conditions, cTnI and GAPDH were visualized in soluble, Triton-soluble and myofilament-containing Triton-insoluble fractions by Western immunoblot analysis. While cTnI was observed in input lysates and Triton-insoluble fractions only, GAPDH was detected in input lysates and was mainly present in the soluble fraction, as expected (Fig. 44, A). Under non-reducing harvesting conditions, however, a pronounced signal for GAPDH was also observed in the Triton-insoluble sample of NCA-treated cells. The corresponding band was considerably weaker when cardiac myocytes were harvested under reducing buffer conditions, suggesting that oxidation was crucial for the appearance of this signal. This presumption was supported when input and Triton-insoluble samples from either harvesting condition were compared directly. Whilst cTnI content appeared similar in Triton-insoluble samples from either treatment, the content of GAPDH was significantly increased upon NCA-exposure under non-reducing harvesting conditions in comparison to both its vehicle control and the corresponding signal from reducing harvesting conditions. This clearly showed that the presence of GAPDH in the myofilament-containing Triton-insoluble fraction resulted from oxidation and suggested an oxidation-mediated translocation process as observed for PKA and PP2A subunits. By subcellular fractionation of ARVMs after prolonged treatment with NCA for up to 100 min, the translocation process of GAPDH was monitored over time. In Western immunoblots of crude lysates (input), both cTnI and GAPDH displayed similar signal intensities between different treatment conditions (Fig. 44, B). Whilst the content of cTnI was again comparable in Triton-insoluble fraction samples, the presence of detectable GAPDH was significantly enhanced with increasing duration of NCA-treatment. From these experiments, it could be concluded that GAPDH was susceptible to oxidation-mediated translocation to the Triton-insoluble fraction of cardiac myocyte lysates in response to NCA-treatment.

To substantiate these findings, GAPDH was subjected to the analysis of cysteine oxidation in response to various oxidant interventions by PEG- and biotin-switch methodology (see Figs. 29 and 30).
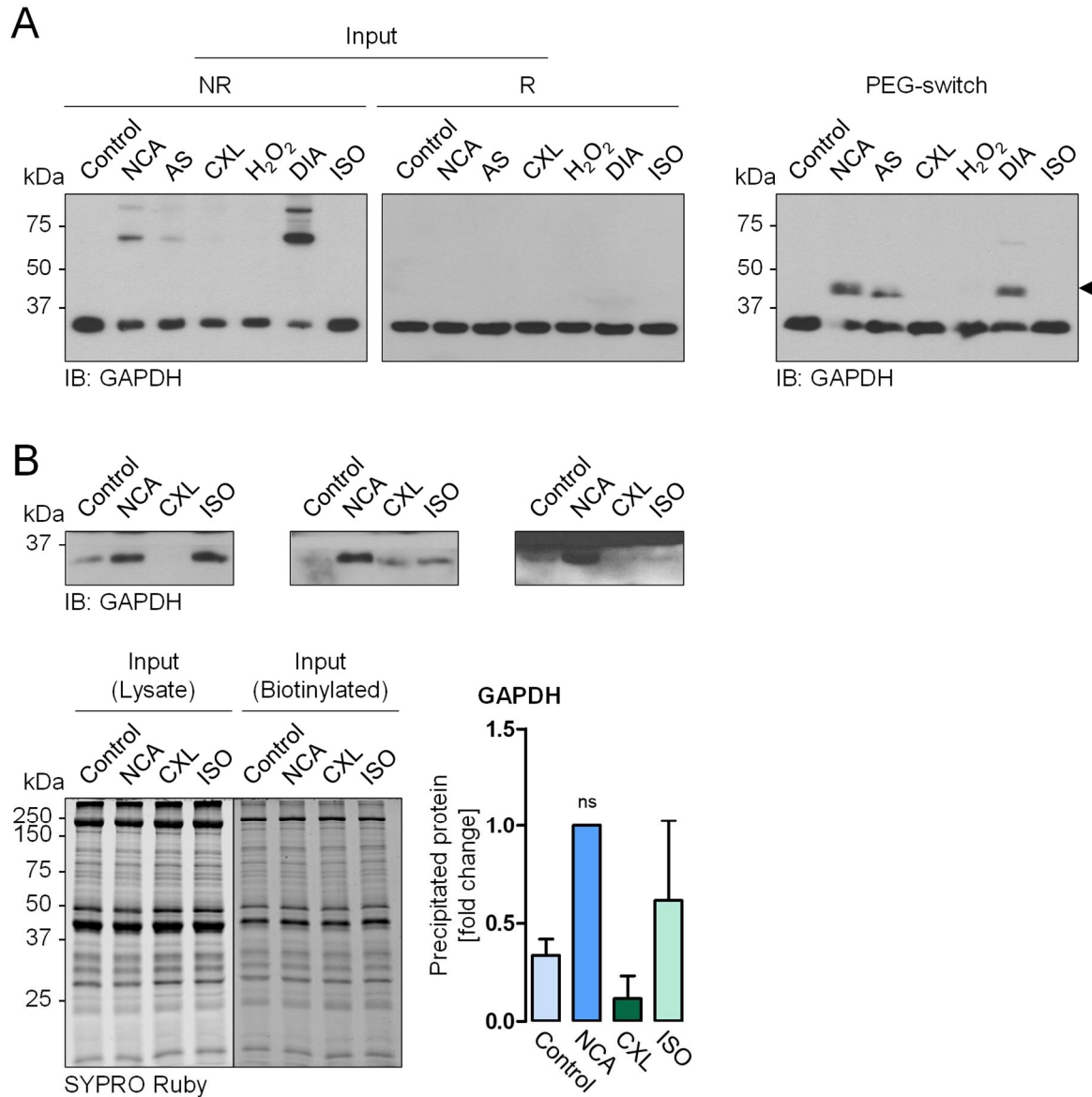
Figure 45: Detection of GAPDH oxidation by PEG- and biotin-switch Oxidation of ARVM proteins was investigated by PEG- or biotin-labeling. **A** ARVMs were exposed to vehicle (control), NCA (100 μmol/L, 30 min), AS (500 μmol/L, 15 min), CXL-1020 (300 μmol/L, 15 min), H_2O_2 (100 μmol/L, 10 min), DIA (500 μmol/L, 10 min) or ISO (10 nmol/L, 10 min) and oxidized proteins labeled with 5 kDa PEG-maleimide. By Western immunoblotting, GAPDH was detected in inputs under both non-reducing (NR) and reducing (R) conditions and in PEG-labeled samples. The arrowhead indicates a PEG-induced shift in molecular weight, reflecting protein oxidation. **B** After incubation with vehicle (control), NCA (100 μmol/L, 30 min), CXL-1020 (300 μmol/L, 15 min) or ISO (10 nmol/L, 10 min), ARVM lysates were processed by biotin-labeling of oxidized thiol groups and subsequent precipitation of biotinylated proteins. The content of GAPDH in collected samples was determined by Western immunoblot analysis. Total protein content in crude lysates and after biotinylation was visualized by staining with SYPRO Ruby. Data of three experiments were normalized to total protein signals of biotinylated inputs and are summarized in the bar chart expressed as fold change of the NCA signal. * $P<0.05$ for comparison with the corresponding vehicle control by one-way ANOVA with Dunnett's Multiple Comparison post-test. ns: not significant

In input lysates of PEG-switch experiments, Western immunoblot analysis of GAPDH displayed bands migrating at increased molecular weight after exposure to NCA, AS and DIA under non-reducing (NR) conditions (Fig. 45, A). These signals were abolished in reduced (R) input samples, indicating that they represented protein complexes formed by oxidation. Upon labeling of oxidized cysteine residues with 5 kDa PEG, bands of increased molecular weight were visible in samples of NCA-, AS- and DIA-treated cardiac myocytes (Fig. 45, A,

arrowhead). This pointed towards a PEG-induced mass increment due to treatment-mediated protein oxidation, which was in line with the detection of extra bands in non-reducing input samples. The slower migration corresponded to a molecular weight increment of approx. 10 kDa and suggested PEG-labeling of two cysteine residues of GAPDH following incubation with NCA, AS and DIA. An additional faint band visible in the DIA sample at approx. 60 kDa most likely corresponded to an incompletely reduced protein complex, which was also detected in the non-reducing input sample. For the investigation of thiol-oxidation by biotin-switch, ARVM lysates were incubated with NCA, CXL or ISO, oxidized proteins biotinylated and subsequently collected by streptavidin-precipitation. As revealed by Western immunoblot analysis, the protein content of GAPDH in samples obtained after treatment with NCA was increased when compared to vehicle controls in all independent repetitions of the experiment (Fig. 45, B). Although changes were non-significant, this again confirmed the oxidation of GAPDH in response to NCA.

3.2 Characterization of Ser250 as a putative cMyBP-C phosphorylation site

Phosphorylation of the sarcomeric protein cMyBP-C at M-motif phosphorylation sites represents an essential mechanism for the maintenance of cardiac myocyte contractility. A novel phosphorylation site was identified at Ser250 of cMyBP-C by mass spectrometry (MS) analysis of human ventricular tissue samples. The detection of Ser250 phosphorylation was mutually exclusive with S-glutathiolation of adjacent Cys249, which represents the main S-glutathiolation site of the cMyBP-C N-terminus. Importantly, S-glutathiolation of cMyBP-C was shown to negatively correlate with functionally critical phosphorylation of M-motif serine residues (Stathopoulou et al. 2016). Consequently, to determine the impact of Ser250 phosphorylation on cMyBP-C S-glutathiolation and potentially associated functional consequences, this novel phosphorylation site was investigated.

3.2.1 Detection of a novel phosphorylation site in human cMyBP-C

Alterations in PTMs of the phosphorylation-regulated thick myofilament-associated protein cMyBP-C were determined in human ventricular tissue samples from healthy donors (non-failing, NF) and patients suffering from dilated or ischemic cardiomyopathy (DCM/ICM) by MS. Prior to analysis, samples were alkylated with N-Ethylmaleimide to block unmodified cysteines and digested with chymotrypsin. To allow peptide sequencing, the most abundantly detected ionized precursor peptides were further fragmented to obtain MS2 spectra.
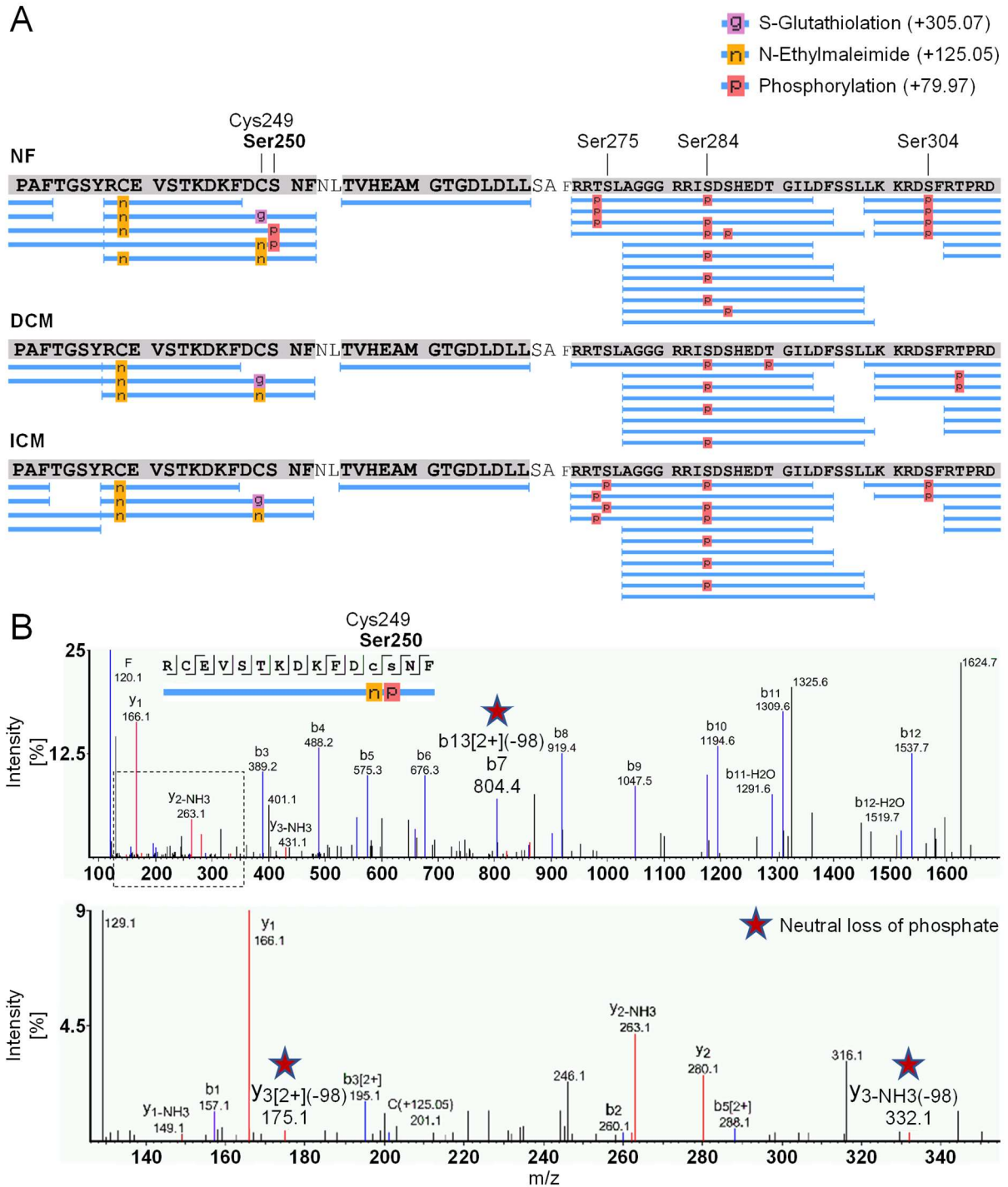
Figure 46: Analysis of cMyBP-C PTMs in human ventricular tissue samples by mass spectrometry PTMs of cMyBP-C from human ventricular tissue of a non-failing donor (NF) or patients with dilated (DCM) or ischemic cardiomyopathy (ICM) were investigated by mass spectrometry (MS). **A** Modifications detected at cMyBP-C (Q14896) between amino acid 231 and 310 and corresponding identified chymotryptic peptides (blue lines) are displayed. The PTMs phosphorylation (on serine, threonine and tyrosine; +79.97; p, red) and S-glutathiolation (on cysteines; +305.07; g, purple) were included in the database search. Cysteine alkylation by N-Ethylmaleimide is shown in orange (n). Novel phosphorylation at Ser250 as well as described S-glutathiolation at Cys249 and M-motif phosphorylation sites are labeled above the amino acid sequence. **B** A MS2 fragmentation spectrum with 'y' (red) and 'b' (blue) ion series of a peptide containing alkylation at Cys249 (n) and phosphorylation at Ser250 (p) is shown (top). The amino acid sequence and a depiction of the peptide are indicated. A magnification of the framed area (dashed black box) is presented in the bottom spectrum. Fragments with a neutral loss of a mass corresponding to phosphate (-98; red star) indicate Ser250 phosphorylation. False discovery rate<1%. m/z: Mass-to-charge ratio

As expected, a mass increment matching with protein phosphorylation was identified for cMyBP-C at the well-described M-motif phosphorylation sites corresponding to Ser275,

Ser284 and Ser304 (Fig. 46, A). Instead of Ser275, phosphorylation was occasionally detected at Thr274. However, these modifications most likely refer to Ser275 and were incorrectly assigned due to missing MS2 fragment information. Notably, in NF tissue a similar increase in mass was detected at Ser250 within the C1 domain, a site for which phosphorylation has not been reported before. MS2 fragments with a neutral loss of 98 Da indicated a loss of phosphate, which is a common feature of serine and threonine phosphorylation (Fig. 46, B). At least four MS2 fragments showed such neutral loss and most likely represented phosphorylation of the corresponding precursor peptide at Ser250. Modification of the recently described adjacent S-glutathiolation site at Cys249 (Stathopoulou et al. 2016) was observed as well, but these two modifications alternated and simultaneous modification of Ser250 and Cys249 could not be detected on any peptide (Fig. 46, A). Ser250 phosphorylation was exclusively observed in healthy tissue (NF) and not in DCM and ICM. These findings suggested Ser250 to represent a novel phosphorylation site of cMyBP-C that might play a regulatory role for cMyBP-C S-glutathiolation.

Investigation of the putative interplay between Ser250 phosphorylation and Cys249 S-glutathiolation was pursued in murine cardiac tissue. Prior to subjection to MS analysis, S-glutathiolation was induced by the exposure of heart homogenates to GSSG. As a blocking reagent, N-Ethylmaleimide or maleimide was applied. Under both alkylation conditions, the site corresponding to human Ser250 (Ser247 in mouse) was found phosphorylated in chymotryptic peptides (Fig. 47, A, top). Ser247 phosphorylation was supported by four MS2 fragments that displayed the characteristic neutral loss of phosphate (Fig. 47, B) and the detection of similar phosphorylation in a second experiment analyzing trypsin-digested protein (Fig. 47, A, bottom). Under all tested experimental conditions, Ser247 phosphorylation was found mutually exclusive with S-glutathiolation of the adjacent cysteine residue (Cys248). These results supported the interplay between phosphorylation and S-glutathiolation at Ser250 and Cys249 (referring to the human sequence), which had been suggested by results obtained from human tissue.
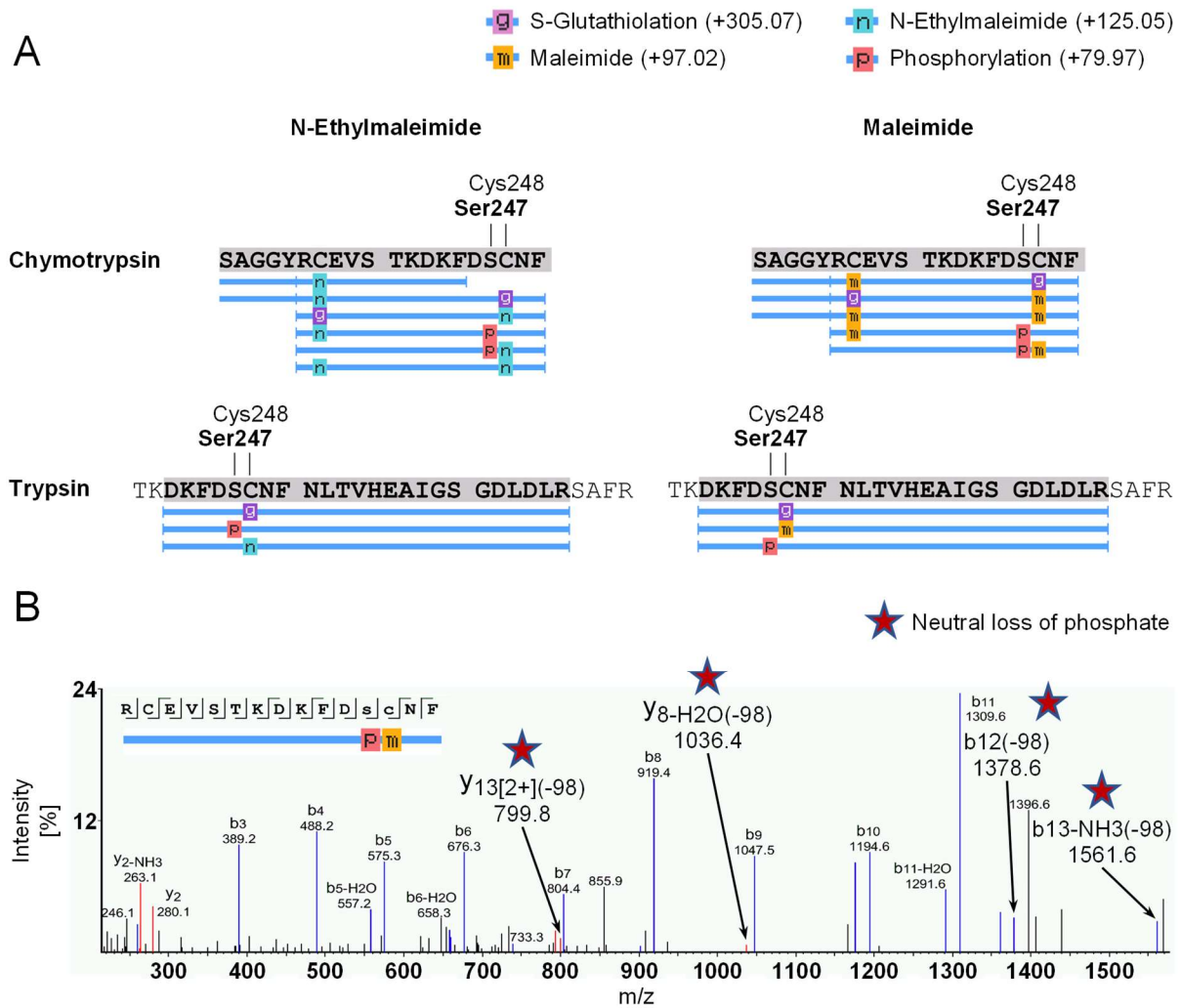
Figure 47: Analysis of cMyBP-C PTMs in GSSG-treated murine heart tissue by mass spectrometry Murine heart tissue homogenates were exposed to 1 mmol/L of GSSG for 30 min and subsequently subjected to mass spectrometry (MS) analysis for the investigation of cMyBP-C PTM. N-Ethylmaleimide or maleimide was used to alkylate cysteine residues and proteins were digested by chymotrypsin or trypsin. **A** Modifications detected at cMyBP-C (O70468) between amino acid 231 and 250 (chymotrypsin) or 241 and 266 (trypsin) and corresponding identified peptides (blue lines) are displayed. The PTMs phosphorylation (on serine, threonine and tyrosine; +79.97; p, red) and S-glutathiolation (on cysteines; +305.07; g, purple) were included in the database search. The addition of N-Ethylmaleimide and maleimide is shown in green (n) or orange (m), respectively. Phosphorylation at Ser247 (corresponding to human Ser250) and S-glutathiolation at Cys248 (corresponding to human Cys249) are labeled above the amino acid sequences. **B** A MS2 fragmentation spectrum with 'y' (red) and 'b' (blue) ion series of a peptide containing phosphorylation at Ser247 (p) and maleimide-mediated alkylation at Cys248 (m) is shown. The amino acid sequence and a depiction of the peptide are indicated. Fragments with a neutral loss of a mass corresponding to phosphate (-98; red star) indicate Ser247 phosphorylation. False discovery rate<1%. m/z: Mass-to-charge ratio

3.2.2 Ser250 phosphorylation: Protein kinase screening using C1-M-C2 proteins

For the investigation of Ser250 as a novel cMyBP-C phosphorylation site, a variety of mutant proteins that comprise the N-terminal C1, M and C2 domains of human cMyBP-C (C1-M-C2) were generated by site-directed mutagenesis and bacterial expression. The C1-M-C2 mutant proteins used in this study are summarized in figure 48.
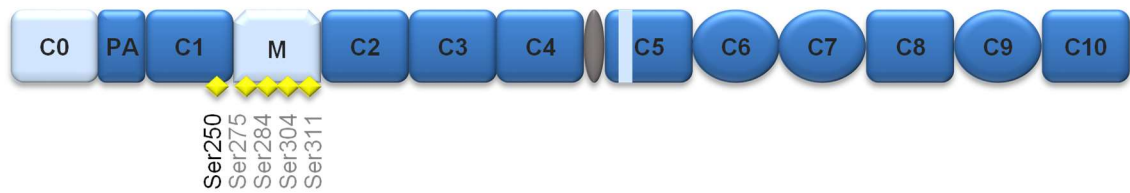
Figure 48: Schematic presentation of cMyBP-C and C1-M-C2 proteins Depiction of full-length human cMyBP-C and N-terminal C1-M-C2 fragments carrying mutations of different phosphorylation sites. **A** cMyBP-C consists of 8 immunoglobulin-like (square) and 3 fibronectin type III-like (circle) domains. The N-terminal C0 domain, a 28-amino acid sequence within the C5 domain and the M-motif (light blue) are specific to the cardiac isoform. Linker regions exist between C0 and C1 (proline/alanine-rich; PA) and C4 and C5 (grey oval) domains. Phosphorylation sites of the M-motif and the novel phosphorylation site at Ser250 are labeled and depicted as yellow diamonds. **B** Recombinant C1-M-C2 mutant proteins consisting of N-terminal domains of human cMyBP-C were generated by site-directed mutagenesis. Abbreviated names of the proteins are shown on the left. Amino acid residue exchanges in each protein are listed on the right. Intact (yellow diamond) and mutated (red diamond) phosphorylation sites are depicted and correspond to Ser250, Ser275, Ser284, Ser304 and Ser311 (left to right). The insertion of phosphomimetic aspartate or a replacement of serine for cysteine is displayed as a green or purple diamond, respectively.

With the aim to identify a protein kinase that has the ability to phosphorylate cMyBP-C at Ser250, a spectrum of protein kinases was analyzed by *in vitro* kinase assays in the presence of radioactively labeled ATP (γ-^{32}P-ATP). Kinase-mediated phosphorylation of the C1-M-C2

wild type (WT) fragment, a mutated protein lacking all M-motif phosphorylation sites (4Ala) and a protein additionally lacking Ser250 (5Ala) was determined.
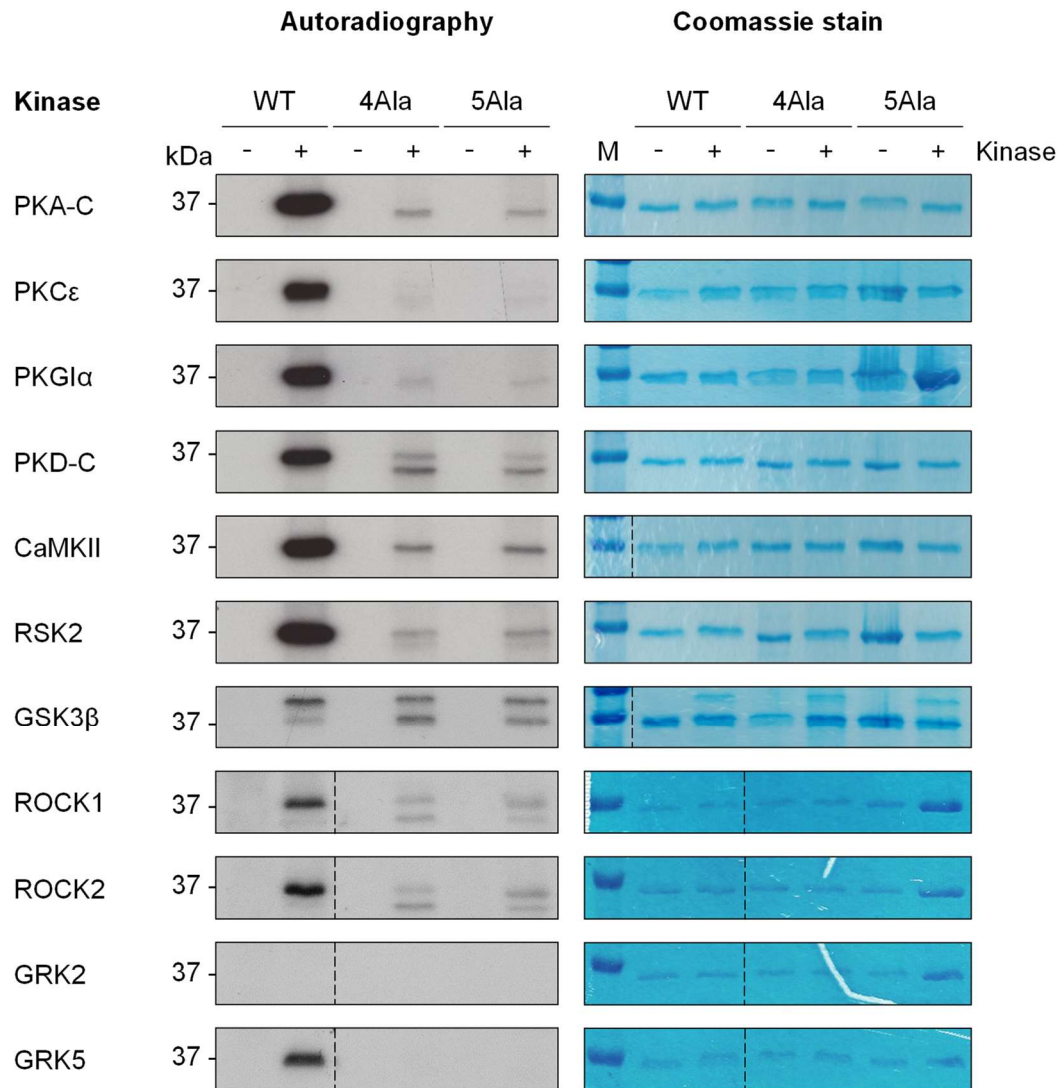
Figure 49: Investigation of cMyBP-C phosphorylation at Ser250 by radioactive in vitro kinase assay Catalytic subunit of PKA (PKA-C), protein kinase Cε (PKCε), PKGIα, catalytic domain of PKD (PKD-C), CaMKII, ribosomal S6 kinase 2 (RSK2), GSK3β, ROCK1, ROCK2 and G protein-coupled receptor kinases 2 or 5 (GRK2, GRK5) were incubated with either the WT, 4Ala or the 5Ala cMyBP-C C1-M-C2 fragment in the presence of γ-^{32}P-ATP for 1 h. For each sample, a kinase-free control was generated. The reaction was stopped by the addition of 3x reducing Laemmli sample buffer, samples resolved by SDS-PAGE and incorporated ^{32}P-detected using chemiluminescence films (left panel). Colloidal Coomassie staining of the gels was performed as loading control (right panel). Dashed lines indicate the rearrangement of lanes from the same film or gel. M: Molecular weight marker

Autoradiographic detection of the 37 kDa C1-M-C2 proteins confirmed phosphorylation of C1-M-C2 WT by the catalytic subunit of PKA (PKA-C), protein kinase Cε (PKCε), PKGIα, the catalytic domain of PKD (PKD-C), CaMKII, ribosomal S6 kinase 2 (RSK2), ROCK1, ROCK2 and G protein-coupled receptor kinase 5 (GRK5; Fig. 49, left panel). In the 4Ala mutant, signals generated by these protein kinases were greatly diminished, suggesting the loss of phosphorylation sites in the M-motif. Band intensities following incubation with PKA-C, PKCε, PKGIα, CaMKII or RSK2 with the 4Ala (containing Ser250) and the 5Ala protein (lacking Ser250) were similar and indicated that Ser250 was not stoichiometrically phosphorylated.

Following incubation with PKD-C, the signal detected for 5Ala was further decreased when compared to the 4Ala mutant fragment and suggested a potential ability of PKD to phosphorylate Ser250. GSK3β did not induce profound phosphorylation of any C1-M-C2 protein. Bands migrating above the 37 kDa marker band in autoradiographs and after Coomassie staining matched with the molecular weight of auto-phosphorylated GSK3β, which was previously reported (Cole et al. 2004). Incubation with G protein-coupled receptor kinase 2 (GRK2) did not induce any detectable C1-M-C2 phosphorylation signals.

Since PKD was hypothesized to potentially phosphorylate Ser250 of cMyBP-C, the impact of cMyBP-C S-glutathiolation on PKD-mediated phosphorylation was investigated. Therefore, the phosphorylation of S-glutathiolated C1-M-C2 WT by PKD was analyzed over time by autoradiography and Western immunoblot analysis following radioactive or non-radioactive *in vitro* kinase assay, respectively.
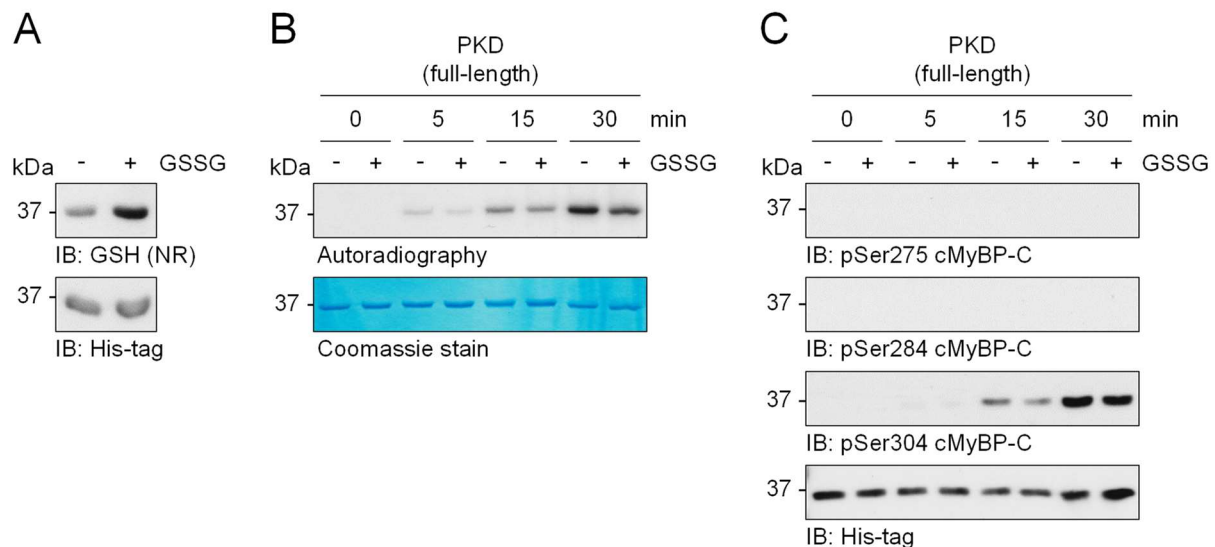
Figure 50: Impact of S-glutathiolation on PKD-mediated phosphorylation of C1-M-C2 protein **A** S-glutathiolation (GSH) and total protein content (His-tag) of C1-M-C2 WT fragment following treatment with GSSG (1 mmol/L) for 30 min was visualized by Western immunoblot analysis under non-reducing conditions. **B/C** Untreated (- GSSG) and S-glutathiolated (+ GSSG) C1-M-C2 WT protein was incubated with protein kinase PKD (full-length) in the presence of γ-^{32}P-ATP (**B**) or non-radioactive ATP (**C**) for 5, 15 or 30 min before the reaction was stopped by addition of 3x reducing Laemmli sample buffer. Control samples (0 min) lacked the protein kinase and were supplemented with 3x reducing Laemmli sample buffer without incubation. **B** Samples were resolved by SDS-PAGE and incorporated ^{32}P detected by autoradiography. Colloidal Coomassie staining of the gel is shown as loading reference. **C** Phosphorylation of C1-M-C2 WT at Ser275, Ser284 and Ser304 (referring to the entire protein) was detected by Western immunoblot analysis using the respective phospho-specific antibodies. His-tagged C1-M-C2 was visualized as loading control.

S-glutathiolation of the C1-M-C2 WT protein in response to incubation with GSSG was confirmed (Fig. 50, A). PKD-mediated phosphorylation of C1-M-C2 increased over time but was reduced after GSSG-pretreatment of the substrate protein, as reflected by reduced phosphorylation signals after 5, 15 and 30 min of incubation compared to untreated C1-M-C2 (Fig. 50, B). Assuming that the observed signal might in part arise from Ser250 phosphorylation, the GSSG-mediated decrease in signal intensity suggested a negative correlation between Ser250 phosphorylation and S-glutathiolation. In non-radioactive

experiments, phosphorylation of sites corresponding to Ser275 and Ser284 in the full protein was not detectable upon incubation with PKD. As expected, PKD induced the phosphorylation of non-oxidized C1-M-C2 at the PKD phosphorylation site Ser304 (corresponding to the entire protein; Bardswell et al. 2010), which was considerably increased after 15 and 30 min of incubation. Again, phosphorylation was reduced after S-glutathiolation of the C1-M-C2 substrate (Fig. 50, C). As these data indicated that PKD-mediated phosphorylation was negatively affected by cMyBP-C S-glutathiolation, this kinase might allow to study the crosstalk between S-glutathiolation and Ser250 phosphorylation of cMyBP-C.

The investigation of the potential phosphorylation of cMyBP-C at Ser250 by PKD was pursued in further radioactive *in vitro* kinase experiments with the use of additional C1-M-C2 mutant proteins either lacking Ser250 or the PKD substrate site Ser304.
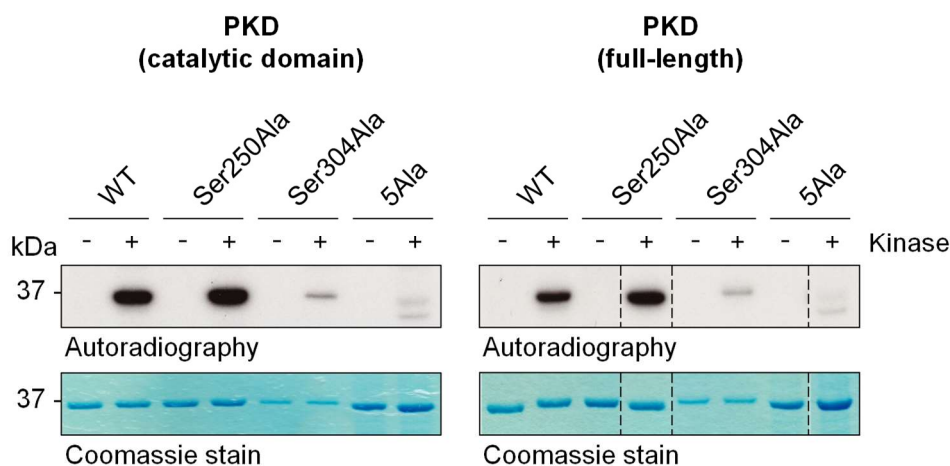
Figure 51: Phosphorylation of C1-M-C2 mutant proteins by PKD The C1-M-C2 WT, Ser250Ala, Ser304Ala and 5Ala proteins were incubated with the catalytic domain or full-length PKD in the presence of γ-^{32}P-ATP for 1 h. For each reaction, a kinase-free control was generated. The reaction was stopped by addition of 3x reducing Laemmli sample buffer, samples resolved by SDS-PAGE and incorporated ^{32}P detected by autoradiography. Colloidal Coomassie staining of the gels was performed as loading control. Dashed lines indicate the rearrangement of lanes from the same film or gel.

As reflected by the detection of radioactive signals, both the catalytic domain and the full-length PKD enzyme distinctly phosphorylated C1-M-C2 WT (Fig. 51). The replacement of Ser304 (Ser304Ala) resulted in a strong reduction of signal intensity as expected. In contrast, the substitution of Ser250 with alanine (Ser250Ala) did not diminish the incorporation of radioactive phosphate in comparison to C1-M-C2 WT, showing that the novel phosphorylation site at Ser250 was not a substrate of PKD.

3.2.3 Characterization of the phospho-specific pSer250 antibody

In vitro kinase assays using C1-M-C2 mutant proteins did not allow identification of a protein kinase with the ability to phosphorylate cMyBP-C at Ser250. In order to enable the investigation of this novel phosphorylation site on the endogenous protein, an antibody with specificity for phosphorylated Ser250 of cMyBP-C was custom-made.
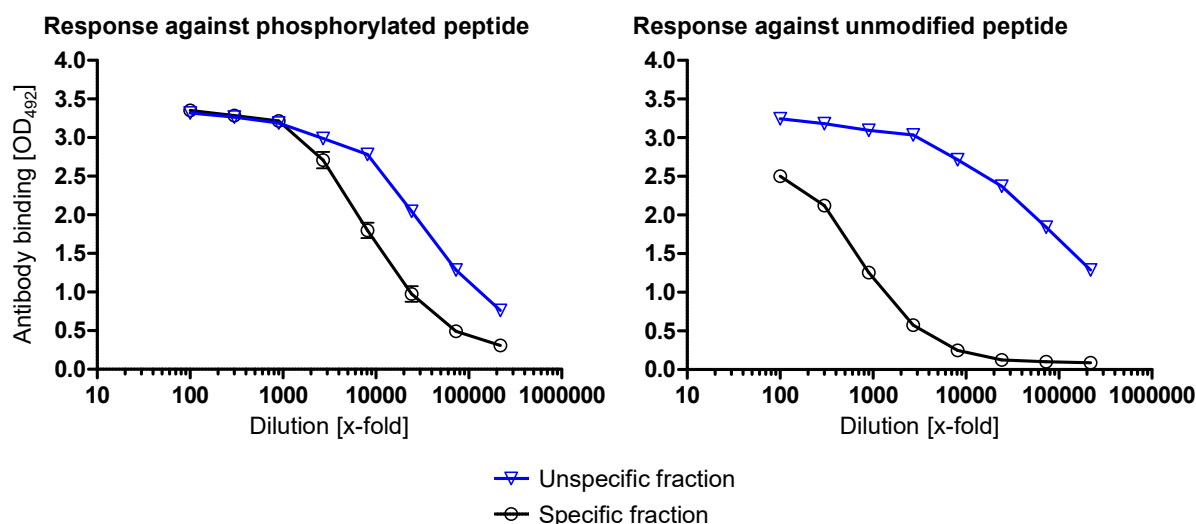
Figure 52: Purification analysis of the pSer250 antibody Sera from rabbits which had been immunized with a peptide corresponding to the amino acid sequence surrounding phosphorylated Ser250 of cMyBP-C were successively purified against the phosphorylated and unmodified peptide. Flow through (specific fraction, black circles) and eluate (unspecific fraction, blue triangles) of the latter purification step were analyzed concerning the binding of obtained antibodies to modified and unmodified peptides. Binding was assessed from a dilution curve by measurement of optical density at 492 nm (OD_{492}) from sample triplicates in an indirect enzyme-linked immunosorbent assay (ELISA).

Binding of obtained antibodies to the corresponding modification at Ser250 was assessed by enzyme-linked immunosorbent assay (ELISA) with subsequent measurement of the optical density at 492 nm wavelength (OD_{492}). Antibodies obtained as the specific fraction (pSer250) from the purification process and those which had been excluded as non-selective to Ser250 phosphorylation (unspecific fraction) displayed similar dilution curves for binding of a peptide phosphorylated at Ser250 (OD_{492} of 2.99 ± 0.07 *vs.* 2.71 ± 0.11 at 1:2700 dilution for the unspecific or specific fraction, respectively; Fig. 52). When tested against an unmodified peptide, the curve obtained for the unspecific antibody fraction again displayed a similar slow decrease of binding upon antibody dilution (OD_{492} of 3.04 ± 0.02 at 1:2700 dilution), indicating a high affinity for the peptide independent from Ser250 modification. In contrast, dilution of the specific fraction resulted in a considerable decrease of antibodies bound to the unmodified peptide (OD_{492} of 0.58 ± 0.03 at 1:2700 dilution), which reflected the specificity of the purified antibody fraction for the phosphorylation of interest that corresponds to pSer250 of cMyBP-C.

Cross-reactivity of the pSer250 antibody with M-motif cMyBP-C phosphorylation sites and its suitability to detect phosphorylation in proteins were investigated by *in vitro* kinase assay. Following incubation with PKA-C, the pSer250 antibody was applied to detect different C1-M-C2 proteins by Western immunoblotting.
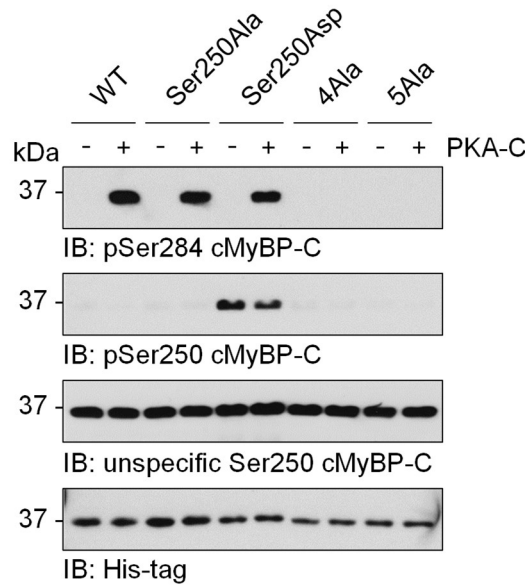
Figure 53: Detection of C1-M-C2 mutant proteins by the pSer250 antibody C1-M-C2 WT, Ser250Ala, Ser250Asp, 4Ala and 5Ala proteins were treated with the catalytic subunit of PKA (PKA-C) in the presence of ATP for 30 min. The reaction was stopped by addition of 3x reducing Laemmli sample buffer. For each condition, a kinase-free control sample was generated. By Western immunoblot analysis, C1-M-C2 phosphorylation at Ser284 (referring to the entire protein) and the signals detected by the phospho-specific (pSer250 cMyBP-C) and unspecific Ser250 antibodies were investigated. His-tagged C1-M-C2 proteins were visualized as loading reference.

Visualization of the phosphorylation at Ser284 (corresponding to the entire protein) in response to treatment with PKA-C, which can phosphorylate all M-motif sites (Gautel et al. 1995; Jia et al. 2010), indicated successful M-motif phosphorylation (Fig. 53). A corresponding signal was present with all C1-M-C2 proteins, except for 4Ala and 5Ala, where M-motif phosphorylation sites were lacking. Importantly, the phosphomimetic Ser250Asp was recognized by the pSer250 antibody and demonstrated that the antibody was able to detect Ser250 phosphorylation in a protein context. Detectability of Ser250Asp was maintained upon PKA-mediated phosphorylation. The C1-M-C2 WT protein and Ser250Ala, which is non-phosphorylatable at Ser250, remained undetected, showing that cross-reactivity with M-motif PKA phosphorylation sites was neglectable. The unspecific fraction from the pSer250 antibody purification (unspecific Ser250 cMyBP-C), which contained antibodies lacking selectivity for phosphorylated Ser250 (see Fig. 52), displayed strong binding to all C1-M-C2 proteins.

While in the amino acid sequence of human cMyBP-C Ser250 is positioned directly following Cys249, these two amino acids are positioned in reverse order in the mouse and rat protein sequence. To examine, whether the pSer250 antibody can bind phosphorylated serine in the reverse order motif, the detection of a C1-M-C2 protein that contains a cysteine at position 250 and a phosphomimetic aspartate at position 249 was tested.
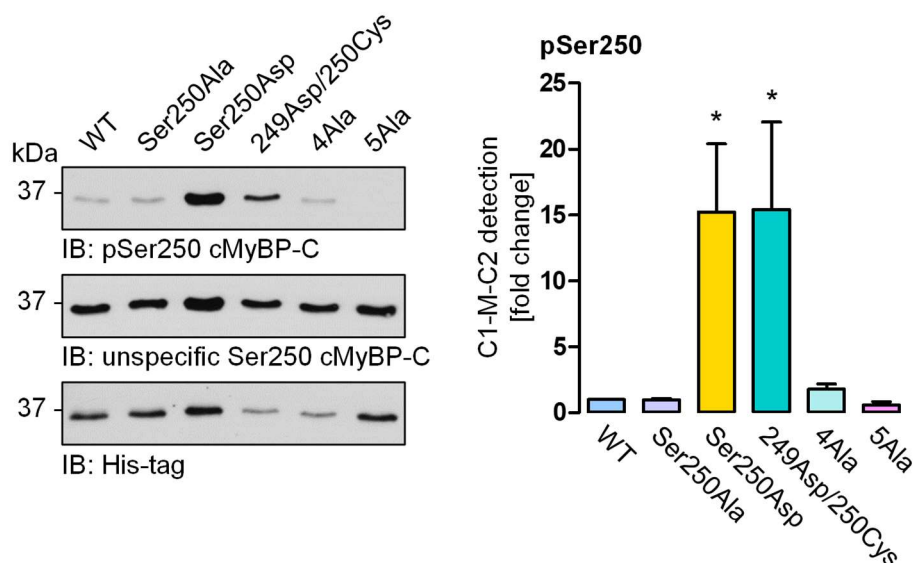
Figure 54: Detection of a phosphomimetic reversed motif C1-M-C2 protein by the pSer250 antibody The C1-M-C2 fragments WT, Ser250Ala, Ser250Asp, 249Asp/250Cys, 4Ala and 5Ala were supplemented with 3x reducing Laemmli sample buffer and examined by Western immunoblot analysis using the phospho-specific (pSer250 cMyBP-C) and unspecific Ser250 antibodies. Detection of His-tagged C1-M-C2 served as loading control. Signal intensities of Ser250 phosphorylation from 3 Western immunoblots were normalized to His-tag signals and are summarized in the bar chart as fold change of C1-M-C2 WT signal. * P<0.05 for comparison with C1-M-C2 WT by one-way ANOVA with Dunnett's Multiple Comparison post-test.

In Western immunoblots probed with the pS250 antibody, no signal was present with the C1-M-C2 WT, Ser250Ala, 4Ala or the 5Ala protein as observed before (Fig. 54). Besides visualization of the phosphomimetic Ser250Asp mutant, the pSer250 antibody also generated a pronounced band for the reverse motif protein 249Asp/250Cys. Normalized signal intensities for both proteins were significantly increased and indicated the suitability of the pSer250 antibody to detect Ser250-corresponding phosphorylation in rat and mouse protein. Immunodetection by the unspecific Ser250 antibody fraction again appeared similar between the proteins, as the signals exhibited a pattern similar to that obtained by the detection of total C1-M-C2 protein (His-tag).

3.2.4   Analysis of cMyBP-C Ser250 phosphorylation in ARVM and tissue lysates

To determine the working conditions of the pSer250 antibody for Western immunoblotting of cardiac myocyte samples, initial testing was performed with lysates from ARVMs following treatment with reagents that induce oxidation (H_2O_2, DIA) or receptor-mediated activation of different signaling pathways (ISO; phenylephrine, PE; endothelin 1, ET).
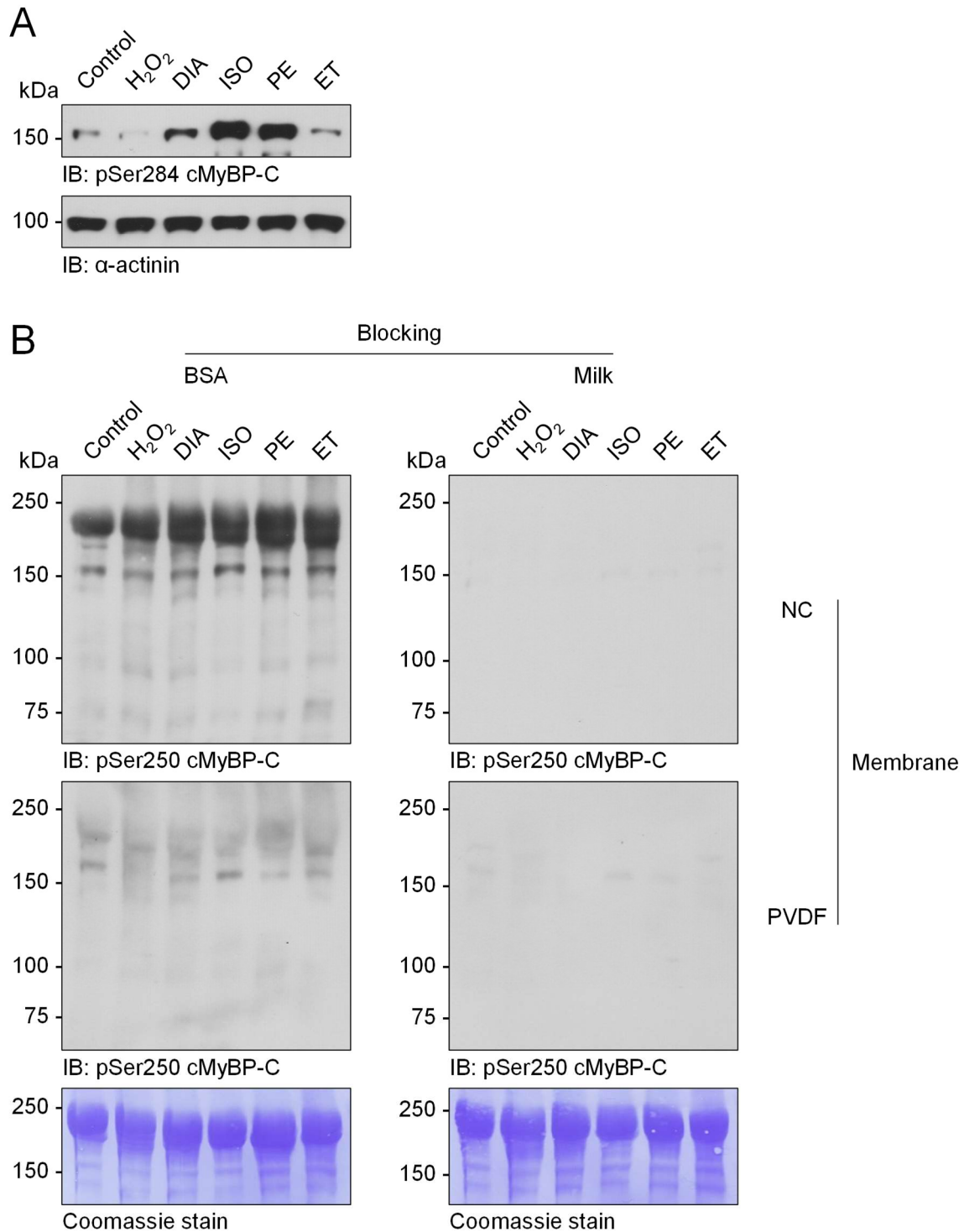
Figure 55: Performance of the pSer250 antibody at different Western immunoblotting conditions ARVMs were supplemented with H_2O_2 (100 µmol/L), DIA (500 µmol/L), ISO (10 nmol/L), PE (10 µmol/L), ET (50 nmol/L) or left untreated as control and incubated for 10 min. Cell lysates were analyzed by Western immunoblot analysis. **A** The effect of ARVM stimulation on cMyBP-C phosphorylation at Ser284 is shown. α-Actinin served as loading reference. **B** Performance of the cMyBP-C pSer250 antibody was assessed in Western immunoblots after transfer to a polyvinylidene difluoride (PVDF) or nitrocellulose (NC) membrane and blocking with 5% BSA/TBST (BSA) or 10% milk/TBST (milk). Coomassie staining of PVDF membranes confirmed successful protein transfer. BSA: Bovine serum albumin, TBST: Tris-buffered saline containing 0.1% Tween® 20

The response of cardiac myocytes to stimulation was validated by the visualization of cMyBP-C phosphorylation at Ser284, which was enhanced upon exposure to DIA, ISO and PE as expected (Fig. 55, A). Detection of cMyBP-C phosphorylation corresponding to human Ser250

was tested after transfer to polyvinylidene difluoride (PVDF) or nitrocellulose (NC) membranes and blocking with either bovine serum albumin (BSA) solution or milk (Fig. 55, B). On BSA-blocked NC, bands matching with the molecular weight of cMyBP-C were detected at 150 kDa in all lanes. Signal intensities were slightly enhanced following treatment with ISO, PE and ET, suggesting that signaling pathways activated by these compounds might potentially lead to kinase-mediated Ser250 phosphorylation. A pronounced band detected below the 250 kDa marker band and faint signals at 100 and 75 kDa suggested cross-reactivity of the pSer250 antibody with additional proteins. Only unspecific signals, which were most pronounced under control conditions and after exposure to ISO, were found at the expected size of 150 kDa when samples were analyzed on PVDF blocked in BSA solution. For the same exposure time, no clear signals were detected when blocking was performed with milk solution, suggesting that a combination of protein transfer to NC and blocking in BSA solution may provide the best outcome for the analysis of cMyBP-C phosphorylation at Ser250 in ARVM lysates.

The pSer250 antibody and its non-phospho-specific counterpart were further evaluated by Western immunoblot analysis of ventricular homogenates derived from WT and cMyBP-C KO mice.
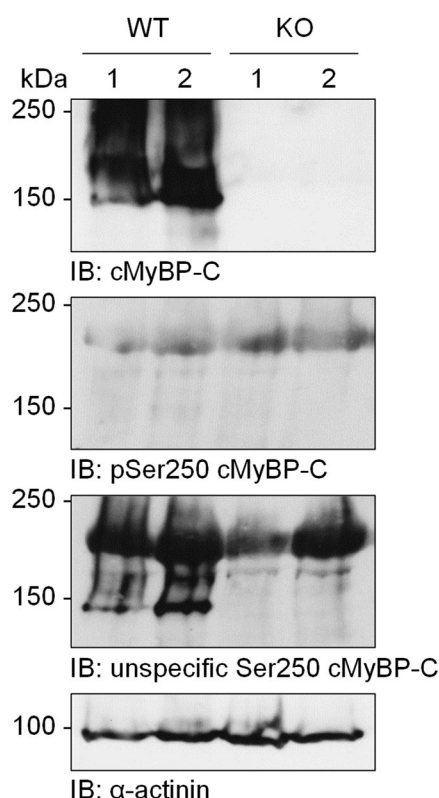
Figure 56: Investigation of the pSer250 antibody in ventricular homogenates from wild type and cMyBP-C knockout mice Homogenates of wild type (WT) and cMyBP-C knockout (KO) mouse ventricles were investigated by Western immunoblotting concerning signals obtained with the phospho-specific (pSer250 cMyBP-C) or unspecific Ser250 antibodies. For comparison, cMyBP-C was visualized. The detection of α-actinin served as loading reference.

Detection of cMyBP-C confirmed the lack of protein expression in tissue prepared from *Mybpc3*-targeted KO mice (Fig. 56). The pSer250 antibody did not allow the visualization of recognizable signals at the molecular weight of cMyBP-C at 150 kDa in KO samples but neither in WT homogenates, possibly suggesting Ser250 phosphorylation to be absent under basal conditions. As observed before, an additional band migrating at approx. 220 kDa was present in each lane. Western immunoblotting with the Ser250 antibody that lacks specificity for the phosphorylation (unspecific Ser250 cMyBP-C) generated signals at the expected molecular weight of 150 kDa in WT homogenates, but not in the KO samples. In addition to the visualization of C1-M-C2 mutant protein shown before (see Figs. 53 and 54), this suggested that the unspecific antibody also detects endogenous cMyBP-C. Like the specific pSer250 antibody, the unspecific equivalent showed additional bands migrating above cMyBP-C as well, which most likely represent cross-reactivity with another protein.

To achieve the activation of a protein kinase that might mediate the phosphorylation of endogenous cMyBP-C at Ser250, ARVMs were exposed to different stimuli, which activate various cellular signaling pathways. Pursuing the data presented in figure 55, ARVMs were treated with H_2O_2, DIA, ISO, PE or ET and pSer250 antibody signals analyzed by Western immunoblotting.
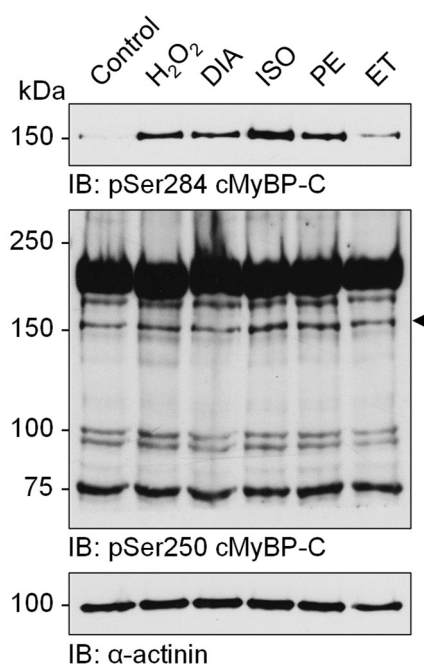
Figure 57: Ser250 phosphorylation of cMyBP-C in response to ARVM-stimulation Following exposure of ARVMs to H_2O_2 (100 µmol/L), DIA (500 µmol/L), ISO (10 nmol/L), PE (10 µmol/L) or ET (50 nmol/L) for 10 min, phosphorylation of cMyBP-C at Ser284 and Ser250 was investigated by Western immunoblot analysis. Visualization of α-actinin served as loading reference. Myocytes harvested as control sample were left untreated.

Upon incubation with ISO, phosphorylation of cMyBP-C at Ser284 was enhanced, showing the responsiveness of the cardiac myocytes to stimulation (Fig. 57). H_2O_2, DIA and PE also induced Ser284 phosphorylation, although to a lower degree. The pSer250 antibody generated

a band with a molecular weight matching with cMyBP-C at 150 kDa, which displayed increased intensity in ISO- and PE-treated samples (Fig. 57, arrowhead). Slightly pronounced bands had been observed after incubation with these stimuli in previous experiments (see Fig. 55) and supported the hypothesis that ISO and PE might lead to the activation of a protein kinase capable of phosphorylating Ser250. Several additional distinct signals migrating at molecular weights of approx. 220, 100 and 75 kDa, as well as a faint band migrating immediately below 150 kDa, were generated by the pSer250 antibody.

Different concentrations of the pSer250 antibody were applied to test whether varying the dilution could reduce unspecific antibody binding. Moreover, the technical reproducibility of enhanced Western immunoblot signals obtained with the pSer250 antibody from ARVM lysates in response to ISO and PE was assessed by repetitive analysis of the same samples.
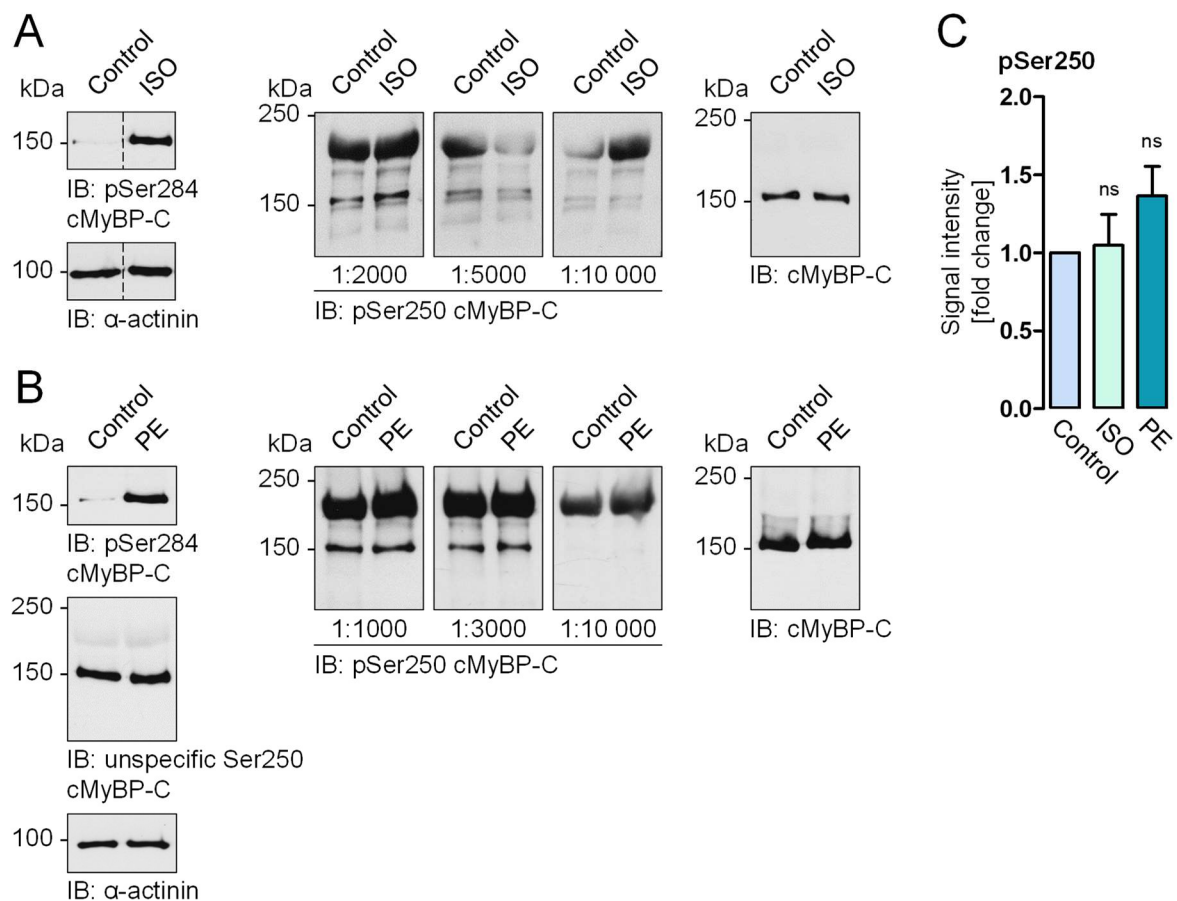
Figure 58: Repetitive sample analysis with pSer250 antibody dilutions **A** ARVMs were incubated with ISO (10 nmol/L, 10 min) or left untreated (control) and samples analyzed by Western immunoblotting with the pSer284 antibody and different concentrations of the pSer250 cMyBP-C antibody. α-Actinin was used as loading reference, the detection of cMyBP-C indicated the expected position of pSer250 signals. Dashed lines indicate the rearrangement of lanes from the same film. The samples used in this experiment were taken from the sample set previously presented in figure 57. **B** Following treatment with PE (100 µmol/L) or H_2O (control) for 10 min, ARVMs were lysed and examined by Western immunoblot analysis with the pSer284 antibody, the unspecific Ser250 antibody and different concentrations of the pSer250 cMyBP-C antibody. α-Actinin was used as loading reference. CMyBP-C was detected to indicate the expected position of pSer250 signals. **C** Signals from repeated pSer250 Western immunoblot analysis of the same control/ISO and control/PE samples (n=7) are summarized in the bar chart. Band intensities were normalized to corresponding α-actinin signals and expressed as fold change of the signal from the corresponding control. * $P<0.05$ for comparison with C1-M-C2 WT by one-way ANOVA with Dunnett's Multiple Comparison post-test. ns: not significant

The ISO sample and its corresponding control that were used for this investigation were taken from the sample set presented in figure 57. As shown previously, the exposure of ARVMs to ISO expectedly resulted in the phosphorylation of cMyBP-C at Ser284 (Fig. 58, A). At a dilution of 1:2000, the pSer250 antibody detected two narrow bands migrating at a molecular weight of 150 kD, which were intensified after exposure to ISO. The comparison with signals obtained for cMyBP-C suggested the upper band of the two to represent the phosphorylated protein. As observed before, a strong additional signal was present at approx. 220 kDa. The intensity of this high molecular weight band decreased only slightly when the same samples were analyzed with 1:5000 or 1:10 000 diluted antibody, whilst signals visualized at 150 kDa were considerably weakened. Notably, with different antibody concentrations, the ratio of signal intensities between control and ISO sample varied considerably. Like for ISO, ARVM responsiveness to the stimulation by PE was confirmed by the induction of Ser284 phosphorylation of cMyBP-C (Fig. 58, B). Similar to signals produced by the α-actinin loading control, band intensities obtained from the unspecific Ser250 antibody were unaltered following PE-incubation, once more arguing for the detection of endogenous cMyBP-C by this antibody. Western immunoblots probed with the pSer250 antibody (1:1000) displayed a strong signal corresponding to a molecular weight of approx. 220 kD and a single band matching with signals detected for cMyBP-C. As observed in ISO samples, increased dilution of the antibody during examination of the same samples resulted in the reduction of signal intensities for the band migrating at 150 kDa, but barely reduced the unspecific high molecular weight signal. Determination of the intensities from pSer250 bands that were obtained at different antibody concentrations and exhibited the same migration behavior as cMyBP-C showed that signals after exposure to ISO and PE were inconsistent and therefore not significantly increased (Fig. 58, C). Thus, protein kinases activated in response to ISO and PE did not mediate Ser250 phosphorylation of cMyBP-C.

In Western immunoblots of ARVM lysates, the pSer250 cMyBP-C antibody had generated several bands, which suggested cross-reactivity of the antibody with proteins other than phosphorylated cMyBP-C. To assess the intracellular localization of proteins that are detected by the pSer250 antibody, immunofluorescence staining of ARVMs was performed.
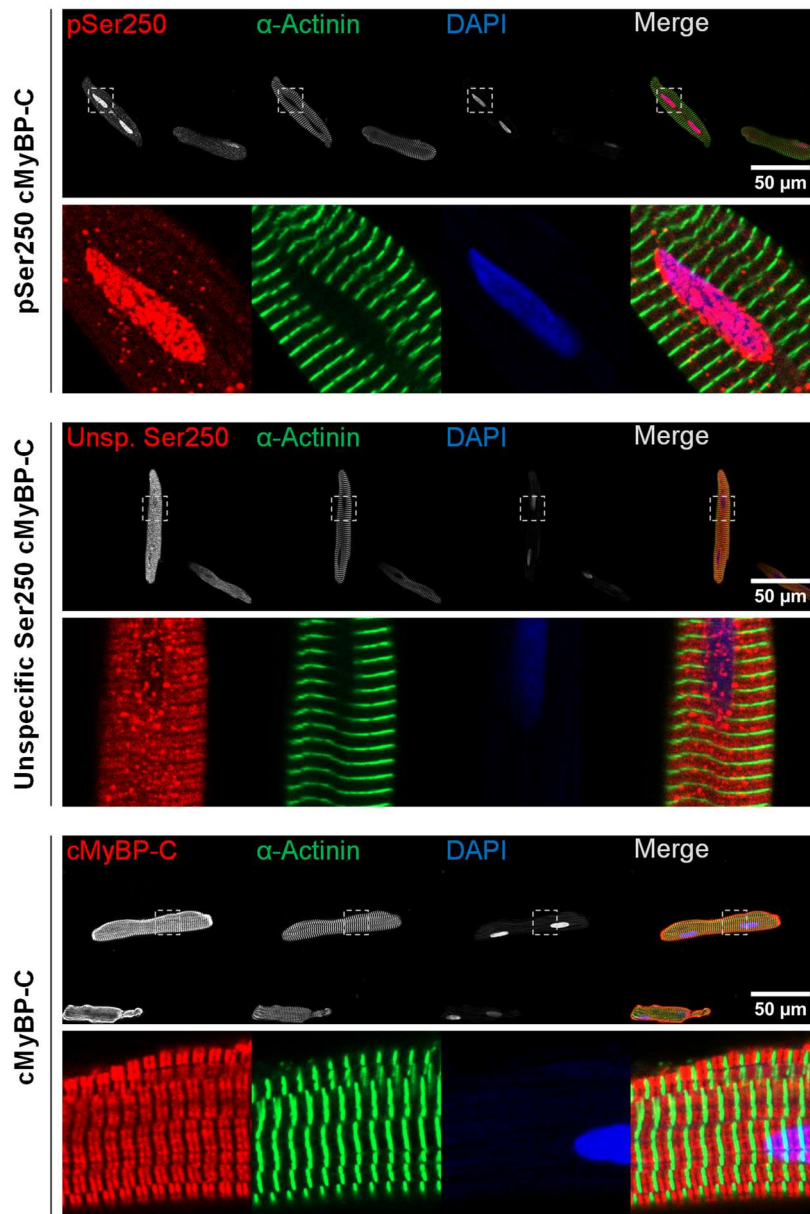
Figure 59: Detection of immunofluorescence signals generated by the pSer250 cMyBP-C antibody
Chemically permeabilized ARVMs were immunolabeled with the specific pSer250 cMyBP-C (1:100), the unspecific
Ser250 (1:500) or the conventional antibody for cMyBP-C detection (1:100). Costaining of α-actinin and DNA was
performed using the appropriate antibody or 4′,6-diamidino-2-phenylindole (DAPI), respectively. α-Actinin and DAPI
were imaged at the same settings in all samples. Dashed boxes indicate the area magnified in the images below.

Immunolabeling of cMyBP-C in chemically permeabilized ARVMs revealed the characteristic
striated doublet pattern (Fig. 59, bottom panel). Samples labeled with the pSer250 cMyBP-C
antibody, however, completely lacked myofilament striations, which was emphasized by the
comparison with Z-disc-signals generated by costaining of α-actinin (Fig. 59, top panel). In
contrast, the pSer250 antibody showed substantial fluorescence that overlaid with nuclear
signals obtained from 4′,6-diamidino-2-phenylindole (DAPI)-costaining, suggesting enhanced
affinity of the pSer250 antibody for nuclear proteins. The unspecific Ser250 antibody, however,
produced the expected striated doublet pattern without staining of nuclei (Fig. 59, middle
panel). Notably, comparison with a commercial cMyBP-C antibody illustrated an increased

number of artifacts and a decreased sharpness of cMyBP-C staining achieved by the unspecific Ser250 antibody at the applied concentration.

Previous experiments had demonstrated that the pSer250 unspecific antibody fraction, which had been obtained from the cMyBP-C pSer250 antibody purification, allowed the detection of endogenous cMyBP-C in Western immunoblots and displayed a striated pattern in permeabilized cardiac myocytes. To evaluate whether this antibody was suitable for immunofluorescence staining of cMyBP-C, it was tested at different concentrations in ARVMs that were either chemically permeabilized or subjected to detergent-mediated removal of the plasma membrane (skinning).
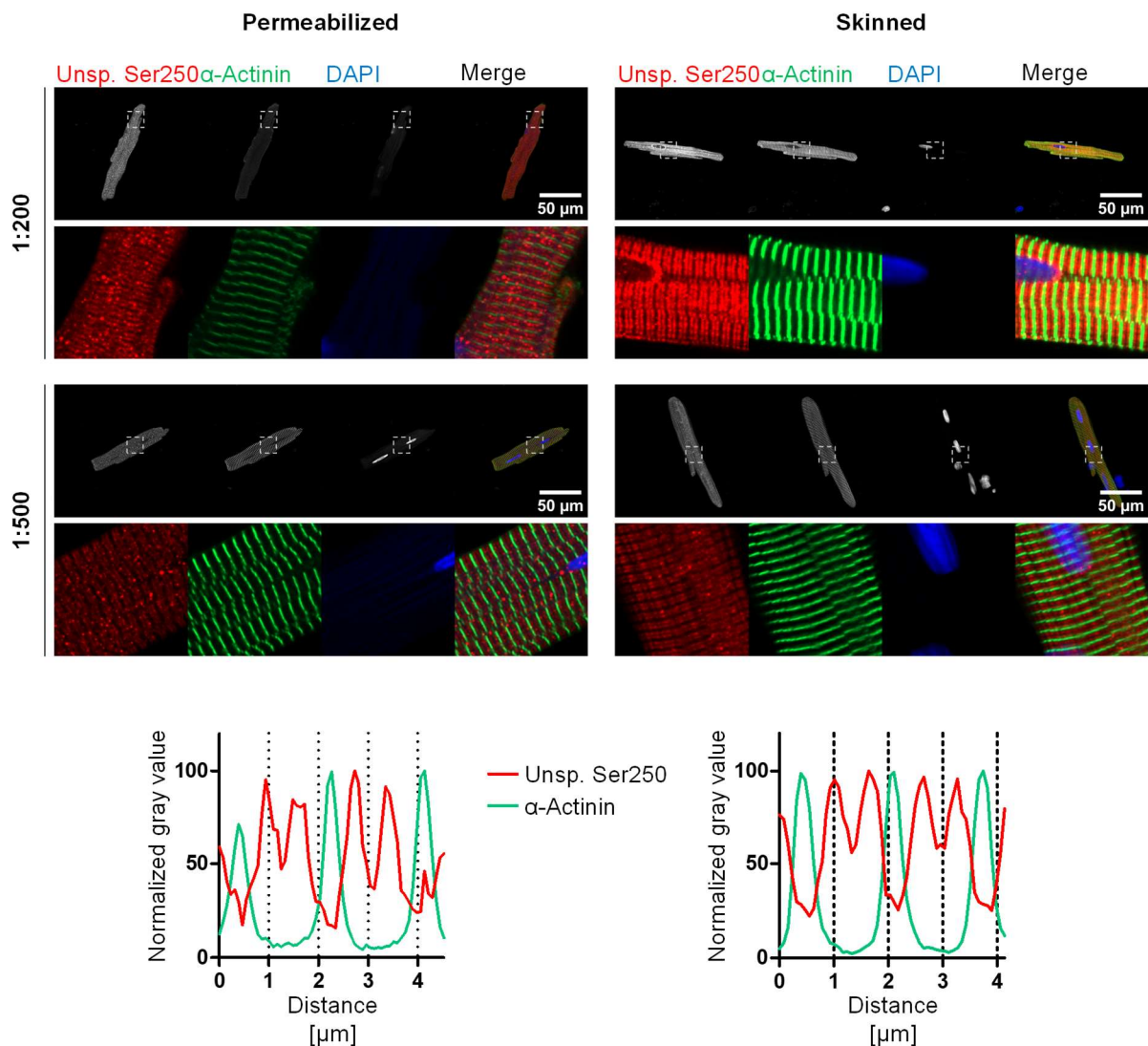
Figure 60: Immunofluorescence detection of cMyBP-C using the unspecific Ser250 antibody ARVMs were fixed and chemically permeabilized in 0.2% Triton or skinned with 1% Triton prior to fixing. The unspecific Ser250 antibody was applied at dilutions of 1:200 and 1:500 for immunofluorescence staining. Costaining of α-actinin and DNA was performed using the appropriate antibody or 4′,6-diamidino-2-phenylindole (DAPI), respectively. All samples were analyzed at the same settings. Dashed boxes indicate the area magnified in the images below. Graphs show intensities of signals obtained from the unspecific Ser250 antibody (1:500) and α-actinin along a myofilament measured in a line report from permeabilized and skinned ARVMs. Values are presented as % of the highest signal intensity measured for each protein.

In permeabilized cells, the unspecific Ser250 antibody generated a striated doublet pattern typically observed for cMyBP-C at a dilution of 1:200 (Fig. 60, left panel). CMyBP-C doublets were interdigitated by striations of the Z-disc protein α-actinin, matching with the localization of cMyBP-C on both sides of the M-line within the myofilament lattice. However, numerous dotted signals were detected additionally to the typical cMyBP-C striations. Further dilution of the unspecific Ser250 antibody (1:500) was accompanied by reduced overall signal intensity but notably reduced dotted artifacts. Assessment of signal intensity distributions showed clear cMyBP-C double peaks surrounded by the Z-disc signal of α-actinin. Applied at a dilution of 1:200 in skinned ARVMs, the unspecific Ser250 antibody produced strong signals, again displaying the expected pattern of doublets separated by α-actinin (Fig. 60, right panel). Upon dilution of the unspecific Ser250 antibody 1:500, overall signal intensity was decreased, but without any negative impact on the quality of the signal, as demonstrated by the sharp doublet pattern in the presentation of signal intensity distributions. Additionally, enhanced signal intensity at the border of the nucleus, which was observed in skinned cardiac myocytes stained at 1:200, was not detected anymore at the higher dilution, suggesting that this signal was an artifact. Overall, signal intensities obtained from the unspecific Ser250 antibody were enhanced in skinned ARVMs. Nonetheless, these imaging experiments showed that the unspecific fraction of the Ser250 antibody can not only be used for Western immunoblot applications but is also suitable for the immunofluorescence detection of cMyBP-C in permeabilized and skinned ARVMs.

4 Discussion

4.1 HNO donor compounds regulate contractile function by impacting on PKA and PP2A signaling

Donor compounds that release HNO exert beneficial effects on cardiac performance and have emerged as promising therapeutic agents for the treatment of ADHF with clinical trials ongoing. The effects of HNO in the heart have been attributed to the formation of disulfide bonds between and within proteins of the contractile machinery and those involved in Ca^{2+} cycling. The data presented in this doctoral thesis show that the HNO donor NCA activates PKA by such disulfide bond formation in ARVMs and leads to the PKA-mediated phosphorylation of substrate proteins. This reveals a yet unknown feature of NCA that is likely to contribute to the positive inotropic and lusitropic effects attributed to HNO donor compounds. Exposure to NCA induced the dimerization of PKA-RI regulatory subunits and oxidation-dependent translocation of the protein kinase to the myofilament fraction, which was accompanied by enhanced phosphorylation of the sarcomeric PKA substrate protein cMyBP-C. Application of the pure HNO donor CXL-1020 also induced PKA-RI dimer formation, however, changes in the

phosphorylation of PKA substrate proteins were not consistent. An inhibitory effect on the catalytic subunit of protein phosphatase PP2A that was determined for CXL-1020 but not for NCA suggests CXL-1020-mediated alterations in the phosphorylation of additional substrate proteins, yet to be identified. In single ARVMs, NCA caused a transient increase in sarcomere shortening and eventually impaired cardiac myocyte contraction, seeming to inflict oxidative damage. In contrast, treatment with CXL-1020 increased ARVM contractility without obvious adverse effects. The divergence of cellular responses elicited by NCA and CXL-1020 indicate factors independent from HNO-release involved in NCA-induced modifications.

Oxidants are still considered as a double-edged sword. In the minds of the majority of people, oxidation in biological systems is solely associated with disease and cellular damage. Indeed, increased production of ROS and RNS has been reported in a broad variety of pathologies, such as cancer, cardiovascular and inflammatory diseases and has been shown to negatively contribute to disease progression (Valko et al. 2006; Takimoto and Kass 2007; Mittal et al. 2014). Therefore, to this day antioxidant supplementation is often considered as a therapeutic approach, although large trials failed and if at all, antioxidant therapy conveyed predominantly harmful effects (Bjelakovic et al. 2014). This surprising outcome of various antioxidant trials is in line with the current perception: Oxidants represent an important class of physiological signaling molecules within the body. Small changes in the local concentration of oxidants result in the specific PTM of protein cysteine residues, which depend on the levels of oxidants generated and exposure time and can alter protein function. The antioxidant capacity of the body is largely relying on the small molecule GSH and the enzyme glutathione reductase to reduce these modifications, turning oxidative PTM into a (mostly) reversible regulatory process. With HNO donors, a class of compounds was generated that has the potential to allow the therapeutic use of redox regulation for the treatment of heart failure. The pharmacological release of HNO not only exerts vasorelaxing effects, but also positive cardiac inotropy and lusitropy without apparent myocardial damage (Fukuto et al. 1992; Paolocci et al. 2001, 2003). As these events are also maintained in failing hearts, HNO donors combine unique beneficial properties that endorse their clinical application in heart failure therapy. Especially in the treatment of ADHF, where detrimental side effects of inotropic agents are still a major problem, HNO donors might prove extremely valuable. Therefore, it is evident that a thorough investigation of these compounds and the molecular mechanisms underlying their biological responses is essential to provide safety for patients during clinical application.

Protein phosphorylation plays a critical role in the regulation and adaptation of cardiac performance in response to neurohumoral stimulation. A variety of cardiac myocyte proteins that are involved in Ca^{2+} cycling or the mechanical contraction of the sarcomere are subject to

protein kinase-mediated phosphorylation, which results in altered protein function and ensures the adjustment of cardiac contractility to the current needs of the body. Oxidative S-glutathiolation of the myofilament protein cMyBP-C by H_2O_2 was found to negatively influence its susceptibility to subsequent regulatory phosphorylation (Stathopoulou et al. 2016). Representing an event that impedes actomyosin interaction, this finding encouraged further investigations about how different oxidative agents affect cardiac myocyte protein phosphorylation and thus contractility. The analysis of such effects would allow to estimate how oxidation-mediating agents can be therapeutically exploited. As compounds that recently received increasing attention in the cardiovascular field, three HNO donor compounds, NCA, AS and CXL-1020, which exert their effects via protein oxidation, were included in this study.

4.1.1   NCA induces cardiac myocyte protein phosphorylation by activating PKA

In ARVM lysates, a phosphoprotein band at a molecular weight of 150 kDa was detected in response to NCA and the β-AR agonist ISO. This signal was hypothesized to represent the well-described PKA substrate protein cMyBP-C. The use of phospho-specific antibodies confirmed NCA-mediated phosphorylation of cMyBP-C at its three M-motif sites Ser275, Ser284 and Ser304 and, additionally, showed the phosphorylation of PLN at Ser16. Both proteins are established substrates of PKA-mediated phosphorylation (Wegener et al. 1989; Gautel et al. 1995). Although the M-motif of cMyBP-C is phosphorylated by several protein kinases, PKA represents the major protein kinase phosphorylating all three M-motif sites (Gautel et al. 1995). The simultaneous occurrence of PLN phosphorylation at Ser16 supported the hypothesis of NCA acting via the activation of PKA. To date, positive inotropic and lusitropic properties of HNO donor compounds are thought to entirely rely on oxidative protein modification and disulfide bonds that form within and between proteins involved in contraction and Ca^{2+}-handling (Tocchetti et al. 2007; Lancel et al. 2009; Gao et al. 2012; Sivakumaran et al. 2013). Protein phosphorylation induced by an HNO donor compound has to our knowledge not been reported before. PKA-mediated phosphorylation of target proteins is associated with accelerated SR Ca^{2+} cycling (Tada and Kirchberger 1976; Kim et al. 1990; Marx et al. 2000), reduced sarcomere Ca^{2+} sensitivity (Garvey et al. 1988) and unrestricted cross-bridge cycling (Gautel et al. 1995; Sadayappan and de Tombe 2012), resulting in enhanced contractility. Therefore, protein phosphorylation by PKA in response to NCA might represent a yet undiscovered mechanism of HNO action that contributes to the reported cardiac effects. Consequently, further experiments were performed to follow up on this important observation. Numerous protein kinases target cMyBP-C and PLN. Moreover, the determination of protein phosphorylation in response to oxidizing agents could be affected by protein oxidation, as this might alter the ability of phospho-specific antibodies to interact with their target. Thus, the effect of NCA on PKA activation was additionally evaluated by a different approach. A change in FRET ratio measured in ARVMs that express the cytosolic A-kinase-activity reporter AKAR3

upon exposure to NCA indicated phosphorylation of the PKA consensus sequence within the sensor and again argued for NCA-mediated activation of PKA. Notably, in the vasculature NCA is known to activate PKGIα (Donzelli et al. 2017). Although PKA and PKGIα are closely related members of the AGC group of protein kinases and share similar consensus sequences (Kennelly and Krebs 1991), the predecessor of the AKAR3 sensor was not modified by PKG and sensor activation was restricted to PKA action (Zhang et al. 2001). For AKAR3, Allen and Zhang (2006) demonstrated its independence from PKC and Ca^{2+}-mediated activation of CaMKII, but did not test other kinases. Active PKGIβ was reported to induce a small AKAR3 response (Gambaryan et al. 2012), but endogenous levels of PKG in cardiac myocytes are low and PKGIα is the dominant isoform (Geiselhöringer et al. 2004). Moreover, the β isoform lacks the redox-sensitive N-terminal cysteine residue 42, which is involved in oxidative subcellular targeting and activation of the kinase (Sandberg et al. 1989; Burgoyne et al. 2007). It can therefore be assumed that FRET signals generated by NCA, which acts via oxidation, reflect an enhancement of PKA activity. The observation that DIA, a potent inducer of disulfide formation (Kosower et al. 1969), shared some of the effects on protein phosphorylation and also induced activation of the FRET sensor, pointed towards thiol-oxidation as the trigger for NCA-mediated effects on PKA.

Phosphorylation of PKA substrate proteins in response to NCA was not affected by blocking of β_1-adrenergic receptors with atenolol, indicating that NCA does not exert its effect via modulation of β-adrenergic receptors but more likely by direct activation of PKA. This was in line with HNO effects on cardiac contractility that were maintained upon β-AR desensitization (El-Armouche et al. 2010) and experimentally induced heart failure (Paolocci et al. 2003) in response to NCA and AS, respectively. The attempt to examine the independence of the NCA response from AC-mediated cAMP production failed, since NKY80, an inhibitor with specificity for AC5 and 6, did not abolish but rather potentiated ISO-induced phosphorylation of the PKA substrate cMyBP-C for yet unknown reasons. Besides alterations in AC activity, an effect on the activity of cAMP-degrading phosphodiesterases could potentially represent a mechanism by which indirect activation of PKA via NCA could occur. Previous studies had shown that cAMP-levels were unaffected by treatment with H_2O_2, AS and CXL-1020, which suggested that cardiac ACs and PDEs are rather insensitive to oxidation (Brennan et al. 2006a; Tocchetti et al. 2007; Zhu et al. 2015). However, cAMP-levels during exposure to NCA have not been assessed and an influence of NCA on AC or PDE activity could therefore not be ruled out in this study.

4.1.2 The functional significance of oxidant-induced PKA RI dimer formation

PKA is commonly activated by cAMP that binds to the regulatory subunits and triggers the release of PKA-C. As a cAMP-independent mechanism for the activation of the protein kinase, oxidant-mediated dimerization by interdisulfide bond formation between PKA-RI subunits had

previously been reported (Brennan et al. 2006a). Consequently, the oxidation of PKA-RI regulatory subunits was assessed, as it might represent a molecular mechanism that underlies the NCA-mediated activation of PKA. Although the formation of RI dimers was most pronounced with NCA and DIA, the observation that exposure to AS, CXL-1020 and H_2O_2 led to the oxidation of RI as well demonstrated a lack of correlation between RI dimerization and the phosphorylation of PKA substrates. It therefore indicated that the oxidative formation of RI dimers alone was insufficient to induce the activation of PKA. Alternatively, some of the oxidizing agents might cause additional effects that prevent PKA activation.

Already under control conditions and to the same extent following exposure to ISO, which activates PKA via the classical cAMP pathway, a large proportion of RI was found in its interdisulfide dimer form. Dimers of PKA-RI form promptly and are highly stable (León et al. 1997), which explains the fact that disulfide bonds between RI monomers were initially assumed to be a constitutive modification (Potter and Taylor 1980). Thus, it is likely that the observed bands in control and ISO-treated samples were based on a combination of (i) basal oxidation and (ii) modifications through atmospheric oxygen during sample processing that occurred before maleimide-mediated alkylation of cysteine residues could prevent their oxidation. Additionally, the antibody used for PKA-RI detection generally produces stronger signals for dimerized protein, suspecting enhanced affinity of the antibody for the dimeric conformation of the protein. For this reason, dimerization was not expressed as % of total PKA-RI, but as a ratio to corresponding signals obtained under control conditions (see Figs. 19 and 20). Similar to the signals obtained for protein phosphorylation discussed above, bands representing dimerized PKA-RI were normalized to the sarcomeric protein α-actinin. To allow a proper comparison of protein content, signal intensities were consistently derived from Western immunoblots performed under reducing conditions, since potential oxidative modifications that might persist under non-reducing sample conditions might obstruct antibody binding. An unexpected and consistently detectable observation was the inability to completely reduce the RI dimers formed after exposure to AS and CXL-1020 with β-mercaptoethanol, which suggested increased stability of the disulfide bonds.

The activation of PKA as a consequence of inducible dimerization of RI subunits had been firstly reported by Brennan and colleagues (2006) in response to H_2O_2. While the finding of RI dimer formation in response to H_2O_2 could be reproduced, it was not paralleled by activation of the PKA FRET sensor AKAR3 nor coincided this event with the phosphorylation of PKA substrate proteins. Certain differences in the experimental setup might in part account for these distinct observations. Although the concentration of applied H_2O_2 was equal in both studies, the incubation time used by Brennan et al. (2006a) was shorter. Substrate phosphorylation in the study of Brennan et al. (2006a) displayed a bell-shaped pattern and decreased at higher H_2O_2 concentrations. A prolonged exposure time, as used here, might result in a similarly

diminished effect and complicate its detection. While experiments presented in this doctoral thesis were based exclusively on cultured ARVMs, Brennan et al. (2006a) in part used freshly isolated ARVMs, which might explain different responses to exogenous stimuli. With a pan-specific antibody that detects phosphorylated PKA substrate proteins, Brennan et al. (2006a) further observed phosphorylation of a protein that corresponded to the molecular weight of cMyBP-C. However, definitive cMyBP-C phosphorylation remained unconfirmed, since antibodies with specificity for cMyBP-C phosphorylation sites were not applied. Moreover, the lack of signal normalization to total protein content and missing reference samples that show the response to ISO hamper the evaluation of the presented phosphorylation signals produced in response to H_2O_2 (Brennan et al. 2006a).

Oxidative RI dimer formation relies on antiparallel interdisulfide bonds that form between the N-terminal cysteine residues Cys17 and Cys38 (referring to rat sequence; Bubis et al. 1987). Accordingly, dimerization is abolished in endothelial cells isolated from the aorta of Cys17Ser PKA-RI knock-in mice (Burgoyne et al. 2015). PKA-RI subunits from both, rat and human, possess two additional cysteine residues at position 346 and 361 within the C-terminal cAMP-binding domain. However, in contrast to the N-terminus, C-terminal products from proteolytic cleavage do not display dimer formation, suggesting that Cys346 and Cys361 do not form disulfide bonds (Zick and Taylor 1982). Also, the finding reported by Brennan et al. (2006a) that both reduced and oxidized PKA-RI can be captured using cAMP-agarose is in line with the unobstructed binding of cAMP to the C-terminal binding sites of the PKA-RI subunit. Therefore, PKA-RI dimerization appears to exclusively rely on Cys17 and Cys38. Consequently, the possibility that different oxidants might give rise to different types of RI dimers that differently affect PKA activity is unlikely and might not explain, why the effects on PKA substrate phosphorylation observed for NCA and DIA were not similarly induced by AS, CXL-1020 and H_2O_2. A potential RI dimer diversity through the hypothetical generation of NCA- and DIA-induced single disulfide bonds or parallel interdisulfides between Cys17 and Cys38 instead of the reported antiparallel bonds might result in altered kinase activity, but these modifications lack evidence and it is questionable, whether the formation of a parallel disulfide bond is spatially possible.

Similar molecular weights that were estimated for RI dimers generated upon treatment with NCA, AS, CXL-1020, H_2O_2 and DIA indicated no difference in the migration behavior and argued for the same structural characteristics to exist in dimers that had formed in response to either compound. While signals representing monomeric PKA-RI were detected at the expected molecular weight of approx. 47 kDa, dimer-corresponding bands were consistently present at a higher molecular weight than the estimated 94 kDa, generating signals slightly above the 100 kDa marker band (see Fig. 21). Comparable slower migrating bands for PKA-RI dimers were also found in other publications (Brennan et al. 2006a; Burgoyne et al. 2015)

and are likely to be explained by the disulfide bond-induced structure of the two linked monomers resulting in an altered restraint of the proteins in the acrylamide polymer. In addition, data from this experiment show the considerable differences that exist in the migration behavior of different protein markers, which can result in varying molecular weight estimations for proteins, when marker bands are used as a reference.

4.1.3   Kinase translocation mediates substrate phosphorylation

To broaden the understanding of a potential connection between NCA-mediated RI dimer formation and kinase activation, the temporal sequence of both events was determined. The delay of at least 10 min that was observed for cMyBP-C phosphorylation when compared to RI oxidation, supported the assumption that the two events were not directly affiliated. Notably, in FRET-experiments signals were obtained from the cytosolic A-kinase activity sensor within a few minutes (see Fig. 15). Considering that PKA type I is predominantly cytosolic and that cMyBP-C is a sarcomeric protein, it was hypothesized that the delay in phosphorylation might be due to an NCA-mediated translocation event of PKA to the myofilament compartment. Indeed, an accumulation of PKA-RI and PKA-C subunits was detected in the myofilament-containing fraction of NCA-treated ARVMs, indicating subcellular translocation of the PKA holoenzyme. Exposure to ISO did not induce this effect, suggesting that ISO-mediated phosphorylation of sarcomeric proteins is mainly accounted to the activation of AKAP-bound PKA type I and II that is anchored to the myofilaments. In line with PKA substrate phosphorylation, translocation was not observed when ARVMs were incubated with H_2O_2 or CXL-1020, while DIA led to enhanced levels of PKA in myofilament-containing fractions like NCA (data not shown).

While PKA-C was consistently found mainly in the cytosolic ARVM fraction, it also displayed minor presence in Triton-soluble membrane samples (see Fig. 22). Contamination with cytosolic material was unlikely, as Western immunoblots of marker proteins demonstrated a successful separation of all fractions. This membrane-associated presence of PKA-C might correspond to the type II PKA holoenzyme. Cardiac myocytes also express a lower amount of PKA-RII (Corbin et al. 1975), which is mostly bound to AKAPs at intracellular structures, such as the plasma membrane or the SR (Corbin et al. 1977; Scott and McCartney 1994). Therefore, catalytic subunits of type II PKA are expected to be present in the Triton-soluble fraction at least to a certain degree.

Importantly, the translocation process of PKA that was induced by NCA was reversed when the reducing agent DTT was added during the harvesting of the ARVMs. This observation demonstrated that oxidation was crucial for translocation and highlighted the dependence on oxidative modification to maintain the new localization of the proteins. It furthermore suggested an altered affinity of oxidized PKA-RI for myofilament binding partners that might represent AKAPs, which matched well with the enhanced phosphorylation of cMyBP-C. In addition,

although fractionation samples were analyzed under reducing conditions, this result suggested that PKA translocation was based on the dimerized form of RI, pointing towards differences that might exist between dimers generated in response to different oxidizing agents discussed above. The reversibility by the reducing agent also showed that protein accumulation in the myofilament-containing fraction after incubation with NCA were not resulting from irreversible protein aggregation, but indicated a rather reversible modification that allows the recovery of a functional protein. This was supported by the observation of comparable cMyBP-C phosphorylation levels that were detected in response to ISO with or without NCA-pretreatment, showing that NCA does not obstruct ISO-mediated PKA signaling (see Fig. 18). Myofilament translocation of PKA occurred within the first 3 min of NCA-treatment and reached significant levels after 10 (catalytic subunit) and 30 min (regulatory subunit). These results of the time course experiments were in accordance with the hypothesis of dimerization-induced PKA translocation that leads to the phosphorylation of the myofilament PKA substrate cMyBP-C in response to NCA-treatment.

Data from subcellular fractionation experiments were supported by immunofluorescence labeling of PKA-RI in skinned ARVMs, where the exposure to NCA induced an accumulation of RI at the sarcomeric Z-discs in-between the doublet signals that represent cMyBP-C. Free PKA-C has the ability to enter and exit the nucleus by diffusion and to phosphorylate nuclear targets independently from regulatory subunits (Harootunian et al. 1993). Consequently, it is well possible that also PKA-C that is released from RI subunits at the Z-disc can reach the C-zone to interact with cMyBP-C, which is approx. 0.5 µm away during diastole and even closer during systole. No enhancement of RI signal was observed for AS, while the incubation with CXL-1020 resulted in a slight increase in the intensity of a rather diffuse PKA-RI signal, which did not allow to draw a conclusion concerning the sarcomeric localization of RI subunits. The NCA-mediated Z-disc localization was paralleled by an enhanced overall myofilament presence of PKA-RI and was in line with the increased phosphorylation of the PKA substrate cMyBP-C. Enhanced levels of colocalization determined between PKA-RI and cMyBP-C or MLC2v, respectively, by PLAs further supported the NCA-induced presence of PKA in proximity to cMyBP-C. Notably, PLAs showed no enhanced colocalization between PKA-RI and the Z-disc protein α-actinin. The sarcomeric Z-disc has a width of approx. 120 nm (Rowe 1973; Frank and Frey 2011), while the PLA generates a signal for proteins that are at most 40 nm apart. This suggests that PKA-RI might locate to the Z-disc without generating a PLA signal with α-actinin but via interaction with other Z-disc proteins. However, α-actinin is the main component of the Z-discs and determines Z-disc width (Luther 2009). Thus, it is unlikely that a protein that displays Z-disc localization by immunofluorescence imaging is more than 40 nm away from an α-actinin protein. Moreover, PLA counts that were comparable to NCA or even increased were obtained for PKA-RI and cMyBP-C or PKA-RI and MLC2v, respectively,

after incubation with ISO. This contrasted with coinciding observations from fractionation and immunofluorescence labeling experiments, in which ISO had shown no effect. These findings are puzzling since cardiac myocyte preparation for PLA and immunofluorescence imaging were largely identical. The myofilament presence of PKA-C could not be analyzed as the available antibody turned out to be not suitable for immunofluorescence analyses.

As mentioned above, the dependence of NCA-induced PKA-RI translocation on oxidation suggested an altered affinity of oxidized PKA-RI for myofilament AKAPs that mediate PKA-anchoring at the sarcomere. Brennan et al. (2006) had suggested α-myosin heavy chain as a novel interaction partner of oxidized PKA-RI. As cMyBP-C is directly associated with myosin in the thick filaments, this would result in PKA to exist in immediate proximity to its substrate. CTnT, which is located within the cross-bridge bearing region of the sarcomere, was also reported to serve as an AKAP (Sumandea et al. 2011) and would anchor PKA in the vicinity to cMyBP-C. Both potential AKAP-interactions would match with the colocalization of PKA-RI with MLC2v and cMyBP-C observed in PLAs and with the enhanced overall signal detected for PKA-RI by immunofluorescence labeling. Thus, binding to cTnT or α-myosin heavy chain potentially contributes to cMyBP-C phosphorylation in response to NCA-mediated PKA translocation. The α-actinin-binding protein myospryn was described as an AKAP present at the Z-disc of the sarcomere (Reynolds et al. 2007). Its interaction with dimerized RI would help to explain the pronounced presence of fluorescence-labeled PKA-RI at the Z-disc. However, coimmunoprecipitation experiments indicated myospryn to specifically interact with PKA-RIIα subunits, but not with RI. Another described AKAP at the Z-disc is synemin, but similar as for myospryn, binding has only been reported for PKA-RII (Russell et al. 2006). Although it remains unclear which AKAPs are involved in NCA-mediated translocation, it is likely that altered binding affinities for scaffolding proteins are involved in the oxidation-dependent anchoring of PKA to distinct myofilament compartments. AKAP18δ was shown to regulate PKA-mediated phosphorylation of PLN at the SR and regulate SR Ca^{2+}-uptake (Lygren et al. 2007). An accumulation of PKA subunits in response to NCA was not detected in SR membrane-containing Triton-soluble fractions (see Fig 22). Nonetheless, although it is unclear whether AKAP18δ can only interact with RII or also with RI, the phosphorylation of PLN that was found upon exposure to NCA might involve a similar AKAP-dependent mechanism.

Notably, the results collected for NCA discussed above matched well with data from Brennan et al. (2006a), which reported an oxidation-dependent mechanism for PKA-RI translocation and led to the hypothesis of oxidation-induced alterations in AKAP affinity. However, Brennan et al. (2006a) observed PKA substrate phosphorylation and PKA-RI subcellular translocation in response to H_2O_2, a stimulus that did not induce either of these in the experiments performed for the study presented here. Interestingly, immunofluorescence labeling of PKA-RI in H_2O_2-treated permeabilized ARVMs by Brennan et al. (2006a) showed a distinct nuclear localization,

while transversally striated signals that typically correspond to myofilament proteins were only slightly more pronounced when compared to control cells. Considering the fact that the myofilament-containing Triton-insoluble fraction besides the myofilaments also contains the nuclei, the H_2O_2-induced elevation of PKA-RI levels in these fractions appeared to predominantly rely on nuclear RI translocation. This again raises questions since the PKA holoenzyme is assumed to be too large to access the nucleus (Adams et al. 1991; Harootunian et al. 1993). In addition, no PKA-RI was observed in ARVM nuclei upon incubation with any of the applied stimuli in the present study, although DAPI staining indicated the presence of intact nuclei in the skinned ARVMs. In total, despite small differences in the experimental procedures such as the application of different PKA-RI antibodies and the use of rat ventricular tissue (Brennan et al. 2006a) versus cultured ARVMs (this study) for fractionation experiments, there remains a surprisingly strong contrast between the results obtained for H_2O_2, which to date lacks a coherent explanation.

Although the translocation of PKA in response to NCA showed a dependence on oxidation and suggested RI dimer formation as the trigger, it is unknown whether NCA-mediated oxidation of RI regulatory subunits is a causal prerequisite for the translocation process and subsequent phosphorylation of sarcomeric PKA substrate proteins. To our knowledge, the translocation of PKA subunits has never been studied in the redox-dead Cys17Ser PKA-RI knock-in mouse that was introduced by Burgoyne et al. (2015). Therefore, no information is available that reliably links PKA-RI oxidation with protein translocation. It thus cannot be excluded that the oxidation of PKA-RI is not necessary or not sufficient to activate the kinase or that the oxidation of additional proteins is involved in the observed PKA activation and translocation processes. Nevertheless, since NCA mainly acts via the formation of disulfide bonds, NCA-mediated RI dimer formation that leads to PKA translocation and the subsequent phosphorylation of target proteins by PKA represents a plausible order of the observed events.

The attempt to label oxidized cysteine residues of PKA-RI with PEG once more emphasized the previously described high susceptibility to oxidation and the resulting resistance of dimerized RI to reducing agents (León et al. 1997). The reduction of RI dimers had not been successful during sample processing, keeping cysteine residues unreceptive for the binding of PEG. However, the apparent susceptibility of PKA-RI to oxidative modification had been shown by the detection of dimerized protein in previous experiments (see Figs. 19-21). Notably, PEG-labeling showed that not only PKA-RI but also PKA-C was susceptible to oxidation by NCA, DIA and to a lesser extent by AS. Incubation with CXL-1020 had no effect. The shift in molecular weight of approx. 10 kDa suggested two cysteine residues being modified in response to either treatment. PKA-C oxidation occurring in response to NCA was supported by results from biotin-switch experiments. Moreover, NCA-mediated oxidation was paralleled by a significant inhibition of recombinant PKA-C activity and the detection of PKA-C as a double

band in non-reducing Western immunoblots (see Fig. 31). The appearance of the extra band was in line with an inhibitory intradisulfide bond that was reported to form between Cys199 in the activation loop and C-terminal Cys343 (Humphries et al. 2002). The inhibitory effect was prevented by the preincubation with ATP and suggested a sterically limited availability of Cys199 for disulfide formation. These data highlight that the phosphorylation of PKA substrate proteins most likely is a result of orchestrated NCA-mediated oxidation events that involve both, the regulatory and the catalytic subunits of PKA. The inhibition of PKA-C was shown to be considerably enhanced following dissociation from regulatory subunits (Humphries et al. 2002, 2005), but during protein translocation PKA most likely exists as a holoenzyme. Therefore, NCA-mediated oxidative inhibition would not affect PKA-C activity before the kinase has reached its new subcellular localization and PKA-C is released in the vicinity to substrate proteins. Moreover, inhibition only seems to apply to PKA-C that has not bound ATP. In this way, NCA presumably induces the translocation of the holoenzyme to myofilament substrates, but also partially inhibits the subsequent activity of free PKA-C. Consequently, protein phosphorylation in response to NCA is increased, but despite the accumulation of PKA subunits in the myofilament-containing fraction, PKA activity remains below levels elicited by ISO that are considered as the maximal stimulation.

4.1.4   Diverse effects of NCA and CXL-1020 on PP2A

Protein phosphorylation is catalyzed by protein kinases but, as a reversible modification, also involves the removal by counteracting protein phosphatases. To assess whether effects associated with NCA-mediated oxidation also involve alterations potentially affecting protein phosphatase function, the activity and cellular distribution of the catalytic and B56α regulatory subunit of PP2A, a major cardiac myocyte protein phosphatase (DeGrande et al. 2013; Lubbers and Mohler 2016), were investigated in ARVM fractions. Contrary to expectations, during incubation with NCA, both B56α and PP2A-C translocated from the cytosol to the myofilaments. In accordance with Yin et al. (2010), who had highlighted the role of B56α in PP2A myofilament translocation, B56α consistently showed a trend to decreased protein levels in Triton-insoluble fractions after incubation with ISO when compared to control samples (Figs. 22-24). However, no statistical evaluation of this relationship was performed. Also, the pronounced localization of B56α at the sarcomeric M-line of immunofluorescence-labeled skinned ARVMs after NCA-exposure was consistent with reports of Yin and colleagues (2010), who observed B56α at both M-line and Z-disc. Like for PKA-C, the corresponding antibody for PP2A-C did not allow the detection of fluorescence signals by confocal imaging. Logically, the increased presence of a protein phosphatase is commonly associated with a decrease in substrate protein phosphorylation, however, the phosphorylation of cMyBP-C, which represents a PP2A substrate, was enhanced in response to NCA (see Fig. 14). This result encouraged the involvement of PP2A in pursuing investigations of oxidant effects to examine

alterations in the oxidation status and activity of the main cardiac myocyte phosphatase responsible for myofilament dephosphorylation.

Lacking signals in NCA- and DIA-treated PEG-switch input samples were restored under reducing conditions, which indicates the inability of the antibody to bind oxidized protein. In the PEG-labeled samples, signals representing reduced B56α were also absent, suggesting an almost entire conversion of B56α into its oxidized state in response to incubation with NCA and DIA. The comparably low intensities of shifted bands in these samples reveal an incomplete reduction during sample processing. As a result, oxidized protein that cannot be detected by the B56α antibody was still present in the PEG-samples. Alternatively, binding by the corresponding antibody might also be impaired after PEG-labeling. B56α contains three cysteine residues within its N-terminal domain that harbors the epitope for the antibody used in this study. The involvement of at least one of these residues in protein oxidation would provide an explanation for the oxidation-mediated absence of Western immunoblot signals. To date, no information is available concerning B56α oxidation or its impact on phosphatase function. The exposure to CXL-1020 did not induce any detectable PEG-shifts. Although reported in previous studies (Rao and Clayton 2002; Foley et al. 2007), none of the applied treatments allowed the detection of PP2A-C oxidation by PEG- or biotin-switch. However, this circumstance might be based on impaired antibody binding and detection of the modified protein as observed for B56α.

Since NCA-treatment of ARVMs was associated with enhanced cMyBP-C phosphorylation, but at the same time with the translocation of PP2A to the myofilament compartment (see Figs. 14 and 22), the impact of oxidation on PP2A catalytic activity was investigated in a fluorescence assay. Surprisingly, substrate dephosphorylation by recombinant PP2A-C was not reduced by NCA. An alternative explanation for the coexistence of PP2A and its phosphorylated substrate cMyBP-C in the same subcellular compartment might be provided by the NCA-mediated oxidation of B56α that was determined by PEG-switch. Although the molecular mechanisms remain elusive, alterations in the interaction between oxidized B56α with PP2A-C or other sarcomeric proteins might affect PP2A function. Anchoring of the PP2A complex to the M-line as found by immunofluorescence labeling (see Fig. 26), for example, might trap the catalytic subunit distant from substrate proteins. In contrast to stimulation with NCA, PP2A activity was significantly reduced by exposure to CXL-1020 and revealed a novel potential mechanism of action for this HNO donor compound. In heart failure, the increased presence and activity of protein phosphatases have been reported (Gupta et al. 2003; El-Armouche et al. 2004; Kohr et al. 2008; Heijman et al. 2013; DeGrande et al. 2013; Meyer-Roxlau et al. 2017). Since these changes are likely to contribute to the decreased phosphorylation levels of many cardiac myocyte proteins and the concomitant contractile dysfunction (Bartel et al. 1996; Messer et al. 2007; El-Armouche et al. 2007; Copeland et al.

2010; Bardswell et al. 2012; Stathopoulou et al. 2016), protein phosphatases are amongst the pharmacological targets for the treatment of cardiac disease. Thus, with the inhibition of PP2A, CXL-1020 exhibits another promising property that is expected to confer beneficial effects in heart failure therapy. Even though no mass increment was detected for PP2A-C by PEG-switch following CXL-1020-incubation, the chemistry of CXL-1020 and previous reports (Foley and Kintner 2005; Foley et al. 2007) suggested this effect to involve protein oxidation.

The fact that exposure to H_2O_2 was shown to inhibit PP2A but had no effect on PP1 and PP2C points towards a special role for PP2A in the redox-regulation of protein phosphorylation (Rao and Clayton 2002). With CXL-1020, no changes had been observed in protein phosphorylation in initial experiments (see Fig. 14), however, unexpectedly further studies showed a slight increase in PLN and cMyBP-C phosphorylation (see Figs. 38 or 41 and 43, respectively). Moreover, the inhibition of PP2A suggested alterations in the phosphorylation status of additional substrate proteins. The PP2A substrates cTnI, the L-type Ca^{2+} channel or the RyR2 have not been investigated in this study, but represent prominent phosphorylation-regulated proteins (Lubbers and Mohler 2016). Thus, their modification should be the topic of future investigations as it might be relevant for the therapeutic application of CXL-1020 and its successor compounds.

4.1.5 NCA and CXL-1020 differently affect ARVM contractility

In isolated ARVMs, NCA induced a fast increase in sarcomere shortening and maximal contraction and relaxation velocities. This effect was only short-lived and converted into a state that was characterized by low contractility and reduced diastolic length, indicating damage of the contractile machinery and relaxation impairment. Sarcomeric defects were confirmed by an attenuated β-AR response upon subsequent application of ISO. A degree of sarcomere shortening comparable to that measured in the acute phase in this study had been observed for NCA in murine ventricular cardiac myocytes by El-Armouche et al. (2010). However, information about the time of measurement or the response to following ISO-exposure was not stated in this publication. Although the harmful effect of NCA on contractile function was apparent, the exact cause remains elusive. It is important to note that, although NCA resulted in the abrogation of the positive inotropic response of ARVMs to ISO, β-AR-mediated activation of PKA signaling seemed unperturbed. This was indicated by the detection of profound ISO-mediated protein phosphorylation in ARVMs following pretreatment with NCA (see Fig. 18), which, however, did not translate into a functional response. Increased phosphorylation levels were also reproducibly observed after 30 to 100 min of incubation with NCA and suggested that PKA and protein phosphorylation were functional (see Fig. 20). Additionally, the rapid onset of positive inotropy suggested that NCA-mediated protein translocation and the subsequent phosphorylation of myofilament proteins were not involved in these effects, as these processes were shown to take several minutes of time (see Fig. 24). NCA was previously

described to modify SR Ca^{2+} cycling as well as myofilament protein function (El-Armouche et al. 2010; Gao et al. 2012). Excessive protein oxidation in response to NCA might lead to constrained Ca^{2+} handling that lacks proper import into the SR and unrestricted Ca^{2+} release and would attenuate the stimulus for contraction and relaxation. Similar effects could be caused by excess or irreversible oxidation of sarcomeric proteins, which might alter Ca^{2+} sensitivity or lock the myofilaments in a certain state of contraction. It is likely that the observed NCA-mediated obstruction represents a combination of these effects, ultimately resulting in contractile dysfunction and a negative lusitropic effect.

Interestingly, CXL-1020 shared most of the acute effects elicited by NCA, but maintained its impact on enhanced contractility, increased contraction and relaxation velocities and accelerated relaxation (time to baseline$_{50\%}$) until a plateau was reached, without inducing obvious detrimental side effects. These observations matched with enhanced sarcomere shortening and a faster relaxation measured in response to CXL-1020 by other groups (Sabbah et al. 2013; Roof et al. 2017) and again highlighted considerable differences between the biological responses to NCA and CXL-1020.

The influence of CXL-1020 on ARVM contractility was further investigated in hiPSC-derived EHTs, which have evolved as a promising model system for the evaluation of cardiac function exerted by pharmacological compounds. However, changes in contractile parameters were similar between control tissues and after exposure to CXL-1020 and assumingly resulted from changes in temperature that occurred during drug application. One major limitation in this experiment was the short $t_{1/2}$ of CXL-1020, which only amounts to 1.9 min (Sabbah et al. 2013). In this setup, sample preparation and the automated measurement take several minutes of time. It is likely that the delay between compound application and completion of the measurement caused CXL-1020-mediated effects on contractility to have already elapsed, thus escaping the measurement.

4.1.6 Effects of CXL-1020 on kinase signaling

Sabbah et al. (2013) and Roof et al. (2017) had observed alterations in $[Ca^{2+}]_i$ transient amplitude and decay, which suggested an accelerated import of Ca^{2+} into the SR to be predominantly responsible for the positive lusitropic effect of CXL-1020. However, the modulation of PLN and SERCA function by modification at critical cysteine thiol groups had been described for AS but was never confirmed for NCA nor for CXL-1020 (Tocchetti et al. 2007; Lancel et al. 2009; Sivakumaran et al. 2013). Results obtained for NCA demonstrated that HNO donor compounds can also influence protein kinase signaling. Thus, besides the possible alteration in protein phosphorylation through the inhibition of PP2A discussed above, CXL-1020 might affect kinase activity directly.

Another protein kinase that phosphorylates PLN and other established PKA substrate proteins is PKG. PKG is involved in cardiac myocyte relaxation (Layland et al. 2002) and both activation

of the cGMP-generating enzyme sGC (Lin et al. 2012) and direct oxidative activation of PKGIα (Donzelli et al. 2017) have been described upon exposure to HNO. Nonetheless, the inhibition of sGC by ODQ had no effect on CXL-1020-induced contractility nor affected phosphorylation of the PKG substrates cMyBP-C and PLN. In line with these data, an sGC-independent mechanism for CXL-1020 had been suggested before (Sabbah et al. 2013; Zhu et al. 2015). However, in contrast to results shown by Zhu et al. (2015), enhanced levels of dimerized PKGIα were observed in response to CXL-1020 in the present study and were paralleled by slightly increased PLN phosphorylation, suggesting direct oxidation-mediated activation of the kinase (see Fig. 38). After treatment with NCA, PKGIα dimer signals were enhanced as well, but an extra band indicating previously reported intradisulfide formation (Donzelli et al. 2017) migrating directly below dimerized PKGIα was also present, again displaying a differential cellular response to CXL-1020 in comparison to NCA.

The comparison of CXL-1020 to the drug G1, a molecule that reportedly induces vasorelaxation via dimerization-mediated activation of PKGIα (Burgoyne et al. 2017), demonstrated that effects exerted by G1 in ARVMs profoundly deviated from reported expectations. Instead of the anticipated positive lusitropy, G1 increased contractility and decelerated sarcomeric relaxation (time to baseline$_{50\%}$). These effects clearly mismatched with the activation of PKGIα and indicated additional mechanisms of action for G1 in ARVMs. With similarity to NCA, G1 compromised myofilament relaxation and attenuated sarcomere shortening in response to subsequent ISO-exposure. Considering the claimed potential of G1 to induce PKGIα dimer formation, the modification of other redox-sensitive proteins appeared plausible to explain the observed contractile response. But astonishingly, neither did exposure to G1 result in the interdisulfide formation of PKGIα nor of the highly oxidation-susceptible PKA-RI and had no effect on the phosphorylation status of sarcomeric cMyBP-C. No differences in kinase dimerization were observed between G1 concentrations of 0.2 to 20 µmol/L, important to mention ARVMs had immediately died upon application of 100 µmol/L G1 during contractility measurements (data not shown). Thus, the potential of G1 to induce interdisulfide dimers appears to be greatly diminished in ARVMs and additional effects apart from dimerization-mediated activation of protein kinases and myofilament protein phosphorylation seem to elicit the contractile effects of G1. The molecular mechanisms underlying this response, however, are underexplored and did not allow the evaluation of a PKGIα involvement in CXL-1020-mediated lusitropy.

Also for the protein kinase ROCK, which belongs to the AGC family of protein kinases like PKA and PKG, the potential to modulate cardiac myocyte contractility has been suggested (Nishimaru et al. 2003; Rajashree et al. 2005). An involvement of ROCK activity in CXL-1020-mediated effects was excluded by pharmacological inhibition of the kinase using the

established ROCK inhibitor H1152, which left the contractile response of ARVMs to CXL-1020 unaffected.

The application of different incubation times and concentrations of CXL-1020 confirmed that the conditions used for ARVM treatments (300 µmol/L, 15 min) were well-suited for the detection of PKA-RI dimer formation. Although no profound effects had been observed in previous experiments, the comparison of CXL-1020 from the standard stock (old vial) and a newly received vial (new vial) in cells derived from the same isolation process highlighted a markedly diminished ability of the new CXL-1020 to induce cMyBP-C phosphorylation. This observation was paralleled with a blunted response of ARVMs to the new CXL-1020 in contractility measurements (data not shown). The apparent differences between the old and new vial of CXL-1020 led to speculation about storage-related changes to the new CXL-1020 that might result in altered decomposition and release characteristics. However, thorough testing of the compound through the manufacturer could not identify any chemical anomalies that would indicate decomposition into other products. After receipt, vials of the solid compound that originated from the identical batch of chemical synthesis were similarly stored at -20 °C and working solutions were prepared immediately prior to use. The only apparent difference between vials was a different number of freeze-thawing cycles that involved the storage at room temperature prior to compound extraction, which was performed to avoid dilution by condensed H_2O. What caused the different cellular responses to compound from the different vials remains unclear, but demonstrates that slight differences can lead to considerable deviations in CXL-1020 activity, which calls for special caution to avoid misinterpretation of results and limits the value for clinical application. Since increased concentrations of CXL-1020 from the new vial induced contractile effects similar to those elicited by 300 µmol/L of old vial CXL-1020, contractility and Western immunoblot experiments involving drug G1 were performed with 1 mmol/L of new vial CXL-1020 as indicated. (For all other experiments 300 µmol/L of CXL-1020 from the old vial was applied.) Interestingly, in these experiments, the phosphorylation of cMyBP-C at Ser284 was clearly elevated after exposure to 1 mmol/L of new vial CXL-1020 (see Fig. 41), however, treatment under equal conditions did not induce phosphorylation in the concentration curve experiment (see Fig. 43). A notable difference in cMyBP-C phosphorylation was also apparent between time course treatment and the concentration curve obtained with old vial CXL-1020. N-numbers in these experiments were comparably low and differences might be explained by biological variance. Nonetheless, these results also suggest a possible involvement of cMyBP-C phosphorylation in CXL-1020-mediated effects at higher compound concentrations and support the experimental observations of kinase activation and phosphatase inhibition.

4.1.7 GAPDH is susceptible to NCA-mediated translocation

In fractionation experiments, the selected cytosolic marker protein GAPDH, whose suitability for the assessment of subcellular fractionation quality was shown before (Yin et al. 2010), displayed a pronounced presence in the Triton-insoluble fraction of NCA-treated cardiac myocytes. In line with numerous oxidative modifications that had been reported for the enzyme (Butterfield et al. 2010; Maller et al. 2011), this finding suggested an oxidation-mediated translocation of GAPDH in response to NCA. As Triton-insoluble fractions also contain cell nuclei, the supposed interaction of oxidized GAPDH with nuclear proteins supported this assumption (Hwang et al. 2009). Notably, it was previously reported that NCA inhibits GAPDH by oxidation, which was suggested to be mediated via the formation of an intradisulfide bond within the active site cysteine residues 149 and 153 and an irreversible modification at Cys244 (Mitroka et al. 2013). Our data revealed reduced levels of translocated enzyme in cells harvested under reducing conditions, arguing for the reversible disulfide modification to induce GAPDH translocation. A shift of approx. 10 kDa in PEG-switch experiments was in line with NCA-mediated intradisulfide formation, indicating the reversible modification of two cysteine residues. However, the presence of bands migrating at molecular weights matching to two molecules of GAPDH in non-reducing inputs suggested the formation of interdisulfide homodimers. GAPDH dimerization had been shown in response to different oxidizing agents (Nakajima et al. 2007), but in the present study corresponding bands were only found following incubation with NCA, DIA and slightly with AS. Taken together, these results suggest NCA-mediated inter- and/or intradisulfide formation to elicit a translocation of GAPDH to the Triton-insoluble ARVM fraction and once more pronounce the special properties of NCA in the generation of protein disulfides.

4.1.8 HNO donor compounds: Similar but significantly different

For the investigation of biological effects elicited by HNO, AS was the most frequently used donor compound. This prototypical HNO donor was applied, when vasorelaxing effects were described for HNO (Fukuto et al. 1992) and it was also used when positive inotropy and lusitropy were reported in dogs for the first time (Paolocci et al. 2001, 2003). The oxidative modification of proteins that regulate SR Ca^{2+} cycling, which is assumed to largely contribute to positive inotropic and lusitropic effects of HNO, was likewise investigated with the use of AS: The induction of activatory SERCA S-glutathiolation (Lancel et al. 2009), oligomerization of PLN that interferes with SERCA-inhibition (Sivakumaran et al. 2013) and increased RyR channel open probability (Tocchetti et al. 2007) were described. Results collected from these experiments were attributed to the release of HNO, although AS decomposition also generates considerable amounts of biologically active nitrite (Bonner and Ravid 1975; Dejam et al. 2004; Gladwin et al. 2005). In fact, several studies took the release of nitrite into account (Fukuto et al. 1992; Tocchetti et al. 2007; Kohr et al. 2010), but this was not always the case (Paolocci et

al. 2003; Sivakumaran et al. 2013). With the increasing interest in HNO as a promising candidate molecule for the treatment of cardiovascular disease, more donor compounds were developed to allow the investigation of different HNO-release kinetics and a reduced generation of by-products. Astonishingly, many findings made with AS, like the effects exerted on SERCA, PLN and RyR, were assumed to apply to chemically distinct donor compounds without further testing, as they were thought to be mediated by the release of HNO that all donors have in common. This is especially remarkable since novel compounds are intended for therapeutic use in patients and should be well-characterized. It is true, that the HNO donors AS, NCA and CXL-1020 have their predominant properties to enhance vasorelaxation (Fukuto et al. 1992; Donzelli et al. 2013; Zhu et al. 2015) and cardiac myocyte contractility (Tocchetti et al. 2007; El-Armouche et al. 2010; Sabbah et al. 2013) in common. Nonetheless, findings cannot be transferred from one HNO donor to another. This is nicely depicted by a study from Gao et al. (2012), in which "[o]ne key observation [ ] was that treatment with HNO donors NCA and AS had distinct effects on the myofilaments". Gao and colleagues (2012) had detected the oxidation of actin and tropomyosin in response to NCA, but not after incubation with AS. This finding had suggested the formation of a disulfide-linked actin-tropomyosin heterodimer that could explain differences determined in NCA- and AS-mediated effects on myofilament Ca^{2+} sensitivity (Dai et al. 2007; Gao et al. 2012).

The data presented in this PhD thesis highlight considerably different effects elicited by the HNO donors NCA, AS and CXL-1020. NCA induced reproducible phosphorylation of cMyBP-C and PLN, but only minor phosphorylation levels were occasionally observed with CXL-1020 (see Figs. 14, 38, 41 and 43). For AS, no alteration in protein phosphorylation was detected. Dimerization of PKA-RI and PKGIα was induced by both NCA and CXL-1020 (see Figs. 19 and 41), but only NCA additionally mediated the formation of PKGIα intradisulfide bonds (see Fig. 38). Cysteine oxidation of PKA-C and B56α was detected after exposure to NCA and AS, while CXL-1020 had no effect (see Fig. 29). In contrast, inhibition of recombinant PP2A-C was not determined for NCA, but was found to be exclusive to CXL-1020 (see Figs. 32). Finally, the contractility of single ARVMs was impaired by NCA, but displayed the expected enhancement with CXL-1020 (see Figs. 33-35). The molecular observations obtained for NCA and CXL-1020 are summarized in table 1.

Table 1: Summary of effects observed in response to NCA and CXL-1020 Inhibition of PP2A was analyzed using recombinant PP2A-C. All other listed effects were investigated in ARVMs. +: positive effect, (+): minor effect, -: no effect, +/-: transient increase with subsequent impairment

Molecular observation	NCA	CXL-1020
Phosphorylation	+	(+)
PKA-RI dimer formation	+	+
PKGIα dimer formation	+	+
PKGIα intradisulfide formation	+	-
Oxidation of PKA-C and B56α	+	-
PP2A-C inhibition	-	+
Contractility	+/-	+

Differences in biological effects that exist between HNO donor compounds may involve different compound concentrations and HNO-release kinetics. While a compound with a long $t_{1/2}$ leads to continuous exposure to low concentrations of HNO, a short $t_{1/2}$ is associated with a sudden bolus release, which also implies a high degree of HNO inactivation via dimerization and dehydration (Shafirovich and Lymar 2002). Additionally, a quick release of HNO might convert neighboring reactive thiol groups into the N-hydroxysulfenamide intermediate state (Wong et al. 1998) and prevent their interaction with each other. As a result of different HNO concentrations and thiol accessibility, it can be assumed that a redox-sensitive thiol group that forms a disulfide bond when exposed to one donor compound is not necessarily modified upon incubation with another. The concentrations and incubation times selected for ARVM-treatment in this study considered the different release kinetics of the applied HNO donor compounds. The conditions used for NCA (100 µmol/L, 30 min) and AS (500 µmol/L, 15 min) had been determined in previous studies by our group (Donzelli et al. 2017) and were comparable to those applied in other publications involving NCA and AS (Lancel et al. 2009; El-Armouche et al. 2010). For CXL-1020, treatment conditions (300 µmol/L, 15 min) were adapted from Sabbah et al. (2013) and both time course and concentration curve experiments confirmed the suitability of the treatment conditions (see Fig. 43). With $t_{1/2}$ values of 2.3 (Maragos et al. 1991) and 1.9 min (Sabbah et al. 2013), respectively, AS and CXL-1020 led to a considerably faster bolus release of HNO compared to NCA ($t_{1/2}$ 800-890 min; Sha et al. 2006). Although the quick release by AS and CXL-1020 is expected to involve dimerization- and dehydration-mediated inactivation of HNO, this indicates that ARVMs were exposed to higher concentrations of HNO during treatment with AS and CXL-1020 than during incubation with NCA. It cannot be excluded that increased exposure to HNO in response to AS and CXL-1020 could elicit additional events that might prevent the occurrence of certain cellular effects that were observed with NCA. However, also considering that all HNO donors led to the enhanced formation of PKA-RI dimers (see Fig. 19), NCA-effects to be absent in response to AS and CXL-1020 was most likely not a result of insufficient HNO-release.

Another possible explanation for the observed differences might be the release of by-products that have distinct signaling properties such as NO or nitrite, whose generation has been described for NCA at low levels (Sha et al. 2006). However, the decomposition of AS also generates substantial amounts of nitrite (Bonner and Ravid 1975), which again is thought to serve as a storage pool for NO (Dejam et al. 2004). Although CXL-1020 was described as a pure donor that directly decomposes into HNO and an inactive scaffold (Sabbah et al. 2013), unpublished observations suggest that also CXL-1020 might release low amounts of NO. Nitrite and NO can affect cellular responses (Dejam et al. 2004), for example by the induction of PTMs such as S-nitrosylation (Broillet 1999; Hess et al. 2005), which in turn has been proposed to represent a transient intermediate in the formation of disulfide bonds (Wolhuter et al. 2018). Additionally, NO is a potent activator of sGC and induces the generation of cGMP (Russwurm and Koesling 2004). However, contractile effects in response to AS and CXL-1020 were shown to be sGC-independent (Tocchetti et al. 2007; Zhu et al. 2015) and since its release of NO and nitrite is marginal, the same can be assumed for NCA. As NCA, AS and potentially CXL-1020 seem to generate minor levels of related by-products, this property is unlikely to explain the considerably different biological effects that are elicited by the HNO donor compounds. Moreover, DIA, an agent that solely acts via the introduction of disulfide bonds, induced the activation of PKA and PKA substrate phosphorylation like NCA (see Figs. 14 and 15). This strongly confirms the hypothesis that the NCA-response relies on thiol oxidation and, in accordance with the perception in the literature, renders the hypothesis of by-product-effects inconclusive.

A repeated matter of discussion is the ability of NCA to directly interact with target thiols without the release of HNO. Shoman et al. (2011) suggested the direct addition of a thiolate to the nitroso group of acyloxy nitroso compounds like NCA, finally resulting in the formation of a disulfide without the generation of HNO. This mechanism would explain the unexpectedly fast effects, which the slow HNO donor NCA displayed when RI dimer formation, FRET and ARVM contractility were determined (see Figs. 15, 19 and 33-34). The ability of NCA to directly interact with thiols might result in the oxidative modification of different cellular targets, as it does not rely on unstable HNO that in addition can be scavenged by GSH. However, the distinction between direct and HNO-mediated effects of NCA is especially difficult because both mechanisms generate the same reaction products. The hydrolysis of NCA results in the generation of HNO and cyclohexanone and the subsequent reaction of HNO with a thiolate produces the N-hydroxysulfenamide intermediate, which further reacts with a second thiol to form a disulfide and hydroxylamine. Hydroxylamine, again, can react with cyclohexanone to produce cyclohexanone oxime. The same final products, a disulfide and cyclohexanone oxime, would result from the supposed direct NCA-mediated disulfide formation. In contradiction to the theory of the HNO-independent mechanism for NCA, El-Armouche et al. (2010) and Gao

et al. (2012) had observed enhanced contractility of single cardiac myocytes or isolated cardiac muscle, respectively, in response to NCA but not upon exposure to chemically related non-HNO-releasing molecules. Thus, the property of NCA to induce disulfide bonds by this non-hydrolytic mechanism might occur but requires further elucidation.

Taken together, it is unlikely that the different effects elicited by NCA, AS and CXL-1020 are explained by different HNO-release kinetics or by-products. However, the finding that despite a $t_{1/2}$ of about 15 h, NCA-mediated effects are apparent within a few minutes of treatment, suggests a molecular mechanism of action for NCA that involves the direct interaction with thiol groups. But whichever way, by some means NCA clearly appears to exert an oxidizing capacity towards thiol groups that is superior to that elicited by AS and CXL-1020. The presented results highlight that different HNO donors can exert highly divergent biological effects. Consequently, findings obtained from one donor cannot be simply transferred to another HNO-releasing compound but require thorough revision. The need for careful and extensive characterization of HNO donor compounds is especially emphasized by the effort that is made to realize their clinical application in humans to treat heart failure.

The findings obtained during this PhD study for the first time provide evidence for the involvement of HNO donor compounds in the regulation of cardiac myocyte protein kinase and phosphatase balance. NCA induces the oxidation of PKA and PP2A subunits, which is associated with protein translocation and the phosphorylation of PKA substrate proteins. Via the inhibition of PP2A-C and potential involvement of PKGIα signaling, CXL-1020 is likely to affect the phosphorylation status of PLN, cMyBP-C or other yet unidentified proteins. Although the molecular background requires further research, both donor molecules displayed novel mechanisms of action, which presumably participate in the contractile response elicited by either compound and consequently need to be considered in the further development of HNO donors intended for clinical use. Moreover, the results presented in this thesis highlight the major differences that exist between HNO donor compounds and demonstrate that triggered cellular responses cannot simply be accounted to HNO, but appear to involve compound-dependent effects apart from HNO-release. Thus, the data provided here improve the understanding of the molecular mechanisms that underlie the biological effects of HNO donor compounds and contribute to their progression towards a safer and targeted therapy for heart failure patients.

4.2 Characterization of Ser250 as a putative cMyBP-C phosphorylation site

The phosphorylation of cMyBP-C within its N-terminal M-motif represents a critical regulatory mechanism for unimpaired cardiac function. It is apparent that oxidative S-glutathiolation of

cMyBP-C interferes with M-motif phosphorylation and has the potential to negatively affect cardiac function in health and disease (Stathopoulou et al. 2016). The results provided here describe the investigation of a potential novel N-terminal phosphorylation site of cMyBP-C, which was identified at Ser250 in human ventricular tissue. Mass spectrometry analysis detected phosphorylation of Ser250 mutually exclusive with S-glutathiolation of the main N-terminal acceptor site at Cys249, suggesting a role of Ser250 in the regulation of oxidant-susceptibility of cMyBP-C. *In vitro* kinase assays using N-terminal C1-M-C2 mutant proteins of cMyBP-C suggested the inability of PKA, PKCε, PKGIα, PKD, CaMKII, RSK2, GSK3β, ROCK1, ROCK2, GRK2 and GRK5 to phosphorylate Ser250. The characterization of an antibody specifically targeting phosphorylated Ser250 showed successful detection of Ser250-phosphomimetic C1-M-C2 proteins and confirmed the absence of cross-reactivity with M-motif phosphorylation sites. In ARVM lysates H_2O_2, DIA, ISO, PE and ET did not generate a reproducible enhancement of pSer250 signal intensities, suggesting that a protein kinase catalyzing Ser250 phosphorylation was not activated in response to these stimuli. However, the emergence of unspecific bands in Western immunoblots and nuclear fluorescence detected in ARVMs following application of the pSer250 antibody indicated undesired cross-reactivity. Further investigation is required to determine the suitability of the pSer250 antibody to investigate cMyBP-C phosphorylation at the respective site in cell lysates. Subsequently, the effort to characterize Ser250 phosphorylation and its impact on S-glutathiolation will expand the understanding of the crosstalk between oxidative and non-oxidative PTMs and oxidant-mediated cardiac myocyte function.

Fine-tuning of cardiac contraction is predominantly mediated via neurohumoral stimulation and the subsequent phosphorylation of cellular targets by protein kinases (Solaro 2008). A major component of this regulatory mechanism is the sarcomeric protein cMyBP-C, which limits actomyosin interaction in the unphosphorylated state, but allows unperturbed contraction upon phosphorylation at N-terminal M-motif sites (Gruen et al. 1999). The critical role of cMyBP-C phosphorylation is emphasized by impaired cardiac function that has been reported upon replacement of cMyBP-C phosphorylation sites (Gupta and Robbins 2014). Moreover, cMyBP-C mutations that result in abnormal or truncated proteins are a major contributor to the development of heart disease and associated with an increased risk of sudden cardiac death (Teirlinck et al. 2012; Carrier et al. 2015; Calore et al. 2015). Notably, the susceptibility of cMyBP-C for phosphorylation at its M-motif is reduced by oxidative S-glutathiolation (Stathopoulou et al. 2016). In diseased heart tissue of patients suffering from DCM or ICM, conditions which are commonly associated with increased oxidant load, elevated cMyBP-C S-glutathiolation negatively correlates with M-motif phosphorylation. In failing hearts, a similar decrease in overall phosphorylation of cMyBP-C was reported by different groups (El-

Armouche et al. 2007; Zaremba et al. 2007; Copeland et al. 2010). These data suggest the potential of S-glutathiolation to play a major role in the pathological alteration of cMyBP-C function and cardiac contractility by directly affecting the phosphorylation status of cMyBP-C. Despite the negative consequences that are attributed to S-glutathiolation of cMyBP-C in advanced and end-stage cardiac disease, under physiological conditions reversible S-glutathiolation is protective, as it prevents irreversible oxidative modification of proteins (Mallis et al. 2002; Dalle-Donne et al. 2009; Hill and Bhatnagar 2012). Moreover, protein S-glutathiolation is not restricted to situations of oxidative stress, but was also shown to exists under basal conditions and, therefore, is likely to represent a physiological regulatory mechanism (Hill and Bhatnagar 2012). Thus, basal S-glutathiolation of cMyBP-C might exert a cardioprotective role by reducing M-motif phosphorylation and, consequently, limiting actomyosin interaction and energy consumption.

4.2.1 Ser250 phosphorylation as a regulator of cMyBP-C S-glutathiolation

cMyBP-C phosphorylation at Ser275, Ser284 and Ser304 (referring to the human sequence) of the M-motif is well-described and regulates cardiac function by mediating the interaction between cMyBP-C and myosin S2 (Gautel et al. 1995; Gruen et al. 1999). By MS analysis, a novel potential phosphorylation site was detected at Ser250 of cMyBP-C located in the N-terminal C1 domain. Although the C1-domain might also participate in the phosphorylation-regulated myosin S2 binding, the immediate vicinity of Ser250 to the main S-glutathiolation acceptor site of the cMyBP-C N-terminus at Cys249 (Stathopoulou et al. 2016) suggested an additional distinct role for this novel phosphorylation site. By MS analysis, Ser250 phosphorylation was found mutually exclusive with Cys249 S-glutathiolation, suggesting a negative crosstalk to exist between these two covalent modifications. This hypothesis was in line with a negative impact of cMyBP-C S-glutathiolation on M-motif phosphorylation that had been reported before (Stathopoulou et al. 2016). In addition, exclusive detection of modified Ser250 in healthy donor tissue and not in DCM and ICM samples, matched with the previously determined correlation of reduced cMyBP-C phosphorylation levels with elevated S-glutathiolation in ventricular tissue from DCM and ICM patients (Stathopoulou et al. 2016). In DCM and ICM, disease progression is commonly paralleled by oxidative stress (Dewald et al. 2003; Giordano 2005; Sugamura and Keaney 2011). Thus, reduced Ser250 phosphorylation in the diseased tissue might result from an interference with a ROS-mediated increase in S-glutathiolation or other irreversible oxidative PTMs and supports the hypothesis of a negative crosstalk. Within the C1 domain, crystallography revealed Ser250 to be located at the protein surface, allowing access of protein kinases (Govada et al. 2008).

Since S-glutathiolation refers to the addition of GSH, a modified tripeptide, a sterical hindrance that restricts access for protein kinases to phosphorylate Ser250 would provide an explanation for how S-glutathiolation of Cys249 could hinder Ser250 phosphorylation. *Vice versa*, a sterical

hindrance through Ser250 phosphorylation is unlikely to cause the interference with Cys249 S-glutathiolation. More probable is a mechanism that involves Cys249 reactivity. Oxidative PTMs like S-glutathiolation preferably occur at deprotonated thiolates. The presence of basic histidine, lysine or arginine amino acids in the microenvironment of a cysteine residue substantially lowers its pK_a and stabilizes the more reactive thiolate state (Hill and Bhatnagar 2012; Rudyk and Eaton 2014). Negative charges in proximity to the cysteine amino acid, however, tend to increase the pK_a (Chung et al. 2013). Consequently, the negative charge introduced by phosphorylation at Ser250 is likely to reduce the susceptibility of Cys249 for oxidative S-glutathiolation and, in this way, might protect from the functional consequences associated with oxidative modification. The potential of such interplay between oxidative and non-oxidative PTMs to mediate alterations in protein function is emphasized by a crosstalk of S-glutathiolation and phosphorylation that was reported for the catalytic subunit of PKA. The S-glutathiolation of PKA-C at Cys199 was shown to induce the dephosphorylation of functionally important proximate Thr197, thereby contributing to the inhibition of the enzyme (Humphries et al. 2002, 2005). The data encouraged further investigation of the role Ser250 phosphorylation might play in the regulation of Cys249 S-glutathiolation. The coordinated modification of these two residues might contribute to M-motif cMyBP-C phosphorylation, which in turn is essential for unimpaired cardiac contractility. Moreover, Cys/Ser motifs might represent a regulatory feature acting like a PTM switch to modulate protein function and require further elucidation.

4.2.2   Major cardiac protein kinases do not target Ser250 in C1-M-C2 proteins

For the investigation of a protein phosphorylation site and its physiological importance, identification of the protein kinase responsible for the phosphorylation is essential. Knowledge regarding the enzyme that is able to catalyze the phosphorylation allows directed induction or inhibition of the modification of interest, the analysis of resulting cellular responses and their classification into the cellular context. Concerning Ser250 of cMyBP-C, the impact of phosphorylation on cMyBP-C S-glutathiolation and functional consequences on cardiac myocyte contractility were of major interest. To identify a protein kinase that has the ability to phosphorylate Ser250, C1-M-C2 proteins carrying various mutations were applied. Such proteins that consist of the N-terminal cMyBP-C domains are commonly used in experiments that aim to investigate PTMs and protein-protein interactions of the cMyBP-C M-motif and the adjacent C1 and C2 domains *in vitro* (Gruen and Gautel 1999; Sadayappan et al. 2011; Cuello et al. 2011; Stathopoulou et al. 2016). Despite representing solely a small proportion of a large multimodular protein, recombinantly expressed C1-M-C2 can be used to characterize the ability of protein kinases to phosphorylate individual M-motif sites and allow examinations with the use of phospho-specific antibodies. Probably due to the linear arrangement of the compact globular cMyBP-C domains (Hartzell and Sale 1985; Craig et al. 2014), C1-M-C2 proteins

suitably mimic the corresponding section of the endogenous protein. This is shown by examples like studies investigating the phosphorylation-dependent interaction between C1-M-C2 and myosin S2 (Gruen et al. 1999). Mutations in myosin S2, which have been associated with familial hypertrophic cardiomyopathy, were shown to reduce the affinity for C1-M-C2 protein and thus provided a mechanistic explanation for the pathological outcome of these genetic defects (Gruen and Gautel 1999).

As expected, the C1-M-C2 WT protein was substantially phosphorylated by PKA, PKCε, PKGIα, PKD, CaMKII, RSK2 and ROCK2 in *in vitro* kinase assays. For these protein kinases, the ability to phosphorylate at least one of the M-motif sites of cMyBP-C had been reported previously (Jeacocke and England 1980; Schlender and Bean 1991; Vahebi et al. 2005; Bardswell et al. 2010; Sadayappan et al. 2011; Cuello et al. 2011; Thoonen et al. 2015). The observed phosphorylation of C1-M-C2 WT by ROCK1 and GRK5, to our knowledge, has not been reported before and suggested cMyBP-C to represent a previously undescribed substrate. For GSK3β, phosphorylation of cMyBP-C at Ser133 in the PA linker region was described (Kuster et al. 2013). Consistent with the lack of this part of the protein in C1-M-C2 fragments, no phosphorylation was detected by GSK3β. Of the protein kinases tested, solely for PKD the potential to phosphorylate Ser250 was suggested by initial *in vitro* kinase experiments. Nonetheless, unchanged phosphorylation signals obtained with a protein that lacked Ser250 implied that also PKD in this experimental setting was unable to phosphorylate cMyBP-C at the novel site.

In the same experiment, the replacement of the PKD substrate site Ser304 (Bardswell et al. 2010) in C1-M-C2 led to a significantly diminished signal intensity as expected, but a residual signal remained in the Ser304Ala mutant, which was abrogated in the 5Ala protein (see Fig. 51). This further reduction in signal intensity suggested one of the remaining mutated sites, Ser275, Ser284 or Ser311, to be phosphorylated in addition to Ser304. The use of phospho-specific antibodies, however, demonstrated that Ser275 and Ser284 were not modified by PKD (see Fig. 50), while an involvement of Ser311 was excluded in an additional radioactive *in vitro* kinase assay using a Ser311Ala mutant protein (data not shown). As the remaining signal detected in Ser304Ala could not be assigned to any of the phosphorylation sites, a potential contribution of Ser250 phosphorylation could eventually not be ruled out.

4.2.3 The pSer250 antibody: A reliable tool?

In vitro kinase experiments with C1-M-C2 mutant proteins discussed above excluded numerous potential candidate protein kinases for Ser250 phosphorylation. However, with increasing number, the introduction of mutations to these C1-M-C2 proteins might ultimately induce structural alterations and consequently affect protein kinase-mediated phosphorylation. Moreover, *in vitro* phosphorylation of a C1-M-C2 protein can give a strong indication for a protein kinase to interact with cMyBP-C. But whether this event actually occurs in a cellular or

organ context underlies numerous regulatory processes that determine the spatiotemporal activity of protein kinases, which cannot be predicted using *in vitro* experiments. To avoid such false-positive results and enable the investigation of endogenous Ser250 phosphorylation, an antibody with specificity for phosphorylated Ser250 and the surrounding amino acids of cMyBP-C (pSer250) was generated. Phospho-specific antibodies have been successfully applied for the investigation of M-motif cMyBP-C phosphorylation sites in the past and contributed markedly to the understanding of cMyBP-C function (El-Armouche et al. 2007; Copeland et al. 2010; Cuello et al. 2011; Stathopoulou et al. 2016). Application of the pSer250 antibody, however, has not yet allowed the identification of a protein kinase that induces Ser250 phosphorylation.

The pSer250 antibody, which was raised against a short 13 amino acid peptide sequence, successfully detected phosphomimetic C1-M-C2 proteins in Western immunoblots (see Figs. 53 and 54). As discussed above, cMyBP-C has a linear architecture, which limits interactions between the compact domains (Hartzell and Sale 1985; Craig et al. 2014). Therefore, an antibody that can interact with a C1-M-C2 fragment is likely to also allow detection of the endogenous full-length protein. However, whether the immunoblot signal that was produced by the pSer250 antibody at the corresponding molecular weight of cMyBP-C (150 kDa) in ARVM samples actually represents the Ser250-phosphorylated protein remains questionable. Generally, the intensities of bands migrating at 150 kDa that were generated upon application of the pSer250 antibody displayed no considerable difference between stimulated cardiac myocytes and control samples. The exposure of ARVMs to H_2O_2 had induced S-glutathiolation of Cys249 in initial experiments (Stathopoulou et al. 2016) and this modification was detected mutually exclusive with Ser250 phosphorylation in MS data (see Figs. 46 and 47). Thus, ARVM-treatment with H_2O_2 was assumed to potentially reduce Ser250 phosphorylation. Although cMyBP-C S-glutathiolation following exposure to H_2O_2 was not analyzed in this experiment, the unaltered pSer250 antibody signals suggested that band intensities might not represent the phosphorylation status at Ser250. The thiol-oxidizing agent DIA induces protein disulfide bonds (Kosower et al. 1969), but was also shown to activate PKA (see Fig. 15). ISO as well acts mainly via PKA (Madamanchi 2007), while PE and ET activate PKC and downstream kinases like PKD and members of the Ras/Raf/MEK/ERK pathway (Xiao et al. 2001; Sugden 2003; Bossuyt et al. 2011; O'Connell et al. 2013). Together, these stimuli covered the activation of several prominent signaling pathways in cardiac myocytes, but none of the interventions resulted in reproducible alterations in pSer250 signal intensities. Although it is possible that Ser250 phosphorylation is mediated by another protein kinase, which was not activated by any of the interventions, this result might also indicate the inability of the pSer250 antibody to visualize changes in Ser250 modification.

Another observation that questioned pSer250 antibody specificity for the respective modification of cMyBP-C was the cross-reactivity with additional proteins that was demonstrated by several additional signals in Western immunoblots. The most pronounced band that was reproducibly detected at a molecular weight of approx. 220 kDa might arise from cross-detection of the thick filament protein myosin heavy chain, which is regularly observed on Coomassie-stained membranes (see Fig. 55). Cross-reactivity could not be reduced by dilution of the antibody and indicated the affinity for additional proteins to exceed its affinity for cMyBP-C. This apparent low specificity for the pSer250 modification raised further doubts, whether the band migrating at 150 kDa actually corresponded to cMyBP-C. Within the N-terminal C1 domain, Ser250 is located at the protein surface (Govada et al. 2008) and the N-terminus of cMyBP-C extends into the space between thick and thin filaments of the sarcomere (Moolman-Smook et al. 2002; Kulikovskaya et al. 2003; Squire et al. 2003). However, despite the suggested antibody accessibility, none of the characteristic cMyBP-C myofilament striations were generated by the pSer250 antibody in immunofluorescence-labeled ARVMs. The absence of myofilament signals might be explained by the inability of the antibody to detect basally unmodified cMyBP-C. Moreover, unlike Western immunoblotting, where denatured proteins are detected, fixation of cells with paraformaldehyde (PFA) for immunofluorescence applications largely maintains protein structure (Mason and O'Leary 1991; Thavarajah et al. 2012). It is therefore not surprising that antibodies that work well in immunoblot applications are often not suitable to detect the target protein in fixed cells. Nonetheless, the pronounced pSer250 antibody-mediated fluorescence of ARVM nuclei is in line with the unspecific binding observed in Western immunoblots and argues for antibody cross-reactivity with nuclear components. Taken together, there are reasonable doubts that the signal migrating at 150 kDa, which is generated by the pSer250 antibody, is reliably representative for cMyBP-C phosphorylation at Ser250.

Various explanations are conceivable for the deficit of the pSer250 antibody to properly detect the corresponding modification of cMyBP-C. Besides phosphorylation, cMyBP-C is subject to several other PTMs and some of them occur at the C1 domain. These include acetylation, which has been reported at four sites within the C1 domain (Govindan et al. 2012). Protein acetylation also takes place in prokaryotes (Jones and O'Connor 2011), but it can be assumed that bacterially produced C1-M-C2 is differently modified than endogenous cMyBP-C of cardiac myocytes. Although acetyl groups are small, an impact of cMyBP-C acetylation on pSer250 antibody binding cannot be fully ruled out. CMyBP-C can be S-glutathiolated at Cys249 (Stathopoulou et al. 2016), which, as discussed above, is expected to interfere with Ser250 phosphorylation, but might also spatially obstruct pSer250 detection by the antibody. However, S-glutathiolation mainly occurs when enhanced levels of oxidized GSSG are formed, which is only expected to occur under conditions of enhanced oxidant load (Forman et al. 2009;

Hill and Bhatnagar 2012). Moreover, maintained pSer250 signals after ARVM treatment with S-glutathiolation-inducing H_2O_2 suggested no considerable influence on antibody binding (see Fig. 53 and 55). The latter assumption applies only if the produced signals actually refer to Ser250-phosphorylated cMyBP-C. A key factor contributing to the inability of the pSer250 antibody to detect the corresponding cMyBP-C modification is most likely cross-reactivity. The generation of many additional intense bands indicates a considerable degree of antibody to be scavenged by these unspecific interactions. As mentioned above, the pronounced signal migrating at 220 kDa might represent myosin heavy chain, which is a component of the thick filaments like cMyBP-C. An increased affinity of the antibody for myosin heavy chain might intercept pSer250 antibody in the vicinity to cMyBP-C, thus preventing cMyBP-C detection.

Another simple explanation for the difficulties in detecting cMyBP-C Ser250 phosphorylation may be the fact that this modification ultimately might not exist in ARVMs or in general. An indication that speaks against Ser250 as a phosphorylation site is the surrounding amino acid sequence. Initial *in silico* analysis had shown that Ser250 does not provide a typical consensus sequence for known protein kinases. However, the mass increment that was detected in human and mouse cardiac tissue samples by MS matched with protein phosphorylation (see Figs. 46 and 47). Moreover, the modification was identified in a number of MS approaches using different thiol-blocking reagents and peptide generation by different proteases. The detection of a characteristic neutral loss of mass in fragments containing Ser250 (or corresponding Ser247 in mouse) further argued for phosphorylation to exist at this site. On the other hand, phosphorylation of Ser250 was not identified in a second series of human samples (data not shown). Furthermore, another less common PTM exists that can induce a similar increase in mass and may mimic phosphorylation. While phosphorylation adds 79.9663 Da to a peptide, rarely studied O-sulfonation induces a mass addition of 79.9568 Da (Medzihradszky et al. 2004). Thus, only re-measuring of samples with high-resolution MS may allow to distinguish between these two modifications. In conclusion, the MS data are highly supportive of Ser250 being a phosphorylation site but must be confirmed, since a false-positive result cannot be excluded at this moment in time.

In contrast to the pSer250 antibody, its modification-unspecific counterpart allowed the detection of endogenous cMyBP-C in ARVMs by Western immunoblotting and immunofluorescence labeling (see Figs. 58 and 60). Since cross-reactivity signals were neglectable, this antibody proved to be suitable for further application in Western immunoblot and immunofluorescence applications.

The observed alternation of Ser250 phosphorylation and Cys249 S-glutathiolation and the enhanced detectability of pSer250 in healthy *vs.* diseased tissue determined by MS is in line with the previously described crosstalk between S-glutathiolation and phosphorylation of

cMyBP-C. As these findings suggested Ser250 and Cys249 to represent a regulatory switch that might control cMyBP-C function, the need for pursuing research was obvious. The data presented here show that the endeavor to identify a protein kinase for Ser250 phosphorylation has not yet succeeded. Although the collected data argue for the exclusion of many protein kinases, it remains unanswered, whether the custom-made antibody allows the detection of Ser250 phosphorylation in cardiac myocytes. With improved tools, further investigation will reveal the significance of cMyBP-C Ser250 phosphorylation for Cys249 S-glutathiolation and ultimately determine the impact of differentially modified Ser/Cys motif on cMyBP-C and cardiac myocyte function. The resulting findings may provide new insight regarding the regulatory aspects of a PTM interplay and its potential to regulate signal transduction.

5 Materials and methods

5.1 Materials

5.1.1 Antibodies and reagents for Western immunoblotting, immunofluorescence staining and proximity ligation assay (PLA)

Primary labeling antibodies for Western immunoblotting

Reactivity	Host	Working dilution	Supplier
Anti-B56α, monoclonal	Mouse	1:2000	BD Biosciences (San Jose, USA)
Anti-cMyBP-C, polyclonal	Rabbit	1:2000	Santa Cruz (Dallas, USA)
Anti-cTnI, polyclonal	Rabbit	1:1000	Cell Signaling Technology (Danvers, USA)
Anti-GAPDH monoclonal	Mouse	1:1000	HyTest (Turku, Finland)
Anti-GSH	Mouse	1:1000, Pierce® Protein-Free T20 (TBS) Blocking Buffer	ViroGen (Watertown, USA)
Anti-His (G-18), polyclonal	Rabbit	1:500	Santa Cruz (Dallas, USA)
Anti-His (H-3), monoclonal	Mouse	1:500	Santa Cruz (Dallas, USA)
Anti-NKA subunit α-1, monoclonal	Mouse	1:2000	Merck Millipore (Billerica, USA)
Anti-PKA-C, monoclonal	Mouse	1:1000	BD Biosciences (San Jose, USA)
Anti-PKA-RI, monoclonal	Mouse	1:1000, 5% milk/TBST	BD Biosciences (San Jose, USA)
Anti-PKGI, polyclonal	Rabbit	1:1000	Enzo Life Sciences (Farmingdale, USA)

Anti-PP2A-C (demethylated), monoclonal	Mouse	1:200	Santa Cruz (Dallas, USA)
Anti-pSer16 PLN, polyclonal	Rabbit	1:2000	Badrilla (Leeds, UK)
Anti-pSer250 cMyBP-C, polyclonal	Rabbit	1:1000 – 1:10 000, 1% BSA/TBST or 1% milk/TBST	Eurogentec (Seraing, Belgium)
Anti-pSer275 cMyBP-C	Rabbit	1:1000	Kind gift of S. Sadayappan (University of Cincinnati, USA)
Anti-pSer284 cMyBP-C	Rabbit	1:2000	Enzo Life Sciences (Farmingdale, USA)
Anti-pSer304 cMyBP-C	Rabbit	1:1000	Kind gift of S. Sadayappan (University of Cincinnati, USA)
Anti-Ser250 cMyBP-C (unspecific), polyclonal	Rabbit	1:10 000 – 1:50 000, 1% BSA/TBST	Eurogentec (Seraing, Belgium)
Anti-α-actinin, monoclonal	Mouse	1:1000	Sigma-Aldrich (St. Louis, USA)

Antibody dilutions were prepared in 1% milk/TBST, if not stated otherwise.

Secondary labeling antibodies and reagents for Western immunoblotting

Reactivity	Host	Working dilution	Supplier
ECL™ Anti-mouse IgG, HRP linked whole antibody	Sheep	1:2000	GE Healthcare (Chicago, USA)
ECL™ Anti-rabbit IgG, HRP linked whole antibody	Donkey	1:2000	GE Healthcare (Chicago, USA)
ECL™Anti-rabbit IgG, HRP linked F(ab')$_2$ fragment	Donkey	1:2000	GE Healthcare (Chicago, USA)
Pierce® High Sensitivity Streptavidin-HRP	-	1:10 000	Thermo-Fisher Scientific (Waltham, USA)

Secondary antibodies were prepared in the same solution used for primary antibody dilution.

Primary antibodies for immunofluorescence staining and PLA

Reactivity	Host	Working dilution	Supplier
Anti-B56α, monoclonal	Mouse	1:100	BD Biosciences (San Jose, USA)
Anti-cMyBP-C, polyclonal	Rabbit	1:100	Santa Cruz (Dallas, USA)
Anti-MLC2v, (PLA only) polyclonal	Rabbit	1:100	Proteintech (Rosemont, USA)
Anti-PKA-RI, monoclonal	Mouse	1:100	BD Biosciences (San Jose, USA)
Anti-pSer250 cMyBP-C, polyclonal	Rabbit	1:100	Eurogentec (Seraing, Belgium)

Anti-Ser250 cMyBP-C (unspecific), polyclonal	Rabbit	1:200/1:500	Eurogentec (Seraing, Belgium)
Anti-α-actinin, monoclonal	Mouse	1:200	Sigma-Aldrich (St. Louis, USA)
Anti-α-actinin, (PLA only) polyclonal	Rabbit	1:800	Sigma-Aldrich (St. Louis, USA)

Primary antibodies for immunofluorescence staining were diluted in BSA/Gold buffer.

Secondary labeling antibodies and reagents for immunofluorescence staining

Reactivity	Host	Working dilution	Supplier
4′,6-Diamidino-2-phenylindole (DAPI)	-	1:100	Sigma-Aldrich (St. Louis, USA)
Alexa Fluor® 488 anti-mouse IgG	Goat	1:100	Thermo-Fisher Scientific (Waltham, USA)
Anti-mouse IgG1, Biotin-XX	Goat	1:500	Thermo-Fisher Scientific (Waltham, USA)
Anti-rabbit IgG: DyLight®549	Sheep	1:100	Bio-Rad (Hercules, USA)
Cy™2-conjugated Streptavidin	-	1:2000	Jackson ImmunoResearch (West Grove, USA)

Secondary antibodies and reagents for immunofluorescence staining were diluted in BSA/Gold buffer.

5.1.2 Bacteria

E. coli strain	Supplier
One Shot® BL21 Star™ (DE3) Chemically Competent Cells	Thermo-Fisher Scientific (Waltham, USA)
Subcloning Efficiency™ DH5α™	Thermo-Fisher Scientific (Waltham, USA)
XL10-Gold® Ultracompetent Cells (as component of the QuikChange II XL Site-Directed Mutagenesis Kit)	Agilent Technologies (Santa Clara, USA)

5.1.3 Chemicals

Substance	Supplier
(±)-Carnitine hydrochloride	Sigma-Aldrich (St. Louis, USA)
[γ-^{32}P] Adenosine 5'-triphosphate (γ-^{32}P-ATP)	Hartmann Analytic (Braunschweig, Germany)
1, 4-Dithiothreitol (DTT)	Roth (Arlesheim, Germany)
2,3-Butanedione monoxime (BDM)	Sigma-Aldrich (St. Louis, USA)
2-Propanol	Merck Millipore (Billerica, USA)
30% Acrylamide/Bis Solution 37.5:1	Bio-Rad (Hercules, USA)
6,8-Difluoro-4-methylumbelliferyl phosphate (DiFMUP)	Endotherm (Saarbrücken, Germany)
Acetic acid (glacial) 100%	Merck Millipore (Billerica, USA)
Acetone	Th. Geyer (Renningen, Germany)
Acetonitrile	Th. Geyer (Renningen, Germany)
Adenosine 5'-triphosphate (ATP) 10 mM	Merck Millipore (Billerica, USA)

Adenosine 5'-triphosphate (ATP) 10 mM	New England BioLabs (Ipswich, USA)
Agarose UltraPure™	Thermo-Fisher Scientific (Waltham, USA)
Ammonium bicarbonate (NH_4HCO_3)	Honeywell (Morristown, USA)
Ammonium persulfate (APS)	Bio-Rad (Hercules, USA)
Ammonium sulfate ((NH_4)$_2SO_4$)	Merck Millipore (Billerica, USA)
Ampicillin trihydrate	SERVA Electrophoresis (Heidelberg, Germany)
Bacto™ Agar	BD Biosciences (San Jose, USA)
Bacto™ Tryptone	BD Biosciences (San Jose, USA)
Bacto™ Yeast Extract	BD Biosciences (San Jose, USA)
Biotin	Sigma-Aldrich (St. Louis, USA)
Bovine serum albumin (BSA)	Sigma-Aldrich (St. Louis, USA)
Bromophenol blue	Bio-Rad (Hercules, USA)
$CaCl_2$ (20 mM) 10X	New England BioLabs (Ipswich, USA)
Calcium chloride dihydrate ($CaCl_2 \cdot 2 H_2O$)	Merck (Darmstadt, Germany)
Calmodulin (12 µM) 10X	New England BioLabs (Ipswich, USA)
Carbon dioxide (CO_2)	SOL Deutschland (Krefeld, Germany)
Coomassie Brilliant Blue R-250 / G-250	Bio-Rad (Hercules, USA)
Creatine	Sigma-Aldrich (St. Louis, USA)
D(+)-Glucose	Roth (Arlesheim, Germany)
Digitonin	Merck Millipore (Billerica, USA)
di-Sodium hydrogen phosphate dihydrate ($Na_2HPO_4 \cdot 2 H_2O$)	Merck Millipore (Billerica, USA)
Ethidium bromide	Sigma-Aldrich (St. Louis, USA)
Ethylene glycol bis-(β-aminoethyl ether) N,N,N′,N′-tetraacetic acid (EGTA)	Sigma-Aldrich (St. Louis, USA)
Ethylenediaminetetraacetic acid (EDTA) disodium salt dihydrate	Roth (Arlesheim, Germany)
EZ-Link® Maleimide-PEG$_2$-Biotin	Thermo-Fisher Scientific (Waltham, USA)
Formic acid	Roth (Arlesheim, Germany)
Gelatin solution	Sigma-Aldrich (St. Louis, USA)
Glycerol	Merck Millipore (Billerica, USA)
Glycine PUFFERAN®	Roth (Arlesheim, Germany)
HEPES PUFFERAN®	Roth (Arlesheim, Germany)
Hydrochloric acid (HCl)fuming 37%	Merck Millipore (Billerica, USA)
Imidazole	Merck (Darmstadt, Germany)
Isopropyl β-D-1-thiogalactopyranoside (IPTG), dioxane-free	Thermo-Fisher Scientific (Waltham, USA)
Ivabradine hydrochloride	Sigma-Aldrich (St. Louis, USA)
Laminin from Engelbreth-Holm-Swarm murine sarcoma basement membrane	Sigma-Aldrich (St. Louis, USA)
Magnesium chloride hexahydrate ($MgCl_2 \cdot 6H_2O$)	Sigma-Aldrich (St. Louis, USA)
Magnesium sulfate heptahydrate ($MgSO_4 \cdot 7 H_2O$)	Merck (Darmstadt, Germany)
Maleimide	Sigma-Aldrich (St. Louis, USA)

Methanol	Avantor Performance Materials (Center Valley, USA)
Methoxypolyethylene glycol (PEG) maleimide (MW: 5 kDa)	Sigma-Aldrich (St. Louis, USA)
N,N,N′,N′-Tetramethylethylenediamine (TEMED)	Bio-Rad (Hercules, USA)
NEBuffer™ for Protein Kinases (PK) 10X	New England BioLabs (Ipswich, USA)
N-Ethylmaleimide	Sigma-Aldrich (St. Louis, USA)
Nitrogen (N_2), liquid	SOL Deutschland (Krefeld, Germany)
Normal goat serum (NGS)	Sigma-Aldrich (St. Louis, USA)
N-Propyl gallate	Sigma-Aldrich (St. Louis, USA)
ortho-Phosphoric acid 85%	Merck Millipore (Billerica, USA)
Paraformaldehyde (PFA) 16% solution (methanol-free)	Agar Scientific (Stansted, UK)
PKC Lipid Activator	Merck Millipore (Billerica, USA)
Potassium chloride (KCl)	Merck (Darmstadt, Germany)
Potassium dihydrogen phosphate (KH_2PO_4)	Merck (Darmstadt, Germany)
Potassium hydrogen carbonate ($KHCO_3$)	Merck (Darmstadt, Germany)
Powdered milk	Roth (Arlesheim, Germany)
ProteaseMAX™ Surfactant, Trypsin Enhancer	Promega (Mannheim, Germany)
Sodium acetate ($C_2H_3NaO_2$)	Merck Millipore (Billerica, USA)
Sodium chloride (NaCl)	Avantor Performance Materials (Center Valley, USA)
Sodium deoxycholate monohydrate	Sigma-Aldrich (St. Louis, USA)
Sodium dihydrogen phosphate monohydrate ($NaH_2PO_4 \cdot H_2O$)	Merck (Darmstadt, Germany)
Sodium dodecyl sulfate (SDS) pellets	Roth (Arlesheim, Germany)
Sodium fluoride (NaF)	Sigma-Aldrich (St. Louis, USA)
Sodium hydrogen carbonate ($NaHCO_3$)	Merck Millipore (Billerica, USA)
Sodium hydroxyde (NaOH) solution 0.1 mol/L	Roth (Arlesheim, Germany)
Streptavidin Agarose Resin 50% slurry	Thermo-Fisher Scientific (Waltham, USA)
Taurine	Sigma-Aldrich (St. Louis, USA)
Thiourea	Sigma-Aldrich (St. Louis, USA)
Triton® X 100	Roth (Arlesheim, Germany)
Trizma® base	Sigma-Aldrich (St. Louis, USA)
Tween® 20	Sigma-Aldrich (St. Louis, USA)
Urea	ICN Biomedicals (Aurora, USA)
β-Mercaptoethanol	Sigma-Aldrich (St. Louis, USA)

5.1.4 Devices

Name	Manufacturer
accu-jet® pipette controller	BRAND (Wertheim, Germany)
Analytical balance Genius®	Sartorius (Göttingen, Germany)
Autoclave VARIOKLAV®	HP Medizintechnik (Oberschleißheim, Germany)

Benchtop incubator WS 60	JULABO (Seelbach, Germany)
Biological safety cabinet Herasafe™ HS 12 class II	Thermo-Fisher Scientific (Waltham, USA)
Bioruptor® Plus sonication device	Diagenode (Liège, Belgium)
Centrifuge 5415 D	Eppendorf (Hamburg, Germany)
Centrifuge 5415 R	Eppendorf (Hamburg, Germany)
Centrifuge Heraeus™ Biofuge fresco	Thermo-Fisher Scientific (Waltham, USA)
Centrifuge J2-21 with rotor JA-14	Beckman Coulter (Brea, USA)
ChemiDoc™ Imaging System	Bio-Rad (Hercules, USA)
CO_2 incubator Heracell™ 240	Thermo-Fisher Scientific (Waltham, USA)
Dry block heater Thermostat 5320	Eppendorf (Hamburg, Germany)
ECL Semi-Dry Transfer Unit TE 77	GE Healthcare (Chicago, USA)
EHT analysis instrument	EHT Technologies (Hamburg, Germany)
FRET setup: DV2 DualView emission splitting system Light source pE-100 (440 nm) DMI3000b inverted microscope with 40x objective optiMOS™ Camera	Photometrics (Tucson, USA) CoolLED (Andover, UK) Leica Camera (Wetzlar, Germany) QImaging (Surrey, Canada)
Gel dryer Model 583	Bio-Rad (Hercules, USA)
Heat block Dri-Block® DB-1	Techne (Staffordshire, UK)
Hot wire dish cutter	Custom-made by Bülent Aksehirlioglu
HPLC system Dionex UltiMate 3000	Thermo-Fisher Scientific (Waltham, USA)
Inclined orbital shaker Polymax 2040	Heidolph Instruments (Schwabach, Germany)
Incubator Shaker C25	Eppendorf (Hamburg, Germany)
Ion Source Nanospray Flex™	Thermo-Fisher Scientific (Waltham, USA)
Laboratory agitator RZR 1	Heidolph Instruments (Schwabach, Germany)
Mass spectrometer Q Exactive™ Plus Hybrid Quadrupole-Orbitrap™	Thermo-Fisher Scientific (Waltham, USA)
Microplate reader safire II	Tecan (Männedorf, Switzerland)
Microscope Axiovert 25	Carl Zeiss (Oberkochen, Germany)
Mini Rocker Shaker MR-1	Biosan (Riga, Latvia)
Mini-Shaker Model Kühner	B. Braun Melsungen (Melsungen, Germany)
PCR Thermal Cycler 2720	Thermo-Fisher Scientific (Waltham, USA)
pH meter	Mettler Toledo (Greifensee, Switzerland)
pipetus®-akku	Hirschmann Laborgeräte (Eberstadt, Germany)
Power source EC570-90	E-C Apparatus Corporation (St. Petersburg, USA)
PowerPac™ HC / Basic	Bio-Rad (Hercules, USA)
Precision balance Pioneer®	OHAUS (Parsippany, USA)
Rotating mixer RM 5	Ingenieurbüro CAT (Ballrechten-Dottingen, Germany)
Scanner CanoScan LiDE 60	Canon (Tokyo, Japan)

Single cell contractility setup: Fluorescence System Interface MyoCam-S Digital CCD Video Camera MyoPacer EP Field Stimulator	IonOptix (Westwood, USA)
C-Stim superfusion chamber system	Cell MicroControls (Norfolk, USA)
Spectrophotometer NanoDrop® ND-1000	Thermo-Fisher Scientific (Waltham, USA)
Spectrophotometer SmartSpec™ 3000	Bio-Rad (Hercules, USA)
Thermomixer comfort	Eppendorf (Hamburg, Germany)
TissueLyser	QIAGEN (Hilden, Germany)
Transilluminator UVStar	Biometra (Göttingen, Germany)
Ultracentrifuge Optima L-90K with rotor SW 32 Ti	Beckman Coulter (Brea, USA)
Ultrasonic homogenizer SONOPULS HD 2200	BANDELIN electronic (Berlin, Germany)
Variable mode imager Typhoon 9400	GE Healthcare (Chicago, USA)
Vortex shaker	Heidolph Instruments (Schwabach, Germany)
Water purification system Milli-Q	Merck Millipore (Billerica, USA)
Zeiss LSM 510 META	Carl Zeiss (Oberkochen, Germany)
Zeiss LSM 800	Carl Zeiss (Oberkochen, Germany)

5.1.5 Enzymes

Name	Source	Supplier
CaMKII	Rat; recombinant from Sf9 cells	New England BioLabs (Ipswich, USA)
Chymotrypsin, Sequencing Grade	Bovine pancreas	Promega (Mannheim, Germany)
Collagenase, Type 2	*C. histolyticum*	Worthington Biochemical Corporation (Lakewood, USA)
Difco™ Trypsin 250	n/a	BD Biosciences (San Jose, USA)
GRK2	n/a	Kind gift of K. Lorenz (Leibniz-Institute for Analytical Siences, Dortmund, Germany)
GRK5	n/a	
GSK3β	Rabbit skeletal muscle; recombinant from *E. coli*	New England BioLabs (Ipswich, USA)
PKA, catalytic subunit	Bovine heart	Merck Millipore (Billerica, USA)
PKCε	Human; recombinant from Sf21 cells	Merck Millipore (Billerica, USA)
PKCµ (PKD; full length)	Human; recombinant from Sf21 cells	Merck Millipore (Billerica, USA)
PKD catalytic domain (amino acids 519-918)	n/a; recombinant from Sf21 cells	Kind gift of P. Parker (Francis Crick Institute, London, UK)

122

PKG, Iα	Bovine lung	Merck Millipore (Billerica, USA)
PP2A C subunit	Human; recombinant from insect cells	Cayman Chemicals (Ann Arbor, USA)
ROCK1	Human; recombinant from Sf9 cells	SignalChem (Richmond, Canada)
ROCK2	Human; recombinant from Sf9 cells	SignalChem (Richmond, Canada)
RSK2	Human; recombinant from Sf21 cells	Merck Millipore (Billerica, USA)
Sequencing Grade Modified Trypsin	Pig	Promega (Mannheim, Germany)

5.1.6 Eukaryotic cells and tissues

Cell/tissue type	Source	Animal supplier
ARVMs	Male Wistar rats	Charles River Laboratories (Sulzfeld, Germany)
Hearts from WT mice	Black Swiss mice	Kindly provided by L. Carrier (University Medical Center Hamburg-Eppendorf, Germany)
NMVMs from *Mybpc3*-targeted knockout (KO) mice	C57BL/6J mice	
Ventricular tissue powder from WT and *Mybpc3*-targeted knockout (KO) mice	Male Black Swiss mice, 13 weeks of age	

Cell/tissue type	Source	Provided by
Human left ventricular myocardial tissue	Human patients	Kindly provided by T. Eschenhagen (University Medical Center Hamburg-Eppendorf, Germany)

5.1.7 Expendable materials

Name	Supplier
µClear black 96 well plate	Greiner Bio-One (Frickenhausen, Germany)
225 mL Graduated conical tube with cap	Corning Incorporated (Corning, USA)
4-15% Mini-Protean® TGX™ Precast Protein Gel	Bio-Rad (Hercules, USA)
AccuMarQ™ Pre-stained Molecular Weight Markers	Badrilla (Leeds, UK)
All-purpose glue	UHU (Bühl, Germany)
Amersham™ ECL™ / ECL Select™ Western Blotting Detection Reagents	GE Healthcare (Chicago, USA)
Amersham™ Hybond™ PVDF / Amersham™ Protran™ Nitrocellulose (NC) Blotting Membranes	GE Healthcare (Chicago, USA)
Amersham™ Hyperfilm™ ECL	GE Healthcare (Chicago, USA)
Assistent® Cover glass 25 mm Ø	Glaswarenfabrik Karl Hecht (Sondheim v. d. Rhön, Germany)

Assistent® Elka object slide	Glaswarenfabrik Karl Hecht (Sondheim v. d. Rhön, Germany)
Cell scraper 2-position blade	Sarstedt (Nümbrecht, Germany)
CELLSTAR® 6 well cell culture plate	Greiner Bio-One (Frickenhausen, Germany)
cOmplete™ Protease inhibitor cocktail tablet	Roche Diagnostics (Risch, Switzerland)
Comply™ Lead Free Steam Indicator Tape	3M Deutschland (Neuss, Germany)
Cotton bud	Meditrade (Kiefersfelden, Germany)
Cover glass 30 mm Ø	VWR International (Radnor, USA)
Cuvette	Sarstedt (Nümbrecht, Germany)
Dialysis tubing visking, cellulose	Roth (Arlesheim, Germany)
Disposable pipette	Sarstedt (Nümbrecht, Germany)
DMEM (high glucose)	Thermo-Fisher Scientific (Waltham, USA)
Ethanol 96% denatured	Roth (Arlesheim, Germany)
Gibco® Dulbecco's phosphate-buffered saline (DPBS), no calcium, no magnesium	Thermo-Fisher Scientific (Waltham, USA)
Gibco® Fetal Bovine Serum	Thermo-Fisher Scientific (Waltham, USA)
Gibco® Medium 199 (1x), Hanks' Balanced Salts	Thermo-Fisher Scientific (Waltham, USA)
Gibco® Penicillin-Streptomycin	Thermo-Fisher Scientific (Waltham, USA)
GSK3 reaction buffer	New England BioLabs (Ipswich, USA)
Hanks' Balanced Salt Solution (HBSS), no calcium, no magnesium	Thermo-Fisher Scientific (Waltham, USA)
Heparin	Rotexmedica (Trittau, Germany)
Latex gloves powder-free	VWR International (Radnor, USA)
Liberase™	Roche Diagnostics (Risch, Switzerland)
MICROMAN® Capillaries and Pistons	Gilson (Middleton, USA)
Nail polish	Cosnova (Sulzbach, Germany)
Ni-NTA Agarose	QIAGEN (Hilden, Germany)
Ni-NTA Superflow column	QIAGEN (Hilden, Germany)
Nitrile Examination Gloves	Ansell (Iselin, USA)
Parafilm	Pechiney Plastic Packaging (Chicago, USA)
Pasteur pipette	Heinz Herenz Medizinalbedarf (Hamburg, Germany)
Petri dish 92x16 mm with cams	Sarstedt (Nümbrecht, Germany)
PhosSTOP™ Phosphatase inhibitor cocktail tablet	Roche Diagnostics (Risch, Switzerland)
Pierce® Protein-Free T20 (TBS) Blocking Buffer	Thermo-Fisher Scientific (Waltham, USA)
Pipette tips 10, 200, 1000 µL	Sarstedt (Nümbrecht, Germany)
Precision Plus Protein™ All Blue / Dual Color Standards	Bio-Rad (Hercules, USA)
Pro-Q™ Diamond phosphoprotein gel stain	Thermo-Fisher Scientific (Waltham, USA)
Rapid Fixer / Developer for medical X-ray film processing	Agfa (Mortsel, Belgium)
Reaction tubes 1.5, 2 mL	Sarstedt (Nümbrecht, Germany)
Serological pipettes 1, 2, 5, 10, 25 mL	Sarstedt (Nümbrecht, Germany)

Sterile scalpel blade	C. Bruno Bayha (Tuttlingen, Germany)
Sterile tube	Sarstedt (Nümbrecht, Germany)
Sterile water (H$_2$O)	B. Braun Melsungen (Melsungen, Germany)
Stripette® disposable serological pipette	Corning Incorporated (Corning, USA)
Super PAP pen Liquid Blocker	Daido Sangyo (Tokyo, Japan)
SYPRO™ Ruby protein gel stain	Thermo-Fisher Scientific (Waltham, USA)
tapira® cleansing tissue	GVS-GROSSVERBRAUCHERSPEZIALISTEN (Friedewald, Germany)
Test tubes 15, 50 mL	Greiner Bio-One (Frickenhausen, Germany)
Thinwall Polyallomer Tube	Beckman Coulter Life Sciences (Brea, USA)
Tissue culture dish 35x10 mm	Sarstedt (Nümbrecht, Germany)
Whatman® chromatography paper 3MM CHR	GE Healthcare (Chicago, USA)
Zeba™ Spin Desalting Column, 7K MWCO, 0.5 mL	Thermo-Fisher Scientific (Waltham, USA)

5.1.8 Further equipment

Name	Supplier
Attofluor™ Cell Chamber, for microscopy	Thermo-Fisher Scientific (Waltham, USA)
Electrophoresis chamber Mini-PROTEAN® 3 / Tetra Cell	Bio-Rad (Hercules, USA)
Electrophoresis chamber Sub-Cell® GT	Bio-Rad (Hercules, USA)
Eppendorf Reference® / Eppendorf Research® pipettes	Eppendorf (Hamburg, Germany)
Injection syringe 25 µL	Hamilton (Reno, USA)
MICROMAN® pipettes	Gilson (Middleton, USA)
Mini-PROTEAN® Comb, 10- / 15-well	Bio-Rad (Hercules, USA)
PIPETMAN® pipettes	Gilson (Middleton, USA)
Short Plate / Spacer Plate for Mini-PROTEAN®	Web Scientific (Cheshire, UK) / Bio-Rad (Hercules, USA)
X-ray cassette	Wardray (Surrey, UK)
X-ray cassette 18 x 24 cm	Rego X-Ray (Augsburg, Germany)

5.1.9 Kits

Name	Supplier
Duolink® In Situ Orange Starter Kit Mouse/Rabbit	Merck Millipore (Billerica, USA)
HiSpeed® Plasmid Maxi Kit	QIAGEN (Hilden, Germany)
NucleoSpin® Plasmid	Macherey-Nagel (Düren, Germany)
QuikChange II XL Site-Directed Mutagenesis Kit	Agilent Technologies (Santa Clara, USA)

5.1.10 Oligonucleotide primers

Name	Sequence
C1-M-C2 sequencing	5'-cacatcaccgatgcccagc-3'
Mutagenesis primers:	(base exchanges in **bold**)
Cys249Asp/Ser250Cys For	5'-ccaccaaggacaaatttgac**ga**ct**g**caacttcaatctcactg-3'
Cys249Asp/Ser250Cys Rev	5'-cagtgagattgaagttg**c**agt**tc**gtcaaatttgtccttggtgg-3'
Ser250Ala For	5'-caaggacaaatttgactgc**g**ccaacttcaatctcactgt-3'
Ser250Ala Rev	5'-acagtgagattgaagttgg**c**gcagtcaaatttgtccttg-3'
Ser250Asp For	5'-ccaaggacaaatttgactgc**ga**caacttcaatctcactgtcc-3'
Ser250Asp Rev	5'-ggacagtgagattgaagttg**tc**gcagtcaaatttgtccttgg-3'
Ser275Ala For	5'-cttccgccgcacg**gc**cctggctggaggt-3'
Ser275Ala Rev	5'-acctccagccagg**gc**cgtgcggcggaag-3'
Ser284Ala For	5'-ggtggtcggcggatc**gc**tgatagccatgagga-3'
Ser284Ala Rev	5'-tcctcatggctatca**gc**gatccgccgaccacc-3'
Ser304Ala For	5'-tgctgaaaaagagagac**gc**tttccggaccccgagg-3'
Ser304Ala Rev	5'-cctcggggtccggaaa**gc**gtctctcttttttcagca-3'
Ser311Ala For	5'-accccgagggac**g**cgaagctggagg-3'
Ser311Ala Rev	5'-cctccagcttcg**c**gtccctcggggt-3'

5.1.11 Plasmids

Name	Encoded protein	Source
C1-M-C2 WT in pET-8c	Human C1-M-C2 (amino acids 153-451 of cMyBP-C)	Kind gift of M. Gautel (King's College London, UK)
Mutagenesis-derived C1-M-C2 variants:		
249Asp/250Cys	C1-M-C2 Cys249Asp, Ser250Cys	Self-made
4Ala	C1-M-C2 Ser(275, 284, 304, 311)Ala	Self-made
5Ala	C1-M-C2 Ser(250, 275, 284, 304, 311)Ala	Self-made
Ser250Ala	C1-M-C2 Ser250Ala	Self-made
Ser250Asp	C1-M-C2 Ser250Asp	Self-made
Ser304Ala	C1-M-C2 Ser304Ala	Self-made

All C1-M-C2 proteins possess a N-terminal His_6-tag.

5.1.12 Reagents for the treatment of ARVMs and active enzymes for *in vitro* assays

Substance	Solvent	Supplier
(R)-(-)-Phenylephrine hydrochloride	H_2O	Sigma-Aldrich (St. Louis, USA)
1-Nitrosocyclohexyl acetate (NCA)	DMSO	Axon Medchem (Groningen, Netherlands)
3-Isobutyl-1-methylxanthine (IBMX)	DMSO	Santa Cruz (Dallas, USA)
Angeli's salt (AS)	10 mmol/L NaOH	Cayman Chemicals (Ann Arbor, USA)

Atenolol	H_2O	Sigma-Aldrich (St. Louis, USA)
CXL-1020	DMSO	Axon Medchem (Groningen, Netherlands)
Diamide (DIA)	H_2O	Sigma-Aldrich (St. Louis, USA)
Dimethyl sulfoxide (DMSO)	-	Sigma-Aldrich (St. Louis, USA)
Drug G1	DMSO	Axon Medchem (Groningen, Netherlands)
Endothelin1 (ET)	DPBS	Merck Millipore (Billerica, USA)
Forskolin (FOR)	DMSO	Sigma-Aldrich (St. Louis, USA)
H1152	H_2O	Bio-Techne (Minneapolis, USA)
H-89, Dihydrochloride	DMSO	Sigma-Aldrich (St. Louis, USA)
Hydrogen peroxide (H_2O_2) solution 30% (w/w) in H_2O	H_2O	Sigma-Aldrich (St. Louis, USA)
Isoprenaline hydrochloride (ISO)	H_2O	Sigma-Aldrich (St. Louis, USA)
L-Glutathione oxidized (GSSG)	H_2O	Sigma-Aldrich (St. Louis, USA)
NKY80	DMSO	Cayman Chemicals (Ann Arbor, USA)
ODQ	DMSO	Cayman Chemicals (Ann Arbor, USA)
Okadaic acid	DMSO	Enzo Life Sciences (Farmingdale, USA)

5.1.13 Software

Name	Supplier
ACD/ChemSketch	Advanced Chemistry Development, Inc. (Toronto, Canada)
CanoScan Toolbox	Canon (Tokyo, Japan)
GelQuant.NET	BiochemLabSolutions.com (San Francisco, USA)
ImageJ with Fiji (version 1.51h) and µManager (version 1.4.5)	Wayne Rasband
IonWizard with SarcLen acquisition module	IonOptix (Westwood, USA)
NanoDrop® 1000 3.8.1	Thermo-Fisher Scientific (Waltham, USA)
Peaks® 7 Studio software for proteomics	Bioinformatics Solutions (Waterloo, Canada)
Prism 5	GraphPad Software (La Jolla, USA)
Serial Cloner	Serial Basics
Typhoon scanner control	GE Healthcare (Chicago, USA)

Word, PowerPoint, Excel	Microsoft (Redmond, USA)
Xfluor4 Safire II plugin for Excel	Tecan (Männedorf, Switzerland) / Microsoft (Redmond, USA)

5.1.14 Viruses

Name	Type	Source
AKAR3-NES	Adenovirus	Kind gift of G. Vandecasteele (University of Paris-Sud, France)
BirA-cMyBP-C	Adeno-associated virus serotype 6	Generated using pcDNA3.1 mycBioID (Addgene plasmid #35700) and kindly provided by S. Schulz (University Medical Center Hamburg-Eppendorf, Germany)

5.2 Buffers, solutions and media

If not stated otherwise, Milli-Q water purification system-derived ultrapure H_2O was used for the preparation of buffers and solutions listed below.

HEPES buffer (1 mol/L)

Reagent	Final concentration
HEPES	1000 mmol/L

Adjust pH as desired.

Tris-HCl buffer

Reagent	Final concentration
Tris base	as desired

Adjust pH as desired.

5.2.1 Cloning and recombinant protein purification

Dialysis buffer

Reagent	Final concentration
Tris-HCl buffer pH 8.1	50 mmol/L
NaCl	25 mmol/L
DTT	1 mmol/L
EDTA	1 mmol/L
Glycerol	50% (v/v)
Triton® X 100	0.1% (v/v)

Lysis buffer

Reagent	Final concentration
NaCl	300 mmol/L
NaH$_2$PO$_4$	50 mmol/L
Imidazole	10 mmol/L

| cOmplete™ Protease inhibitor | 1 tablet/50 mL |

Adjust pH to 8.0.

Lysogeny broth (LB)

Reagent	Final concentration
NaCl	85.6 mmol/L
Tryptone	1% (w/v)
Yeast extract	0.5% (w/v)

Adjust pH to 7.4, autoclave.

Lysogeny broth (LB) agar plates

Reagent	Final concentration
NaCl	85.6 mmol/L
Agar	1.5% (w/v)
Tryptone	1% (w/v)
Yeast extract	0.5% (w/v)
Ampicillin*	0.01% (w/v)

* Add directly before casting.
Autoclave and let cool down to 60 °C before casting.

Ni-NTA elution buffer

Reagent	Final concentration
NaCl	300 mmol/L
Imidazole	250 mmol/L
NaH_2PO_4	50 mmol/L

Adjust pH to 8.0.

SOC medium

Reagent	Final concentration
Glucose*	20 mmol/L
$MgCl_2$	10 mmol/L
$MgSO_4$	10 mmol/L
NaCl	10 mmol/L
KCl	2.5 mmol/L
Tryptone	2% (w/v)
Yeast extract	0.5% (w/v)

* Add after autoclaving.
Adjust pH to 7.0, autoclave.

Wash buffer

Reagent	Final concentration
NaCl	300 mmol/L
NaH_2PO_4	50 mmol/L
Imidazole	20 mmol/L

Adjust pH to 8.0.

5.2.2 Immunofluorescence staining

BSA/Gold buffer

Reagent	Final concentration
NaCl	155 mmol/L
Tris base	10 mmol/L
EGTA	2 mmol/L
$MgCl_2$	2 mmol/L
BSA*	1% (w/v)

* Add after pH adjustment.
Adjust pH to 7.2.

Lisbeth's solution

Reagent	Final concentration
Tris-HCl buffer pH 9.5	30 mmol/L
N-Propyl gallate*	5% (w/v)
Glycerol	70% (v/v)

* Dissolve in glycerol by shaking overnight. Add Tris-HCl buffer pH 9.5 and shake overnight another time.

Normal goat serum (NGS) blocking solution

Add to BSA/gold buffer:

Reagent	Final concentration
NGS	5% (v/v)

Permeabilization solution

Add to DPBS:

Reagent	Final concentration
Triton® X 100	0.2% (v/v)

PFA solution

Add to DPBS:

Reagent	Final concentration
PFA 16% solution	4% (v/v)

Skinning solution

Add to DPBS:

Reagent	Final concentration
Triton® X 100	1% (v/v)

5.2.3 Mass spectrometry sample preparation

MS destaining solution

Reagent	Final concentration
NH_4HCO_3	50 mmol/L
Methanol	60% (v/v)

MS digestion solution

Reagent	Final concentration
NH_4HCO_3	50 mmol/L
$CaCl_2$	1 mmol/L
ProteaseMAX™	0.01% (v/v)

MS elution buffer

Reagent	Final concentration
Acetonitrile	30% (v/v)
Formic acid	3% (v/v)

MS resolving buffer

Reagent	Final concentration
Acetonitrile	1% (v/v)
Formic acid	0.5% (v/v)

5.2.4 Myocyte isolation and cultivation

Digestion buffer

Add to Perfusion buffer:

Reagent	Final concentration
$CaCl_2$	0.0125 mmol/L
Liberase™	0.01% (w/v)

Laminin coating solution

Reagent	Final concentration
Laminin	1.5% (v/v)

Maintenance medium

Add to 80% DMEM (high glucose) and 20% Medium 199:

Reagent	Final concentration
Penicillin-streptomycin	1% (v/v)
Fetal bovine serum, heat-inactivated*	1% (v/v)

* Fetal bovine serum is inactivated by incubation at 60 °C for 1 h. Serum was omitted in serum-free maintenance medium.

MC culture medium

Add to Medium 199:

Reagent	Final concentration
Taurine	5 mmol/L
Carnitine	2 mmol/L
Creatine	2 mmol/L
Penicillin-streptomycin	100 U/mL

Perfusion buffer (stock)

Reagent	Final concentration
NaCl	113 mmol/L
Taurine	30 mmol/L
NaHCO$_3$	12 mmol/L
HEPES buffer pH 7.4	10 mmol/L
KHCO$_3$	10 mmol/L
KCl	4.7 mmol/L
MgSO$_4$	1.2 mmol/L
KH$_2$PO$_4$	0.6 mmol/L
Na$_2$HPO$_4$	0.6 mmol/L

Perfusion buffer

Add to Perfusion buffer (stock):

Reagent	Final concentration
Glucose	5.6 mmol/L
BDM	10 mmol/L
Penicillin-streptomycin	100 U/mL

Stop solution 1

Add to Perfusion buffer:

Reagent	Final concentration
CaCl$_2$	0.0125 mmol/L
Fetal bovine serum	10% (v/v)

Stop solution 2

Add to Perfusion buffer:

Reagent	Final concentration
CaCl$_2$	0.0125 mmol/L
Fetal bovine serum	5% (v/v)

5.2.5 PEG-switch, biotin-switch and biotinylation of NMVM proteins

Acetone solution (80%)

Reagent	Final concentration
Acetone	80% (v/v)

BioID lysis buffer

Reagent	Final concentration
NaCl	500 mmol/L
Tris-HCl buffer pH 7.4	50 mmol/L
DTT	1 mmol/L
SDS	0.2% (w/v)
PhosSTOP™ Phosphatase inhibitor	1 tablet/10 mL
cOmplete™ Protease inhibitor	1 tablet/50 mL

Biotin-switch harvesting buffer

Reagent	Final concentration
NaCl	150 mmol/L
N-Ethylmaleimide	100 mmol/L
Tris-HCl buffer pH 7.4	100 mmol/L
Triton® X 100	1% (v/v)
cOmplete™ Protease inhibitor	1 tablet/50 mL

PEG-switch harvesting buffer

Reagent	Final concentration
Maleimide	100 mmol/L
Tris-HCl buffer pH 7.4	100 mmol/L
SDS	34.7 mmol/L
cOmplete™ Protease inhibitor	1 tablet/50 mL

RIPA buffer

Reagent	Final concentration
NaCl	150 mmol/L
Tris-HCl buffer pH 7.4	25 mmol/L
SDS	0.1% (w/v)
Sodium deoxycholate	0.1% (w/v)
Triton® X 100	1% (v/v)

SDS solution (20%)

Reagent	Final concentration
SDS	20% (w/v)

Streptavidin-agarose elution buffer

Add to DPBS:

Reagent	Final concentration
Urea	6000 mmol/L
Thiourea	2000 mmol/L
Biotin	30 mmol/L
SDS	2% (w/v)

Triton solution (20%)

Reagent	Final concentration
Triton® X 100	20% (v/v)

5.2.6 SDS-PAGE and Western immunoblotting

Acetic acid (5%)

Reagent	Final concentration
Acetic acid (glacial) 100%	5% (v/v)

APS (10%)

Reagent	Final concentration
APS	10% (w/v)

BSA/TBST (1%)

Add to TBST:

Reagent	Final concentration
BSA	1% (w/v)

BSA/TBST (5%)

Add to TBST:

Reagent	Final concentration
BSA	5% (w/v)

Colloidal Coomassie destaining solution

Reagent	Final concentration
Methanol	20% (v/v)

Colloidal Coomassie staining solution

Reagent	Final concentration
Methanol	20% (v/v)
Ammonium sulfate	8% (w/v)
ortho-Phosphoric acid 85%	1.88% (v/v)
Coomassie Brilliant Blue G-250*	0.08% (w/v)

* Dissolve in H_2O to obtain a 5% (w/v) solution.

Coomassie destaining solution

Reagent	Final concentration
Methanol	50% (v/v)
Acetic acid (glacial) 100%	10% (v/v)

Coomassie staining solution

Reagent	Final concentration
Methanol	45% (v/v)
Acetic acid (glacial) 100%	10% (v/v)
Coomassie Brilliant Blue R-250	0.2% (w/v)

Developer solution

Reagent	Final concentration
Developer	16.7% (v/v)

Fixing solution

Reagent	Final concentration
Rapid fixer	20% (v/v)

Glycerol solution (20%)

Reagent	Final concentration
Glycerol	20% (v/v)

Laemmli sample buffer, reducing (6x)

Reagent	Final concentration
Tris-HCl buffer pH 6.8	375 mmol/L
SDS	12% (w/v)
Bromophenol blue	0.06% (w/v)
Glycerol	60% (v/v)
β-Mercaptoethanol	18% (v/v)

Laemmli sample buffer, reducing (3x)

Reagent	Final concentration
Tris-HCl buffer pH 6.8	187.5 mmol/L
SDS	6% (w/v)
Bromophenol blue	0.03% (w/v)
Glycerol	30% (v/v)
β-Mercaptoethanol	9% (v/v)

Laemmli sample buffer, non-reducing (3x)

Reagent	Final concentration
Tris-HCl buffer pH 6.8	187.5 mmol/L
Maleimide	100 mmol/L
SDS	6% (w/v)
Bromophenol blue	0.03% (w/v)
Glycerol	30% (v/v)

Milk/TBST (1%)

Add to TBST:

Reagent	Final concentration
Powdered milk	1% (w/v)

Milk/TBST (5%)

Add to TBST:

Reagent	Final concentration
Powdered milk	5% (w/v)

Milk/TBST (10%)

Add to TBST:

Reagent	Final concentration
Powdered milk	10% (w/v)

Pro-Q™ Diamond destaining solution

Reagent	Final concentration
Sodium acetate solution pH 4	50 mmol/L
Acetonitrile	20% (v/v)

Pro-Q™ Diamond fixing solution

Reagent	Final concentration
Methanol	50% (v/v)
Acetic acid (glacial) 100%	10% (v/v)

Reservoir buffer (10x)

Reagent	Final concentration
Glycine	1918.2 mmol/L
Tris base	249.3 mmol/L
SDS	34.7 mmol/L

Resolving buffer (4x)

Reagent	Final concentration
Tris base	1502.4 mmol/L
SDS	13.9 mmol/L

Adjust pH to 8.7.

Sodium acetate solution (1 mol/L)

Reagent	Final concentration
Sodium acetate	1000 mmol/L

Adjust pH to 4.

Stacking buffer (4x)

Reagent	Final concentration
Tris base	499.4 mmol/L
SDS	13.9 mmol/L

Adjust pH to 6.8.

SYPRO™ Ruby fixing solution

Reagent	Final concentration
Methanol	50% (v/v)
Acetic acid (glacial) 100%	7% (v/v)

SYPRO™ Ruby wash solution

Reagent	Final concentration
Methanol	10% (v/v)
Acetic acid (glacial) 100%	7% (v/v)

Transfer buffer

Reagent	Final concentration
Tris base	47.9 mmol/L

Glycine	38.6 mmol/L
SDS	1.3 mmol/L
Methanol	20% (v/v)

Tris-buffered saline (TBS, 10x)

Reagent	Final concentration
NaCl	1368.9 mmol/L
Tris base	199.8 mmol/L

Adjust pH to 7.6.

Tris-buffered saline + 0.1% Tween® 20 (TBST)

Reagent	Final concentration
Tris-buffered saline (10x)	10% (v/v)
Tween® 20	0.1% (v/v)

5.2.7 Further buffers and solutions

Fractionation buffer

Reagent	Final concentration
NaF	100 mmol/L
Tris-HCl buffer pH 7.5	50 mmol/L
EGTA	5 mmol/L
EDTA	2 mmol/L
Digitonin*	0.05% (w/v)
cOmplete™ Protease inhibitor	1 tablet/50 mL

* Dissolve in H_2O to obtain a 4% solution by boiling.

FRET buffer

Reagent	Final concentration
NaCl	144 mmol/L
HEPES	10 mmol/L
KCl	5.4 mmol/L
$MgCl_2$	1 mmol/L

Adjust pH to 7.3.

Homogenization buffer

Add to Tris-HCl buffer pH 7.4 (100 mmol/L):

Reagent	Final concentration
NaCl	1800 mmol/L
Triton® X 100	6% (v/v)

IonOptix buffer

Add to IonOptix buffer (stock):

Reagent	Final concentration
Glucose	20 mmol/L
$CaCl_2$	1.5 mmol/L

IonOptix buffer (stock)

Reagent	Final concentration
NaCl	135 mmol/L
HEPES buffer pH 7.46	10 mmol/L
KCl	4.7 mmol/L
$MgSO_4$	1.2 mmol/L
KH_2PO_4	0.6 mmol/L
Na_2HPO_4	0.6 mmol/L

Kinase assay buffer

Reagent	Final concentration
Tris-HCl buffer pH 7.4	30 mmol/L
$MgCl_2$	15 mmol/L
DTT*	1 mmol/L

* DTT was omitted when effects of protein oxidation were examined.

Phosphatase assay buffer

Reagent	Final concentration
Tris-HCl buffer pH 7.5	40 mmol/L
$MgCl_2$	34 mmol/L
EDTA	4 mmol/L
BSA	0.005% (w/v)

PKG harvesting buffer

Reagent	Final concentration
NaCl	150 mmol/L
Tris-HCl buffer pH 7.4	20 mmol/L
NaF	2 mmol/L
EDTA	1 mmol/L
EGTA	1 mmol/L
cOmplete™ Protease inhibitor	1 tablet/50 mL

5.3 Biochemical methods

5.3.1 ARVM isolation and culture

The isolation of primary adult rat ventricular myocytes (ARVMs) from male Wistar rats was performed in compliance with the Guide for the Care and Use of Laboratory Animals issued by the National Research Council (US) Committee for the Update of the Guide for the Care and Use of Laboratory Animals (2011). Specifications of the German law for the protection of animals were met.

Male Wistar rats were injected with heparin (1 International Unit/g) intraperitoneally 20 min prior to the experimental protocol. Following anesthetization with carbon dioxide, rats were sacrificed by decapitation. The heart was excised, cannulated and mounted on a temperature-

controlled perfusion system providing a constant temperature of 37 °C at the outlet cannula and a constant flow rate of 10 mL/min. Perfusion of the heart was performed for 10 min with perfusion buffer followed by 8 min of digestion with digestion buffer. The ventricles were removed and dissociated in digestion buffer with sterile forceps for 1.5 min. By the addition of one volume stop solution 1, enzyme activity was inhibited. The cells were transferred into a 15 mL test tube and further dissociated by 1 min of pipetting with a wide-necked serological pipette. The presence of intact cardiac myocytes was confirmed by light microscopy. Undigested tissue was left to sediment at room temperature (RT) by gravity for 3 min before the supernatant was collected in a 50 mL test tube. The pellet was kept. Cardiac myocytes were again allowed to sediment by gravity for 20 min. Subsequently, the cell pellet was resuspended in 10 mL stop solution 2 and transferred into a petri dish. The retained pellet from the previous step was also supplemented with 10 mL stop solution 2. After 3 min of sedimentation, the supernatant was added to the petri dish. By increasing concentrations of $CaCl_2$, Ca^{2+} was gradually reintroduced to the cells (Tab. 2).

Table 2: Gradual re-introduction of Ca^{2+} to freshly isolated ARVMs

Step	$CaCl_2$ stock [mmol/L]	Stock volume [µL]	$CaCl_2$ final [mmol/L]
1	10	100	0.0625
2	10	100	0.1125
3	10	200	0.2125
4	100	60	0.5
5	100	100	1

After each addition, the cells were mixed gently by slewing and incubated at RT for 4 min. The cells were transferred into a new 50 mL test tube, allowed to sediment for 20 min and finally carefully resuspended in MC culture medium. Subsequently, the cells were counted, and the cell suspension distributed into laminin-coated 6 well cell culture plates or single tissue culture dishes. The cell number per dish amounted to 200 000 – 300 000. The medium was exchanged 2 h after seeding to remove non-adherent cells. ARVMs were left in culture at 7% CO_2 for at least 16 h.

The isolation and culture of ARVMs was kindly performed by Angelika Piasecki. For single cell contractility measurements, after Ca^{2+} reintroduction ARVMs were equilibrated in IonOptix buffer by resuspending sedimented cells twice. After buffer exchange, ARVMs were allowed to recover for at least 1 h prior to the experiment. For FRET experiments, approx. 5000 cells were distributed on laminin-coated 25 mm Ø cover glasses placed in 6 well cell culture plates.

5.3.2 Biotin-switch assay

The biotin-switch protocol was adapted from the PEG-switch protocol of Burgoyne et al. (2013).
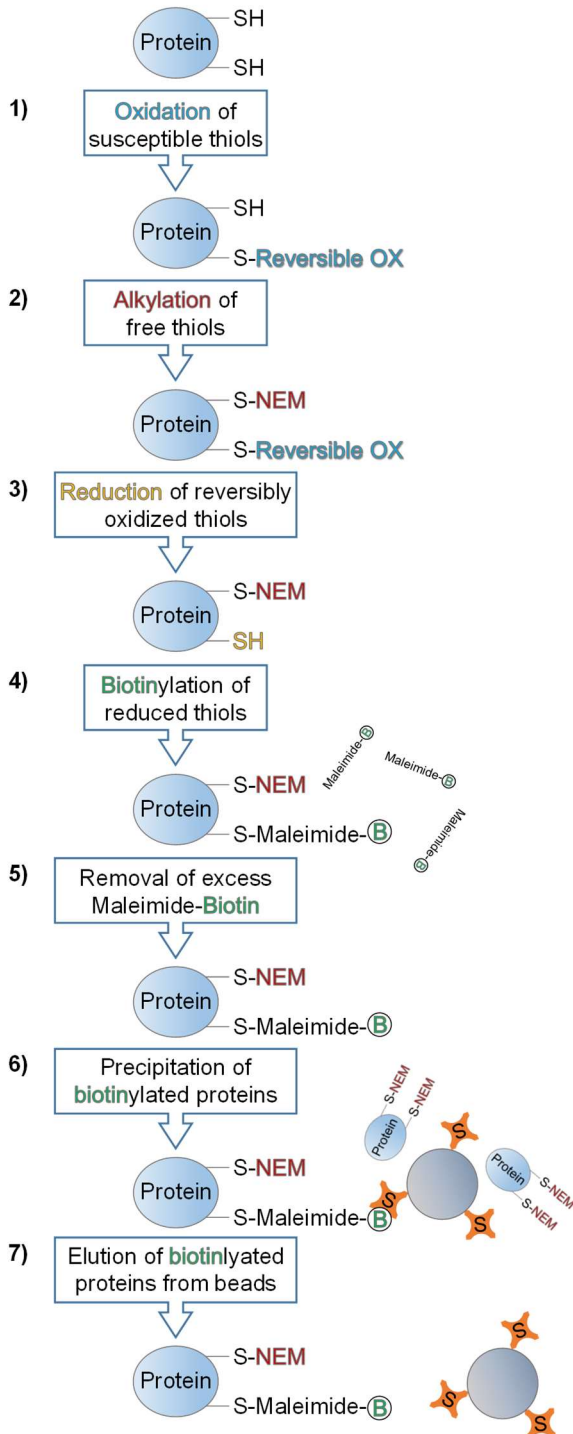
Figure 61: Diagrammatic representation of the biotin-switch method Following exposure to oxidants, free thiol groups of ARVM proteins were blocked with N-Ethylmaleimide (NEM). Thiol oxidation was reversed with DTT and reduced thiols labeled with biotin-maleimide. Excess biotin-maleimide was removed by acetone precipitation and labeled proteins precipitated using streptavidin-agarose beads. The relative amount of precipitated protein detected by Western immunoblotting indicates the degree of protein oxidation induced by the initial oxidant-treatment.

Cultured ARVMs were treated with vehicle dimethyl sulfoxide (DMSO; 30 min), NCA (100 µmol/L, 30 min), AS (500 µmol/L, 15 min), CXL-1020 (300 µmol/L, 15 min), H_2O_2 (100 µmol/L, 10 min), DIA (500 µmol/L, 10 min) or ISO (10 nmol/L, 10 min) at 37 °C and 7% CO_2 (Fig. 61, **1)**). After a washing step with 1 mL ice-cold Tris-HCl buffer (100 mmol/L, pH 7.4), 70 µL ice-cold harvesting buffer was pipetted on the cells and the cell culture plate frozen in liquid N_2. The ARVMs were thawed, harvested and incubated at RT for 10 min. SDS (1%; applied as 20% solution) was added to the lysates and samples were incubated at 50 °C and 300 rpm for 25 min to block free thiol groups by alkylation with N-Ethylmaleimide contained in the harvesting buffer (Fig. 61, **2)**). Subsequently, a sample volume of 130 µL was desalted by a Zeba™ Spin desalting column to remove N-Ethylmaleimide. The residual volume was kept as input. Oxidized protein thiol groups of desalted samples were reduced by the addition of 50 mmol/L DTT (Fig. 61, **3)**). Following 20 min of incubation at RT, DTT was removed by another desalting step. The biotinylation reagent EZ-Link® Maleimide-PEG$_2$-Biotin (1 mmol/L) and 0.5% SDS (applied as 20% solution) were added sequentially and samples incubated on a laboratory agitator at RT for 2 h in the dark (Fig. 61, **4)**). To remove unbound Maleimide-PEG$_2$-Biotin, four volumes of acetone (-20 °C) were added to the samples and proteins precipitated at -20 °C for 1 h. Proteins were

pelleted by centrifugation at 16 000 g and 2 °C for 10 min. The supernatant was removed and the pellets washed twice with 731 µL 80% acetone (-20 °C) by detaching the pellet from the tube, centrifugation and discarding the supernatant (Fig. 61, **5)**). Residual acetone was left to evaporate for 2 min, then 400 µL Tris-HCl buffer (100 mmol/L, pH 7.4) was added to the protein pellets. Resuspension was supported by vortexing and ultrasonic homogenization. After a quick centrifugation step, 40 µl of the supernatant was kept as input (biotinylated). The residual volume was added to 100 µL streptavidin-agarose beads (50% slurry) and incubated overnight on a laboratory agitator at 4 °C to bind biotinylated proteins (Fig. 61, **6)**). The beads were washed three times with 1 mL RIPA buffer for 5 min at RT on the agitator followed by two washes with Tris-HCl buffer (100 mmol/L, pH 7.4). After each washing step the beads were sedimented by centrifugation (1 min, 3000 g). Eventually, 50 µL elution buffer was added to the beads and the samples successively incubated at RT and at 95 °C for 15 min each. The beads were pelleted by centrifugation at 16 100 g for 10 min. Subsequently, the supernatant was decanted and supplemented with 6x reducing Laemmli sample buffer (Fig. 61, **7)**). The precipitation of proteins, which indicated the biotinylation of cysteine residues as a consequence of protein oxidation in response to the initial treatment, was analyzed by SDS-PAGE and Western immunoblotting (see 5.3.20).

5.3.3 Biotinylation of neonatal mouse ventricular myocyte (NMVMs) proteins by BirA-fused cMyBP-C

The isolation of primary neonatal mouse ventricular myocytes (NMVMs) from C57BL/6 mice was performed in compliance with the Guide for the Care and Use of Laboratory Animals issued by the National Research Council (US) Committee for the Update of the Guide for the Care and Use of Laboratory Animals (2011). Specifications of the German law for the protection of animals were met. Isolated ventricular cardiac myocytes from neonatal *Mybpc3*-targeted KO mice were kindly provided by Leonard Oelze and obtained by adaptation of the protocols described by Stöhr (2012) and Mearini et al. (2014). Briefly, hearts from at least 20 0-3 days old cMyBP-C KO animals were harvested and subjected to predigestion with 0.5 mg/mL trypsin 250 in Hanks' Balanced Salt Solution (HBSS) overnight. NMVMs were isolated and collected by repeated digestion of heart tissue with 240 U/mL of collagenase type II in HBSS. CMyBP-C KO NMVMs were cultivated in maintenance medium in a gelatin-coated 6 well cell culture plate (415 000 cells/well) for 3 days at 37 °C and 7% CO_2. Following 5 h of incubation in serum-free maintenance medium, cells were transduced with an adeno-associated virus of serotype 6 (MOI 500 000) to induce the expression of biotin ligase BirA fused to the N-terminus of cMyBP-C. Serum was reintroduced to the medium after 4 h of incubation. The medium was exchanged after 2 days. At day 3 after transduction, NMVMs were exposed to 100 µmol/L biotin for 4 h before treatment with vehicle DMSO (30 min), NCA (100 µmol/L, 30 min) or ISO (10 nmol/L, 10 min) was performed. During treatment, cells were

kept at 37 °C and 7% CO_2. The cells were washed with Dulbecco's phosphate-buffered saline (DPBS) twice and harvested in 200 µl/well BioID lysis buffer. Lysates were supplemented with 10% of a 20% Triton solution, mixed by vortexing and frozen in liquid N_2 before storage at -80 °C. For processing of the samples, lysates were thawed on ice and sonicated twice in 5 cycles for 5 s with 30 s pause. Samples were supplemented with 82% volume of Tris-HCl buffer (50 mmol/L, pH 7.4) and sonicated once more. After centrifugation at 16 100 g and 4 °C for 15 min, the supernatant was decanted and 15 µl of each sample taken as input. The residual volume was added to 100 µl streptavidin-agarose beads (50% slurry), which had been equilibrated in BioID lysis buffer (supplemented with 10% of a 20% Triton solution and 50 mmol/L Tris-HCl buffer, pH 7.4), and incubated overnight on a laboratory agitator at 4 °C to bind biotinylated proteins. After centrifugation at 3000 g for 1 min, the supernatant was removed and stored. The beads were washed with 1 mL RIPA buffer for 5 min at RT on the agitator three times and with Tris-HCl buffer (100 mmol/L, pH 7.4) twice with centrifugation (3000 g for 1 min) and removal of the supernatant after each washing step. Washed beads were incubated in 20 µL elution buffer for 15 min at RT and for 15 min at 95 °C with occasional flicking. Subsequently, the beads were pelleted by centrifugation at 16 100 g for 10 min, the supernatant containing the biotinylated proteins was collected and supplemented with 3x reducing Laemmli sample buffer. The samples were analyzed by SDS-PAGE and Western immunoblotting (see 5.3.20).

5.3.4 Colorimetric staining of total protein in polyacrylamide gels and on membranes

For colorimetric visualization of total protein content in polyacrylamide gels, samples were resolved by SDS-PAGE (see 5.3.20) and gels stained in colloidal Coomassie staining solution overnight. Background signal was reduced by destaining in colloidal Coomassie destaining solution for up to 6 h, followed by rinsing the gel in H_2O.

For Coomassie staining of blotting membranes, samples were resolved by SDS-PAGE and subjected to Western immunoblotting involving semi-dry transfer to a PVDF membrane. Following chemiluminescence detection, proteins attached to the membrane were stained by incubation in Coomassie staining solution for at least 1 h. Thereafter, the membrane was destained with Coomassie destaining solution for 2 min, rinsed in TBST and air-dried.

All incubation steps were performed on an orbital shaker at RT.

5.3.5 Contractility measurements with engineered heart tissues (EHTs)

EHTs generated from hiPSC-derived cardiac myocytes as described by Mannhardt et al. (2017) were kindly provided by Umber Saleem. Tissue contraction was analyzed by video-optical analysis as previously described (Hansen et al. 2010, Mannhardt et al. 2017). EHTs (65 days of age) were incubated in 24 well cell culture plates equipped with carbon pacing electrodes and containing 2 mL DMEM (high glucose) supplemented with 1.8 mmol/L Ca^{2+} per well for 30 min. Tissues were electrically stimulated at a frequency 1.5x above the frequency

of spontaneous contraction. To reduce contraction force by approx. 50%, excess Ca^{2+} was removed by incubation of EHTs in 0.2 mmol/L Ca^{2+} DMEM (high glucose) for 20 min and subsequent transfer into DMEM (high glucose) containing 0.6 mmol/L Ca^{2+} ($\triangleq EC_{50}$). During another 20 min of incubation, force of contraction was monitored by video-optical recording using an EHT analysis instrument. Finally, EHTs were placed in a cell culture plate containing 0.6 mmol/L Ca^{2+} DMEM (high glucose) supplemented with vehicle DMSO or 300 µmol/L CXL-1020 (final concentration of DMSO: 0.1%) and contractile analysis was performed by immediate video-optical recording. Contraction frequency, force of contraction, the time needed from 20% to peak (100%) force (time to peak$_{-80\%}$) and the duration of 80% maximal relaxation (relaxation time$_{80\%}$) were determined during measurements.

EHT measurements were kindly performed by Umber Saleem. Cell culture plates containing DMEM (high glucose) and Ca^{2+} at the desired concentrations (2 mL/well) were equilibrated overnight prior to use. Ca^{2+} concentrations were obtained by buffer supplementation with $CaCl_2$. All incubation steps, contractile measurements and buffer equilibration were executed at 37 °C, 7% CO_2 and 40% O_2. If spontaneous beating frequency was supposed to be reduced, EHTs were incubated in DMEM (high glucose; 0.6 mmol/L Ca^{2+}) supplemented with 300 nmol/L ivabradine for 2 h. In those EHTs, the effect of CXL-1020 was also assessed in the presence of 300 nmol/L ivabradine.

5.3.6 Fluorescence imaging of phosphoproteins in polyacrylamide gels

For the detection of phosphoproteins in polyacrylamide gels, the Pro-Q™ Diamond phosphoprotein gel stain was used as instructed by the manufacturer's protocol. In brief, following treatment of cultured ARVMs with different stimuli, crude lysates were prepared in reducing Laemmli sample buffer (see 5.3.15) and samples resolved by SDS-PAGE (see 5.3.20). Gels were fixed in fixing solution twice for 30 min and washed with H_2O three times for 10 min. Following incubation with Pro-Q™ Diamond stain for 90 min in the dark, gels were destained with destaining solution three times for 30 min and washed with H_2O twice for 5 min before imaging in a Typhoon 9400 imager at excitation/emission settings of 532/580 nm.

All incubation steps were performed at RT with gentle shaking. Gels were continued to use for total protein detection with SYPRO™ Ruby stain (see 5.3.7).

5.3.7 Fluorescence imaging of total protein in polyacrylamide gels

For the detection of total protein content in polyacrylamide gels, the SYPRO™ Ruby protein gel stain was used in accordance with the manufacturer's protocol. Briefly, samples of cultured ARVMs were prepared in reducing Laemmli sample buffer, subjected to SDS-PAGE (see 5.3.20) and gels fixed in fixing solution twice for 30 min. Proteins were stained by incubation with SYPRO™ Ruby stain in the dark overnight. Gels were transferred into a new container and washed with wash solution for 30 min, followed by two washing steps with H_2O for 10 min and subsequent imaging with a ChemiDoc™ imager.

All incubation steps were performed at RT with gentle shaking. If used as a post-stain after Pro-Q™ Diamond staining, SYPRO™ Ruby was immediately added to the gel without further fixing. Gels were subsequently used for staining with colloidal Coomassie (see 5.3.4).

5.3.8 Förster resonance energy transfer (FRET) experiments in ARVMs

For the measurement of FRET, approx. 5000 freshly isolated ARVMs were seeded on laminin-coated 25 mm cover glasses placed in 6 well cell culture plates (see 5.3.1) During medium exchange 2 h after seeding, the cells were transduced with an adenovirus encoding the nuclear export signal-coupled A-kinase activity reporter AKAR3-NES with an MOI of 300. The AKAR3 sensor consists of cyan fluorescent protein (CFP) and yellow fluorescent protein (YFP), which are attached to a consensus PKA substrate sequence and a phosphoamino acid binding domain. Upon phosphorylation by PKA, the sensor undergoes a conformational change, which reduces the distance between the fluorophores and consequently results in a change in the ratio of light emitted by CFP and YFP. After 48 h of cultivation, the cover glasses were placed in a microscopy cell chamber and briefly washed with FRET buffer. FRET measurements were performed at RT using a Leica DMI3000b inverted microscope equipped with a 40x magnification immersion oil objective and a multichannel imaging system. Fluorescence of CFP and YFP was simultaneously recorded with an optiMOS™ camera and a DV2 DualView emission splitting system at a frame rate of 1 per 5 s after excitation at 405 nm by a light-emitting diode. After the establishment of a baseline in FRET buffer, ARVMs were exposed to vehicle DMSO, NCA (100 µmol/L), H_2O_2 (100 µmol/L) or DIA (500 µmol/L). As soon as a plateau was reached, the cells were exposed to a combination of 10 µmol/L FOR and 100 µmol/L IBMX to generate maximal cAMP levels and induce maximal sensor activation.

Data were processed using ImageJ µManager with a customized plugin and Excel to record and analyze FRET experiments. To calculate sensor activation in response to a stimulus, the baseline signal was subtracted and the increase in FRET ratio expressed as % of the effect caused by FOR/IBMX. During some measurements, the application of NCA generated an artifact represented by a spontaneous decrease in FRET ratio. If appropriate, in these measurements the data point selected as baseline value was adjusted to obtain true activation values. FRET measurements and data evaluation were in a large part executed by Sophie Schobesberger.

5.3.9 Generation of a pSer250 phospho-specific antibody for cMyBP-C

Production of the polyclonal antibody for the detection of cMyBP-C phosphorylation at Ser250 was commissioned at Eurogentec. In brief, a rabbit was immunized with a 13 amino acid peptide (KFDCpSNFNLTVHE) corresponding to phosphorylated Ser250 of cMyBP-C and surrounding amino acids. Crude serum (60 mL) was collected from the animal and subjected to affinity purification using a column coated with the modified immunization peptide to remove unrelated antibodies. Subsequently, immunoglobulin G antibodies (IgGs) with affinity for the

corresponding peptide that lacks the modification at Ser250 were captured and excluded in a second affinity purification. Thus, the flow through from the second purification step contained the desired IgGs that are specific to the modified peptide, which mimics Ser250 phosphorylation of cMyBP-C. Antibodies eluted from the second column represented the modification-unspecific fraction. The purity of the modification-specific pSer250 antibody was assessed by SDS-PAGE analysis using the bioanalyzer system from Agilent Technologies (Santa Clara, USA) and amounted to 89.1%.

Antibody binding to modified and unmodified peptide was tested by indirect ELISA. Wells of the ELISA plate were coated with a constant amount (between 5 and 15 µg/well) of the modified or unmodified peptide at 4 °C for 16 h. Free binding sites were blocked by incubation with BSA (1 mg/mL) at 25 °C for 2 h. Subsequently, flow through and eluate of the second affinity purification, which were expected to contain pSer250-specific and unspecific antibodies, respectively, were applied at dilutions ranging from 1:100 to 1:218 700. Thereafter, a secondary anti-rabbit-IgG-horseradish peroxidase (HRP) conjugate was incubated in the wells at 25 °C for 2 h. Finally, the HRP substrate O-phenylenediamine (0.4 mg/mL) was added, incubated at 25 °C for 20 min and the resulting color reaction, which indicates peptide binding of the antibody, analyzed by measurement of OD_{492}. The ELISA protocol and antibody binding data were provided by Eurogentec.

5.3.10 Immunofluorescence staining of ARVMs and confocal microscopy

ARVMs that were cultured in single tissue culture dishes were left untreated or were exposed to vehicle DMSO (30 min), NCA (100 µmol/L, 30 min), AS (500 µmol/L, 15 min), CXL-1020 (300 µmol/L, 15 min), H_2O_2 (100 µmol/L, 10 min), DIA (500 µmol/L, 10 min) or ISO (10 nmol/L) while incubated in a CO_2 incubator at 37 °C and 7% CO_2 and subsequently washed twice with 2 mL ice-cold DPBS. For isolation of the cellular contractile machinery (skinning), cells were incubated in 1 mL skinning solution for 15 min at 4 °C to solubilize membranous and cytosolic content. Then the dishes were washed with 2 mL ice-cold DPBS and fixed with 1 mL PFA solution for 10 min at RT without moving. Alternatively, after treatment and the initial washing steps, ARVMs were immediately fixed with PFA solution without previous skinning. In any case, fixation was followed by three brief washing steps with 2 mL ice-cold DPBS each and the storage of dishes in 3 mL DPBS at 4 °C until further processing. For immunolabeling of proteins of interest, dishes that had been directly fixed without skinning were incubated in 1 mL permeabilization solution for 5 min at RT without moving. After permeabilization, three washing steps of 5 min were executed with 2 mL cold DPBS at RT on an orbital shaker. Skinned ARVMs did not require permeabilization and were solely washed for 5 min at RT on an orbital shaker. The edges of the dishes were dried with a cotton bud and retraced with a liquid blocker pen. NGS blocking solution (100 µL) was pipetted onto the cells, dishes placed in a humid chamber and incubated on an orbital shaker at RT for 20 min. After three washes with cold DPBS (2 mL,

5 min, RT), 100 μL primary antibody solution (prepared in BSA/Gold buffer), containing a pair of antibodies with one derived from mouse (anti-PKA-RI, anti-B56α or anti-α-actinin) and one from rabbit (anti-cMyBP-C; anti-Ser250 cMyBP-C, unspecific or anti-pSer250 cMyBP-C), was added to the cells (see 5.1.1). Dishes were incubated in a humid chamber on an orbital shaker at 4 °C overnight.
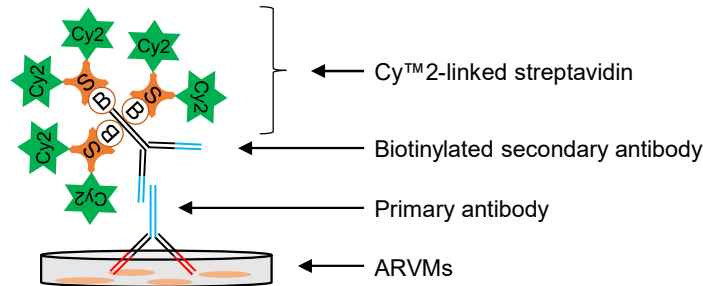
Figure 62: Overview of biotin-streptavidin-mediated signal amplification in immunofluorescence microscopy For enhancement of signal intensity and an improved background to signal-ratio, the biotin-streptavidin interaction was utilized for immunolabeling of proteins of interest in ARVMs. Following incubation with a primary antibody, a biotinylated secondary antibody was applied. Streptavidin linked to the fluorophore Cy™2 was used to achieve amplified labeling of the protein of interest with an increased number of fluorophore molecules. B: biotin, S: streptavidin

Afterwards, the cells were washed with cold DPBS three times (2 mL, 5 min, RT) and then incubated with a secondary solution (100 μL, prepared in BSA/Gold buffer, see 5.1.1) containing fluorescence-labeled secondary antibodies for 3.5 h on an orbital shaker in the dark (humid chamber, RT). For immunofluorescence staining of PKA-RI and B56α, an additional incubation step was included to amplify fluorescence signals (Fig. 62). Thus, labeling with primary antibodies was followed by incubation with a biotinylated secondary anti-mouse antibody (100 μL, prepared in BSA/Gold buffer) for 3.5 h (humid chamber, RT) on an orbital shaker. Subsequently, dishes were washed (3x 2 mL cold DPBS for 5 min at RT) and incubated for another 3.5 h (humid chamber, RT) with a solution containing fluorescent Cy™2-conjugated streptavidin and a fluorophore-linked anti-rabbit antibody (100 μL, prepared in BSA/Gold buffer; see 5.1.1) on an orbital shaker in the dark. After fluorescence labeling, dishes were subjected to three more washes with DPBS (2 mL, 5 min, RT, in the dark). Thereafter, 4 μL Lisbeth's solution was given on a 30 mm Ø cover glass, the glass gently dropped headfirst onto the cells and subsequently fixed with nail polish. The side walls of the dishes were removed with the use of a hot wire and samples stored at 4 °C in the dark. Staining of DNA with DAPI was always performed along with fluorophore-labeling in the last incubation step. Immunofluorescent ARVMs were analyzed by confocal microscopy using the laser scanning microscope LSM 510 META or LSM 800 with Plan-NEOFLUAR 40x oil immersion objective. Images were saved as CZI file and processed using ImageJ with Fiji plugin. The same software was applied for the determination of longitudinal signal intensity distributions in a selected area of immunolabeled cardiac myocytes.

5.3.11 *In vitro* kinase assays

<u>Impact of NCA on PKA catalytic activity (non-radioactive)</u>

Active PKA catalytic subunit was diluted in kinase assay buffer 1:80 and 5 µL of the dilution incubated with ATP (100 µmol/L), the PKA inhibitor H-89 (25 µmol/L) or unsupplemented kinase assay buffer at 37 °C for 10 min. Reaction volumes amounted to 44 (ATP-treatment) or 39.1 µL (H-89-treatment and unsupplemented control), respectively. Subsequent treatment with vehicle DMSO or NCA (100 µmol/L) was performed at 37 °C for 30 min. Thereafter, ATP (100 µmol/L) was added to H-89 and unpretreated samples. The kinase reaction was started by the addition of 100 pmol of the recombinant substrate C1-M-C2 WT, which comprises the N-terminal domains of human cMyBP-C. Phosphorylation by PKA-C was allowed at 30 °C for 30 min in a final volume of 50 µL. The reaction was stopped by supplementation with 3x non-reducing Laemmli sample buffer. For each sample, a control lacking PKA-C was prepared and processed equally. Samples were analyzed by SDS-PAGE and Western immunoblotting (see 5.3.20). For the visualization of C1-M-C2 phosphorylation and total C1-M-C2, samples were reduced by the addition of 10% (v/v) β-mercaptoethanol.

The kinase assay buffer used in this experiment was prepared without DTT.

<u>Phosphorylation of C1-M-C2 proteins by various protein kinases (radioactive)</u>

Protein kinase reactions were prepared in kinase assay buffer with a final volume of 50 µL. For GSK3β, GSK3 reaction buffer was used instead. The C1-M-C2 proteins WT, Ser250Ala, Ser304Ala, 4Ala or 5Ala (100 pmol) were supplemented with active PKA catalytic subunit (1:80 in kinase assay buffer, 5 µL), PKCε (5 µL + 5 µL PKC lipid activator), PKGIα (1:80 in kinase assay buffer, 5 µL), PKD catalytic domain (1 µL), full-length PKD (1:30 in kinase assay buffer, 5 µL + 5 µL PKC lipid activator), CaMKII (3 µL activation reaction*), RSK2 (1:40 in kinase assay buffer, 5 µL), GSK3β (1 µL), ROCK1 (3:4 in kinase assay buffer, 1 µL), ROCK2 (1 µL), GRK2 (1 µL) or GRK5 (1 µL). The reaction was initiated by the addition of 5 µL of 1 mmol/L ATP containing 2.5% of radioactively labeled γ-^{32}P-ATP (3000 Ci/mmol, 10 mCi/mL). Following incubation at 30 °C for 1 h, 25 µL 3x reducing Laemmli sample buffer was added to terminate the reaction. For each reaction, a kinase free control sample was generated. Samples were resolved by SDS-PAGE (see 5.3.20) and gels stained in colloidal Coomassie solution overnight. Subsequently, background staining was reduced by incubation in colloidal Coomassie destaining solution for 45 min, gels were briefly washed in 20% glycerol (v/v), placed on chromatography paper and dried in a vacuum gel dryer for 2 h. Finally, gels were placed in an X-ray cassette and chemiluminescence films used to detect ^{32}P incorporation that reflects protein phosphorylation.

* Before application, CaMKII was activated by supplementation of 1 µL protein kinase with 1 µL ATP (10 mM), 2 µL NEBuffer™ for Protein Kinases (PK) 10X, 2 µL CaCl$_2$ (20 mM) 10X and

2 µL calmodulin (12 µM) 10X and incubation at 30 °C for 10 min in a total volume of 20 µL. All reagents were supplied with the CaMKII protein kinase.

<u>Impact of S-glutathiolation on PKD-mediated phosphorylation of C1-M-C2 WT (radioactive and non-radioactive)</u>

C1-M-C2 WT protein was treated with H_2O as control or 1 mmol/L GSSG for 30 min at RT to achieve protein S-glutathiolation. Samples were dialyzed in 500 mL kinase assay buffer for 1 h and the protein concentration determined with a NanoDrop® spectrophotometer.

Radioactive approach: In a final volume of 50 µL and in the presence of 5 µl PKC lipid activator and 5 µL of 1 mmol/L ATP spiked with 2.5% γ-^{32}P-ATP (3000 Ci/mmol, 10 mCi/mL), 100 pmol of control or S-glutathiolated protein was incubated with 5 µL of protein kinase PKD (full-length; 1:30 in kinase assay buffer) at 30 °C for 5, 15 or 30 min. The reaction was stopped by the addition of 3x reducing Laemmli sample buffer. A control set of samples (0 min treatment) did not receive PKD and was supplemented with 3x reducing Laemmli sample buffer without incubation. Samples were resolved by SDS-PAGE (see 5.3.20) and gels stained in colloidal Coomassie solution overnight. After incubation in destaining solution for 45 min and a short wash in 20% glycerol (v/v), gels were dried in a vacuum gel dryer for 2 h. Phosphorylation of C1-M-C2 WT in the dried gel was visualized by autoradiography using chemiluminescence films.

Non-radioactive approach: In a final volume of 50 µl, 100 pmol of control or S-glutathiolated C1-M-C2 WT was incubated with 5 µL of protein kinase PKD (full-length; 1:30 in kinase assay buffer) in the presence of 5 µl PKC lipid activator and 5 µL of 1 mmol/L ATP at 30 °C for 5, 15 or 30 min. The reaction was stopped by addition of 3x reducing Laemmli sample buffer. A control set of samples (0 min treatment) did not receive PKD and was supplemented with 3x reducing Laemmli sample buffer without incubation. Samples were analyzed by SDS-PAGE and Western immunoblotting (see 5.3.20).

The kinase assay buffer used in this experiment (radioactive and non-radioactive approach) was prepared without DTT.

<u>PKA-C-mediated phosphorylation of C1-M-C2 proteins for pSer250 antibody evaluation (non-radioactive)</u>

Active PKA catalytic subunit was diluted in kinase assay buffer 1:80 and 5 µL of the dilution added to 100 pmol C1-M-C2 WT, Ser250Ala, Ser250Asp, 4Ala or 5Ala protein. Reactions were performed in a final volume of 50 µL and initiated by the addition of ATP (100 µmol/L).

After incubation at 30 °C for 30 min, 3x reducing Laemmli sample buffer was added to terminate the reaction. For each sample, a control lacking PKA-C was prepared. Samples were analyzed by SDS-PAGE and Western immunoblotting (see 5.3.20).

5.3.12 Mass spectrometry (MS) analysis of human ventricular tissue samples and mouse hearts

The procedures of sample collection for human left ventricular myocardial tissue were approved by the Ethics Committee of the Medical Association of Hamburg (532/116/9.71991). Data from donor patients were handled anonymously and in accordance with the World Medical Association Declaration of Helsinki (World Medical Association 2013). DCM and ICM tissue samples were collected from patients who underwent heart transplantation, while no cardiac abnormalities were known for NF tissue donors. Patient characteristics are summarized in table 6 (see 7.1).

Mass spectrometry analysis of cardiac tissue samples from human NF, DCM or ICM ventricles or mouse hearts was performed as described by Stathopoulou et al. (2016). In brief, 10% tissue homogenates (w/v) were prepared in Tris-HCl buffer (100 mmol/L, pH 7.4) containing 1% Triton. Mouse samples were treated with GSSG (1 mmol/L) for 30 min at RT. Homogenates were centrifuged (16 000 g, 10 min), resulting pellets resuspended in Tris-HCl buffer (100 mmol/L, pH 7.4) supplemented with 50 mmol/L N-Ethylmaleimide and incubated at RT for 10 min. An additional set from mouse samples was treated with maleimide instead of N-Ethylmaleimide. After the addition of 1% SDS (applied as 20% solution) and 5% glycerol (v/v), samples were resolved by SDS-PAGE under non-reducing conditions and proteins stained in colloidal Coomassie solution. The bands corresponding to the molecular weight of cMyBP-C (150 kDa) were excised and the gel pieces destained in MS destaining solution. Subsequently, samples were digested with trypsin or chymotrypsin (sequencing grade) at 37 °C or RT, respectively, in MS digestion solution for 16 h. Peptides were collected in MS elution buffer, dried and finally resuspended in MS resolving buffer. Sample analysis was performed using the ultra-high-performance liquid chromatography (HPLC) unit Dionex UltiMate 3000 coupled to a Nanospray Flex™ Ion Source and a Q Exactive™ Plus Hybrid Quadrupole-Orbitrap™ mass spectrometer. MS data were recorded by data-dependent acquisition. Between MS scans, ten most abundant precursor ions were selected for high energy collision dissociation fragmentation to generate MS2 spectra for peptide sequencing. Selected ions were further excluded in a time frame of 30 s to gain MS2 information of lower abundant peptides. Raw Xcalibur files were analyzed by Peaks® 7 Studio software for proteomics. The modification by N-Ethylmaleimide (+125.05), *S*-glutathiolation (+305.07) on cysteines, phosphorylation on serines/threonines/tyrosines (+79.97) and oxidation on methionine (+15.99) were selected for evaluation. In mouse samples, maleimide (+97.02) was selected in addition. Peptides and proteins were identified from *de novo* sequencing of spectra by using the reviewed human reference proteome set (download from Uniprot, 2015; www.uniprot.org) or the reviewed mouse proteome set (download from Uniprot, 2014). Sample preparation was kindly performed by Friederike Cuello and Konstantina Stathopoulou. Mass

spectrometry measurements, as well as data acquisition and analysis were kindly done by Ilka Wittig.

5.3.13 Molecular weight estimation of PKA-RI dimers

Following exposure to various oxidative reagents, cultured ARVMs were harvested in 3x non-reducing Laemmli sample buffer (see 5.3.15) and samples subjected to SDS-PAGE (see 5.3.20) using precast gels with a polyacrylamide gradient of 4-15%. Two different molecular weight markers were resolved along with the samples. The electrophoresis was stopped when the dye front had reached the bottom part of the gel. Both the top of the resolving gel and the position of the dye front were labeled on the PVDF blotting membrane during the preparation of the semi-dry transfer. Subsequent to the transfer, the membrane was processed for immunodetection of PKA-RI (see 5.3.20).
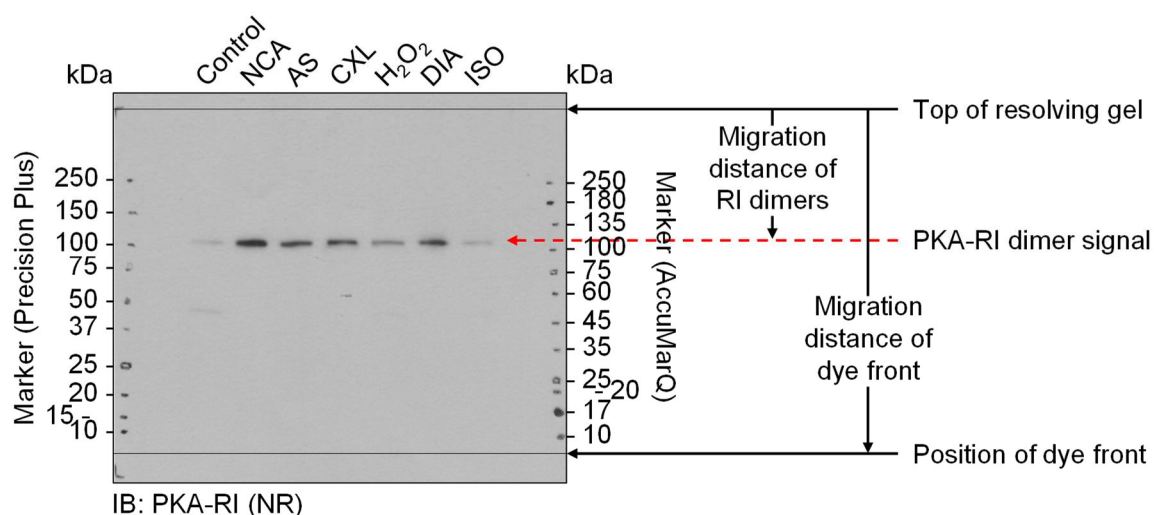
Figure 63: Illustration of protein molecular weight estimation from Western immunoblots ARVMs were exposed to various stimuli and samples, flanked by two molecular weight markers, resolved by SDS-PAGE under non-reducing (NR) conditions using precast polyacrylamide gradient gels. The top of the resolving gel and the position of the dye front were labeled on the PVDF membrane and following a semi-dry transfer, PKA-RI was detected by Western immunoblotting. The migration distance of each molecular weight marker band from the top of the resolving gel was divided by the migration distance of the dye front. Resulting retardation factors (R_f) were used to establish standard curves, where the logarithm of the molecular weight log(MW) was plotted against the corresponding R_f of each marker band. Using the functional equation from a linear curve fit from standard curves and the R_f calculated for PKA-RI dimer bands, the molecular weight of dimerized PKA-RI was estimated.

The location of molecular weight marker bands, as well as the top of the resolving gel and the position of the dye front were transferred to the resulting chemiluminescence film. From the top of the resolving gel, the migration distance of each marker band and of the dye front was measured. The corresponding R_f values, reflecting protein retardation in the gel, were calculated by the equation R_f = *migration distance of protein/migration distance of dye front* and used to establish a standard curve for each molecular weight marker by plotting the logarithm of marker band molecular weight log(MW) against R_f. From a fit with linear regression, the functional equations for both markers were generated. Eventually, migration distances of chemiluminescence signals on the film that corresponded to PKA-RI dimers were

also measured, R_f values calculated and finally inserted into the functional equations obtained from the protein markers to estimate the molecular weight of dimerized PKA-RI.

5.3.14 PEG-switch assay

The PEG-switch protocol was adapted from Burgoyne et al. (2013). Cultured ARVMs were treated with vehicle DMSO (30 min), NCA (100 µmol/L, 30 min), AS (500 µmol/L, 15 min), CXL-1020 (300 µmol/L, 15 min), H_2O_2 (100 µmol/L, 10 min), DIA (500 µmol/L, 10 min) or ISO (10 nmol/L, 10 min) at 37 °C and 7% CO_2 (Fig. 64, **1)**). After a washing step with 2 mL ice-cold Tris-HCl buffer (100 mmol/L, pH 7.4), 100 µL ice-cold harvesting buffer was pipetted on the cells and the cell culture plate frozen in liquid N_2. The ARVMs were thawed, collected and 130 µL of each lysate was incubated at 50 °C and 300 rpm for 25 min to block free thiol groups by alkylation with maleimide contained in the harvesting buffer (Fig. 64, **2)**). The residual sample volume was kept as input and one half each supplemented with 3x non-reducing or reducing Laemmli sample buffer. Maleimide from the harvesting buffer was removed by desalting with Zeba™ Spin desalting column. Desalted samples were supplemented with 50 mmol/L DTT, causing the reduction of oxidized protein thiols (Fig. 64, **3)**). Followed by 20 min incubation at RT, another desalting step was performed to remove DTT. After sequential addition of the thiol labeling reagent PEG-maleimide (2 mmol/L, 5 kDa) and 0.5% SDS (applied as 20% solution), samples were incubated on a laboratory agitator at RT for 2 h in the dark (Fig. 64, **4)**). Finally, each sample was supplemented with 3x non-reducing Laemmli sample buffer and subjected to Western immunoblot analysis (see 5.3.20). The detection of a shift in molecular weight of a protein indicated PEG-labeling and the oxidation of cysteine residues in response to the initial treatment.

Figure 64: Diagrammatic representation of the PEG-switch method After oxidant-treatment, free thiol groups of ARVM proteins were blocked with maleimide. Thiol oxidations were reversed with DTT and reduced thiols labeled with 5 kDa PEG-maleimide to induce a mass increment. Slower migrating bands in a Western immunoblot represent proteins that were oxidized by the initial treatment.

5.3.15 Pharmacological treatment of ARVMs for Western immunoblotting

In different experimental setups, cultured ARVMs (see 5.3.1) were exposed to different pharmacological stimuli. Incubation steps were performed under cell culture conditions in a CO_2 incubator at 37 °C and 7% CO_2. Cardiac myocytes were directly harvested in 150–200 µL

(in accordance with cell density) of 3x non-reducing or 3x reducing Laemmli sample buffer and subsequently subjected to SDS-PAGE and Western immunoblot analysis (see 5.3.20).

Effect of oxidants on protein oxidation and phosphorylation

ARVMs were treated with vehicle DMSO (30 min), NCA (100 µmol/L, 30 min), AS (500 µmol/L, 15 min), CXL-1020 (300 µmol/L, 15 min), H_2O_2 (100 µmol/L, 10 min), DIA (500 µmol/L, 10 min) or ISO (10 nmol/L, 10 min) and harvested in 3x non-reducing or 3x reducing Laemmli sample buffer. Samples were analyzed by SDS-PAGE, which was followed by Western immunoblot analysis (see 5.3.20) or phosphoprotein staining of the polyacrylamide gel (see 5.3.6).

The role of β-AR activation in NCA-mediated phosphorylation

ARVMs were pretreated with 1 µmol/L of the $β_1$-AR antagonist atenolol for 5 min or were left untreated. Subsequently, the cells were exposed to vehicle DMSO (30 min), NCA (100 µmol/L, 30 min) or ISO (10 nmol/L, 10 min) and harvested in 3x reducing Laemmli sample buffer.

The role of AC activation for NCA-mediated phosphorylation

ARVMs were pretreated with vehicle DMSO or 100 µmol/L of the AC type V/VI inhibitor NKY80 for 10 min, followed by incubation with vehicle DMSO (30 min), NCA (100 µmol/L, 30 min) or ISO (10 nmol/L, 10 min) and harvesting in 3x reducing Laemmli sample buffer. This experiment was in part kindly executed by Angelika Piasecki.

Effect of HNO-treatment on ISO-mediated PKA activation

ARVMs were treated with vehicle DMSO, NCA (100 µmol/L, 30 min) or CXL-1020 (300 µmol/L, 15 min) and subsequently exposed to DPBS or ISO (10 nmol/L) for 10 min. Cells were harvested in 3x reducing Laemmli sample buffer.

Time course treatment with NCA

ARVMs were treated with vehicle DMSO for 100 min, NCA (100 µmol/L) for 3, 10, 30 or 100 min or ISO (10 nmol/L) for 10 min and harvested in 3x non-reducing Laemmli sample buffer.

The role of sGC activation for CXL-1020 mediated effects

ARVMs were pretreated with vehicle DMSO or 20 µmol/L of the sGC inhibitor ODQ for 10 min, followed by incubation with vehicle DMSO (30 min), NCA (100 µmol/L, 30 min), CXL-1020 (300 µmol/L, 15 min) or ISO (10 nmol/L, 10 min). Cells were washed with 2 mL ice-cold DPBS, then PKG harvesting buffer (120 µl/well) was added and cells were frozen in liquid N_2. After thawing and harvesting, half of each lysate was supplemented with 3x non-reducing and the other with 3x reducing Laemmli sample buffer.

Comparison of protein kinase oxidation and cMyBP-C phosphorylation in response to CXL-1020 and drug G1

ARVMs were treated with vehicle DMSO (15 min), 0.2, 2 or 20 µmol/L drug G1 (15 min), 300 µmol/L CXL-1020 (15 min) or 10 nmol/L ISO (10 min). Alternatively, ARVMs were exposed to vehicle DMSO or NCA (100 µmol/L) for 30 min, CXL-1020 (1 mmol/L) or G1 (2 µmol/L) for 15 min or H_2O_2 (100 µmol/L) or ISO (10 nmol/L) for 10 min. Cells were harvested in 3x non-reducing Laemmli sample buffer.

In experiments that included drug G1, applied CXL-1020 was derived from the new vial (see 3.1.7 and 4.1.6).

Time course treatment with CXL-1020

ARVMs were treated with vehicle DMSO for 15 min, CXL-1020 (300 µmol/L) for 1, 3, 5 or 15 min or ISO (10 nmol/L) for 10 min and harvested in 3x non-reducing Laemmli sample buffer. CXL-1020 was either derived from the standard stock (old vial) or the new vial as indicated (see 3.1.8 and 4.1.6).

Concentration curve with CXL-1020

ARVMs were treated with vehicle DMSO for 15 min, CXL-1020 at concentrations of 30, 100, 300 or 1000 µmol/L for 15 min or ISO (10 nmol/L) for 10 min and harvested in 3x non-reducing Laemmli sample buffer.

CXL-1020 was either derived from the standard stock (old vial) or the new vial as indicated (see 3.1.8 and 4.1.6).

Detectability of cMyBP-C pSer250 in response to stimulating agents

ARVMs were left untreated or were exposed to H_2O_2 (100 µmol/L), DIA (500 µmol/L), ISO (10 nmol/L), PE (10 µmol/L) or ET (50 nmol/L) for 10 min. Alternatively, ARVMs were exposed to vehicle H_2O or PE (100 µmol/L) for 10 min. Cells were harvested in 3x reducing Laemmli sample buffer.

The volume of the vehicle was always matched with the volume of the applied stimulant. The time of exposure to the vehicle always corresponded to the longest duration of treatment. To analyze cells that were harvested in non-reducing Laemmli sample buffer under reducing conditions, samples were supplemented with 10% (v/v) of β-mercaptoethanol. Samples collected under reducing conditions were subjected to a boiling step (4 min, 95 °C) before analysis by SDS-PAGE and Western immunoblotting.

5.3.16 Preparation of mouse ventricular tissue samples

Powder from adult WT or *Mybpc3*-targeted KO mouse ventricles was kindly provided by Lucie Carrier. Tris-HCl buffer pH 7.4 (100 mmol/L) supplemented with protease inhibitor was applied to generate 10% (w/v) homogenates from ventricular powder. Samples were vortexed and

homogenized twice by a metal bead in a TissueLyser at 25 Hz for 30 s. Subsequently, 20% of homogenization buffer was added and lysates mixed with 3x reducing Laemmli sample buffer. Samples were analyzed by SDS-PAGE and Western immunoblotting (see 5.3.20).

5.3.17 Protein phosphatase 2A (PP2A) activity assay

The activity of protein phosphatase 2A catalytic subunit (PP2A-C) was investigated using the fluorogenic phosphatase substrate DiFMUP in a fluorescence assay. DiFMUP was prepared as 10 mmol/L stock solution in Tris-HCl buffer (50 mM, pH 7.0) and stored at -20 °C. Stock solutions of NCA (100 mmol/L), CXL-1020 (300 mmol/L) and the serine/threonine protein phosphatase inhibitor OA (10 µmol/L) were prepared in DMSO and diluted in phosphatase assay buffer to obtain solutions of 250 µmol/L, 750 µmol/L and 25 nmol/L, respectively. Of each compound, 40 µL was added to 50 µL phosphatase assay buffer containing DiFMUP (1 mmol/L) in a black 96 well plate. Recombinant human PP2A-C (specific activity: batch 1: 1.91 U/mg; batch 2: 4.25 U/mg; Unit definition: One unit of enzyme produces 1 µmol p-nitrophenol/min at 37 °C.) was prepared in phosphatase assay buffer to obtain a solution of 12.1 µU/µL. The reaction was started by the addition of 10 µL phosphatase solution (121 µU/well), resulting in a final volume of 100 µL and concentrations of 500 µmol/L DiFMUP, 100 µmol/L NCA, 300 µmol/L CXL-1020 and 10 nmol/L OA. For each sample, a phosphatase-free control was prepared and measured in parallel. The dephosphorylation of DiFMUP to fluorescent DiFMU was monitored in a safire II microplate reader at excitation/emission wavelengths of 358/455 λ for 40 min (1 read/min) at 30 °C. Average activities expressed as ΔRFU/min were calculated from the slope of a linear curve fit through the origin of the coordinate system from averaged normalized values of 5-6 independent assays.

5.3.18 Proximity ligation assay (PLA)

The Duolink® methodology was used to perform PLAs. The procedure was performed according to the manufacturer's Duolink® In Situ - Fluorescence protocol using custom solutions and reagents from the Duolink® In Situ Orange Starter Kit Mouse/Rabbit. In this method, the proximity of two intracellular proteins, which are at most 40 nm apart, is indicated by the emergence of fluorescence signals, whose detection allows to evaluate protein colocalization. After exposure to vehicle DMSO (30 min), NCA (100 µmol/L, 30 min) or ISO (10 nmol/L, 10 min) in a CO_2 incubator at 37 °C and 7% CO_2, ARVMs were skinned and fixed as described in 5.3.10. After a brief wash with 2 mL cold DPBS, the edges of the dish and the middle line were dried and made hydrophobic using a liquid blocker pen. Only one half of the culture dish was processed further and used for the experiment. To prevent unspecific binding, 50 µL NGS blocking solution was applied to the cells and incubated at RT in a humid chamber under orbital shaking for 20 min. This was followed by three washing steps with cold DPBS of 5 min each. ARVMs were incubated with pairs of primary antibodies (prepared in BSA/Gold buffer, see 5.1.1), one raised in mouse (anti-PKA-RI) and the other one in rabbit (anti-α-actinin,

anti-MLC2v or anti-cMyBP-C), in a humid chamber on an orbital shaker at 4° C overnight. The following day, the dishes were washed for 10 min with DPBS at RT twice and the humid chamber was prewarmed to 37 °C. In the meantime, the MINUS and PLUS PLA probes were mixed, diluted (per sample: 8 µL MINUS PLA probe, 8 µL PLUS PLA probe and 24 µL BSA/Gold buffer) and incubated at RT for 20 min. The PLA probe solution was then pipetted on the dish and incubated in the warm humid chamber at 37 °C for 1 h. Subsequently, dishes were washed with Buffer A for 5 min at RT twice and then incubated with the Ligation-Ligase solution (per sample: 8 µL 5x ligation stock solution, 1 µL ligase and 31 µL H_2O) in the humid chamber at 37 °C for 30 min. Dishes were then washed twice with Buffer A for 2 min at RT and incubated with the Amplification-Polymerase solution (per sample: 8 µL 5x amplification stock solution, 0.5 µL polymerase and 31.5 µL H_2O) in the darkened humid chamber at 37 °C for 100 min. Thereafter, the dishes were washed with Buffer B for 10 min twice at RT and once for 2 min with a 1:100 dilution of Buffer B. A drop of mounting medium containing DAPI was pipetted on a 30 mm Ø cover glass, which was then placed in the dish upside down. Finally, the border of the cover glass was sealed with nail polish and the side walls of the dish were removed with a hot wire. The confocal laser scanning microscope LSM 800 with Plan-NEOFLUAR 40x oil immersion objective and Cy3 filter were used for sample imaging. Recordings were performed as Z-stacks with a 2 µm interval and, additionally, brightfield images of the cardiac myocytes were obtained. Image analysis was performed using ImageJ with Fiji plugin. For the assessment of PLA signal counts, the maximum intensity projection of each Z-stack experiment was applied and thresholding was achieved by selecting the 'Intermodes' function available in the software.

PLA experiments and data analysis were kindly performed by Konstantina Stathopoulou. Incubations steps in the humid chamber at 37 °C were performed without shaking. Buffer A, Buffer B, MINUS and PLUS PLA probes, 5x ligation stock solution, ligase, 5x amplification stock solution, polymerase and the mounting medium were included in the kit.

5.3.19 Single cardiac myocyte contractility measurements

Contractile behavior of single ARVMs was recorded using an IonOptix system consisting of a pacer (MyoPacer), a camera (MyoCam) and an interface unit, which connects the components with the IonWizard software. Freshly isolated ARVMs (see 5.3.1) were equilibrated in IonOptix buffer and stored at RT for at least 1 h to allow recovery from the isolation process. After gentle inversion, 300 µL of the cell suspension was pipetted into the chamber insert of a C-Stim superfusion chamber and cardiac myocytes paced at 1 Hz (15 V, pulse duration: 4 ms). Contraction of a selected single cell was monitored under baseline conditions for at least 1 min. Subsequently, vehicle DMSO, or solutions of NCA, CXL-1020 or G1 were prediluted in IonOptix buffer and 50 µl added to the ARVMs, resulting in final concentrations of 100 µmol/L NCA, 300 µmol/L or 1 mmol/L CXL-1020 (see below) or 2 µmol/L G1, respectively. The volume

of DMSO did not exceed 0.33% of the total sample volume. When the contractile response reached a steady state, 50 µL ISO (diluted in IonOptix buffer) was added to the cells (final concentration: 10 nmol/L). The recording was stopped when the ISO-response plateaued. The parameters determined during measurements were diastolic sarcomere length (in µm), sarcomere shortening (as % of diastolic sarcomere length), maximal contraction and relaxation velocities reached (maximal change in sarcomere length over time; dL/dt max), as well as the time needed to reach maximal contraction (time to peak, in s) and the state of 50% maximal relaxation (time to baseline$_{50\%}$; in s).

The data were recorded and analyzed with the IonWizard software. In experiments involving the inhibition of sGC, ARVMs were exposed to vehicle DMSO or the inhibitor ODQ (20 µmol/L) for 10 min before cells were subjected to the measurement. To inhibit the protein kinase ROCK, prior to contractility measurements ARVMs were pretreated with vehicle H_2O or the inhibitor H1152 (1 µM) for 30 min. After preincubation with either inhibitor, baseline contractile parameters and the response to 300 µmol/L CXL-1020 and, subsequently, ISO were determined. Apart from experiments performed to compare contractile effects between CXL-1020 and drug G1, where 1 mmol/L CXL-1020 (new vial; see 3.1.7 and 4.1.6) was applied, ARVMs were consistently exposed to a final concentration of 300 µmol/L CXL-1020.

5.3.20 Sodium dodecyl sulfate-polyacrylamide gel electrophoresis (SDS-PAGE) and Western immunoblot analysis

Protein-containing samples supplemented with non-reducing or reducing Laemmli sample buffer were resolved by SDS-PAGE performed in reservoir buffer at 200 V with the use of self-made tris-glycine gels (Tab. 3).

Table 3: SDS-PAGE tris-glycine gel compositions

Reagent	Stacking gel	Resolving gel					
		6%	7.5%	9%	10.5%	12%	15%
	Volume [mL]	Volume [mL]					
Stacking buffer (4x)	2.5	-	-	-	-	-	-
Resolving buffer (4x)	-	2.5	2.5	2.5	2.5	2.5	2.5
Acrylamide solution	1.16	2	2.5	3	3.5	4	5
H_2O	6.23	5.39	4.89	4.39	3.89	3.39	2.39
10% APS	0.1	0.1	0.1	0.1	0.1	0.1	0.1
TEMED	0.01	0.01	0.01	0.01	0.01	0.01	0.01
Final volume	10	10	10	10	10	10	10

Proteins were transferred from the gel to PVDF or NC blotting membranes by semi-dry transfer. Prior to use, PVDF membranes were activated in methanol. Membranes and chromatography paper with dimensions of 5.5 x 8.5 cm each were preincubated in transfer buffer for at least 15 min and the transfer carried out at 45 mA/membrane in a semi-dry transfer unit for 2 h. Membranes were blocked in 10% milk/TBST or 5% BSA/TBST for at least 45 min. Subsequently, primary antibody solution containing the corresponding antibody for detection of the protein or protein modification of interest (see 5.1.1) was applied and membranes incubated on an orbital shaker at 4 °C overnight. After four washing steps in TBST with shaking at RT for 12 min each, membranes were incubated in secondary antibody solution (see 5.1.1) on an orbital shaker at RT for 1 h. Following another four washing steps in TBST, 1 mL/membrane of each solution from Amersham™ ECL™ Western Blotting Detection Reagents was added and membranes incubated for 2 min with gentle shaking. Excessive volume was removed and membranes placed in an X-ray cassette. In a dark room, chemiluminescence films were exposed to the immunoblot to detect light emission from HRP-conjugated secondary labeling reagents. Developing of the films was performed by gentle shaking in developer solution for 2 min, a brief wash in 5% acetic acid and fixation in fixing solution for at least 2 min. The films were then washed with H_2O, air-dried, labeled and digitized for further analyses.

Samples collected under reducing conditions were subjected to a boiling step (4 min, 95 °C) before analysis by SDS-PAGE. For the examination of samples prepared in non-reducing Laemmli sample buffer under reducing conditions, supplementation with 10% (v/v) β-mercaptoethanol was performed. Both blocking and secondary antibody solutions were prepared in accordance with the solvate used for the preparation of the primary antibody. If Wester immunoblotting was performed under non-reducing conditions, this is indicated below the presented data as 'NR'. To detect PP2A-C, membranes were demethylated in NaOH (100 mmol/L) for 30 min before blocking and subsequent incubation in a solution of primary antibody specific for demethylated PP2A-C. For the analysis of biotinylated proteins, membranes were blocked in 5% BSA/TBST at 4 °C overnight, incubated with streptavidin-HRP for 1 h on an orbital shaker at RT and washed with TBST (four times 12 min, RT) before proceeding with protein detection. The Amersham™ ECL Select™ Western Blotting Detection Reagents was applied to increase signal intensity if necessary.

5.3.21 Subcellular fractionation of ARVMs

The protocol for subcellular fractionation was adapted from (Snabaitis et al. 2006). Cultured ARVMs were treated with vehicle DMSO (30 min), NCA (100 µmol/L, 30 min), or ISO (10 nmol/L, 10 min). For NCA time course fractionation experiments, ARVMs were exposed to vehicle DMSO for 100 min, NCA (100 µmol/L) for 3, 10, 30 or 100 min or ISO (10 nmol/L) for 10 min. During treatment, cells were incubated in a CO_2 incubator at 37 °C and 7% CO_2. The

cells were washed with 2 mL ice-cold DPBS and covered with 180 µL/well ice-cold fractionation buffer. The cell culture plates or dishes were frozen in liquid N_2, thawed at RT and cells harvested into precooled reaction tubes. Lysates of equally treated ARVMs were pooled. An input sample was taken and supplemented with 3x reducing Laemmli sample buffer. Cell lysates were vortexed alternatingly for 5 min and in the meantime kept on ice. Following centrifugation at 10 000 g for 2 min at 4 °C, the supernatant comprising soluble proteins, was collected and supplemented with 3x reducing Laemmli sample buffer. The pellet was resuspended in fractionation buffer containing 1% Triton (67.5 µL/contained well of cells) by pipetting and vortexing. The samples were again centrifuged at 10 000 g for 2 min at 4 °C, the supernatant comprising Triton-soluble membrane-associated proteins was pipetted off and subsequently mixed with 3x reducing Laemmli sample buffer. Finally, the Triton-insoluble pellet containing myofilament proteins was solubilized in 3x reducing Laemmli sample buffer (67.5 µL/contained well of cells). In NCA time course fractionation experiments, Triton-insoluble proteins were isolated by one-step fractionation. This was achieved by direct harvesting of ARVMs in fractionation buffer containing 1% Triton and resuspension of the Triton-insoluble pellet, which was obtained by one centrifugation step (10 000 g, 2 min, 4 °C), in 3x reducing Laemmli sample buffer. Apart from that, the procedure was as described above. Subcellular fraction samples were analyzed by SDS-PAGE and Western immunoblotting (see 5.3.20).

To harvest cells under reducing conditions, the fractionation buffer was supplemented with DTT (5 mmol/L).

5.4 Molecular biological methods

5.4.1 Bacterial expression and purification of human C1-M-C2 proteins

By previous test-induction (see 5.4.7), a transformed BL21 Star™ bacteria colony was selected for the recombinant expression of N-terminally His_6-tagged C1-M-C2 protein, which comprises the N-terminal domains of human cMyBP-C. A preculture of 40 mL lysogeny broth (LB; containing 100 µg/mL ampicillin) was inoculated with 100 µL BL21 Star™ culture from the corresponding colony and bacteria grown overnight in a platform shaking incubator at 37 °C and 180 rpm. The preculture was then added to 280 mL LB (containing 100 µg/mL ampicillin) and placed back into the shaking incubator. When an OD_{600} of 0.8 was reached, the expression of recombinant protein was induced by the addition of 5 mmol/L isopropyl β-D-1-thiogalactopyranoside (IPTG). After incubation at 30 °C for 3 h, the bacteria culture was centrifuged at 4000 g and 4 °C for 20 min in two centrifuge bottles and the supernatant removed. Cell pellets were washed with ice-cold DPBS and then frozen in liquid N_2. A total volume of 10 mL ice-cold lysis buffer was used to resuspend the bacteria pellets on ice. Subsequently, the cell suspension was transferred into a 50 mL test tube and sonicated on ice

five times for 25 s with 20 s interval (38% power, 3 x 10% cycle), which was followed by ultracentrifugation of the cell suspension at 175 000 g and 4 °C for 35 min. In the meantime, 1 mL slurry Ni-NTA agarose beads was equilibrated in lysis buffer. The equilibrated beads were resuspended with the cleared supernatant from the bacteria cell suspension and transferred into a bottom-sealed superflow column. The residual volume of supernatant was added and the sealed column incubated for 1 h at 4 °C on a rotating mixer. Thereafter, in a cold room (4 °C) the columns were placed upright and non-bound lysate was allowed to flow through by gravity. The Ni-NTA matrix was washed with 4 mL wash buffer twice. Elution of recombinant proteins was performed by four times application of 0.5 mL elution buffer. The eluate was transferred into a dialysis tube, which was sealed and gently stirred in 500 mL dialysis buffer at 4 °C overnight. The protein solution was collected from the dialysis tube, protein concentration determined by Bradford protein assay and aliquots stored at -20 °C.

5.4.2 Bacterial transformation of DH5α™ and BL21 Star™ cells by heat shock

Transformation of Subcloning Efficiency™ DH5α™ cells was performed when the amplification of a DNA plasmid of interest was desired. For the expression of recombinant human C1-M-C2 proteins, One Shot® BL21 Star™ (DE3) chemically competent cells were used for transformation. A vial of DH5α™ or BL21 Star™ was thawed on ice and 50 µL of the cells were gently mixed with 5-10 ng of plasmid DNA that was supposed to be amplified or encoded for the desired C1-M-C2 protein, respectively. After incubation on ice for 30 min, the cells were subjected to a heat shock of 42 °C for 20 (DH5α™) or 30 s (BL21 Star™) and immediately placed back on ice. Following the addition of 250 µL SOC medium (preheated to 37 °C), the transformation reaction was incubated at 37 °C and 300 (DH5α™) or 225 rpm (BL21 Star™) for at least 1 h in a shaking incubator. Volumes of 50 and 200 µL were plated on two preheated LB agar plates (containing 100 µg/mL ampicillin) and incubated at 37 °C overnight to allow the growth of bacteria colonies.

For plasmid amplification, the transformation of DH5α™ was followed by the preparation of plasmid DNA (see 5.4.4 and 5.4.5). After the transformation of BL21 Star™, obtained bacteria colonies were applied for test-induction of recombinant C1-M-C2 protein expression (see 5.4.7).

5.4.3 Glycerol stock preparation

For long-time storage of bacteria, 600 µL of a saturated bacteria culture was added to 200 µL sterile glycerol, mixed by flicking and stored at -80 °C.

5.4.4 Preparation of plasmid DNA (large scale)

For plasmid DNA preparation from high volume bacteria cultures (250 mL), the HiSpeed® Plasmid Maxi Kit was applied following the supplier's protocol. A low volume starter culture (5 mL LB containing 100 µg/mL ampicillin) was inoculated with a single colony of DH5α™ that

was grown on an LB agar plate and contained the DNA plasmid to be enriched. After 8 h of cultivation at 37 °C and 300 rpm in a platform shaking incubator, the whole culture volume was added to 250 mL LB (containing 100 µg/mL ampicillin) and incubated at 37 °C and 300 rpm overnight. Bacteria were harvested by centrifugation at 6000 g for 15 min at 4 °C in two centrifuge bottles and cell pellets resuspended in 10 mL Buffer P1. After the addition of 10 mL Buffer P2, the solutions were mixed by inverting and incubated at RT for 5 min. Subsequently, 10 mL cold Buffer P3 was added and samples immediately mixed by inverting the tube, before the lysate was poured into the barrel of the QIAfilter cartridge. During an incubation step of 10 min at RT, the HiSpeed® Maxi tip was equilibrated with 10 mL Buffer QBT. Thereafter, the lysate was filtered into the HiSpeed® tip and allowed to pass the resin by gravity. After washing with 60 mL Buffer QC, the plasmid DNA was eluted from the HiSpeed® tip by the addition of 15 mL Buffer QF. Eluted DNA was precipitated with 10.5 mL isopropanol for 5 min at RT. The eluate/isopropanol mixture was transferred into a 30 mL syringe and filtered through an attached QIAprecipitator. Plasmid DNA bound to the QIAprecipitator was washed by passing 2 mL 70% ethanol through the syringe, then the QIAprecipitator was dried by passing air through the syringe. Finally, the QIAprecipitator was attached to a 5 mL syringe, bound DNA eluted with 350 µL H_2O and the eluate reused to repeat the eluation step another three times. The concentration of obtained plasmid DNA was measured in a NanoDrop® spectrophotometer and the sample stored at -20 °C.

5.4.5 Preparation of plasmid DNA (small scale)

Plasmid DNA preparation from low volume bacteria cultures (up to 7 mL) was performed with the use of the NucleoSpin® Plasmid kit according to the manufacturer's guidelines. A single colony of transformed DH5α™ or XL10-Gold® Ultracompetent bacteria carrying the plasmid of interest was collected from an LB agar plate with a sterile pipette tip and used to inoculate 4-7 mL LB supplemented with 100 µg/mL ampicillin. Following incubation at 37 °C and 300 rpm in a platform shaking incubator overnight, the saturated cell suspension was successively transferred into a 1.5 mL reaction tube, cells pelleted by centrifugation for 30 s and the supernatant discarded. The bacteria pellet was resuspended in 250 µL Buffer A1 by vortexing before 250 µL Buffer A2 was added. The solutions were mixed by gentle inverting followed by 5 min of incubation at RT. Subsequently, 300 µL Buffer A3 was added and the sample inverted until it turned colorless. The sample was centrifuged for 5 min and the supernatant transferred onto the silica membrane of a NucleoSpin® Plasmid column in a 2 mL collection tube. After 1 min of centrifugation, the flow-through was discarded, the membrane washed once with 500 µL Buffer AW and once with 600 µL Buffer A4 by centrifugation for 1 min before the column was dried by centrifugation for 2 min. For the elution 40 µL sterile H_2O was pipetted onto the column. After 1 min of incubation at RT, plasmid DNA was collected by centrifugation for 1 min. The collected eluate was used to repeat the elution step. The concentration of plasmid DNA in

the obtained solution was measured with a NanoDrop® spectrophotometer and the sample stored at -20 °C.

All the centrifugation steps were carried out at 11 000 g.

5.4.6 Site-directed mutagenesis of C1-M-C2-encoding plasmids

The mutagenesis of plasmids that encode for N-terminal C1-M-C2 fragments of cMyBP-C was performed with the use of the QuikChange II XL Site-Directed Mutagenesis Kit and in accordance with the manufacturer's protocol. A pET-8c vector encoding for the human N-terminally His-tagged C1-M-C2 WT protein served as starting material. The desired base exchanges were achieved by polymerase chain reaction (PCR) with linear amplification and the use of oligonucleotide primers carrying the mutations to be introduced. The PCR reaction was composed as follows (Tab. 4):

Table 4: Site-directed mutagenesis PCR composition For oligonucleotide primer sequences see 5.1.10.

Component	Stock concentration	Volume [µL]
Template plasmid DNA	10 ng/µL	1
dNTP mix*	(proprietary)	1
Mutant primer For	10 pmol/µL	1
Mutant primer Rev	10 pmol/µL	1
QuikSolution*	n/a	3
10x reaction buffer*	10x	5
Sterile H$_2$O		38
		50
+ *PfuUltra* HF DNA polymerase*	2.5 U/µL	1
		51 (final volume)

* Included in the kit.

The PCRs comprised the following incubation steps (Tab. 5):

Table 5: Site-directed mutagenesis PCR cycling parameters

Duration [min]	Temperature [°C]		Function
1	95		Denaturation (initial)
0:50	95		Denaturation
0:50	60	18x	Annealing
12	68		Elongation
7	68		Elongation (final)
∞	4		Storage

After the PCR, template plasmid was digested by the addition of 1 µL DpnI restriction enzyme (10 U/µL) to the reaction volume and subsequent incubation at 37 °C for 1 h. XL10-Gold® Ultracompetent Cells (40 µL) were thawed on ice, incubated with 2 µL XL10-Gold® β-mercaptoethanol mix for 10 min and supplemented with 4 µL DpnI-treated DNA. After 30 min

of incubation on ice, the cells were subjected to transformation by a heat shock of 42 °C for 30 s and immediately placed back on ice for another 2 min. After the addition of 250 µL SOC medium (preheated to 37 °C), the transformation reaction was placed on a shaking incubator at 1000 rpm and 37 °C for at least 1 h. Volumes of 50 and 240 µL were plated on two preheated LB agar plates (containing 100 µg/mL ampicillin) and allowed to grow at 37 °C overnight. Three colonies were collected from the LB agar plate using a sterile pipette tip and used to inoculate each 7 mL LB (containing 100 µg/mL ampicillin) in a sterile tube. Bacteria were cultivated in a platform shaking incubator at 37 °C and 300 rpm overnight. From each bacteria culture, a glycerol stock was generated (see 5.4.3) and the residual volume used for the preparation of plasmid DNA (see 5.4.5). The successful introduction of the DNA base exchange of interest was confirmed by Sanger sequencing. Plasmid samples were stored at -20 °C.

The mutated plasmid was subjected to further DNA base exchange by additional mutagenesis rounds using the corresponding oligonucleotide primers (see 5.1.10). Alternatively, the plasmid was applied to the transformation of One Shot® BL21 Star™ (DE3) chemically competent cells (see 5.4.2) and subsequent expression of the recombinant C1-M-C2 protein (see 5.4.7 and 5.4.1). The dNTP mix, QuikSolution, 10x reaction buffer, *PfuUltra* HF DNA polymerase, DpnI restriction enzyme, XL10-Gold® Ultracompetent Cells and the XL10-Gold® β-mercaptoethanol mix were included in the kit.

5.4.7   Test-induction of recombinant protein expression

Four single BL21 Star™ bacteria colonies transformed for recombinant expression of a C1-M-C2 protein (see 5.4.2) were collected from an LB agar plate with a sterile pipette tip and used to inoculate 5 mL LB (containing 100 µg/mL ampicillin) each. The bacteria cultures were incubated at 37 °C and 225 rpm in a platform shaking incubator overnight. Subsequently, two 100 µL aliquots of every culture were used to inoculate 900 µL LB each (containing 100 µg/mL ampicillin) in 1.5 mL reaction tubes. Cultures were grown in a shaking incubator at 37 °C and 225 rpm. After 1 h of incubation, one set of reaction tubes was supplemented with 5 mmol/L IPTG to induce bacterial expression of the plasmid-encoded C1-M-C2 protein. Following another 3 h of incubation, bacteria were collected by centrifugation at 16 100 g and RT for 20 min and lysed in 100 µL reducing Laemmli sample buffer. IPTG-induced recombinant protein expression was examined by SDS-PAGE followed by colloidal Coomassie staining (see 5.3.4) and Western immunoblotting using an anti-His antibody to detect His-tagged C1-M-C2 protein (see 5.3.20).

Successful identification of a bacteria colony that expresses the recombinant protein was followed by upscaled bacterial expression and subsequent purification of the C1-M-C2 protein (see 5.4.1).

5.5 Statistical analysis

Statistical comparison of data was performed by one-way ANOVA followed by Bonferroni's or Dunnett's Multiple Comparison Test or two-way ANOVA with Bonferroni post-test. For statistical comparison of two groups, paired or unpaired two-tailed t-test were applied according to suitability. The applied statistical analysis is indicated in the respective figure legend. Data are given as mean ± standard error of the mean (SEM) and a value of $P<0.05$ was considered significant.

6 Literature

Ababou A, Rostkova E, Mistry S, Le Masurier C, Gautel M, Pfuhl M (2008) Myosin binding protein C positioned to play a key role in regulation of muscle contraction: structure and interactions of domain C1. J Mol Biol, 384:615–630

Adams SR, Harootunian AT, Buechler YJ, Taylor SS, Tsien RY (1991) Fluorescence ratio imaging of cyclic AMP in single cells. Nature, 349:694–697

Allen MD, Zhang J (2006) Subcellular dynamics of protein kinase A activity visualized by FRET-based reporters. Biochem Biophys Res Commun, 348:716–21

Alonso A, Sasin J, Bottini N, Friedberg I, Friedberg I, Osterman A, Godzik A, Hunter T, Dixon J, Mustelin T (2004) Protein tyrosine phosphatases in the human genome. Cell, 117:699–711

Alyonycheva TN, Mikawa T, Reinach FC, Fischman DA (1997) Isoform-specific interaction of the myosin-binding proteins (MyBPs) with skeletal and cardiac myosin is a property of the C-terminal immunoglobulin domain. J Biol Chem, 272:20866–20872

Amatore C, Arbault S, Ducrocq C, Hu S, Tapsoba I (2007) Angeli's salt (Na2N2O3) is a precursor of HNO and NO: a voltammetric study of the reactive intermediates released by Angeli's salt decomposition. ChemMedChem, 2:898–903

Andrews KL, Irvine JC, Tare M, Apostolopoulos J, Favaloro JL, Triggle CR, Kemp-Harper BK (2009) A role for nitroxyl (HNO) as an endothelium-derived relaxing and hyperpolarizing factor in resistance arteries. Br J Pharmacol, 157:540–550

Andrews KL, Lumsden NG, Farry J, Jefferis A-M, Kemp-Harper BK, Chin-Dusting JPF (2015) Nitroxyl: a vasodilator of human vessels that is not susceptible to tolerance. Clin Sci (Lond), 129:179–187

Angeli A (1896) Sopra la nitroidrossilammina. Gazz Chim Ital, 26:17–25

Ardito F, Giuliani M, Perrone D, Troiano G, Muzio L Lo (2017) The crucial role of protein phosphorylation in cell signalingand its use as targeted therapy (Review). Int J Mol Med, 40:271–280

Banky P, Huang LJ, Taylor SS (1998) Dimerization/docking domain of the type Ialpha regulatory subunit of cAMP-dependent protein kinase. Requirements for dimerization and docking are distinct but overlapping. J Biol Chem, 273:35048–35055

Bardswell SC, Cuello F, Kentish JC, Avkiran M (2012) cMyBP-C as a promiscuous substrate: phosphorylation by non-PKA kinases and its potential significance. J Muscle Res Cell Motil, 33:53–60

Bardswell SC, Cuello F, Rowland AJ, Sadayappan S, Robbins J, Gautel M, Walker JW, Kentish JC, Avkiran M (2010) Distinct sarcomeric substrates are responsible for protein kinase D-mediated regulation of cardiac myofilament Ca2+ sensitivity and cross-bridge cycling. J Biol Chem, 285:5674–5682

Bartel S, Stein B, Eschenhagen T, Mende U, Neumann J, Schmitz W, Krause EG, Karczewski P, Scholz H (1996) Protein phosphorylation in isolated trabeculae from nonfailing and failing human hearts. Mol Cell Biochem, 157:171–179

Bartos DC, Grandi E, Ripplinger CM (2015) Ion channels in the heart. Compr Physiol, 5:1423–1464

Beebe SJ, Oyen O, Sandberg M, Frøysa A, Hansson V, Jahnsen T (1990) Molecular cloning of a tissue-specific protein kinase (Cγ) from human testis - representing a third isoform for the catalytic subunit of cAMP-dependent protein kinase. Mol Endocrinol, 4:465–475

Belch JJF, Bridges AB, Scott N, Chopra M (1991) Oxygen free radicals and congestive heart failure. Br Heart J, 65:245–248

Belletti A, Castro ML, Silvetti S, Greco T, Biondi-Zoccai G, Pasin L, Zangrillo A, Landoni G (2015) The Effect of inotropes and vasopressors on mortality: a meta-analysis of randomized clinical trials. Br J Anaesth, 115:656–675

Bergmann O, Zdunek S, Felker A, Salehpour M, Alkass K, Bernard S, Sjostrom SL, Szewczykowska M, Jackowska T, dos Remedios C, Malm T, Andrä M, Jashari R, Nyengaard JR, Possnert G, Jovinge S, Druid H, Frisén J (2015) Dynamics of Cell Generation and Turnover in the Human Heart. Cell, 161:1566–1575

Bers DM (2008) Calcium cycling and signaling in cardiac myocytes. Annu Rev Physiol, 70:23–49

Bers DM (2002) Cardiac excitation-contraction coupling. Nature, 415:198–205

Bhuiyan MS, Gulick J, Osinska H, Gupta M, Robbins J (2012) Determination of the critical residues responsible for cardiac myosin binding protein C's interactions. J Mol Cell Cardiol, 53:838–847

Bistola V, Chioncel O (2017) Inotropes in acute heart failure. CCE, 3:107–116

Bjelakovic G, Nikolova D, Gluud C (2014) Antioxidant supplements and mortality. Curr Opin Clin Nutr Metab Care, 17:40–44

Blumenthal DK, Stull JT, Gill GN (1978) Phosphorylation of cardiac troponin by guanosine 3':5'-monophosphate-dependent protein kinase. J Biol Chem, 253:324–326

Bonner FT, Ravid B (1975) Thermal decomposition of oxyhyponitrite (sodium trioxodinitrate(II)) in aqueous solution. Inorg Chem, 14:558–563

Bossuyt J, Chang C-W, Helmstadter K, Kunkel MT, Newton AC, Campbell KS, Martin JL, Bossuyt S, Robia SL, Bers DM (2011) Spatiotemporally distinct protein kinase D activation in adult cardiomyocytes in response to phenylephrine and endothelin. J Biol Chem, 286:33390–33400

Brennan JP, Bardswell SC, Burgoyne JR, Fuller W, Schröder E, Wait R, Begum S, Kentish JC, Eaton P (2006a) Oxidant-induced activation of type I protein kinase A is mediated by RI subunit interprotein disulfide bond formation. J Biol Chem, 281:21827–21836

Brennan JP, Miller JIA, Fuller W, Wait R, Begum S, Dunn MJ, Eaton P (2006b) The utility of N,N-biotinyl glutathione disulfide in the study of protein S-glutathiolation. Mol Cell Proteomics, 5:215–225

Brennan JP, Wait R, Begum S, Bell JR, Dunn MJ, Eaton P (2004) Detection and mapping of widespread intermolecular protein disulfide formation during cardiac oxidative stress using proteomics with diagonal electrophoresis. J Biol Chem, 279:41352–41360

Bristow MR, Ginsburg R, Minobe W, Cubicciotti RS, Sageman WS, Lurie K, Billingham ME, Harrison DC, Stinson EB (1982) Decreased catecholamine sensitivity and β-adrenergic-receptor density in failing human hearts. N Engl J Med, 307:205–211

Broillet MC (1999) S-nitrosylation of proteins. Cell Mol Life Sci, 55:1036–1042

Bubis J, Vedvick TS, Taylor SS (1987) Antiparallel alignment of the two protomers of the regulatory subunit dimer of cAMP-dependent protein kinase I. J Biol Chem, 262:14961–14966

Bünemann M, Gerhardstein BL, Gao T, Hosey MM (1999) Functional regulation of L-type calcium channels via protein kinase A- mediated phosphorylation of the β2 subunit. J Biol Chem, 274:33851–33854

Burgoyne JR, Eaton P (2010) Oxidant sensing by protein kinases A and G enables integration of cell redox state with phosphoregulation. Sensors (Basel), 10:2731–2751

Burgoyne JR, Madhani M, Cuello F, Charles RL, Brennan JP, Schröder E, Browning DD, Eaton P (2007) Cysteine redox sensor in PKGIa enables oxidant-induced activation. Science, 317:1393–1397

Burgoyne JR, Mongue-Din H, Eaton P, Shah AM (2012) Redox signaling in cardiac physiology and pathology. Circ Res, 111:1091–1106

Burgoyne JR, Oviosu O, Eaton P (2013) The PEG-switch assay: a fast semi-quantitative

method to determine protein reversible cysteine oxidation. J Pharmacol Toxicol Methods, 68:297–301

Burgoyne JR, Prysyazhna O, Richards DA, Eaton P (2017) Proof of Principle for a Novel Class of Antihypertensives That Target the Oxidative Activation of PKG Iα (Protein Kinase G Iα). Hypertension, 70:577–586

Burgoyne JR, Rudyk O, Cho H, Prysyazhna O, Hathaway N, Weeks A, Evans R, Ng T, Schröder K, Brandes RP, Shah AM, Eaton P (2015) Deficient angiogenesis in redox-dead Cys17Ser PKARIα knock-in mice. Nat Commun, 6:7920

Butterfield DA, Hardas SS, Bader Lange ML (2010) Oxidatively modified glyceraldehyde-3-phosphate dehydrogenase (GAPDH) and Alzheimer disease: many pathways to neurodegeneration. J Alzheimers Dis, 20:369–393

Cadd GG, McKnight GS (1989) Distinct patterns of cAMP-dependent protein kinase gene expression in mouse brain. Neuron, 3:71–79

Calore C, De Bortoli M, Romualdi C, Lorenzon A, Angelini A, Basso C, Thiene G, Iliceto S, Rampazzo A, Melacini P (2015) A founder MYBPC3 mutation results in HCM with a high risk of sudden death after the fourth decade of life. J Med Genet, 52:338–347

Carlisle Michel JJ, Dodge KL, Wong W, Mayer NC, Langeberg LK, Scott JD (2004) PKA-phosphorylation of PDE4D3 facilitates recruitment of the mAKAP signalling complex. Biochem J, 381:587–592

Carr DW, Stofko-Hahn RE, Fraser IDC, Bishop SM, Acott TS, Brennan RG, Scott JD (1991) Interaction of the regulatory subunit (RII) of cAMP-dependent protein kinase with RII-anchoring proteins occurs through an amphipathic helix binding motif. J Biol Chem, 266:14188–14192

Carrier L, Knöll R, Vignier N, Keller DI, Bausero P, Prudhon B, Isnard R, Ambroisine M-L, Fiszman M, Ross J, Schwartz K, Chien KR (2004) Asymmetric septal hypertrophy in heterozygous cMyBP-C null mice. Cardiovasc Res, 63:293–304

Carrier L, Mearini G, Stathopoulou K, Cuello F (2015) Cardiac myosin-binding protein C (MYBPC3) in cardiac pathophysiology. Gene, 573:188–197

Cazorla O, Szilagyi S, Vignier N, Salazar G, Krämer E, Vassort G, Carrier L, Lacampagne A (2006) Length and protein kinase A modulations of myocytes in cardiac myosin binding protein C-deficient mice. Cardiovasc Res, 69:370–380

Chen MJ, Dixon JE, Manning G (2017) Genomics and evolution of protein phosphatases. Sci Signal, 10:eaag1796

Cheong E, Tumbev V, Abramson J, Salama G, Stoyanovsky DA (2005) Nitroxyl triggers Ca2+ release from skeletal and cardiac sarcoplasmic reticulum by oxidizing ryanodine receptors. Cell Calcium, 37:87–96

Chung HS, Wang S-B, Venkatraman V, Murray CI, Van Eyk JE (2013) Cysteine oxidative posttranslational modifications: emerging regulation in the cardiovascular system. Circ Res, 112:382–392

CIBIS II Investigators and Committees (1999) The Cardiac Insufficiency Bisoprolol Study II (CIBIS-II): a randomised trial. Lancet, 353:9–13

Clegg CH, Cadd GG, Mcknight GS (1988) Genetic characterization of a brain-specific form of the type I regulatory subunit of cAMP-dependent protein kinase. Proc Natl Acad Sci U S A, 85:3703–3707

Cole A, Frame S, Cohen P (2004) Further evidence that the tyrosine phosphorylation of glycogen synthase kinase-3 (GSK3) in mammalian cells is an autophosphorylation event. Biochem J, 377:249–255

Cooke R (1997) Actomyosin interaction in striated muscle. Physiol Rev, 77:671–697

Copeland O, Sadayappan S, Messer AE, Steinen GJM, van der Velden J, Marston SB (2010) Analysis of cardiac myosin binding protein-C phosphorylation in human heart muscle. J Mol Cell Cardiol, 49:1003–1011

Corbin JD, Keely SL, Park CR (1975) The distribution and dissociation of cyclic adenosine 3':5' monophosphate dependent protein kinases in adipose, cardiac, and other tissues. J Biol Chem, 250:218–225

Corbin JD, Sugden PH, Lincoln TM, Keely SL (1977) Compartmentalization of adenosine 3':5'-monophosphate and adenosine 3':5'-monophosphate-dependent protein kinase in heart

tissue. J Biol Chem, 252:3854–3861

Couto N, Wood J, Barber J (2016) The role of glutathione reductase and related enzymes on cellular redox homoeostasis network. Free Radic Biol Med, 95:27–42

Craig R, Lee KH, Mun JY, Torre I, Luther PK (2014) Structure, sarcomeric organization, and thin filament binding of cardiac myosin-binding protein-C. Pflugers Arch, 466:425–431

Cuello F, Bardswell SC, Haworth RS, Ehler E, Sadayappan S, Kentish JC, Avkiran M (2011) Novel role for p90 ribosomal S6 kinase in the regulation of cardiac myofilament phosphorylation. J Biol Chem, 286:5300–5310

Cuello F, Wittig I, Lorenz K, Eaton P (2018) Oxidation of cardiac myofilament proteins: Priming for dysfunction? Mol Aspects Med, 63:47–58

Dai T, Tian Y, Tocchetti CG, Katori T, Murphy AM, Kass DA, Paolocci N, Gao WD (2007) Nitroxyl increases force development in rat cardiac muscle. J Physiol, 580:951–960

Dalle-Donne I, Rossi R, Colombo G, Giustarini D, Milzani A (2009) Protein S-glutathionylation: a regulatory device from bacteria to humans. Trends Biochem Sci, 34:85–96

Defer N, Best-Belpomme M, Hanoune J (2000) Tissue specificity and physiological relevance of various isoforms of adenylyl cyclase. Am J Physiol Renal Physiol, 279:F400–F416

DeGrande ST, Little SC, Nixon DJ, Wright P, Snyder J, Dun W, Murphy N, Kilic A, Higgins R, Binkley PF, Boyden PA, Carnes CA, Anderson ME, Hund TJ, Mohler PJ (2013) Molecular mechanisms underlying cardiac protein phosphatase 2A regulation in heart. J Biol Chem, 288:1032–1046

Dejam A, Hunter CJ, Schechter AN, Gladwin MT (2004) Emerging role of nitrite in human biology. Blood Cells Mol Dis, 32:423–429

Dewald O, Frangogiannis NG, Zoerlein M, Duerr GD, Klemm C, Knuefermann P, Taffet G, Michael LH, Crapo JD, Welz A, Entman ML (2003) Development of murine ischemic cardiomyopathy is associated with a transient inflammatory reaction and depends on reactive oxygen species. Proc Natl Acad Sci U S A, 100:2700–2705

DiFrancesco D (2010) The role of the funny current in pacemaker activity. Circ Res, 106:434–446

DiFrancesco D, Borer JS (2007) The funny current: cellular basis for the control of heart rate. Drugs, 67:15–24

Diviani D, Dodge-Kafka KL, Li J, Kapiloff MS (2011) A-kinase anchoring proteins: scaffolding proteins in the heart. Am J Physiol Heart Circ Physiol, 301:H1742–H1753

Donzelli S, Fischer G, King BS, Niemann C, DuMond JF, Heeren J, Wieboldt H, Baldus S, Gerloff C, Eschenhagen T, Carrier L, Boger RH, Espey MG (2013) Pharmacological Characterization of 1-Nitrosocyclohexyl Acetate, a Long-Acting Nitroxyl Donor That Shows Vasorelaxant and Antiaggregatory Effects. J Pharmacol Exp Ther, 344:339–347

Donzelli S, Goetz M, Schmidt K, Wolters M, Stathopoulou K, Diering S, Prysyazhna O, Polat V, Scotcher J, Dees C, Subramanian H, Butt E, Kamynina A, Schobesberger S, King SB, Nikolaev VO, de Wit C, Leichert LI, Feil R, Eaton P, Cuello F (2017) Oxidant sensor in the cGMP-binding pocket of PKGIα regulates nitroxyl-mediated kinase activity. Sci Rep, 7:9938

Doyle MP, Mahapatro SN, Broene RD, Guy JK (1988) Oxidation and reduction of hemoproteins by trioxodinitrate(II). The role of nitrosyl hydride and nitrite. J Am Chem Soc, 110:593–599

El-Armouche A, Eschenhagen T (2009) Beta-adrenergic stimulation and myocardial function in the failing heart. Heart Fail Rev, 14:225–241

El-Armouche A, Pamminger T, Ditz D, Zolk O, Eschenhagen T (2004) Decreased protein and phosphorylation level of the protein phosphatase inhibitor-1 in failing human hearts. Cardiovasc Res, 61:87–93

El-Armouche A, Pohlmann L, Schlossarek S, Starbatty J, Yeh Y-H, Nattel S, Dobrev D, Eschenhagen T, Carrier L (2007) Decreased phosphorylation levels of cardiac myosin-binding protein-C in human and experimental heart failure. J Mol Cell Cardiol, 43:223–229

El-Armouche A, Wahab A, Wittköpper K, Schulze T, Böttcher F, Pohlmann L, King SB, DuMond JF, Gerloff C, Böger RH, Eschenhagen T, Carrier L, Donzelli S (2010) The new HNO donor, 1-nitrosocyclohexyl acetate, increases contractile force in normal and β-

adrenergically desensitized ventricular myocytes. Biochem Biophys Res Commun, 402:340–344

England J, Loughna S (2013) Heavy and light roles: myosin in the morphogenesis of the heart. Cell Mol Life Sci, 70:1221–1239

Eschenhagen T (2008) Beta-adrenergic signaling in heart failure-adapt or die. Nat Med, 14:485–487

Fagerberg L, Hallström BM, Oksvold P, Kampf C, Djureinovic D, Odeberg J, Habuka M, Tahmasebpoor S, Danielsson A, Edlund K, Asplund A, Sjöstedt E, Lundberg E, Szigyarto CA-K, Skogs M, Takanen JO, Berling H, Tegel H, Mulder J, Nilsson P, Schwenk JM, Lindskog C, Danielsson F, Mardinoglu A, Sivertsson A, von Feilitzen K, Forsberg M, Zwahlen M, Olsson I, Navani S, Huss M, Nielsen J, Ponten F, Uhlén M (2014) Analysis of the human tissue-specific expression by genome-wide integration of transcriptomics and antibody-based proteomics. Mol Cell Proteomics, 13:397–406

Farah CS, Reinach FC (1995) The troponin complex and regulation of muscle contraction. FASEB J, 9:755–767

Felker GM, O'Connor CM, Braunwald E (2009) Loop diuretics in acute decompensated heart failure: necessary? Evil? A necessary evil? Circ Heart Fail, 2:56–62

Fert-Bober J, Sokolove J (2014) Proteomics of citrullination in cardiovascular disease. Proteomics Clin Appl, 8:522–533

Finichiu PG, Larsen DS, Evans C, Larsen L, Bright TP, Robb EL, Trnka J, Prime TA, James AM, Smith RAJ, Murphy MP (2015) A mitochondria-targeted derivative of ascorbate: MitoC. Free Radic Biol Med, 89:668–678

First EA, Taylor SS (1989) Selective modification of the catalytic subunit of cAMP-dependent protein kinase with sulfhydryl-specific fluorescent probes. Biochemistry, 28:3598–3605

Fitts RH (2008) The cross-bridge cycle and skeletal muscle fatigue. J Appl Physiol, 104:551–558

Foley TD, Kintner ME (2005) Brain PP2A is modified by thiol-disulfide exchange and intermolecular disulfide formation. Biochem Biophys Res Commun, 330:1224–1229

Foley TD, Petro LA, Stredny CM, Coppa TM (2007) Oxidative inhibition of protein phosphatase 2A activity: role of catalytic subunit disulfides. Neurochem Res, 32:1957–1964

Forman HJ, Zhang H, Rinna A (2009) Glutathione: overview of its protective roles, measurement, and biosynthesis. Mol Aspects Med, 30:1–12

Francis SH, Corbin JD (1994) Structure and function of cyclic nucleotide-dependent protein kinases. Annu Rev Physiol, 56:237–272

Frank D, Frey N (2011) Cardiac Z-disc signaling network. J Biol Chem, 286:9897–9904

Froehlich JP, Mahaney JE, Keceli G, Pavlos CM, Goldstein R, Redwood AJ, Sumbilla C, Lee DI, Tocchetti CG, Kass DA, Paolocci N, Toscano JP (2008) Phospholamban thiols play a central role in activation of the cardiac muscle sarcoplasmic reticulum calcium pump by nitroxyl. Biochemistry, 47:13150–13152

Fukuto JM, Carrington SJ (2011) HNO signaling mechanisms. Antioxid Redox Signal, 14:1649–1657

Fukuto JM, Chiang K, Hszieh R, Wong P, Chaudhuri G (1992) The pharmacological activity of nitroxyl: a potent vasodilator with activity similar to nitric oxide and/or endothelium-derived relaxing factor. J Pharmacol Exp Ther, 263:546–551

Fürst DO, Nave R, Osborn M, Weber K (1989) Repetitive titin epitopes with a 42 nm spacing coincide in relative position with known A band striations also identified by major myosin-associated proteins. An immunoelectron-microscopical study on myofibrils. J Cell Sci, 94:119–125

Fürst DO, Vinkemeier U, Weber K (1992) Mammalian skeletal muscle C-protein: purification from bovine muscle, binding to titin and the characterization of a full-length human cDNA. J Cell Sci, 102:769–778

Gambaryan S, Butt E, Kobsar A, Geiger J, Rukoyatkina N, Parnova R, Nikolaev VO, Walter U (2012) The oligopeptide DT-2 is a specific PKG i inhibitor only in vitro, not in living cells. Br J Pharmacol, 167:826–838

Gane EJ, Weilert F, Orr DW, Keogh GF, Gibson M, Lockhart MM, Frampton CM, Taylor KM, Smith RAJ, Murphy MP (2010) The mitochondria-targeted anti-oxidant mitoquinone

decreases liver damage in a phase II study of hepatitis C patients. Liver Int, 30:1019–1026

Gao T, Yatani A, Dell'Acqua ML, Sako H, Green SA, Dascal N, Scott JD, Hosey MM (1997) cAMP-dependent regulation of cardiac L-type Ca2+ channels requires membrane targeting of PKA and phosphorylation of channel subunits. Neuron, 19:185–196

Gao WD, Murray CI, Tian Y, Zhong X, DuMond JF, Shen X, Stanley BA, Foster DB, Wink DA, King SB, Van Eyk JE, Paolocci N (2012) Nitroxyl-mediated disulfide bond formation between cardiac myofilament cysteines enhances contractile function. Circ Res, 111:1002–1011

Garvey JL, Kranias EG, Solaro RJ (1988) Phosphorylation of C-protein, troponin I and phospholamban in isolated rabbit hearts. Biochem J, 249:709–714

Gautel M, Zuffardi O, Freiburg A, Labeit S (1995) Phosphorylation switches specific for the cardiac isoform of myosin binding protein-C: a modulator of cardiac contraction? EMBO J, 14:1952–1960

Geiselhöringer A, Gaisa M, Hofmann F, Schlossmann J (2004) Distribution of IRAG and cGKI-isoforms in murine tissues. FEBS Lett, 575:19–22

Giordano FJ (2005) Oxygen, oxidative stress, hypoxia, and heart failure. J Clin Invest, 115:500–508

Gladwin MT, Schechter AN, Kim-Shapiro DB, Patel RP, Hogg N, Shiva S, Cannon RO, Kelm M, Wink DA, Espey MG, Oldfield EH, Pluta RM, Freeman BA, Lancaster JR, Feelisch M, Lundberg JO (2005) The emerging biology of the nitrite anion. Nat Chem Biol, 1:308–314

Govada L, Carpenter L, da Fonseca PCA, Helliwell JR, Rizkallah P, Flashman E, Chayen NE, Redwood C, Squire JM (2008) Crystal structure of the C1 domain of cardiac myosin binding protein-C: implications for hypertrophic cardiomyopathy. J Mol Biol, 378:387–397

Govindan S, Sarkey J, Ji X, Sundaresan NR, Gupta MP, de Tombe PP, Sadayappan S (2012) Pathogenic properties of the N-terminal region of cardiac myosin binding protein-C in vitro. J Muscle Res Cell Motil, 33:17–30

Granzier HL, Irving TC (1995) Passive tension in cardiac muscle: contribution of collagen, titin, microtubules, and intermediate filaments. Biophys J, 68:1027–1044

Gruen M, Gautel M (1999) Mutations in β-myosin S2 that cause familial hypertrophic cardiomyopathy (FHC) abolish the interaction with the regulatory domain of myosin-binding protein-C. J Mol Biol, 286:933–949

Gruen M, Prinz H, Gautel M (1999) cAPK-phosphorylation controls the interaction of the regulatory domain of cardiac myosin binding protein C with myosin-S2 in an on-off fashion. FEBS Lett, 453:254–259

Gupta MK, Gulick J, James J, Osinska H, Lorenz JN, Robbins J (2013) Functional dissection of myosin binding protein C phosphorylation. J Mol Cell Cardiol, 64:39–50

Gupta MK, Robbins J (2014) Post-translational control of cardiac hemodynamics through myosin binding protein C. Pflugers Arch, 466:231–236

Gupta RC, Mishra S, Rastogi S, Imai M, Habib O, Sabbah HN (2003) Cardiac SR-coupled PP1 activity and expression are increased and inhibitor 1 protein expression is decreased in failing hearts. Am J Physiol Heart Circ Physiol, 285:H2373–H2381

Guzman-Villanueva D, Mendiola MR, Nguyen HX, Weissig V (2015) Influence of Triphenylphosphonium (TPP) Cation Hydrophobization with Phospholipids on Cellular Toxicity and Mitochondrial Selectivity. Symbiosis. doi: 10.15226/2374-6866/2/1/00121

Hansen A, Eder A, Bönstrup M, Flato M, Mewe M, Schaaf S, Aksehirlioglu B, Schwörer A, Uebeler J, Eschenhagen T (2010) Development of a drug screening platform based on engineered heart tissue. Circ Res, 107:35–44

Harootunian AT, Adams SR, Wen W, Meinkoth JL, Taylor SS, Tsien RY (1993) Movement of the free catalytic subunit of cAMP-dependent protein kinase into and out of the nucleus can be explained by diffusion. Mol Biol Cell, 4:993–1002

Harris SP, Bartley CR, Hacker TA, McDonald KS, Douglas PS, Greaser ML, Powers PA, Moss RL (2002) Hypertrophic cardiomyopathy in cardiac myosin binding protein-C knockout mice. Circ Res, 90:594–601

Hartman JC, del Rio CL, Reardon JE, Zhang K, Sabbah HN (2018) Intravenous Infusion of the Novel HNO Donor BMS-986231 Is Associated With Beneficial Inotropic, Lusitropic, and

Vasodilatory Properties in 2 Canine Models of Heart Failure. JACC Basic Transl Sci, 3:625–638

Hartzell HC, Sale WS (1985) Structure of C protein purified from cardiac muscle. J Cell Biol, 100:208–215

Heijman J, Dewenter M, El-Armouche A, Dobrev D (2013) Function and regulation of serine/threonine phosphatases in the healthy and diseased heart. J Mol Cell Cardiol, 64:90–98

Hess DT, Matsumoto A, Kim SO, Marshall HE, Stamler JS (2005) Protein S-nitrosylation: purview and parameters. Nat Rev Mol Cell Biol, 6:150–166

Hill BG, Bhatnagar A (2012) Protein S-glutathiolation: redox-sensitive regulation of protein function. J Mol Cell Cardiol, 52:559–567

Hofmann PA, Greaser ML, Moss RL (1991) C-protein limits shortening velocity of rabbit skeletal muscle fibres at low levels of Ca2+ activation. J Physiol, 439:701–715

Huang LJ, Durick K, Weiner JA, Chun J, Taylor SS (1997) Identification of a novel protein kinase A anchoring protein that binds both type I and type II regulatory subunits. J Biol Chem, 272:8057–8064

Humphries KM, Deal MS, Taylor SS (2005) Enhanced dephosphorylation of cAMP-dependent protein kinase by oxidation and thiol modification. J Biol Chem, 280:2750–2758

Humphries KM, Juliano C, Taylor SS (2002) Regulation of cAMP-dependent protein kinase activity by glutathionylation. J Biol Chem, 277:43505–43511

Huxley AF, Niedergerke R (1954) Measurement of muscle striations in stretch and contraction. J Physiol, 124:46–47P

Huxley HE, Brown W (1967) The low-angle x-ray diagram of vertebrate striated muscle and its behaviour during contraction and rigor. J Mol Biol, 30:383–434

Huxley HE, Hanson J (1954) Changes in the cross-striations of muscle during contraction and stretch and their structural interpretation. Nature, 173:973–976

Hwang NR, Yim S-H, Kim YM, Jeong J, Song EJ, Lee Y, Lee JH, Choi S, Lee K-J (2009) Oxidative modifications of glyceraldehyde-3-phosphate dehydrogenase play a key role in its multiple cellular functions. Biochem J, 423:253–264

Ide T, Tsutsui H, Kinugawa S, Utsumi H, Kang D, Hattori N, Uchida K, Arimura KI, Egashira K, Takeshita A (1999) Mitochondrial electron transport complex I is a potential source of oxygen free radicals in the failing myocardium. Circ Res, 85:357–363

Ikehara T, Imamura S, Sano T, Nakashima J, Kuniyoshi K, Oshiro N, Yoshimoto M, Yasumoto T (2009) The effect of structural variation in 21 microcystins on their inhibition of PP2A and the effect of replacing cys269 with glycine. Toxicon, 54:539–544

Irvine JC, Favaloro JL, Widdop RE, Kemp-Harper BK (2007) Nitroxyl anion donor, Angeli's salt, does not develop tolerance in rat isolated aortae. Hypertension, 49:885–892

Janssens V, Goris J (2001) Protein phosphatase 2A: a highly regulated family of serine/threonine phosphatases implicated in cell growth and signalling. Biochem J, 353:417–439

Jeacocke SA, England PJ (1980) Phosphorylation of a myofibrillar protein of Mr 150 000 in perfused rat heart, and the tentative identification of this as C-protein. FEBS Lett, 122:129–132

Jia W, Shaffer JF, Harris SP, Leary JA (2010) Identification of novel protein kinase A phosphorylation sites in the M-domain of human and murine cardiac myosin binding protein-C using mass spectrometry analysis. J Proteome Res, 9:1843–1853

Jideama NM, Crawford BH, Hussain AA, Raynor RL (2006) Dephosphorylation specificities of protein phosphatase for cardiac troponin I, troponin T, and sites within troponin T. Int J Biol Sci, 2:1–9

Johnston AS, Lehnart SE, Burgoyne JR (2015) Ca(2+) signaling in the myocardium by (redox) regulation of PKA/CaMKII. Front Pharmacol, 6:166

Jones JD, O'Connor CD (2011) Protein acetylation in prokaryotes. Proteomics, 11:3012–3022

Kasahara H, Itoh M, Sugiyama T, Kido N, Hayashi H, Saito H, Tsukita S, Kato N (1994) Autoimmune myocarditis induced in mice by cardiac C-protein. Cloning of complementary DNA encoding murine cardiac C-protein and partial characterization of the antigenic peptides. J Clin Invest, 94:1026–1036

Katrukha IA (2013) Human cardiac troponin complex. Structure and functions. Biochemistry (Mosc), 78:1447–1465

Katz AM (2006) Physiology of the Heart, Fourth Edition. Lippincott Williams & Wilkins, Philadelphia

Kelso GF, Porteous CM, Coulter C V, Hughes G, Porteous WK, Ledgerwood EC, Smith RAJ, Murphy MP (2001) Selective targeting of a redox-active ubiquinone to mitochondria within cells: antioxidant and antiapoptotic properties. J Biol Chem, 276:4588–4596

Kennelly PJ, Krebs EG (1991) Consensus sequences as substrate specificity determinants for protein kinases and protein phosphatases. J Biol Chem, 266:15555–15558

Kentish JC, McCloskey DT, Layland J, Palmer S, Leiden JM, Martin AF, Solaro RJ (2001) Phosphorylation of troponin I by protein kinase A accelerates relaxation and crossbridge cycle kinetics in mouse ventricular muscle. Circ Res, 88:1059–1065

Kim C, Xuong N-H, Taylor SS (2005) Crystal structure of a complex between the catalytic and regulatory (RIα) subunits of PKA. Science, 307:690–696

Kim HW, Steenaart NAE, Ferguson DG, Kranias EG (1990) Functional reconstitution of the cardiac sarcoplasmic reticulum Ca2+-ATPase with phospholamban in phospholipid vesicles. J Biol Chem, 265:1702–1709

Klauck TM, Faux MC, Labudda K, Langeberg LK, Jaken S, Scott JD (1996) Coordination of three signaling enzymes by AKAP79, a mammalian scaffold protein. Science, 271:1589–1592

Klomsiri C, Karplus PA, Poole LB (2011) Cysteine-based redox switches in enzymes. Antioxid Redox Signal, 14:1065–77

Knighton DR, Zheng J, Ten Eyck LF, Ashford VA, Xuong N-H, Taylor SS, Sowadski JM (1991) Crystal structure of the catalytic subunit of cyclic adenosine monophosphate-dependent protein kinase. Science, 253:407–414

Kobayashi T, Solaro RJ (2005) Calcium, thin filaments, and the integrative biology of cardiac contractility. Annu Rev Physiol, 67:39–67

Kohr MJ, Aponte AM, Sun J, Wang G, Murphy E, Gucek M, Steenbergen C (2011) Characterization of potential S-nitrosylation sites in the myocardium. Am J Physiol Heart Circ Physiol, 300:H1327–H1335

Kohr MJ, Kaludercic N, Tocchetti CG, Dong Gao W, Kass DA, Janssen PML, Paolocci N, Ziolo MT (2010) Nitroxyl enhances myocyte Ca2+ transients by exclusively targeting SR Ca2+-cycling. Front Biosci (Elite Ed), 2:614–626

Kohr MJ, Wang H, Wheeler DG, Velayutham M, Zweier JL, Ziolo MT (2008) Targeting of phospholamban by peroxynitrite decreases β-adrenergic stimulation in cardiomyocytes. Cardiovasc Res, 77:353–361

Kooij V, Holewinski RJ, Murphy AM, Van Eyk JE (2013) Characterization of the cardiac myosin binding protein-C phosphoproteome in healthy and failing human hearts. J Mol Cell Cardiol, 60:116–120

Kosower NS, Kosower EM, Wertheim B, Correa WS (1969) Diamide, a new reagent for the intracellular oxidation of glutathione to the disulfide. Biochem Biophys Res Commun, 37:593–596

Krall J, Taskén K, Staheli J, Jahnsen T, Movsesian MA (1999) Identification and quantitation of cAMP-dependent protein kinase R subunit isoforms in subcellular fractions of failing human myocardium. J Mol Cell Cardiol, 31:971–980

Kulikovskaya I, McClellan G, Flavigny J, Carrier L, Winegrad S (2003) Effect of MyBP-C binding to actin on contractility in heart muscle. J Gen Physiol, 122:761–774

Kumar NT, Liestøl K, Løberg EM, Reims HM, Mæhlen J (2014) Postmortem heart weight: relation to body size and effects of cardiovascular disease and cancer. Cardiovasc Pathol, 23:5–11

Kuster DWD, Sequeira V, Najafi A, Boontje NM, Wijnker PJM, Witjas-Paalberends ER, Marston SB, dos Remedios CG, Carrier L, Demmers JAA, Redwood C, Sadayappan S, van der Velden J (2013) GSK3β phosphorylates newly identified site in the proline-alanine-rich region of cardiac myosin-binding protein C and alters cross-bridge cycling kinetics in human: short communication. Circ Res, 112:633–639

Lancel S, Zhang J, Evangelista A, Trucillo MP, Tong X, Siwik DA, Cohen RA, Colucci WS

(2009) Nitroxyl activates SERCA in cardiac myocytes via glutathiolation of cysteine 674. Circ Res, 104:720–723

Layland J, Li JM, Shah AM (2002) Role of cyclic GMP-dependent protein kinase in the contractile response to exogenous nitric oxide in rat cardiac myocytes. J Physiol, 540:457–467

León DA, Herberg FW, Banky P, Taylor SS (1997) A stable α-helical domain at the N terminus of the RIα subunits of cAMP-dependent protein kinase is a novel dimerization/docking motif. J Biol Chem, 272:28431–28437

Lin BL, Song T, Sadayappan S (2017) Myofilaments: Movers and Rulers of the Sarcomere. Compr Physiol, 7:675–692

Lin EQ, Irvine JC, Cao AH, Alexander AE, Love JE, Patel R, McMullen JR, Kaye DM, Kemp-Harper BK, Ritchie RH (2012) Nitroxyl (HNO) stimulates soluble guanylyl cyclase to suppress cardiomyocyte hypertrophy and superoxide generation. PLoS One, 7:e34892

Lohse MJ, Engelhardt S, Eschenhagen T (2003) What is the role of beta-adrenergic signaling in heart failure? Circ Res, 93:896–906

Lovelock JD, Monasky MM, Jeong EM, Lardin HA, Liu H, Patel BG, Taglieri DM, Gu L, Kumar P, Pokhrel N, Zeng D, Belardinelli L, Sorescu D, Solaro RJ, Dudley SC jr. (2012) Ranolazine improves cardiac diastolic dysfunction through modulation of myofilament calcium sensitivity. Circ Res, 110:841–850

Lubbers ER, Mohler PJ (2016) Roles and regulation of protein phosphatase 2A (PP2A) in the heart. J Mol Cell Cardiol, 101:127–133

Luther PK (2009) The vertebrate muscle Z-disc: sarcomere anchor for structure and signalling. J Muscle Res Cell Motil, 30:171–185

Luther PK, Bennett PM, Knupp C, Craig R, Padrón R, Harris SP, Patel J, Moss RL (2008) Understanding the organisation and role of myosin binding protein C in normal striated muscle by comparison with MyBP-C knockout cardiac muscle. J Mol Biol, 384:60–72

Lygren B, Carlson CR, Santamaria K, Lissandron V, McSorley T, Litzenberg J, Lorenz D, Wiesner B, Rosenthal W, Zaccolo M, Taskén K, Klussmann E (2007) AKAP complex regulates Ca2+ re-uptake into heart sarcoplasmic reticulum. EMBO Rep, 8:1061–1067

MacDougall LK, Jones LR, Cohen P (1991) Identification of the major protein phosphatases in mammalian cardiac muscle which dephosphorylate phospholamban. Eur J Biochem, 196:725–734

Madamanchi A (2007) Beta-adrenergic receptor signaling in cardiac function and heart failure. Mcgill J Med, 10:99–104

Maller C, Schröder E, Eaton P (2011) Glyceraldehyde 3-phosphate dehydrogenase is unlikely to mediate hydrogen peroxide signaling: studies with a novel anti-dimedone sulfenic acid antibody. Antioxid Redox Signal, 14:49–60

Mallis RJ, Hamann MJ, Zhao W, Zhang T, Hendrich S, Thomas JA (2002) Irreversible thiol oxidation in carbonic anhydrase III: protection by S-glutathiolation and detection in aging rats. Biol Chem, 383:649–662

Mannhardt I, Saleem U, Benzin A, Schulze T, Klampe B, Eschenhagen T, Hansen A (2017) Automated Contraction Analysis of Human Engineered Heart Tissue for Cardiac Drug Safety Screening. J Vis Exp. doi: 10.3791/55461

Manning G, Whyte DB, Martinez R, Hunter T, Sudarsanam S (2002) The protein kinase complement of the human genome. Science, 298:1912–1934

Maragos CM, Morley D, Wink DA, Dunams TM, Saavedra JE, Hoffman A, Bove AA, Isaac L, Hrabie A, Keefer LK (1991) Complexes of .NO with nucleophiles as agents for the controlled biological release of nitric oxide. Vasorelaxant effects. J Med Chem, 34:3242–3247

Maruyama K, Yoshioka T, Higuchi H, Ohashi K, Kimura S, Natori R (1985) Connectin filaments link thick filaments and Z lines in frog skeletal muscle as revealed by immunoelectron microscopy. J Cell Biol, 101:2167–2172

Marx SO, Reiken S, Hisamatsu Y, Jayaraman T, Burkhoff D, Rosemblit N, Marks AR (2000) PKA phosphorylation dissociates FKBP12.6 from the calcium release channel (ryanodine receptor): defective regulation in failing hearts. Cell, 101:365–376

Mason JT, O'Leary TJ (1991) Effects of formaldehyde fixation on protein secondary structure:

a calorimetric and infrared spectroscopic investigation. J Histochem Cytochem, 39:225–229

Mattfeldt T, Krämer KL, Zeitz R, Mall G (1986) Stereology of myocardial hypertrophy induced by physical exercise. Virchows Arch A Pathol Anat Histopathol, 409:473–484

Mearini G, Stimpel D, Geertz B, Weinberger F, Krämer E, Schlossarek S, Mourot-Filiatre J, Stoehr A, Dutsch A, Wijnker PJM, Braren I, Katus HA, Müller OJ, Voit T, Eschenhagen T, Carrier L (2014) Mybpc3 gene therapy for neonatal cardiomyopathy enables long-term disease prevention in mice. Nat Commun, 5:5515

Medzihradszky KF, Darula Z, Perlson E, Fainzilber M, Chalkley RJ, Ball H, Greenbaum D, Bogyo M, Tyson DR, Bradshaw RA, Burlingame AL (2004) O-sulfonation of serine and threonine: mass spectrometric detection and characterization of a new posttranslational modification in diverse proteins throughout the eukaryotes. Mol Cell Proteomics, 3:429–440

Meister A (1988) Glutathione metabolism and its selective modification. J Biol Chem, 263:17205–17208

Messer AE, Jacques AM, Marston SB (2007) Troponin phosphorylation and regulatory function in human heart muscle: dephosphorylation of Ser23/24 on troponin I could account for the contractile defect in end-stage heart failure. J Mol Cell Cardiol, 42:247–259

Meyer-Roxlau S, Lämmle S, Opitz A, Künzel S, Joos JP, Neef S, Sekeres K, Sosalla ST, Schöndube F, Alexiou K, Maier LS, Dobrev D, Guan K, Weber S, El-Armouche A (2017) Differential regulation of protein phosphatase 1 (PP1) isoforms in human heart failure and atrial fibrillation. Basic Res Cardiol, 112:43

Miller ER 3rd, Pastor-Barriuso R, Dalal D, Riemersma RA, Appel LJ, Guallar E (2005) Meta-analysis: high-dosage vitamin E supplementation may increase all-cause mortality. Ann Intern Med, 142:37–46

Mitroka S, Shoman ME, DuMond JF, Bellavia L, Aly OM, Abdel-Aziz M, Kim-Shapiro DB, King SB (2013) Direct and nitroxyl (HNO)-mediated reactions of acyloxy nitroso compounds with the thiol-containing proteins glyceraldehyde 3-phosphate dehydrogenase and alkyl hydroperoxide reductase subunit C. J Med Chem, 56:6583–6592

Mittal M, Siddiqui MR, Tran K, Reddy SP, Malik AB (2014) Reactive oxygen species in inflammation and tissue injury. Antioxid Redox Signal, 20:1126–1167

Mittmann K, Jaquet K, Heilmeyer LMG jr. (1990) A common motif of two adjacent phosphoserines in bovine, rabbit and human cardiac troponin I. FEBS Lett, 273:41–45

Moolman-Smook J, Flashman E, de Lange W, Li Z, Corfield V, Redwood C, Watkins H (2002) Identification of novel interactions between domains of Myosin binding protein-C that are modulated by hypertrophic cardiomyopathy missense mutations. Circ Res, 91:704–711

Moos C, Offer G, Starr R, Bennett P (1975) Interaction of C-protein with myosin, myosin rod and light meromyosin. J Mol Biol, 97:1–9

Nag AC (1980) Study of non-muscle cells of the adult mammalian heart: a fine structural analysis and distribution. Cytobios, 28:41–61

Nagayama T, Takimoto E, Sadayappan S, Mudd JO, Seidman J, Robbins J, Kass DA (2007) Control of in vivo left ventricular [correction] contraction/relaxation kinetics by myosin binding protein C: protein kinase A phosphorylation-dependent and -independent regulation. Circulation, 116:2399–2408

Nakajima H, Amano W, Fujita A, Fukuhara A, Azuma Y-T, Hata F, Inui T, Takeuchi T (2007) The active site cysteine of the proapoptotic protein glyceraldehyde-3-phosphate dehydrogenase is essential in oxidative stress-induced aggregation and cell death. J Biol Chem, 282:26562–26574

National Research Council (US) Committee for the Update of the Guide for the Care and Use of Laboratory Animals (2011) Guide for the Care and Use of Laboratory Animals. 8th edition

Nishimaru K, Tanaka Y, Tanaka H, Shigenobu K (2003) Inhibition of agonist-induced positive inotropy by a selective Rho-associated kinase inhibitor, Y-27632. J Pharmacol Sci, 92:424–427

O'Connell TD, Jensen BC, Baker AJ, Simpson PC (2013) Cardiac alpha1-adrenergic receptors: novel aspects of expression, signaling mechanisms, physiologic function, and

clinical importance. Pharmacol Rev, 66:308–333

Offer G, Moos C, Starr R (1973) A new protein of the thick filaments of vertebrate skeletal myofibrils. Extractions, purification and characterization. J Mol Biol, 74:653–676

Okagaki T, Weber FE, Fischman DA, Vaughan KT, Mikawa T, Reinach FC (1993) The major myosin-binding domain of skeletal muscle MyBP-C (C protein) resides in the COOH-terminal, immunoglobulin C2 motif. J Cell Biol, 123:619–626

Osborne BW, Wu J, McFarland CJ, Nickl CK, Sankaran B, Casteel DE, Woods VL, Kornev AP, Taylor SS, Dostmann WR (2011) Crystal structure of cGMP-dependent protein kinase reveals novel site of interchain communication. Structure, 19:1317–1327

Packer M (1993) The development of positive inotropic agents for chronic heart failure: how have we gone astray? J Am Coll Cardiol, 22:119A–126A

Packer M, Carver JR, Rodeheffer RJ, Ivanhoe RJ, DiBianco R, Zeldis SM, Hendrix GH, Bommer WJ, Elkayam U, Kukin ML, Mallis GI, Sollano JA, Shannon J, Tandon PK, DeMets DL (1991) Effect of oral milrinone on mortality in severe chronic heart failure. N Engl J Med, 325:1468–1475

Page E (1978) Quantitative ultrastructural analysis in cardiac membrane physiology. Am J Physiol, 235:C147–C158

Paolocci N, Jackson MI, Lopez BE, Miranda K, Tocchetti CG, Wink DA, Hobbs AJ, Fukuto JM (2007) The pharmacology of nitroxyl (HNO) and its therapeutic potential: not just the Janus face of NO. Pharmacol Ther, 113:442–458

Paolocci N, Katori T, Champion HC, St. John ME, Miranda KM, Fukuto JM, Wink DA, Kass DA (2003) Positive inotropic and lusitropic effects of HNO/NO- in failing hearts: independence from beta-adrenergic signaling. Proc Natl Acad Sci U S A, 100:5537–5542

Paolocci N, Saavedra WF, Miranda KM, Martignani C, Isoda T, Hare JM, Espey MG, Fukuto JM, Feelisch M, Wink DA, Kass DA (2001) Nitroxyl anion exerts redox-sensitive positive cardiac inotropy in vivo by calcitonin gene-related peptide signaling. Proc Natl Acad Sci U S A, 98:10463–10468

Perry S V, Cole HA (1974) Phosphorylation of troponin and the effects of interactions between the components of the complex. Biochem J, 141:733–743

Petersen JW, Felker GM (2008) Inotropes in the management of acute heart failure. Crit Care Med, 36:S106–S111

Pohlmann L, Kröger I, Vignier N, Schlossarek S, Krämer E, Coirault C, Sultan KR, El-Armouche A, Winegrad S, Eschenhagen T, Carrier L (2007) Cardiac myosin-binding protein C is required for complete relaxation in intact myocytes. Circ Res, 101:928–938

Posner JB, Stern R, Krebs EG (1965) Effects of electrical stimulation and epinephrine on muscle phosphorylase, phosphorylase b kinase, and adenosine 3' ,5'-phosphate. J Biol Chem, 240:982–985

Potter LR, Abbey-Hosch S, Dickey DM (2006) Natriuretic peptides, their receptors, and cyclic guanosine monophosphate-dependent signaling functions. Endocr Rev 27:47–72

Potter RL, Taylor SS (1980) The structural domains of cAMP-dependent protein kinase I. Characterization of two sites of proteolytic cleavage and homologies to cAMP-dependent protein kinase II. J Biol Chem, 255:9706–9712

Pyriochou A, Papapetropoulos A (2005) Soluble guanylyl cyclase: more secrets revealed. Cell Signal, 17:407–413

Rajashree R, Blunt BC, Hofmann PA (2005) Modulation of myosin phosphatase targeting subunit and protein phosphatase 1 in the heart. Am J Physiol Heart Circ Physiol, 289:H1736–H1743

Rao RK, Clayton LW (2002) Regulation of protein phosphatase 2A by hydrogen peroxide and glutathionylation. Biochem Biophys Res Commun, 293:610–616

Raulf A, Horder H, Tarnawski L, Geisen C, Ottersbach A, Röll W, Jovinge S, Fleischmann BK, Hesse M (2015) Transgenic systems for unequivocal identification of cardiac myocyte nuclei and analysis of cardiomyocyte cell cycle status. Basic Res Cardiol, 110:33

Reynolds JG, McCalmon SA, Tomczyk T, Naya FJ (2007) Identification and mapping of protein kinase A binding sites in the costameric protein myospryn. Biochim Biophys Acta, 1773:891–902

Robertson SP, Johnson JD, Holroyde MJ, Kranias EG, Potter JD, Solaro RJ (1982) The effect

of troponin I phosphorylation on the Ca2+-binding properties of the Ca2+-regulatory site of bovine cardiac troponin. J Biol Chem, 257:260–263

Rodriguez EK, Hunter WC, Royce MJ, Leppo MK, Douglas AS, Weisman HF (1992) A method to reconstruct myocardial sarcomere lengths and orientations at transmural sites in beating canine hearts. Am J Physiol, 263:H293--H306

Roof SR, Ueyama Y, Mazhari R, Hamlin RL, Hartman JC, Ziolo MT, Reardon JE, del Rio CL (2017) CXL-1020, a novel nitroxyl (HNO) prodrug, is more effective than milrinone in models of diastolic dysfunction-a cardiovascular therapeutic: an efficacy and safety study in the rat. Front Physiol, 8:894

Rowe RWD (1973) The ultrastructure of Z disks from white, intermediate, and red fibers of mammalian striated muscles. J Cell Biol, 57:261–277

Rudyk O, Eaton P (2014) Biochemical methods for monitoring protein thiol redox states in biological systems. Redox Biol, 2:803–813

Russell MA, Lund LM, Haber R, McKeegan K, Cianciola N, Bond M (2006) The intermediate filament protein, synemin, is an AKAP in the heart. Arch Biochem Biophys, 456:204–215

Russwurm M, Koesling D (2004) NO activation of guanylyl cyclase. EMBO J, 23:4443–4450

Sabbah HN, Tocchetti CG, Wang M, Daya S, Gupta RC, Tunin RS, Mazhari R, Takimoto E, Paolocci N, Cowart D, Colucci WS, Kass DA (2013) Nitroxyl (HNO): A novel approach for the acute treatment of heart failure. Circ Heart Fail, 6:1250–1258

Sabine B, Willenbrock R, Haase H, Karczewski P, Wallukat G, Dietz R, Krause EG (1995) Cyclic GMP-mediated phospholamban phosphorylation in intact cardiomyocytes. Biochem Biophys Res Commun, 214:75–80

Sadayappan S, de Tombe PP (2012) Cardiac myosin binding protein-C: redefining its structure and function. Biophys Rev, 4:93–106

Sadayappan S, Gulick J, Osinska H, Martin LA, Hahn HS, Dorn GW 2nd, Klevitsky R, Seidman CE, Seidman JG, Robbins J (2005) Cardiac myosin-binding protein-C phosphorylation and cardiac function. Circ Res, 97:1156–1163

Sadayappan S, Gulick J, Osinska H, Barefield D, Cuello F, Avkiran M, Lasko VM, Lorenz JN, Maillet M, Martin JL, Brown JH, Bers DM, Molkentin JD, James J, Robbins J (2011) A critical function for Ser-282 in cardiac myosin binding protein-C phosphorylation and cardiac function. Circ Res, 109:141–150

Sadayappan S, Osinska H, Klevitsky R, Lorenz JN, Sargent M, Molkentin JD, Seidman CE, Seidman JG, Robbins J (2006) Cardiac myosin binding protein C phosphorylation is cardioprotective. Proc Natl Acad Sci U S A, 103:16918–16923

Sandberg M, Natarajan V, Ronander I, Kalderon D, Walter U, Lohmann SM, Jahnsen T (1989) Molecular cloning and predicted full-length amino acid sequence of the type Iβ isozyme of cGMP-dependent protein kinase from human placenta. Tissue distribution and developmental changes in rat. FEBS Lett, 255:321–329

Santana LF, Cheng EP, Lederer WJ (2010) How does the shape of the cardiac action potential control calcium signaling and contraction in the heart? J Mol Cell Cardiol, 49:901–903

Santos CXC, Raza S, Shah AM (2016) Redox signaling in the cardiomyocyte: From physiology to failure. Int J Biochem Cell Biol, 74:145–151

Satoh M, Ogita H, Takeshita K, Mukai Y, Kwiatkowski DJ, Liao JK (2006) Requirement of Rac1 in the development of cardiac hypertrophy. Proc Natl Acad Sci U S A, 103:7432–7437

Schlender KK, Bean LJ (1991) Phosphorylation of chicken cardiac C-protein by calcium/calmodulin-dependent protein kinase II. J Biol Chem, 266:2811–2817

Schlender KK, Hegazy MG, Thysseril TJ (1987) Dephosphorylation of cardiac myofibril C-protein by protein phosphatase 1 and protein phosphatase 2A. Biochim Biophys Acta, 928:312–319

Scott JD, McCartney S (1994) Localization of A-kinase through anchoring proteins. Mol Endocrinol, 8:5–11

Scott JD, Stofko RE, McDonald JR, Comer JD, Vitalis EA, Mangili JA (1990) Type II regulatory subunit dimerization determines the subcellular localization of the cAMP-dependent protein kinase. J Biol Chem, 265:21561–21566

Sequeira V, Witjas-Paalberends ER, Kuster DWD, van der Velden J (2014) Cardiac myosin-binding protein C: hypertrophic cardiomyopathy mutations and structure–function

relationships. Pflugers Arch, 466:201–206

Sha X, Isbell TS, Patel RP, Day CS, King SB (2006) Hydrolysis of acyloxy nitroso compounds yields nitroxyl (HNO). J Am Chem Soc, 128:9687–9692

Shafirovich V, Lymar SV (2002) Nitroxyl and its anion in aqueous solutions: spin states, protic equilibria, and reactivities toward oxygen and nitric oxide. Proc Natl Acad Sci U S A, 99:7340–7345

Shi Y (2009) Serine/threonine phosphatases: mechanism through structure. Cell, 139:468–484

Shoman ME, Dumond JF, Isbell TS, Crawford JH, Brandon A, Honovar J, Vitturi DA, White CR, Patel RP, King SB (2011) Acyloxy nitroso compounds as nitroxyl (HNO) donors: kinetics, reactions with thiols, and vasodilation properties. J Med Chem, 54:1059–1070

Sivakumaran V, Stanley BA, Tocchetti CG, Ballin JD, Caceres V, Zhou L, Keceli G, Rainer PP, Lee DI, Huke S, Ziolo MT, Kranias EG, Toscano JP, Wilson GM, O'Rourke B, Kass DA, Mahaney JE, Paolocci N (2013) HNO enhances SERCA2a activity and cardiomyocyte function by promoting redox-dependent phospholamban oligomerization. Antioxid Redox Signal, 19:1185–1197

Snabaitis AK, D'Mello R, Dashnyam S, Avkiran M (2006) A novel role for protein phosphatase 2A in receptor-mediated regulation of the cardiac sarcolemmal Na+/H+exchanger NHE1. J Biol Chem, 281:20252–20262

Snow BJ, Rolfe FL, Lockhart MM, Frampton CM, O'Sullivan JD, Fung V, Smith RAJ, Murphy MP, Taylor KM (2010) A double-blind, placebo-controlled study to assess the mitochondria-targeted antioxidant MitoQ as a disease-modifying therapy in Parkinson's disease. Mov Disord, 25:1670–1674

Solaro RJ (2008) Multiplex kinase signaling modifies cardiac function at the level of sarcomeric proteins. J Biol Chem, 283:26829–26833

Squire JM, Luther PK, Knupp C (2003) Structural evidence for the interaction of C-protein (MyBP-C) with actin and sequence identification of a possible actin-binding domain. J Mol Biol, 331:713–724

Starr R, Offer G (1971) Polypeptide chains of intermediate molecular weight in myosin preparations. FEBS Lett, 15:40–44

Starr R, Offer G (1978) The interaction of C-protein with heavy meromyosin and subfragment-2. Biochem J, 171:813–816

Stathopoulou K, Wittig I, Heidler J, Piasecki A, Richter F, Diering S, van der Velden J, Buck F, Donzelli S, Schröder E, Wijnker PJM, Voigt N, Dobrev D, Sadayappan S, Eschenhagen T, Carrier L, Eaton P, Cuello F (2016) S-glutathiolation impairs phosphoregulation and function of cardiac myosin-binding protein C in human heart failure. FASEB J, 30:1849–1864

Stelzer JE, Patel JR, Moss RL (2006) Protein kinase A-mediated acceleration of the stretch activation response in murine skinned myocardium is eliminated by ablation of cMyBP-C. Circ Res, 99:884–890

Stöhr A (2012) Murine engineered heart tissue (EHT) as a tool for modeling cardiac diseases and angiogenesis screening (Doctoral dissertation). Retrieved from http://ediss.sub.uni-hamburg.de/volltexte/2012/5939/pdf/Dissertation.pdf

Sugamura K, Keaney JF jr. (2011) Reactive oxygen species in cardiovascular disease. Free Radic Biol Med, 51:978–992

Sugden PH (2003) An overview of endothelin signaling in the cardiac myocyte. J Mol Cell Cardiol, 35:871–886

Sumandea CA, Garcia-Cazarin ML, Bozio CH, Sievert GA, Balke CW, Sumandea MP (2011) Cardiac troponin T, a sarcomeric AKAP, tethers protein kinase a at the myofilaments. J Biol Chem, 286:530–541

Tada M, Kirchberger MA (1976) Significance of the membrane protein phospholamban in cyclic AMP-mediated regulation of calcium transport by sarcoplasmic reticulum. Recent Adv Stud Cardiac Struct Metab, 11:265–272

Takeuchi T, Takahashi N, Ishi K, Kusayanagi T, Kuramochi K, Sugawara F (2009) Antitumor antibiotic fostriecin covalently binds to cysteine-269 residue of protein phosphatase 2A catalytic subunit in mammalian cells. Bioorg Med Chem, 17:8113–8122

Takimoto E, Kass DA (2007) Role of oxidative stress in cardiac hypertrophy and remodeling. Hypertension, 49:241–248

Tang Y, Nyengaard JR, Andersen JB, Baandrup U, Gundersen HJG (2009) The application of stereological methods for estimating structural parameters in the human heart. Anat Rec, 292:1630–1647

Taylor SS, Kim C, Cheng CY, Brown SHJ, Wu J, Kannan N (2008) Signaling through cAMP and cAMP-dependent protein kinase: diverse strategies for drug design. Biochim Biophys Acta, 1784:16–26

Teirlinck CH, Senni F, Malti R El, Majoor-Krakauer D, Fellmann F, Millat G, André-Fouët X, Pernot F, Stumpf M, Boutarin J, Bouvagnet P (2012) A human MYBPC3 mutation appearing about 10 centuries ago results in a hypertrophic cardiomyopathy with delayed onset, moderate evolution but with a risk of sudden death. BMC Med Genet, 13:105

Teruya T, Simizu S, Kanoh N, Osada H (2005) Phoslactomycin targets cysteine-269 of the protein phosphatase 2A catalytic subunit in cells. FEBS Lett, 579:2463–2468

Thavarajah R, Mudimbaimannar VK, Elizabeth J, Rao UK, Ranganathan K (2012) Chemical and physical basics of routine formaldehyde fixation. J Oral Maxillofac Pathol, 16:400–405

Thoonen R, Giovanni S, Govindan S, Lee DI, Wang GR, Calamaras TD, Takimoto E, Kass DA, Sadayappan S, Blanton RM (2015) Molecular Screen Identifies Cardiac Myosin-Binding Protein-C as a Protein Kinase G-Iα Substrate. Circ Heart Fail, 8:1115–1122

Tocchetti CG, Stanley BA, Murray CI, Sivakumaran V, Donzelli S, Mancardi D, Pagliaro P, Gao WD, van Eyk J, Kass DA, Wink DA, Paolocci N (2011) Playing with cardiac "redox switches": the "HNO way" to modulate cardiac function. Antioxid Redox Signal, 14:1687–1698

Tocchetti CG, Wang W, Froehlich JP, Huke S, Aon MA, Wilson GM, Di Benedetto G, O'Rourke B, Gao WD, Wink DA, Toscano JP, Zaccolo M, Bers DM, Valdivia HH, Cheng H, Kass DA, Paolocci N (2007) Nitroxyl improves cellular heart function by directly enhancing cardiac sarcoplasmic reticulum Ca2+ cycling. Circ Res, 100:96–104

Trnka J, Elkalaf M, Anděl M (2015) Lipophilic triphenylphosphonium cations inhibit mitochondrial electron transport chain and induce mitochondrial proton leak. PLoS One, 10:e0121837

Tsutsui H, Kinugawa S, Matsushima S (2011) Oxidative stress and heart failure. Am J Physiol Heart Circ Physiol, 301:H2181–H2190

Vahebi S, Kobayashi T, Warren CM, de Tombe PP, Solaro RJ (2005) Functional effects of Rho-kinase-dependent phosphorylation of specific sites on cardiac troponin. Circ Res, 96:740–747

Valko M, Rhodes CJ, Moncol J, Izakovic M, Mazur M (2006) Free radicals, metals and antioxidants in oxidative stress-induced cancer. Chem Biol Interact, 160:1–40

Vermij SH, Abriel H, van Veen TAB (2017) Refining the molecular organization of the cardiac intercalated disc. Cardiovasc Res, 113:259–275

Walsh DA, Perkins JP, Krebs EG (1968) An adenosine 3',5'-monophosphate-dependant protein kinase from rabbit skeletal muscle. J Biol Chem, 243:3763–3765

Weber FE, Vaughan KT, Reinach FC, Fischman DA (1993) Complete sequence of human fast-type and slow-type muscle myosin-binding-protein C (MyBP-C). Differential expression, conserved domain structure and chromosome assignment. Eur J Biochem, 216:661–669

Wegener AD, Simmerman HKB, Lindemann JP, Jones LR (1989) Phospholamban phosphorylation in intact ventricles. Phosphorylation of serine 16 and threonine 17 in response to β-adrenergic stimulation. J Biol Chem, 264:11468–11474

Wegener JW, Nawrath H, Wolfsgruber W, Kühbandner S, Werner C, Hofmann F, Feil R (2002) cGMP-dependent protein kinase I mediates the negative inotropic effect of cGMP in the murine myocardium. Circ Res, 90:18–20

Wink DA, Miranda KM, Katori T, Mancardi D, Thomas DD, Ridnour L, Espey MG, Feelisch M, Colton CA, Fukuto JM, Pagliaro P, Kass DA, Paolocci N (2003) Orthogonal properties of the redox siblings nitroxyl and nitric oxide in the cardiovascular system: a novel redox paradigm. Am J Physiol Heart Circ Physiol, 285:H2264–H2276

Wolhuter K, Whitwell HJ, Switzer CH, Burgoyne JR, Timms JF, Eaton P (2018) Evidence against Stable Protein S-Nitrosylation as a Widespread Mechanism of Post-translational Regulation. Mol Cell, 69:438–450.e5

Wong PS-Y, Hyun J, Fukuto JM, Shirota FN, DeMaster EG, Shoeman DW, Nagasawa HT (1998) Reaction between S-nitrosothiols and thiols: generation of nitroxyl (HNO) and subsequent chemistry. Biochemistry, 37:5362–5371

World Health Organization (2017) Cardiovascular diseases (CVDs). http://www.who.int/news-room/fact-sheets/detail/cardiovascular-diseases-(cvds). Accessed 26 Nov 2018

World Medical Association (2013) World Medical Association Declaration of Helsinki: ethical principles for medical research involving human subjects. JAMA, 310:2191–2194

Xiao L, Pimental DR, Amin JK, Singh K, Sawyer DB, Colucci WS (2001) MEK1/2–ERK1/2 mediates α1-adrenergic receptor-stimulated hypertrophy in adult rat ventricular myocytes. J Mol Cell Cardiol, 33:779–787

Yang L, Liu G, Zakharov SI, Bellinger AM, Mongillo M, Marx SO (2007) Protein kinase G phosphorylates Cav1.2 α1c and β2 subunits. Circ Res, 101:465–474

Yasuda M, Koshida S, Sato N, Obinata T (1995) Complete primary structure of chicken cardiac C-protein (MyBP-C) and its expression in developing striated muscles. J Mol Cell Cardiol, 27:2275–2286

Yin X, Cuello F, Mayr U, Hao Z, Hornshaw M, Ehler E, Avkiran M, Mayr M (2010) Proteomics analysis of the cardiac myofilament subproteome reveals dynamic alterations in phosphatase subunit distribution. Mol Cell Proteomics, 9:497–509

Zaremba R, Merkus D, Hamdani N, Lamers JMJ, Paulus WJ, dos Remedios C, Duncker DJ, Stienen GJM, van der Velden J (2007) Quantitative analysis of myofilament protein phosphorylation in small cardiac biopsies. Proteomics - Clin Appl, 1:1285–1290

Zhang J, Ma Y, Taylor SS, Tsien RY (2001) Genetically encoded reporters of protein kinase A activity reveal impact of substrate tethering. Proc Natl Acad Sci U S A, 98:14997–15002

Zhou P, Pu WT (2016) Recounting Cardiac Cellular Composition. Circ Res, 118:368–370

Zhu G, Groneberg D, Sikka G, Hori D, Ranek MJ, Nakamura T, Takimoto E, Paolocci N, Berkowitz DE, Friebe A, Kass DA (2015) Soluble guanylate cyclase is required for systemic vasodilation but not positive inotropy induced by nitroxyl in the mouse. Hypertension, 65:385–392

Zick SK, Taylor SS (1982) Interchain disulfide bonding in the regulatory subunit of cAMP-dependent protein kinase I. J Biol Chem, 257:2287–2293.

Zima AV, Mazurek SR (2016) Functional impact of ryanodine receptor oxidation on intracellular calcium regulation in the heart. Rev Physiol Biochem Pharmacol, 171:39–62

7 Appendix

7.1 Supplemental information

Table 6: Patient characteristics of ventricular tissue donors The patient data from donors of ventricular tissue analyzed by mass spectrometry (MS) was previously published by Stathopoulou et al. (2016). SAH: subarachnoid hemorrhage, DCM: dilated cardiomyopathy, ICM: ischemic cardiomyopathy, M: male, NYHA: New York Heart Association, nd: not determined, A: angiotensin-converting enzyme inhibitors or angiotensin receptor blockers, D: diuretics, G: cardiac glycosides, N: nitrates, R: antiarrhythmics (except β-blockers)

Sample	Diagnosis	Sex	Age	NYHA class	Drug
NF	SAH	M	44	-	nd
DCM	DCM	M	60	IV	ADGN
ICM	ICM	M	64	IV	DNR

7.2   List of used hazardous substances according to GHS

Substance	Hazard symbol	Hazard Statements	Precautionary Statements
Acetic acid		226, 290, 314	210, 280, 301+330+331, 305+351+338, 308+310
Acetone		225, 319, 336	210, 240, 305+351+338, 403+233
Acetonitrile		225, 302+312+332, 319	210, 240, 302+352, 305+351+338, 403+233
Acrylamide		301, 312, 332, 315, 317, 319, 340, 350, 361f, 372	201, 280, 302+352. 304+340, 305+351+338, 308+310
Ammonium bicarbonate		302	301+312, 330
Ammonium persulfate		272, 302, 315, 317, 319, 334, 335	220, 261, 280, 305+351+338, 342+311
Ampicillin		315, 317, 319, 334, 335	261, 280, 305+351+338, 342+311
Calcium chloride		319	305+351+338
Carbon dioxide		280	403
Diamide		315, 319, 335	264, 302+352, 304+340, 305+351+338, 332+313, 337+313
Digitonin		301, 311, 330	260, 280, 284, 310
1,4-Dithiothreitol		302, 315, 319, 335	261, 305+351+338

Ethidium bromide		302, 330, 341	260, 281, 284, 310
Ethylenediamine-tetraacetic acid		319	305+351+338
N-Ethylmaleimide		300, 311, 314, 317	264, 280, 301+310, 305+351+338, 310
Formic acid		226, 302, 314, 331	210, 280, 303+361+353, 304+340+310, 305+351+338, 403+233
Hydrochloric acid		290, 314, 335	260, 280, 303+361+353, 304+340+310, 305+351+338
Imidazole		360D, 302, 314	201, 280, 301+330+331, 305+351+338, 308+310
Iodoacetamide		301, 317, 334	261, 280, 301+310, 342+311
Maleimide		300, 314, 317	280, 301+330+331, 302+352, 305+351+338, 308+310
2-Mercaptoethanol		301+331, 310, 315, 317, 318, 373, 410	273, 280, 302+352, 304+340, 305+351+338, 308+310
Methanol		225, 331, 311, 301, 370	210, 233, 280, 302+352, 304+340, 308+310, 403+235
Nitrogen		280	403

Okadaic acid		301, 311, 331, 315	261, 271, 280, 264, 304+340, 311, 361, 362, 332+313, 270, 405, 501, 403+233
Paraformaldehyde		228, 302+332, 315, 317, 318, 335, 350	201, 210, 280, 302+352, 305+351+338
Phenylephrine		302, 315, 319, 335	261, 305+351+338
Phosphoric acid		290, 314	280, 301+330+331, 305+351+338, 308+310
2-Propanol		225, 319, 336	210, 233, 240, 305+351+338, 403+235
Propyl gallate		302, 317	280, 302+352
Sodium deoxycholate		302	301+312+330, 330
Sodium dodecyl sulfate		228, 302+332, 315, 318, 335, 412	210, 261, 280, 301+312+330, 305+351+338+310, 370+378
Sodium fluoride		301, 315, 319	302+352, 305+351+338, 308+310
Sodium hydroxide		290, 314	280, 301+330+331, 305+351+338, 308+310
N,N,N',N'-Tetramethyl-ethylenediamine		225, 332, 302, 314	210, 280, 305+351+338, 310

Thiourea		302, 351, 361d, 411	201, 273, 301+312+330, 308+313, 391, 501
Tris(hydroxymethyl)-aminomethane		315, 319, 335	280, 302-352, 305+351+338, 312
Triton® X 100		302, 315, 318, 410	280, 301+312+330, 305+351+338+310

8 Acknowledgment

This thesis would have been much more difficult or even impossible to produce if not supported by a number of people.

At first, I would like to thank Friederike Cuello who was a great supervisor for the entire duration of my PhD. Friederike's passion for science and her many ideas contributed decisively to drive the project forward. For her students, she always showed great commitment and did everything she could to be of support. Even with a full calendar, she always took the time to answer questions, give advice and make corrections. Through Friederike's guidance, I have learned a great deal and experienced a great time as a PhD student. Thank you for your continuing support.

I would also like to thank Konstantina Stathopoulou, who taught me many of the methods I applied in this thesis. Ntina is incredibly helpful, helped where she could and always had an open ear for problems and worries. Her view of things was always an enrichment. She also kindly performed the PLA assays shown in this thesis. Obviously, I am thankful to Angelika Piasecki, as she keeps the lab and even the whole institute together. She produces not only the best cakes but also the best ARVMs. Moreover, she helped with the analysis of NKY80-treated samples. Steven Schulz was a great lab and office mate. I am glad that he is such a clever guy, so he could share his impressive knowledge about image analysis and much, much more. He also shared his cMyBP-C-BirA virus. Overall, the time in the working group Cuello was always enriched by friendly and sympathetic colleagues.

Umber Saleem performed the EHT measurements with CXL-1020 and Sophie Schobesberger considerably contributed to FRET measurements, which were executed in the working group of Viacheslav Nikolaev. They both deserve my thanks. Ilka Wittig executed the MS analysis and data evaluation. I am very grateful for the time she spent to explain the data and provide those used to arrange the figures shown here. Moreover, Ilka fixed her imaging system just so I could use it for the detection of phosphoproteins.

I am also grateful to Thomas Eschenhagen, who always gave valuable input during presentations and let me be a part of this great institute.

Christian Betzel, who kindly agreed to be my second PhD supervisor, supported my project with his advice during meetings and I was always aware that he would help if needed. Thank you.

Markus Fischer and Thomas Lemcke who will be members of the examination board during my disputation also deserve my thanks.

Many other people contributed to this thesis by providing samples, equipment, advice or introduced me to new methods. Therefore, I would like to thank Metin Avkiran, Philip Eaton, Susanne Lutz, Sebastian Pasch, Lucie Carrier, Frederik Flenner, Leonard Oelze, Mathias

Acknowledgment

9 Affidavit / Eidesstattliche Versicherung

Hiermit versichere ich an Eides statt, die vorliegende Dissertation selbst verfasst und keine anderen als die angegebenen Hilfsmittel benutzt zu haben. Die eingereichte schriftliche Fassung entspricht der auf dem elektronischen Speichermedium. Ich versichere, dass diese Dissertation nicht in einem früheren Promotionsverfahren eingereicht wurde.

Hamburg, ____01.04.2019____ _____Simon Diering_____